An Enhanced Mechanistic Analysis Framework for Designing Resilient Airfield Pavements

by

Paula Sutherland Rolim Barbi

A thesis
presented to the University of Waterloo
in fulfillment of the
thesis requirement for the degree of
Doctor of Philosophy
in
Civil Engineering

Waterloo, Ontario, Canada, 2022

Examining Committee Membership

The following served on the Examining Committee for this thesis. The decision of the Examining Committee is by majority vote.

External Examiner	**Dr. Alan Carter** Professor, École de Technologie Supérieure, Département de génie de la construction
Supervisor(s)	**Dr. Susan Tighe** Adjunct Professor, University of Waterloo, Dept. of Civil and Environmental Engineering. Provost and Vice-President, Academic, McMaster University
	Dr. Pejoohan Tavassoti Assistant Professor, Jr. Norman W. McLeod Chair in Sustainable Pavement Engineering, University of Waterloo, Department of Civil and Environmental Engineering,
Internal Member	**Dr. Hassan Baaj** Professor, University of Waterloo, Dept. of Civil and Environmental Engineering
Internal-external Member	**Dr. Alexander Penlidis** Professor, University of Waterloo, Department of Chemical Engineering
Other Member(s)	**Dr. Vimy Henderson** Adjunct Professor, University of Waterloo, Department of Civil & Environmental Engineering
	Dr. Sina Varamini Adjunct Professor, University of Waterloo, Department of Civil & Environmental Engineering

Author`s Declaration

I hereby declare that I am the sole author of this thesis. This is a true copy of the thesis, including any required final revisions, as accepted by my examiners.

I understand that my thesis may be made electronically available to the public.

Abstract

Changes in climatic conditions can directly impact pavement performance. With alarming temperature records and the increased frequency of extreme weather events, Canadian infrastructure could be at risk if adaptation strategies are neglected. One such piece of infrastructure, namely airports, are essential to a country`s economic success. The construction and maintenance of long-lasting pavements at such facilities is not only important from an economic standpoint, but for the sake of safety. Therefore, it is crucial that airport infrastructure support safe and efficient transportation.

In the past two decades, the usage of mechanistic-empirical design procedures for the design of pavement structures has become more prevalent as compared to empirical methods. The use of such methods enables for the implementation of tools that can account for climate variations in pavement design. The mechanistic-empirical approach relies on predicting pavement responses under traffic and relating these responses to field performance. Pavement stress and strain calculations are necessary to estimate the damage to airport pavements over their service life. To this end, several methods are available, which can vary depending on the computational approach used and the way that material properties are considered. The successful mechanistic analysis of flexible pavements requires appropriate models that can accurately reproduce the pavement behavior. However, choosing the model that will best simulate the pavement responses can be a complex task.

This thesis examined some of the available computational approaches used for mechanistic analysis of airfield pavements to summarize the state-of-the-practice and to identify enhancement opportunities. Then, selected software packages were compared with field measurements from two case studies. The first case study compared three full scale pavement sections built for the A380 Pavement Experimental Program (PEP) with linear elastic simulations from KENLAYER, NonPAS and ABAQUS. The second case study analyzed the full-scale results from the National Airport Pavement Test Facility (NAPTF) and compared with non-linear elastic simulations modeled in KENLAYER, NonPAS and GT-PAVE. The outcome indicated that KENLAYER and NonPAS presented good results when predicting pavement vertical strains and stresses at the top of the subgrade in both case studies, however, the vertical displacements predicted in case two were quite far from the field measurements. ABAQUS and GT-PAVE successfully predicted the pavement compressive stresses as well as the vertical displacements.

The utilization of a design and structural analysis method that can accurately reproduce the pavement behavior can ultimately improve long-term performance and decrease the frequency of maintenance. Such method can provide realistic assessment of the performance evolution with time and hence allow for more effective and timely pavement management interventions to avoid premature failures. To this end, accounting for environmental factors in airport pavement design remains a challenge since most design methods do not consider inputs such as moisture and temperature variation. Between several airport pavement design methods, only two climatic factors are currently considered in the structural design, i.e., frost depth penetration and the reduction in subgrade bearing capacity due to spring thawing. Therefore, to address this research gap and improve the resilience of airport pavements, this research proposes a new methodology for the structural design of flexible airport pavements, utilizing an enhanced mechanistic-empirical approach that can better accommodate the climate change considerations.

The methodology proposed in this research was applied to a case study of Toronto Pearson International Airport, using actual field data. A total of five scenarios were evaluated including (1) the Current Climate, (2) Temperature Increase, (3) Lower Matric Suction, (4) and (5) two Flooding Events. The results of the "Current Climate" showed that the traditional FAARFIELD analysis can possibly overestimate fatigue damage and underestimate rutting damage.

Among all climate change scenarios evaluated, fatigue damage was found to be slightly affected by changes in soil saturation, which is present at the "Lower Matric Suction" scenario, and "Flooding Events". However, the effects of the "Temperature Increase" scenario presented fatigue damages that are 43% higher than the "Current Climate" scenario. From the results of climate change scenarios, it could be recognized that changes in soil saturation have a direct effect in the rutting damage. Both the "Lower Matric Suction" and the "Flooding Events" had great impact in rutting damage, however, the highest damage records happened due to the "Lower Matric Suction" scenario. The lowering of the matric suction due to an increase in the ground water table and precipitation levels affects the soil saturation and lowers the subgrade stiffness. The results showed that a significant decrease in the matric suction in Pearson International Airport could elevate damage in the order of about 117% when compared to the "Current Climate" scenario and decrease the pavement service life down to only a few years.

Considering the variations in climatic conditions due to the climate change, the proposed methodology can yield major benefits in terms of quantifying these impacts, which can ultimately help with design of more resilient transportation infrastructure such as airfield pavements. This platform enables accounting for climate variations, temperature increase, as well as extreme events such as flooding in the design of flexible airport pavements.

The assessment of an optimum design strategy for airport pavements also incorporated an evaluation of frost and thaw changes due to the temperature rise. The increase in temperature may result in the shortening of the freezing season, which can significantly impact airport pavement frost/thaw conditions. In this thesis, the potential effects of the warming temperature in pavement frost/thaw penetration and frost heave were assessed for critical airports across Canada. To that end, the Ministry of Transportation of Ontario (MTO), Ministère des Transports du Québec (MTQ) and Transport Canada Civil Aviation (TCCA) methods were used in the calculations and climate change simulations considering the emission scenario RCP8.5 in a 20 and 40-year horizon. The results show that climate change predictions result in shallower frost penetration depth and possibly less frost heave over the airports not underlain by permafrost, while airports over permafrost areas might experience an increase in thickness of the active layer. Among the different methods used, the Ministère des Transports du Québec's (MTQ) had the best performance in predicting

frost depth of fine soils, while the frost depth of coarse soils was better estimated by the Ministry of Transportation of Ontario (MTO).

This research was the first to propose an enhanced pavement design and analysis framework to improve the resiliency of flexible airfield pavements in face of the changing climate. The proposed framework is unique because it can account for the combined effect of materials properties, loading, and climatic conditions through a detailed analysis of the pavement responses. The implementation of the proposed framework allowed for an assessment of the impacts of temperature increase, lower matric suction, and flooding events in pavement performance in the case study of Toronto Pearson Airport.

Other key contributions include the study of the impacts of climate and climate change on flexible pavement materials, including the identification of the most relevant parameters for flexible airport pavements.

The study of strengths and weaknesses of commonly used methods available to predict pavement responses also provided important contribution, since the influence of using these different tools on the accuracy of the results had not yet been discussed in reference to actual field tests in the existing literature.

Lastly, this research provided a comparative study of the Canadian methods available to calculate frost depth, and its accuracy when compared to field data. The outputs can ease planning of future projects in Canada by facilitating the decision on what methods to use, and how ten (10) major airports in Canada will possibly be affected by the shortening of the freezing season.

Acknowledgements

First and foremost, praises and thanks to God, the Almighty, for his countless blessings, and for giving me strength and knowledge to develop this research. Thank you to my supervisor Prof. Susan Tighe, for providing guidance, for being an inspiration, for carrying about her students and always asking if we are exercising and eating well. Thank you to my co-supervisor Prof. Pejoohan Tavassoti, for tirelessly sharing his knowledge, for his invaluable advice and excellent feedback, for his support and encouragement. Thanks to Kevin Chee from the Greater Toronto Airports Authority, for providing me with field data.

I am deeply grateful to my husband Tiago for accepting to board into this journey with me of moving to a new country to pursue my dream. I also thank him for his love and support throughout my studies. I am thankful to my parents, grandparents, and sisters, for their tremendous encouragement and motivation to succeed. Further thanks to all the members of the Centre for Pavement and Transportation Technology (CPATT) group for being a warm and welcoming family.

Dedication

To my loving husband, Tiago, and my parents Rolim and Berenice

Table of Contents

List of Figures

List of Tables

List of Abbreviations

ALR	Aircraft load rating
APSDS	Airport Pavement Structural Design System
ANOVA	Analysis of Variance
AMT	Annual Mean Temperature
AC	Asphalt Concrete
AC	Asphalt Concrete
GB	Bituminous Gravel
CBR	California Bearing Ratio
CDF	Cumulative Damage Factor
FAA	Federal Aviation Administration
FAA	Federal Aviation Administration
FCVM	Finite Control Volume Method
FED	Finite Element Design
FT	Freeze-Thaw
FI	freezing index
FI	Freezing Index
GAS	Global Aging System
GAS	Global Aging System
GTAA	Greater Toronto Airports Authority
GWT	Ground Water Table
LED	Layered Elastic Design
MAAT	Mean Annual Air Temperature
MEPDG	Mechanistic Empirical Design Guide
MSE	Mean Square for Error
MSTr	Mean Square for Treatments
MTQ	Ministère des Transports du Québec’s
MTO	Ministry of Transportation of Ontario

NAPTF	National Airport Pavement Test Facility
NAPTF	National Airport Pavement Test Facility
NSRD	National Solar Radiation Database
P/C	Pass-to-Coverage ratio
PEP	Pavement Experimental Program
PG	Performance Grading
PGMN	Provincial Groundwater Monitoring Network
RCP	Representative Concentration Pathway
SWCC	Soil-Water Characteristic Curve
TEMPS	Temperature Estimate Model for Pavement Structures
TI	Thawing Index
TMI	Thornthwaite’s Moisture Index
TCCA	Transport Canada Civil Aviation

Chapter 1: Introduction

Scientific evidence for climate change is unequivocal. According to NASA, the recent warming trend has strong probability to be the result of human activity (NASA, 2020). The increasing global temperature is only one element of observed global climate change. Locally, other environmental aspects are changing, such as precipitation patterns, solar incidence, and the frequency of extreme weather events. The National Centers for Environmental Information points that some of the general consequences of climate change include the increase of surface temperature, rise of sea levels, increasing heat content in the ocean, decline in snow cover and shrinking of glacier volume (NOAA, 2020).

Climate change has a direct effect on the infrastructure of transportation systems. Highway, port, airport, and railway infrastructure have been suffering a shortening in service life, and consequently, there is a need for excess maintenance and premature rehabilitation. This contributes to the emission of more greenhouse gases (GHG), contributing to a vicious cycle that only promotes more climate change.

The effects of climate change on transportation systems will vary by region and mode (Brian, et al., 2007). Regarding roads and airport systems, environmental conditions play a significant role in the material properties and pavement responses. Although the effects of climate in pavement materials is evident, more research needs to be done to clarify the implications of climate change in the design, management, and operation of those pavements.

Airports are complex infrastructure systems similar to cities, containing a variety of infrastructure assets, for example, airside pavements (runways, taxiways, and aprons) and buildings, designed and operated to accommodate the takeoff and landing of aircrafts and facilitate passenger transportation. Hub Airports often operate 24 hours per day with intense utilization of runways, taxiways, and aprons. Therefore, maintenance operations taking place on airside areas need to be completed with superior planification and optimal time. Ensuring long lasting pavements at airports is not only important from an economic standpoint, but for safety. Structural pavement design that better incorporates design conditions can improve long term performance while decreasing the frequency of maintenance.

Accounting for environmental factors in airport pavement design can be considered a challenge since most of the design methods do not consider temperature and moisture variations, daily temperature fluctuation, wind, solar incidence, and the possibility of flooding events in its designing practices. Between several airport pavement design methods, the only climatic factors considered are the freezing index and spring thawing (Whiteley, 2006).

Having a better understanding of the implications of climate change in airport pavement performance and design is imperative for determining adaptation actions and building resilient airport infrastructure. However, there is a lack of a comprehensive method that would be able to capture climate variations in the structural design.

This study aims to address this research gap by proposing an enhanced pavement design and analysis framework to improve the resiliency of flexible airfield pavements. To that end, an overview of the impacts of climate and climate change in flexible pavement materials is performed; a review of airfield pavement design tools/methods is provided; methods and software packages available to predict airport pavement responses are compared to field data to assess the accuracy of the results; the proposed design framework is detailed, and a variety of climate change scenarios is accessed through a case study. Other key contributions include an evaluation of tools and methods to determine pavement frost/thaw conditions, recommendations towards the suitability of the approaches available; and lastly, an assessment of the effects of the shortening of the freezing season in pavement frost/thaw conditions to a variety of airports across Canada.

1.1 Hypothesis

The main hypotheses for this research are as follows:

- There is unanticipated pavement damage due to climate change.
- The effects of climate change can result in faster deterioration of pavements and a need for premature maintenance and rehabilitation.
- The change in natural climate can influence the pavement material properties and structural responses.
- The current pavement design practices are inadequate for dealing with future climate changes.
- The use of an enhanced pavement design method to account for climate change implications can improve airport pavement resiliency.

1.2 Objectives

Adaptation strategies for airport pavement design practices are necessary to provide the resilience that airport assets need when faced with challenging climatic changes. Therefore, the primary focus of this research is to propose an enhanced pavement design and analysis framework to improve the resiliency of flexible airfield pavements. The proposed methodology uses a mechanistic-empirical approach and was implemented in a case study using actual field data. The novel framework can contribute to designing more resilient airport pavements in the future, since it is equipped to account for climate variations, temperature, and moisture changes as well as extreme events such as flooding over the design life of flexible airport pavements.

The specific objectives of this research are to:

- Evaluate how different climate parameters can influence the pavement materials properties and structural responses. The following climate parameters were investigated:

  - Maximum temperature
  - Duration of the freezing season
  - Daily thermal oscillation
  - Precipitation and flooding
  - Freezing and thawing cycles

- Assess available tools/methods for the mechanistic analysis of airport pavements. The following methods/tools were investigated:
  - Layered Elastic Design: KENLAYER, and NonPAS
  - Finite Element Method: ABAQUS and GT-PAVE

- Evaluate the implications of climate change in the structural design and cumulative damage of airport pavements through the analysis of different climate scenarios, such as:
  - Current climate
  - Temperature increase
  - Lower matric suction and
  - Flooding events

- Investigate the impacts of the shortening of the freezing season in pavement frost/thaw conditions by:
  - Evaluating current methodologies available to determine frost/thaw depth and frost heave
  - Estimating changes in frost/thaw depth and frost heave due to climate change over several locations across Canada

1.3 Organization

This thesis has been organized in eight chapters. Chapter 1 introduces the study, presents the research hypothesis, and explains the research goals. Chapter 2 encompasses a review of the literature on climate change indicators and its consequences to flexible pavements; it presents a general background and comparison among airport pavement design methods, and provides considerations on the mechanistic analysis to obtain pavement responses.

Chapter 3 presents the general research methodology. Details are provided regarding the proposed pavement design and analysis framework, including a discussion about the methodology used to determine rutting and fatigue damage, as well as the tools available to obtain pavement responses. Considerations are also drawn on pavement frost and thaw conditions. The proposed methodology is summarized in seven steps to facilitate the implementation by designers.

Chapter 4 discusses about different computational tools used for mechanistic analysis of airfield pavements. The chapter provides a review of various software advantages and limitations and accesses several tools by comparing predicted pavement responses with field measurements through two case studies.

Chapter 5 provides the implementation of the proposed methodology through the case study of the Pearson International Airport, using actual field data. To assess the possible effects of climatic parameters and climate change on the airport pavement performance, first, the methodology is cross-verified by the design of a flexible pavement structure using FAARFIELD to ensure that a total CDF=1 is achieved. Then, the same layer thickness resulting from the FAARFIELD design is used to evaluate current climate and climate change effects on the CDF of the most critical aircraft from the traffic fleet mix operated at the airport. A total of five scenarios are evaluated throughout the research, including the Current Climate, Temperature Increase, Lower Matric Suction, and two Flooding Events.

Chapter 6 discusses the implications of the shortening of winter seasons for frost and thaw penetration depths and frost heave in Canadian Airports. A total of three methodologies proposed by the Ministry of Transportation of Ontario (MTO), the Ministère des Transports du Québec’s (MTQ) and Transport Canada Civil Aviation (TCCA) are evaluated.

Chapter 7 presents the general conclusions, main research contributions and recommended future work. Lastly, Chapter 8 provides the study references.

Chapter 2: Literature Review

Climate change has become obvious from current observations in climatic events, such as frequent droughts, heat domes, floods and other extreme weather events. However, it took hundreds of years of research and data to convince the majority of people, even the scientific community, that man could alter the climate of the planet through its actions. Some of the first thoughts about climate change come from 1719, when the Abbé Jean-Baptiste Du Bos wrote a book that relates the change in culture with the change in climate in some regions (Fleming, 2005).

Jean-Baptiste Joseph Fourier, a French mathematician and physicist, born in 1824 is considered to be the first person to study the Earth's temperature from a mathematical perspective. "The analytical theory of heat" (Baron Fourier, 1878) involved calculating the effect of the sun radiation in earth and concluded that the Earth's atmosphere acts like an insulator, what is nowadays called the greenhouse effect. In simple words, the greenhouse effect is a process that occurs when gases in Earth's atmosphere trap the Sun's heat (NASA, 2020).

One of the first scholars that believed in the influence of human activity on climate change was Svante August Arrhenius, who was able to estimate a direct relationship between atmospheric carbon dioxide and the Earth's increasing surface temperature. In 1896 Arrhenius predicted the variation of temperature caused by a given variation of carbonic acid (Arrhenius, 1896).

Despite those and many other studies on greenhouse effect, in the 1970s scientists were still doubting if global warming was tangible or not. It was only in the 1980s that consensus began to form. James Hansen pointed out the rise in temperature between the middle of the 1960's and 1980, and how consistent that is with the calculated greenhouse effect and called the attention to the potential effects on the 21st century, including the erosion of the West Antarctic ice sheet with a consequent worldwide rise in sea level (Hansen, et al., 1981).

The National Aeronautics and Space Administration (NASA) points out that the evidence for rapid climate change is compelling: a global temperature rise, warming oceans, shrinking ice sheets, glacial retreat, decreased snow cover, sea level rise, declining arctic sea ice, ocean acidification, and increase in extreme events occurrence (NASA, 2020). The Intergovernmental Panel on Climate Change (IPCC) says that there will be more frequent hot and fewer cold temperature extremes, and that heat waves will occur with a higher frequency and longer duration (Intergovernmental Panel on Climate Change, 2014). The consequences of climate change are specific for each location. While some areas will experience more precipitation, including frequency and intensity, other locations are suffering from the thawing of the permafrost and shortening of winter season, while others are struggling with drastic short time temperature fluctuations.

The climate change predictions for Canada and all high latitude territories, according to the Intergovernmental Panel on Climate Change (IPCC), is that those areas are likely to experience a reduction in permafrost area near the surface of 37% (RCP2.6 scenario) to 81% (RCP8.5 scenario) by 2100 (Intergovernmental Panel on Climate Change, 2014).

Projected climate and current weather changes have important consequences for the long-term safety and functionality of pavements. For any paved structure, the change in extreme maximum temperature can cause thermal expansion of rigid pavement joints, adversely affecting operations and increasing maintenance costs; it can also increase rutting of flexible pavements. Increased freeze–thaw cycles can induce frost heaves and potholes. Structures built on permafrost will be damaged due to lateral spreading and settlement of embankments. If precipitation rises in large scale, risk of landslides will increase, and flooding will be more likely to occur. This can also result in soil moisture levels becoming too high, compromising the pavement structural integrity (Meyer, et al., 2014).

Adaptation strategies are crucial for helping to avoid or withstand the current and projected climate changes impacts. The adaptation should decrease a system's vulnerability and increase its resilience to impacts (Shaw, Pulhin, & Pereira, 2010).

Hub airports around the world often operate 24 hours per day. At these airports, pavement maintenance and rehabilitation often require the effort of large engineering teams to accomplish operations in a short amount of time to release the pavement for traffic. The improvement in the long-term performance of airport pavements is necessary for decreasing the frequency of maintenance and rehabilitation. Effectively accounting for climate parameters in the design can be beneficial to improve the resiliency of airport pavements, enhance long term performance and reduce the need for maintenance and rehabilitation practices.

The perception of how climate change is affecting airport pavements in Canada varies from region to region. A survey developed at the Centre for Pavement Transportation and Technology (CPATT) at the University of Waterloo (Vanheule, Lu, Dutton, & Tighe, 2017) collected information from a variety of airport authorities around Canada on their perspective on climate change impacts in their infrastructure. A thoughtful analysis on this survey was conducted by Abreu (Abreu, 2019).

The results showed that all airports surveyed were already considering climate change on their decision making, from 38% to 100% of the time. The consequences of climate change were perceived differently between them. All airports reported an increase in early cracking and crack severity, with more evidence in Northern Canada airports. This could be happening due to the increase of freeze-thaw cycles and because of an intensification in thermal fatigue. The provinces of Ontario and British Columbia perceived more rutting, possibly due to the temperature and precipitation increase. Heaving and settlement were more sensed in northern territories, probably due to the melt of permafrost layers in the warmer seasons. Also, the airport of British Columbia and some other airports reported an increase in pumping as a result of elevated water pressure.

All airports surveyed agreed that the main factors contributing to their early degeneration are related to the rise in frequency and intensity of precipitation, the increase in maximum temperatures, and the enlarged number of freeze-thaw cycles, to some extent, while the northern territories agreed that they were also suffering from the decrease of permafrost depth. Among the main barriers reported to contemplate climate change risk and adaptation/mitigation for pavements is the lack of requirements in codes, standards, or policy. When asked if new design strategies were necessary to mitigate climate change impact, the answer was a unanimous yes (Abreu, 2019).

Including environmental factors in airport pavement design can be considered a challenge, since design methods for airport structural pavement design do not consider factors such as precipitation, freezing and thawing cycles, minimum and maximum temperature, daily temperature fluctuations, solar radiation, wind speed, etc. The only current climate parameters effectively being considered are the freezing index and the spring thawing (Whiteley, 2006).

Frost protection means that frost susceptible materials should not be present at any layer and within a certain depth of the subgrade. Therefore, the freezing index has a direct influence on the total thickness of the pavement structure. Reduced strength of the subgrade, due to spring thawing, can be accounted by strength reduction factors recommended by Public Works Canada. Those factors vary between 0 and 50%, depending on the subgrade type. Canadian airport pavements should be designed based on the spring reduced subgrade bearing strength, as this represents the weakest period during the life of the structure. Thus, spring thawing has a direct effect on the thickness of the pavement layers.

Regarding moisture, design methods require a good drainage system to be provided within the pavement structure, but moisture has no direct implication on the thickness of the layers. The temperature maximums and minimums are also not accounted as an influential factor on the thickness of the pavement layers, affecting only the choice of the binder (Whiteley, 2006).

Therefore, there is an urgent need for adaptations on structural airport pavement design to account for climate factors. Measuring more effectively how different climate parameters can influence the pavement material properties and structural responses is the first step in this journey. Section 2.1 will analyze each climate change indicator in more detail, to understand how they can influence the pavement materials and structural performance.

2.1 Climate change indicators

2.1.1 Maximum temperature

The last three decades have been successively warmer at the Earth’s surface than any preceding decade since 1850. The Intergovernmental Panel on Climate Change points out that the period from 1983 to 2012 was likely the warmest 30-year period of the last 1400 years in the Northern Hemisphere, and that it is very likely that heat waves will occur more often and last longer in the near future. On daily and seasonal timescales, it is certain that there will be more frequent hot and fewer cold temperature extremes.

In 2019, a detailed report concerning the temperature changes in Canada was published by Environment and Climate Change Canada. This report presented several crucial facts that could affect the life cycle of transportation infrastructures. Based on this report, by analyzing the temperature data between 1948 to 2019, it can be concluded that the annual average temperature increased by 1.7ºC in Canada.

The average spring and autumn temperature increased by 1.7ºC from 1948 to 2019. Moreover, throughout the very same timeframe, winters got warmer by 3.3ºC. The least change in seasonal average temperature was in the summer, with 1.4ºC increase. The most changes in regional temperature were recorded in northern provinces and territories such as Yukon, Northwest Territories, and Nunavut. These changes can significantly reduce the thickness of glaciers, increase sea levels and significantly endanger species (Environmnet and Climate Change Canada, 2019).

The Government of Canada has developed an online tool with the ability to demonstrate possible scenarios of climate change in Canada. This tool projects twenty-year average changes in three timeframes: Near-term: 2016 to 2035, Mid-term: 2046 to 2065, Long-term: 2081 to 2100. Figure 2.1 shows the long-term projected temperature changes in Canada (Environmnet and Climate Change Canada, 2019).

There are three gas emission scenarios presented in Figure 2.1. They are the Representative Concentration Pathway (RCP) 2.6, 4.5, and 8.5, in the sources of confidence of 25th, 50th, and 75th percentiles.

The change in extreme maximum temperature can cause serious damage to the pavement structure. For flexible pavements, there is a potential increase in rutting and shoving, and a premature age hardening of the asphalt binder (Muench & Dam, 2015). Rutting is a permanent deflection that has two main mechanisms, (a) the AC rutting, which is the AC distortion under the wheel paths due to a densification or dislocation of the AC mix, and (b) the structural rutting that happens in the subgrade due to an accommodation or densification of the subgrade soil. The increase in maximum temperature can increase the phenomenon of rutting in the asphalt concrete mix, diminishing riding quality and safety (Mills, et al., 2017), and it can also increase the structural rutting, since the loss in stiffness of the AC layer can result in elevation of the compressive strains at the subgrade top.

On July 18th, 2022, an extreme heat wave has caused a disruption in flights operations of the Luton Airport, the fifth busiest airport in the United Kingdom. The airport authorities attributed the disruption to an “essential runway repair" that was required "after high surface temperatures caused a small section to lift”. This happened only hours after the Royal Air Force (RAF) paused all flights to and from Brize Norton, its biggest air base in Oxfordshire, after a report from Sky News suggested that the runway had "melted" (CNN, 2022). The word melting, used in the news, is an extreme description of what likely took place, that is, a loss of firmness, or stiffness, in isolated regions.

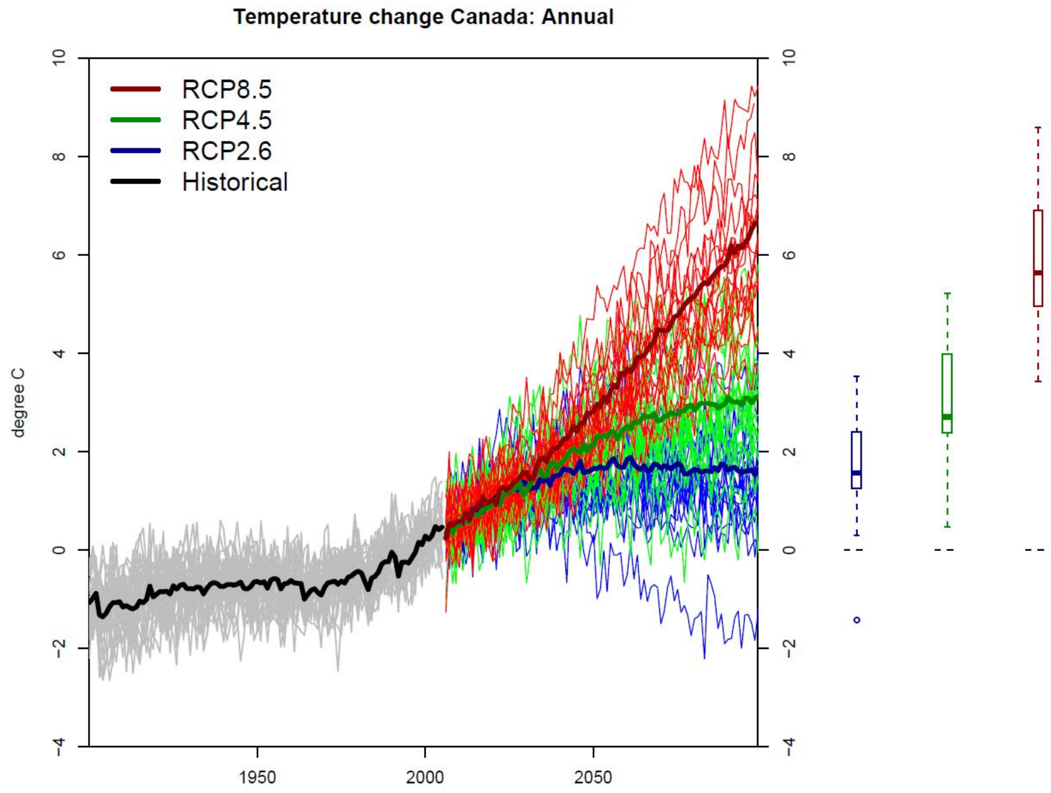

Figure 2.1: Projected Temperature Changes in Canada (Environmnet and Climate Change Canada, 2019)

The rheological properties of asphalt vary significantly with temperature. As asphalt temperature increases, the stiffness decreases, leaving it more susceptible to deformation under heavy loads. Some adjustments to build asphalt concrete mixes less susceptible to extreme heat are (a) to use higher temperature binder grade and possibly increase the use of binder polymerization, (b) to improve aggregate structure by using stone matrix asphalt mixture gradation and (3) to increase the thickness of the AC layer (Muench & Dam, 2015), (Swarna, Hossain, Mehta, & Bernier, 2022).

Another possible consequence of the temperature increase in pavements is the intensification in fatigue deterioration. Fatigue is determined by the rheological status of the mixture (Lundström, Isacsson, & Ekblad, 2003). Since the rheological properties of any HMA mixture are linked to the temperature, it is possible to connect temperature as an important factor in fatigue cracking as well.

In conclusion, there is evidence that the temperature in Canada has increased significantly in the past decades and studies show that if no change is made in the amount of gas emissions, the temperature will continue to increase. In face of that, current design practices must be adjusted to assure rutting and fatigue damage in airport pavements will not be aggravated.

2.1.2 Shortening of Freezing Season

With the temperature increase, the timing and duration of winter freeze and spring thawing are going to change in all cold regions, directly impacting frost and thaw penetration depth (Daniel, et al., 2018).

The study of Daniel et al. (2018) used an ensemble of climate models to forecast how climate change might affect freeze and thawing processes beneath roadways in the Minnesota area. The results of that study showed that the duration for which the pavement cross section is frozen will be significantly decreased in the next 30 years, and that shallower frost depths are projected for the end of the century. Figure 2.2 shows the predicted frost depth in different sites in Minnesota, demonstrating that projected frost depths under emission scenario RCP 8.5 become shallower at a greater rate than the emission scenario RCP 4.5 after the year of 2040. The results also showed that the sites with deeper frost penetration had larger changes over time and larger differences between the low and high-emission scenarios at the end of the century.

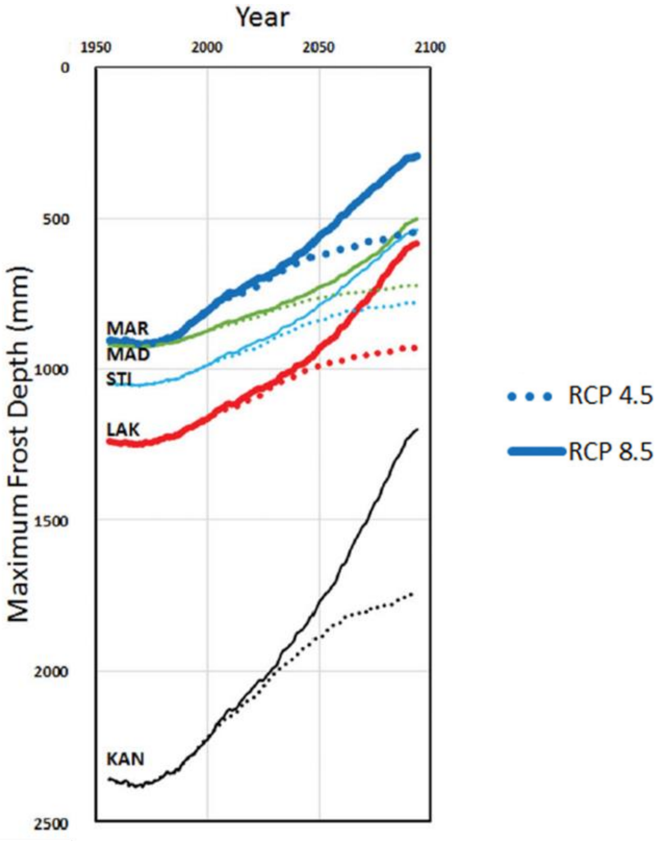

Figure 2.2: The projected maximum frost depths using actual pavement cross-sections. Adapted from (Daniel, et al., 2018).

Similarly, Canadian pavement frost/thaw conditions will be impacted by the warming climate. With shorter freezing season lengths in Canada, not only will the frost penetration depth decrease but also the minimum pavement thickness requirements to cope with frost penetration, which may possibly lower the initial cost of construction. Alternatively, areas underlain by permafrost may suffer a decrease in pavement strength due to melting of the frozen layers.

Permafrost temperature in Canada has increased over the past three to four decades. Regional observations have shown warming rates of about 0.1ºC per decade in the central Mackenzie Valley and 0.3ºC to 0.5ºC per decade in the high Arctic. Such increments might seem modest; however, permafrost layers can be highly vulnerable to thawing since soil temperature in those regions are already close to zero (Environmnet and Climate Change Canada, 2019). Melting of the permafrost soil will increase the seasonal active layer thickness, that is, the upper part of the ground that freezes and thaws each year. It has been reported that the seasonal active layer thickness in the Mackenzie Valley has increased by approximately 10% since 2000 (Environmnet and Climate Change Canada, 2019), making those areas more prone to deformations caused by freeze-thaw cycling.

The use of systems and/or materials that reduce heat transfer between surfaces and permafrost layers have been used with the goal of protecting permafrost layers and maintaining their support. Although such techniques are not the focus of this research, thermal insulation can be a suitable approach to mitigate the effects of the shortening of the freezing season in areas underlain by permafrost. Regardless of the use of thermal insulation, it is important to ensure that pavements are built with appropriate depth of frost/thaw protection.

Knowing how climate change can impact airport pavement frost and thaw conditions is essential for better planning of future projects in Canada. However, there are currently no specific studies available in the literature to assist with decision making in this area. To this end, this thesis will analyze how the shortening of the freezing season can affect frost/thaw penetration and frost heave in several locations across Canada.

2.1.3 Daily Thermal Oscillation

Thermal oscillation is the difference between the highest and the lowest temperature registered in a place during a given period. Sometimes, the difference of temperature extremes can be enormous, for example, in the Arizona desert located in the United States, there can be thermal oscillations of up to 56 °C in the same day (Boreal Science, 2012).

There were global scale changes in the frequency and intensity of daily temperature extremes in the past decades (Intergovernmental Panel on Climate Change, 2014). With the global increase of temperature, thermal oscillation may be more likely to occur and the temperature differences between day and night could be aggravated.

The cycle of temperature increase and decrease generates tension in the pavement due to the expansion and shrinkage of the asphalt concrete (AC) mix. The cracks that are generated when induced thermal fatigue exceeds the fatigue resistance during thermal cycling are called thermal fatigue cracking. This phenomenon can happen in both cold and moderate climates since it depends mostly on the temperature variation.

Damage due to one day-night temperature fluctuation may be imperceptible, but the accumulated damage due to the repetition of cycles may not be small. There are several research evidencing that accumulated daily temperature extremes can cause severe consequences to flexible pavements (Zhao, Shen, & Ma, 2018) (Zhao, Shen, & Ma, 2020).

Although the effects of thermal oscillations on the pavement performance is proved, most pavement design methods predict fatigue performance of asphalt concrete based only on traffic-induced tensile strain at the bottom of the layer. The thermal strain due to day-night temperature fluctuation is not considered since there is no open or closed-form software available that would include the matter in its practices (Islam & Tarefder, 2015). The possible consequences of not considering thermal fatigue are the shortening of the pavement design life and increase in maintenance and rehabilitation frequency.

2.1.4 Precipitation and Flooding

Many studies on climate change show that precipitation patterns will change around the world. Some areas will experience more frequent and possibly more intense precipitation events, while other areas will suffer with drier seasons. According to the Intergovernmental Panel on Climate Change, in the mid-latitude land areas of the Northern Hemisphere, precipitation has increased since 1901 (Warren & Lemmen, 2014). Figure 2.3 presents the patterns of change in annual total precipitation over the period 1950–2010 in Canada, showing that most areas had significant rise in precipitation rates over the studied period.

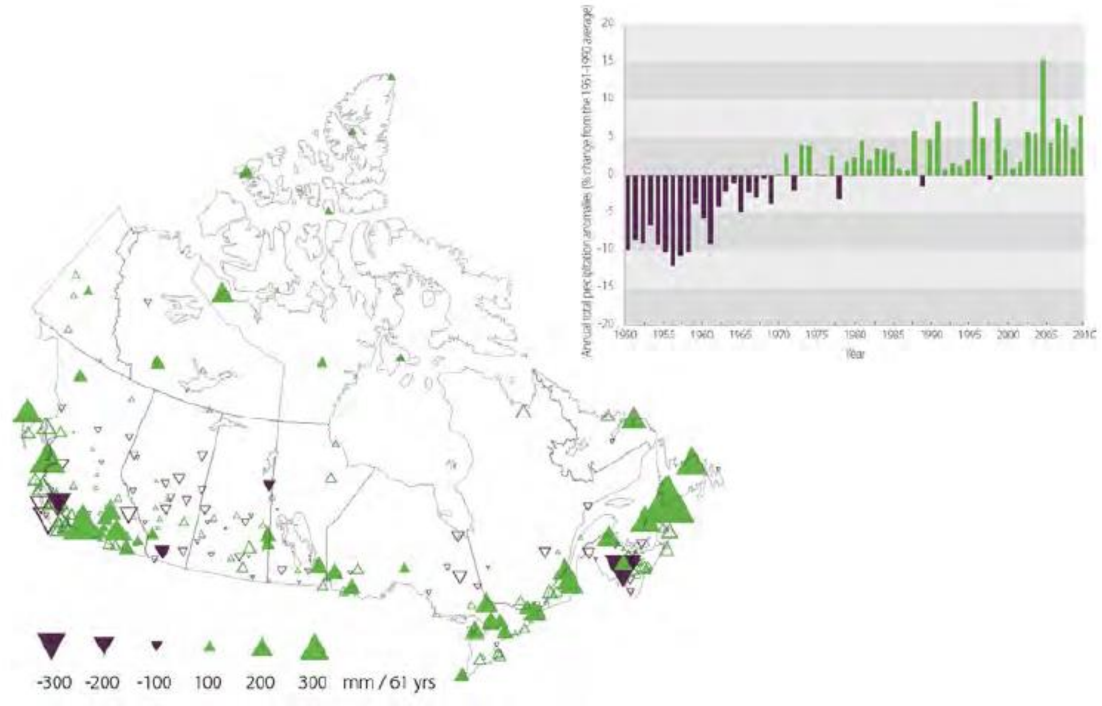

Figure 2.3: Patterns of change in annual total precipitation over the period 1950–2010 in Canada (Warren & Lemmen, 2014).

In general, Canada has become wetter with increasing annual average precipitation trends in many parts of the country and for the nation as a whole. Rare extreme precipitation events are projected to become about twice as frequent by mid-century over most of Canada (Warren & Lemmen, 2014). Flooding is already identified as the most frequent natural hazard in Canada (Government of Canada, 2019), and with climate change, the risks of flooding hazards will possibly increase, becoming even more evident in coastal areas in Canada, due to the rise of sea levels (Donghui, 2020).

Flooding of road and airport infrastructure can jeopardize mobility, safety and functionality, resulting in social and economic losses. On May 13th, 2022, the Hay River/Meryln Carter Airport (CYHY) in the community of Hay River in Canada's Northwest territories was flooded due to rain, snow melt and ice flows. The flooding event affected the airport and roads in the region, impacting the entry to and egress from the community as well as the delivery of supplies, which is heavily dependent on the airport. The extent of flooding in the Hay River/Meryln Carter Airport runway can be seen in Figure 2.4.

Figure 2.4: Flooding in Hay River/Meryln Carter Airport (Godlewski, 2022).

Other major flooding events in airports around the world include the LaGuardia Airport in New York City, USA, which was struck by Hurricane Sandy in 2012, resulting in the flood of airport runways and taxiways. Rockhampton Airport in Australia had its runway inundated and closed for weeks in 2011. In December 2015 the India`s Chennai Airport had water reaching the under carriage of aircraft and an inundated runway after two days of heavy and continuous rain. Flooding has also affected Vanguardia Airport in Villavicencio, Mexico, in May 2022, and Kansai International Airport in Japan, in September 2018.

The moisture content of pavement materials are usually affected by climate through precipitation, surface runoffs, soil type, ground water table (GWT), among other factors. Excessively saturated materials can lead to degradation of pavements through three main mechanisms: (1) A reduction in the resilient modulus of granular layers and subgrade soil can lead to greater permanent deformations; (2) The tensile strain in the bottom of the AC layer can increase in magnitude due to a decrease in support, resulting in more extensive fatigue cracking; (3) Adhesive and cohesive forces in AC can be weakened by moisture content (Canestrari, Cardone, Graziani, Santagata, & Bahia, 2010) leading to pathologies known as stripping or raveling. There are also other secondary degradation mechanisms because of water infiltration, such as, subgrade volume changes, pumping of water and fines through cracks and distresses associated with frost heave (Arnold, 2004). Pavement characteristics such as cross slope, potential for infiltration and length of drainage path can play an important role in the pavement drainage and moisture content.

To avoid rapid degradation of pavements when subject to increased precipitation levels and flooding events, it is important to ensure appropriate drainage at the granular layers. Unbound granular layers need to follow the appropriate layer specifications to cope with gradation limits as well as material requirements.

Other alternatives to mitigate the effects of the increase in pavement saturation levels and potential decrease in subgrade support is to consider soil stabilization through the use of cement, lime, lime-fly ash, among other materials. Lastly, the increase in thickness of the granular layers may also be required to improve the general pavement strength.

In conclusion, the change in climate will most likely impose a general rise in precipitation in Canada, and possibly increase the frequency of flooding events. This could potentially shorten the pavement service life and increase the need for maintenance and rehabilitation; therefore, current design practices must be adjusted to ensure rutting and fatigue damage in airport pavements will not be aggravated.

2.1.5 Freeze-Thaw Cycles

A freeze-thaw (FT) cycle is a fluctuation of the pavement's surface temperature, from above freezing (>0°C) to below freezing (<0°C) and then back to above freezing. The damage of a freeze-thaw cycle starts when the temperature is above zero, and rainwater or snowmelt penetrate in small cracks and air voids of the asphalt pavement. Suddenly, the temperature falls below freezing, and the water contained in those cracks and voids expands, damaging the AC mix from the inside out. After the temperature rises again, the frozen water contained in pores and cracks melts, allowing the water to move deeper into the pavement. When the cycle starts over, the water that moved to lower layers can freeze again, causing frost heave and depressions when melted.

The general rise in temperature in Canada will lead to an increase in the number or freeze-thaw cycles in northern areas, because periods with negative fluctuating temperature will shift to varying from negative to positive, while southern areas in Canada will possibly experience a decrease in the number of FT cycles, since there will be less days during the year when the temperature falls below zero.

Laboratory tests performed at the Centre for Pavement and Transportation Technology (CPATT) at the University of Waterloo showed that freeze-thaw cycles cause the asphalt mix to become softer, making it more susceptible to rutting and shoving (Abreu, 2019). The research tested AC mix samples up to 3 FT cycles, following the standards of AASHTO T 283. The resulting deformation of samples under wheel passes for up to three FT cycles are presented in Figure 2.5 (a).

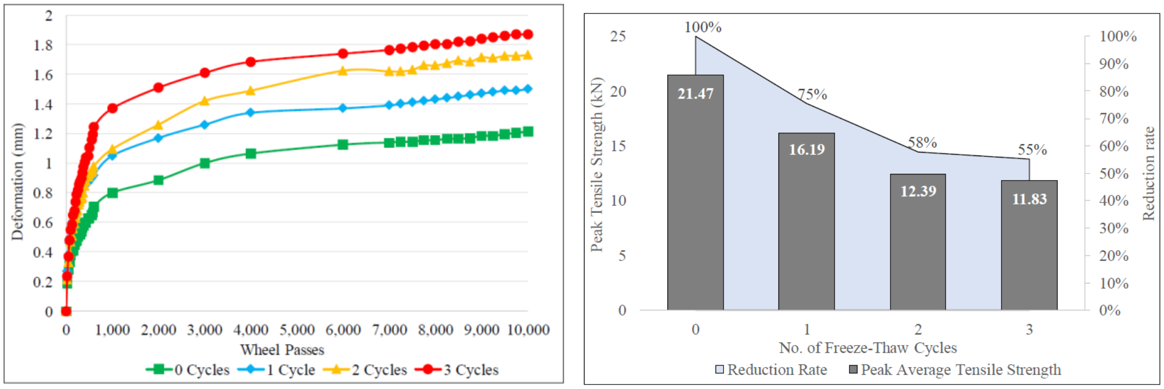

Figure 2.5: (a) Deformation of samples under wheel passes for different number of freeze-thaw cycles; (b) Tensile strength versus the number of freeze-thaw cycles (Abreu, 2019).

In the same study, it was shown that not only deformation under compression forces were increased but the tensile strength was significantly affected by FT cycles in early stages. Figure 2.5 (b) shows the reduction in the tensile strength of the samples under FT cycles.

Additional research has produced similar results regarding the depreciation of AC under this condition. For example, Özgan & Serin showed that the number of FT cycles can decrease the Marshall Stability by 77.4% after 24 days of cycles (Özgan & Serin, 2013). The work of Feng (Feng, Yi , Wang, & Chen, 2010) also shows a decrease in tensile strength ratio when samples were subjected to repeated FT cycles, with very similar pattern from Abreu (2019).

Gong et al. performed the Bending Beam Rheometer (BBR) test in a variety of asphalt mixes and obtained a consistent decrease in the stiffness of all mixes when the number of FT cycles increased. At 32 cycles, the percentage decrease of stiffness ranged from a minimum of 7% up to 27%, at $-6℃$ (Gong, Romero, Dong, & Sudbury, 2016).

The literature review of Teltayev et al. (2019) points out that after 20 cycles of freezing and thawing, the fatigue strength of the asphalt concrete and bitumen can decrease by 37% and 41%, respectively. The same authors point out that there is a critical decrease of dynamic modulus of an asphalt concrete mix after FT cycles having occurred during one single winter season in southern Ontario, Canada (Teltayev, Rossi, Izmailova, & Amirbayev, 2019).

The FT cycles can also impact directly on the compressive strength and resilient modulus of the AC. Research shows that the degradation is sharp during the initial FT cycles, and after 8 cycles, the degradation curve becomes more gentle (Wei, et al., 2015). It is presented in Figure 2.6 that after 14 FT cycles, the compressive strength is reduced by nearly 0.33MPa, or an attenuation of 15.6%, while the resilient modulus reduces by nearly 147 MPa (attenuates by 18.7%).

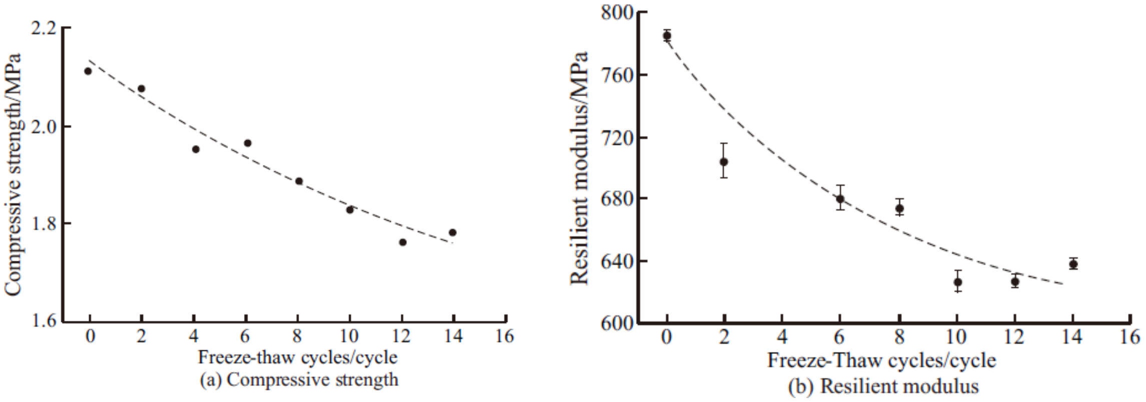

(a) Compressive strength

(b) Resilient modulus

Figure 2.6: Impact of Freeze-Thaw cycles on compressive strength and resilient modulus (Wei, et al., 2015).

The sharpness of the curves presented in Figure 2.6 will depend on the material properties and asphalt aggregate ratio, that is, the percent asphalt binder by total weight of HMA. For example, Figure 2.7 presents what the resilient modulus is under 0, 6, 10 and 14 cycles, and the depreciation ratio is different for all of the different mixes, as the asphalt-aggregate ratio changes.

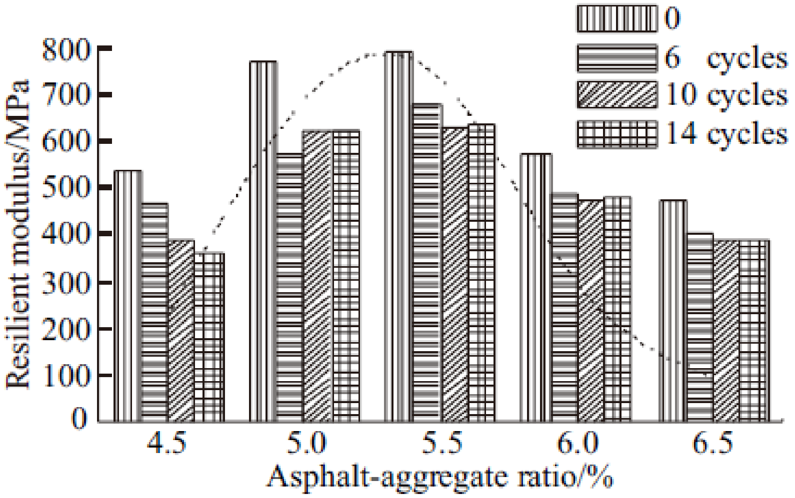

Figure 2.7: Impact of asphalt-aggregate ratio on resilient modulus (Wei, et al., 2015).

As the resilient modulus decreases, rutting resistance also decreases. The work of Wei, et al. (2015), showed that after 50 cycles of freezing and thawing, rut depths formed on the surface of the asphalt concrete samples after 10,000 wheel passes were nearly three times (269.7%) bigger (Wei, et al., 2015). However, modification with polymers was shown to have a positive effect, as all samples modified with polymers after 50 cycles of FT demonstrated an actual increase in rutting resistance. Figure 2.8 presents the results for stone mastic asphalt concrete with neat bitumen, in the first section, and polymer modified stone mastic asphalt concrete in the next sections of the graph.

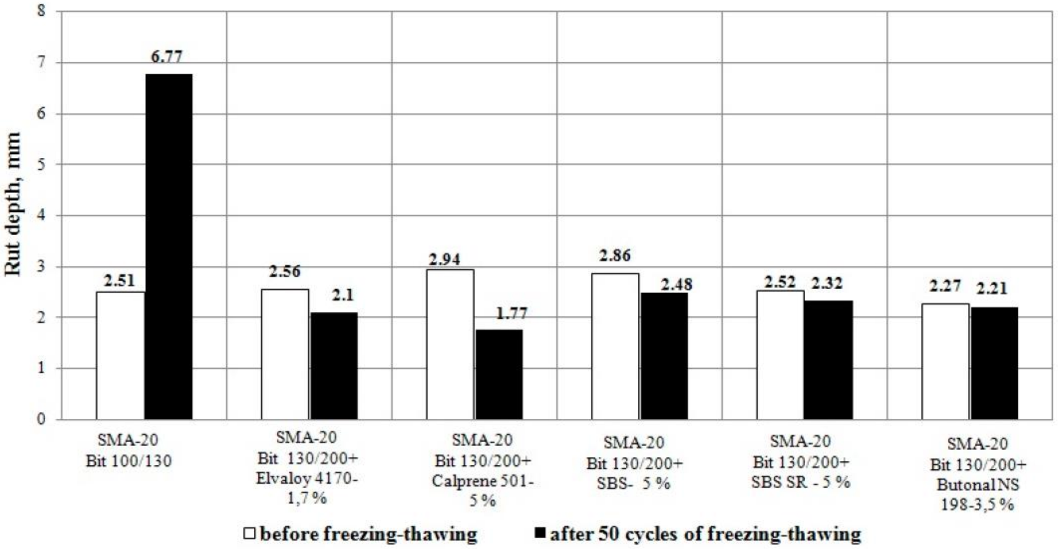

Figure 2.8: Rut depth on the samples of stone mastic asphalt concretes after 10,000 wheel passes (Wei, et al., 2015).

Despite all effort to assess the effects of FT cycles in the mechanic properties of AC mixes, there is no closed equation that relates the number of cycles, the materials properties, and the stiffness. Therefore, it is yet not possible to assertively predict rutting and fatigue damage of asphalt concrete pavements under a certain number of FT cycles.

2.2 Airport pavement design methods

Airport pavements require closer attention than any other pavement because they suffer concentrated high-speed loads, and a structural flaw can lead to serious consequences for the safety of the users. Airport pavement structural design can be classified into three main categories: experience based, empirically based, and mechanistic-empirical.

Experience based methods rely on standard sections that presented good performance in the past and are re-used in cases with similar soil, traffic, and climatic conditions. The empirical methods are based on field observations. They use the results of measured responses to determine pavement limits for successful sections with varying aircraft traffic levels. The empirical methods can provide the design thickness for a set of design gear loadings and subgrade bearing strengths (Whiteley, 2006). Transport Canada Civil Aviation (TCCA) specifies the use of an empirical design methodology presented in the ASG-19 manual.

The mechanistic-empirical approaches addresses the mechanistic analysis of the pavement under any type of loading. This method can calculate the pavement responses and correlate them with damage. The approach allows for design inferences that would be hard to estimate from the limited view of an empirical method. Some of the most well-known mechanistic-empirical software available are the FAARFIELD from the Federal Aviation Administration (FAA), and the APSDS developed in Australia.

The following sections of this chapter will address with more details the three structural pavement design methods mentioned above: FAARFIELD, APSDS and ASG-19.

2.2.1 FAA FAARFIELD

The design of flexible pavements through empirical methods have been used for decades. Even FAA, in the Advisory Circular AC 150/5320-6D (FAA, Advisory Circular, 1995), recommended the use of pavement thickness design charts (nomographs), based on the US Army Corps of Engineers California Bearing Ratio (CBR) pavement design method, before making use of the layered elastic system for flexible pavements. The need for better pavement design came with the introduction of bigger and heavier aircrafts, with complex gear configurations, such as the B777 and A380.

A computer program called LEDFAA 1.3 was released by FAA in 2004. The program had an expanded aircraft library that replaced the concept of the "design aircraft" by the design for fatigue failure expressed in terms of a Cumulative Damage Factor (CDF) using Miner's rule (Gary, Leigh, & Michael, 2016). Another advancement was the use of the elastic modulus E and a poison ratio ν instead of the CBR to characterize the soil strength.

The most recent version of the FAA design software is called FAARFIELD. This is a platform based on Layered Elastic Design (LED) for flexible pavements and three-dimensional Finite Element Method (FEM) for rigid pavements, developed to calculate design thicknesses. For an airfield pavement to be considered compliant with FAA, it must be designed with FAARFIELD, which makes it the most relevant design code for airport pavement engineers in the US (Heymsfield & Tingle, 2019).

The codes used in FAARFIELD can be considered mechanistic-empirical, because they are based on the mechanics of the materials, but the software failure models are calibrated using full-scale test results. This includes work conducted by the U.S. Army Engineer Waterways Experiment Station and more recent pavement testing performed at the FAA William Hughes Technical Center, National Airport Pavement Test Facility (NAPTF) (Heymsfield & Tingle, 2019).

The CDF concept assumes that the contribution of each aircraft type in a given traffic mix results in accumulated damage for the pavement. The process to calculate the thickness of the layers is iterative, consisting of 4 main analysis steps: (1) inputs, including aircraft mix, pavement structure and materials, and definition of design life, (2) mechanistic calculations (stresses/strains), (3) calculation of the allowable aircraft number of departures in the design period, and (4) the cumulative damage. If the cumulative damage is different than 1, the thickness of the layers must be adjusted, and the process goes in a loop until CDF reaches the optimum value. Figure 2.9 illustrates the iterative solution process used in FAARFIELD (Heymsfield & Tingle, 2019).

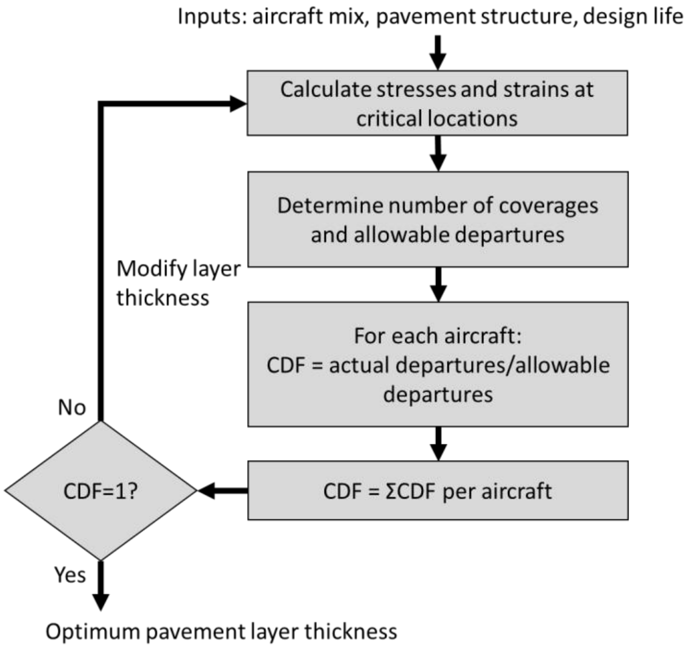

Figure 2.9: FAARFIELD solution process. Modified from (Heymsfield & Tingle, 2019).

Since the configuration of airplane gears can vary a lot, and with the contribution of aircraft wander (natural lateral offset of aircraft from the centreline of the pavement), the total damage to the pavement is better estimated if calculated separately for each aircraft and then summed. Figure 2.10 presents the cumulative damage on the pavement in relation to the centreline, whose position is 0 on the x-axis.

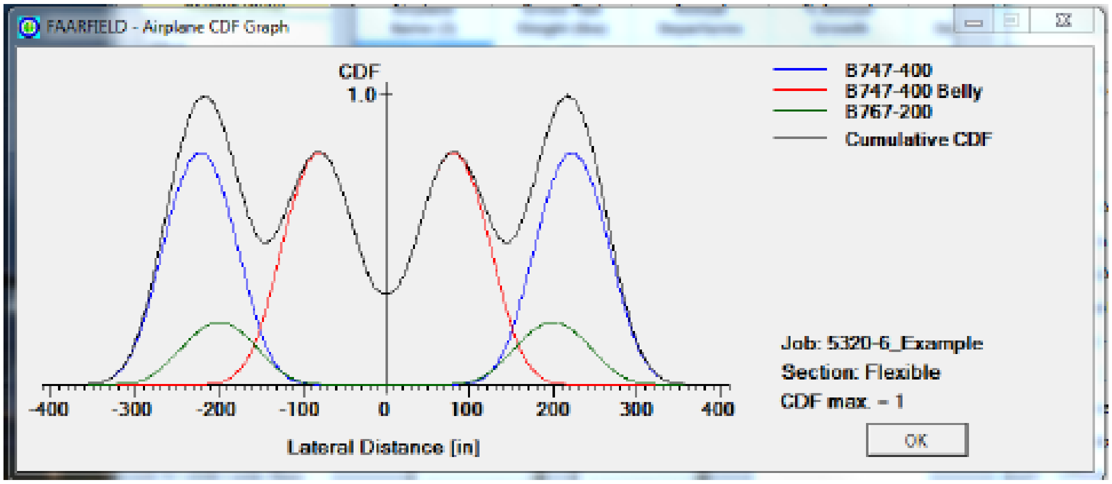

Job: 5320-6_Example
Section: Flexible
CDF max. = 1

Figure 2.10: CDF Contribution for Airplane Mix (FAA, 2016).

FAARFIELD does not require the user to input any climatic information. Different from Mechanistic Empirical Design Guide (MEPDG), that uses the temperature as one of the indicators to predict rutting and fatigue, and that considers precipitation as an important factor for rutting, FAARFIELD disregards climatic information.

As discussed throughout the literature review in section 2.1, climate change indicators have direct consequences on the materials' behavior. For example, the temperature has a direct correlation with the stiffness of the AC mix, however in FAARFIELD, a fixed modulus value for hot mix surfacing is set in the program at 200,000 psi (1380 MPa). The advisory circular 150/5320-6F affirms that this modulus was conservatively chosen and corresponds to a pavement temperature of approximately 32°C (90°F) (FAA, 2016).

Therefore, the software calculates pavement damage considering the AC stiffness corresponding to 32°C all year long. The same happens for precipitation, since the software considers that the granular materials and subgrade soil have constant stiffness over the year, even though it is known that wet seasons will greatly degrade the support capacity of those materials.

2.2.2 APSDS Australia

The Airport Pavement Structural Design System (APSDS) is a software with pavement structural design codes based on the layered elastic theory. In a similar manner to FAARFIELD, it uses transfer functions to convert the calculated mechanistic response values to pavement distress, using equations obtained through full-scale tests. The software is based on design standards used in Australia and New Zealand (Jameson, 2008).

Research has compared the design of airfield pavements using APSDS 5.0 and FAARFIELD 1.32 and showed that there were two main differences between both tools: (1) in APSDS, subgrade strains were computed for all points across the pavement in order to capture damage contributed by all the aircraft wheels, while FAARFIELD computed rutting damage based on a single maximum strain; and (2) there were differences in the calibration parameters used in APSDS to construct failure models (Gary, Leigh, & Michael, 2016).

Due to such differences, the APSDS 5.0 design method yielded pavement structure thicknesses that were far from FAARFIELD v1.32 for CBR smaller than 10% (Gary, Leigh, & Michael, 2016). However, on May 2017, a new version of FAARFIELD was launched, version 1.41, which included new subgrade failure models for flexible pavements using full-scale traffic tests from the National Airport Pavement Test Facility NAPTF construction cycles 3 and 5. The implementation of the new subgrade failure models in FAARFIELD have approximated the results with APSDS 5.0, specially for subgrades with CBR⩾5% (Chai, Bell, McNabb, Wardle, & Oh, 2022).

Figure 2.11 (a) shows the comparison between FAARFIELD 1.302 and APSDS 5.0 design thickness, considering a fleet mix that includes 147,120 movements of the B777-300 ER, 47,280 movements from the B747-400 ER, 13,920 movements of the A340-300, and 4,320 movements of the A340-300. Figure 2.11 (b) shows the comparison between FAARFIELD 1.42 and APSDS 5.0 design thickness, considering 100,000 movements of the B777-300 ER. It is important to note that the configuration of the layers in the analysis made in 2016 is different from the analysis of 2022, and the goal of presenting those images side by side is to show that in general, the results of the most recent analysis have more proximity.

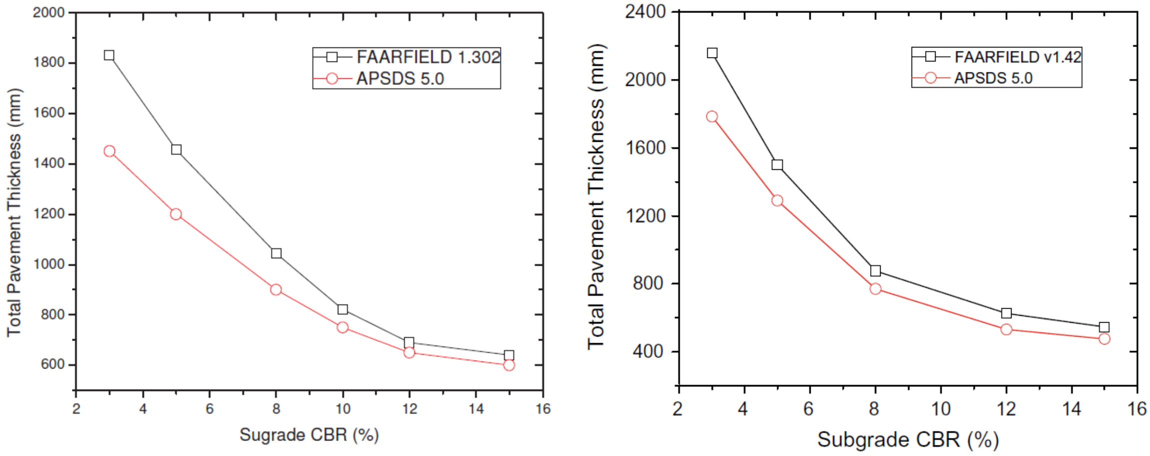

(a) (b)

Figure 2.11: Pavement thicknesses produced by APSDS and FAARFIELD (a) version 1.302 of FAARFIELD (Gary, Leigh, & Michael, 2016), (b) version 1.42 of FAARFIELD (Chai, Bell, McNabb, Wardle, & Oh, 2022).

APSDS considers aircraft wander, modelled by a normal distribution, and calculates the CDF as a function of lateral position across the pavement, varying from 0, no damage, to 1, when the pavement is presumed to have reached its design life (Figure 2.12).

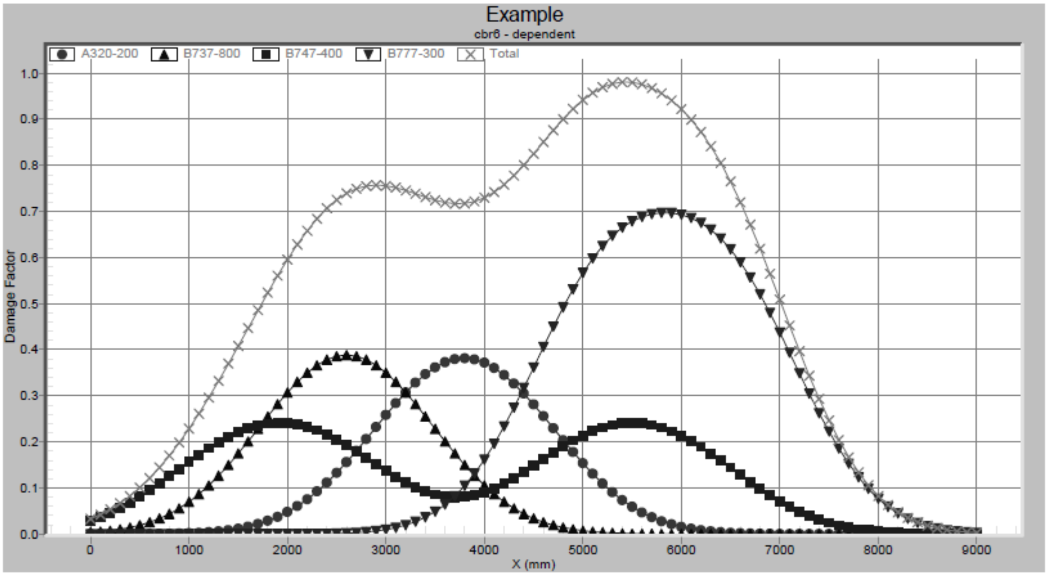

Figure 2.12: APSDS 5.0 CDF Graph showing CDF variation across a pavement (Wardle & Rodway, 2010).

2.2.3 Transport Canada ASG-19

Transport Canada is a federal institution in Canada responsible for transportation policies and programs. Their manuals, ASG-19 (TCCA, 1992) and Pavement Structural Design

Training Manual ATR-021 (TCCA, 1995), presents standards and guidelines on the structural design of airport pavements.

The method is purely empirical, and requires three main inputs: design loading, subgrade bearing strength, and site freezing index. For loading, the method considers classes of aircrafts, providing the users with a series of twelve standard gear loadings, as can be seen in Figure 2.13. Therefore, the method is grounded in the assumption of a design aircraft, instead of a fleet mix. Aircraft load ratings (ALR's) were published in 2008, including the new larger aircraft (NLA) such as the Boeing 777 and the Airbus 380 (TCCA, 2008), however, the original design method did not directly consider the impacts of these NLA.

The subgrade bearing strength is measured as the load required to produce a deflection of 12.5 mm after 10 load repetitions at the subgrade surface through a rigid plate. The value recommended for the design is the lower quartile strength measured along the pavement area. The manual also recommends the use of spring reduction factors in locations where frost penetrates the subgrade soil, to reduce the strength values measured during the summer and fall. The spring reduction factors range from 10% to 50%, depending on the soil type.

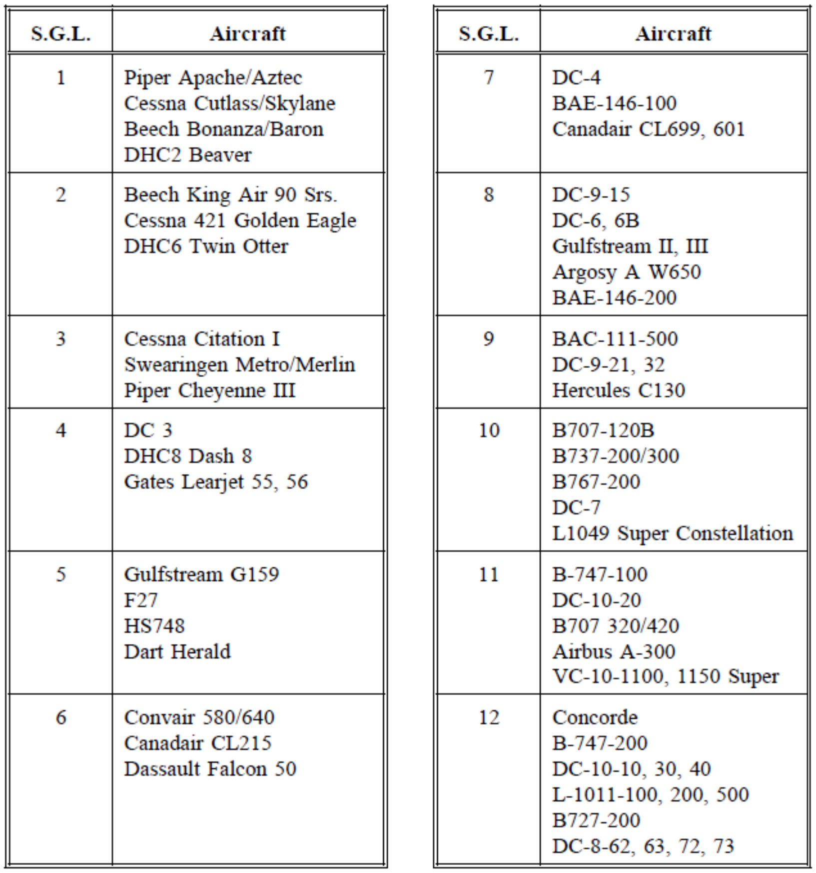

S.G.L.	Aircraft
1	Piper Apache/Aztec Cessna Cutlass/Skylane Beech Bonanza/Baron DHC2 Beaver
2	Beech King Air 90 Srs. Cessna 421 Golden Eagle DHC6 Twin Otter
3	Cessna Citation I Swearingen Metro/Merlin Piper Cheyenne III
4	DC 3 DHC8 Dash 8 Gates Learjet 55, 56
5	Gulfstream G159 F27 HS748 Dart Herald
6	Convair 580/640 Canadair CL215 Dassault Falcon 50

S.G.L.	Aircraft
7	DC-4 BAE-146-100 Canadair CL699, 601
8	DC-9-15 DC-6, 6B Gulfstream II, III Argosy A W650 BAE-146-200
9	BAC-111-500 DC-9-21, 32 Hercules C130
10	B707-120B B737-200/300 B767-200 DC-7 L1049 Super Constellation
11	B-747-100 DC-10-20 B707 320/420 Airbus A-300 VC-10-1100, 1150 Super
12	Concorde B-747-200 DC-10-10, 30, 40 L-1011-100, 200, 500 B727-200 DC-8-62, 63, 72, 73

Figure 2.13: Aircraft corresponding to standard gear loadings

The depth of frost penetration in a frost susceptible soil is calculated based solely on the freezing index, which is a measure of the severity of freezing condition during the winter season in the area. Equivalent granular thickness is used as a common basis to evaluate different design structures.

Some of the limitations in the method proposed by Transport Canada is that it ignores recent advances on the mechanics of the materials, which makes it difficult to account for the implications of climate and climate change on pavement performance.

The Transport Canada manual ASG-19 (TCCA, 1992) has no recommendations towards failure modes, mainly because it is an empirical method, and the failure mode evaluation requires a mechanistical approach that accounts for stresses and strains. Therefore, the increase of temperature and precipitation levels, among other climate factors, as well as its consequent increase in rutting and fatigue cannot be considered in the design practices contained in the ASG-19 manual.

2.3 Mechanistic considerations

Pavement stress and strain calculations are key to estimate damage of airport pavements over their service life. To this end, several methods are available, which can vary depending on the computational approach used and the way that material properties are considered.

The successful mechanistic analysis of flexible pavements requires appropriate models that can accurately reproduce the pavement behavior, however, choosing the model that will best simulate the pavement responses can be a complex task. Although more advanced models and sophisticated techniques can potentially improve the accuracy of the modeling, the required computation time and cost of retrieving the necessary input parameters can be a hurdle. Therefore, selection of the right modeling tool to use will be a trade-off depending on the nature of the analysis and level of accuracy required for a specific task. To this end, one must decide about the right constitutive models to represent the materials properties (e.g., linear elastic and stress dependent models) as well as select the solution approach that can be either analytical or numerical.

The analytical solution has been widely used in the past through the Layered Elastic Design (LED) approach. Flexible pavement structural analysis and design codes typically use this method to estimate pavement responses, however, advances in knowledge on material behavior and computer technology has greatly increased interest in numerical techniques, such as the Finite Element Method (FEM).

There is not a unique answer to prescribe specific constitutive models or a certain type of solution, since each method has its advantages and limitations. Current research often tends to show preference to very complex analysis that can take several hours to converge. However, this may pose some difficulties with respect to practicality for routine analysis cases from an industry perspective. Therefore, the following sections will shed some light on the available options to obtain pavement mechanistic responses.

2.3.1 Layered Elastic Design

Flexible pavement structural analysis and design codes typically use the Layered Elastic Design (LED) approach (Heymsfield & Tingle, 2019), in which, the calculated stresses and strains are translated into distresses through transfer functions, and the design is usually achieved through an iterative process. When using the LED approach, the predicted damage should be smaller than or equal to a certain threshold, with the goal of limiting pavement distresses during its design life.

Layered elastic analysis can compute stresses, strains, and deflections at any given depth of a pavement structure by relating the load applied to the modulus of elasticity and Poisson's ratio. The basic assumption of this type of model is that each layer is homogeneous, isotropic, and linearly elastic (Burmister, Palmer, Barber, & Middlebrooks, 1944). Although it is well known that the pavement materials are not essentially linear elastic, it is common practice to assume that they exhibit linear elastic behavior when subjected to the application of moving traffic loads. These simplifying assumptions have been historically used for the sake of practicality and achieving acceptable accuracy within a reasonable computation cost.

On the other hand, the effect of loads on nonlinear granular materials can be also computed within the layered elastic analysis context through the use of an approximation artifice, that consists of dividing the nonlinear half-space into a number of layers and determining the stresses at the mid-height of each layer using Boussinesq's equations, and finally, calculating the elastic modulus for each layer (Huang, 1993). It is important to notice that this iterative process, present in many LED codes, is only an approximation, and the approach can lead to inaccurate tensile stresses in the granular material layers (Heymsfield & Tingle, 2019).

Despite the limitations of using the Layered Elastic Design for the analysis of flexible pavements, most design packages are based on the layered elastic analysis to compute stresses, strains, and deflections. The flexible airport pavement design software: FAARFIELD, Alize-Airfield, PAVERS and APSDS, all use the layered elastic analysis to compute flexible pavement responses.

Some of the available LED based tools for pavements structural analysis are: KENLAYER, CHEVRON, DAMA, ELSYM5, BISAR, EVERSTRESS, and NonPAS. Both KENLAYER and EVERSTRESS have the ability of considering the nonlinear characteristics of granular materials; however, they only allow using K-θ and Bilinear constitutive models through the iteration technique previously explained. On the other hand, NonPAS allows for more options to perform nonlinear analysis of flexible pavements and utilizes five constitutive models including K-θ, Uzan's, Uzan-Witczak's, MEPDG (2002), and the Bilinear models (Ghanizadeh & Ziaie, 2015).

From a user perspective, it is possible to affirm that the two main advantages of pavement modeling using the multi-layered theory are the simplicity of the analysis and the shorter computational time as compared to the finite element method. When performing structural analysis on a certain pavement, the computational time may not be of the highest concern.

Whereas, for the pavement design purpose, in which the layers thicknesses are determined based on the cumulative damage factor and design life, sometimes hundreds of iterative solutions are processed, before identifying the optimum pavement structure. Therefore, when performing a mechanistic analysis and design of an airport pavement structure, the researcher or engineer should have in mind the level of accuracy one wants to reach as well as the computational time that can be afforded.

2.3.2 Finite Element Method

Another technique that can be used to compute pavement responses is the Finite Element Method (FEM). FEM can offer several advantages over the conventionally used LED techniques such as estimating the responses of a variety of structures (either conventional or unconventional), can accommodate a wider range of materials properties, and provides flexibility to better model the actual wheel loads configuration and contact area.

When comparing pavement responses using linear elastic assumption for the materials properties, the results from both LED and FEM methods should be very close, provided that (1) the FEM elements have reasonable dimensions, (2) boundary conditions are properly defined and do not influence stresses and strains close to the location(s) of the applied load(s), and (3) the layer interfaces are considered to have full friction (i.e., fully bonded condition). In such conditions, the FEM models compared with LED models can present very good correlation. However, when considering visco-elastic or stress dependent materials in both methods, the pavement responses can be different.

Studies have shown that granular unbonded materials, as well as cohesive fine-grained subgrades, usually present nonlinear properties, interpreted in the form of stress dependent moduli (Tutumluer, 1995). There are a few FEM software available in the market, such as ILLI-PAVE, GT-PAVE and MICH-PAVE, that can consider the nonlinearity of the granular pavement layers in a two dimensional (2D) axisymmetric analysis. These three software packages have been widely used in the past for the mechanistic analysis of pavements, and their results showed a good agreement with measurements from full scale studies (Kim, Tutumluer, & Kwon, 2009) (Gopalakrishnan, 2004).

Despite their many advantages, the aforementioned software packages have some limitations that can affect the quality of the analysis. Firstly, they can only consider the asphalt concrete layer as a linear elastic material; therefore, the user does not have the possibility to directly consider the asphalt concrete viscoelastic properties. Furthermore, ILLI-PAVE, GT-PAVE and MICH-PAVE perform two-dimensional (2D) analysis, considering the pavement structure as being axisymmetric, which limits the analysis to one wheel at a time. Therefore, to be able to account for the effect of multiple wheel gear loads, the user would have to manually calculate the responses using the principle of superposition. However, linearity is a core assumption for the superposition principle, and hence such approach can lead to some level of error in the cases where pavement materials nonlinearities are being considered.

To overcome the inconsistencies arising from the 2D axisymmetric finite element analysis and field measurements, many studies have been conducted using a three-dimensional (3D) finite element analysis (Kim, Tutumluer, & Kwon, 2009) (Kim & Tutumluer, 2008). General-purpose FEM programs, such as ABAQUS, ANSYS and ADINA, can deal with three-dimensional problems, however, readily available built-in material models found in these software are not applicable to the nonlinear elastic response of pavement geomaterials, resulting in a need for the researcher to develop user-defined material model sub-routines (UMAT) (Kim, Tutumluer, & Kwon, 2009).

Another downside of using 3D finite element analysis is that the computational time and memory requirement to run the models are much higher compared to the 2D approach, and for this reason, this type of analysis has been mainly performed in research projects and are rarely incorporated into a practical design procedure (Huang, et al., 2019).

As a final perspective, it is important to notice that there are many potential sources of error in any pavement design analysis. The inputs such as traffic loads, material properties and the pavement performance transfer functions all have a certain degree of inaccuracy associated with them. Therefore, the development of sophisticated and complex structural models does not necessarily improve the pavement design procedure (Schwartz, 2002).

2.4 Summary and research gaps

The literature review has shown that climate change has been impacting pavement infrastructure through many mechanisms. It has been discussed that the increase in temperature is affecting asphalt mixes mainly by causing an increase in rutting and shoving, and that the shortening of the freezing season is impacting subgrade frost/thaw conditions, implicating in permafrost thawing and the increase in seasonal active layers over the northern regions. The possibility of an increase in daily thermal oscillations and its implications for pavement performance in terms of fatigue was also discussed in the literature review, as well as the effects of an increase in precipitation patterns and flooding events, which could result in considerable shortening of the pavement service life.

The last climate factor discussed was the change in the number of freeze and thaw cycles, which has been proven to impact the asphalt mix compressive strength and resilient modulus. Although there has been great interest in the implications of climate change in pavement performance in the last decade, there are still many gaps to be addressed. For instance, despite all efforts to assess the effect of freeze-thaw cycles in the mechanical properties of AC mixes, there is no closed-form equation that relates the number of cycles, the materials properties, and the stiffness.

It has been discussed that airport pavement design methods/tools available, such as FAARFIELD, APSDS and ASG-19 do not allow their users to consider the effects of climate change. The method proposed by Transport Canada in the ASG-19 manual has recommendations towards frost protection and subgrade bearing strength spring reductions, however, since it is an empirical method, it becomes impossible to adapt it to the climatic changes. The mechanistic empirical methods for airfield pavements, on the other hand, attribute fixed modulus values for the pavement layers, disregarding the effects of climate on the resilient modulus along the year.

Stress and strain calculations are key to estimate the damage induced on airport pavements over their service lives; therefore, close consideration was given to the mechanistic analysis of airport pavements. Two main solutions to obtain pavement responses were discussed: the layered elastic design and the finite element method. It was found that there is not a unique answer to prescribe a certain type of solution or specific constitutive models, since each method has its advantages and limitations, and the selection of the right modeling tool in each case can be challenging. A summary of the main characteristics, advantages and disadvantages of the airport pavement design methods and mechanistic analysis tools reviewed over Chapter 2: are presented in Table 2.1.

Table 2.1: Summary of airport pavement design methods and mechanistic analysis tools.

Method/ Software	**Main Characteristics**	**Advantages**	**Disadvantages**
FAARFIELD	Mechanistic Empirical. Based on LED for flexible pavements and FEM for rigid pavements	• Design for fatigue failure considering the aircraft mix and aircraft wander	• Does not take into consideration climatic characteristics
APSDS	Mechanistic Empirical. Based on LED for flexible pavements and FEM for rigid pavements	• Design for fatigue failure considering the aircraft mix and aircraft wander	• Does not take into consideration climatic characteristics
Transport Canada ASG-19	Empirical method	• Empirically developed for Canadian environmental conditions • Has shown efficacy under the aircraft conditions to which it has been developed (exclude NLA)	• Design for critical aircraft/standard gear loading, instead of a fleet mix • Has no recommendations towards failure modes, due to its empirical nature • Does not take into consideration climatic information, besides frost penetration and subgrade spring reduction factors

Method/ Software	**Main Characteristics**	**Advantages**	**Disadvantages**
Layered Elastic Design	An analytical method based on the assumption homogeneous, isotropic, and linearly elastic layers	• Simplicity of the analysis and short computational time.	• The effect of loads on nonlinear granular materials needs to be computed through the use of an approximation artifice, which can lead to inaccurate tensile stresses in the granular material layers • Does not provide flexibility to model the wheel loads configuration and contact area
Finite Element Method	General numerical method for solving partial differential equations. FEM subdivides a large system into smaller, simpler parts that are called finite elements.	• 2D analysis takes short computational time • General purpose 3D FEM software can accommodate a wide range of materials properties • General purpose 3D FEM software provides flexibility to model the wheel loads configuration and contact area	• 2D FEM software consider the pavement structure as axisymmetric, which limits the analysis to one wheel at a time • General purpose 3D FEM software do not have readily available built-in pavement material models for non-linear analysis • Computational time and memory requirement to run 3D models are much higher compared to the 2D FEM and LED approach

Chapter 3: Research Methodology

3.1 Overal view

The overall objective of this research is to determine the implications of climate change in airport pavement design and performance in Canada. This goal is achieved through three main phases of this study by:

1. Evaluating how different climate parameters can influence the pavement materials properties and structural responses.
2. Assessing available tools/methods for the mechanistic analysis of airport pavements, and
3. Developing and implementing a methodology for quantifying the influence of climate on the fatigue and rutting damage in a flexible airport pavement structure utilizing a Mechanistic-Empirical approach.

These three main phases are summarized and illustrated in Figure 3.1 and more details on each phase are provided below.

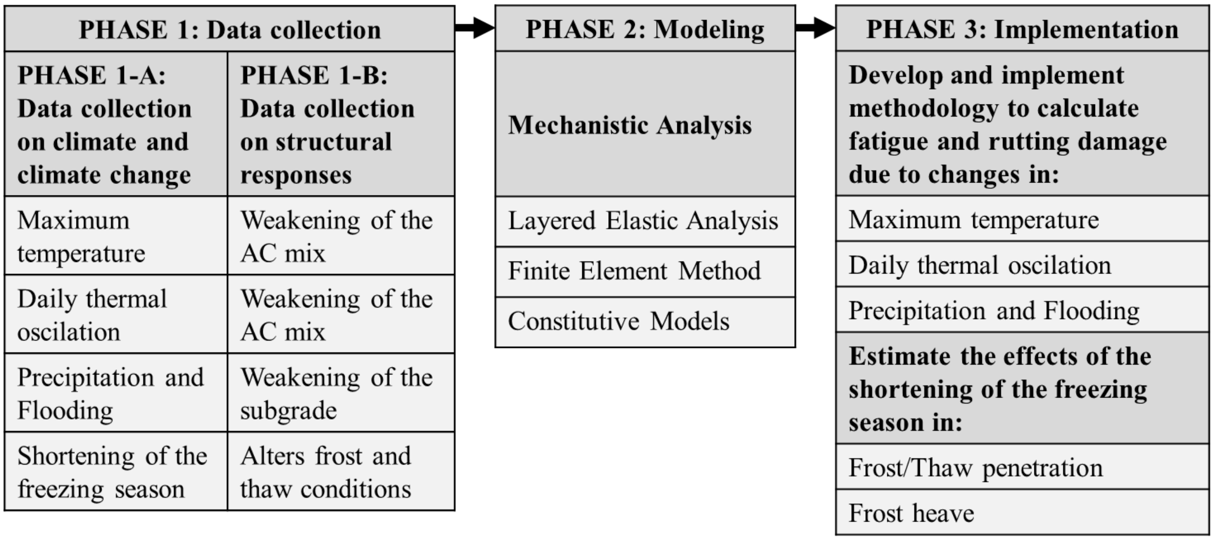

Figure 3.1: Research methodology.

Phase 1 of this methodology consists mainly of data collection. It is divided into two parts, starting with Part 1-a. This part includes data collection and processing on climatic indicators, with the main source of data for this task being the National Solar Radiation Database (National Renewable Energy Laboratory, 2022) for current climate data. For climate change predictions, the Climate Atlas of Canada (Prairie Climate Centre, 2022) and the Weather Morph File Generator available at http://139.62.210.131/weatherGen/ were used.

Phase 1-b includes collecting information on the consequences of climatic indicators on the material’s behavior. For example, it was discussed in section 2.1.1 that an increase in temperature decreases the stiffness of the asphalt concrete mix, diminishing its resistance to rutting and fatigue. The equations that dictate this behavior were studied and included into the implementation portion during Phase 3.

Phase 2 consists of assessing the tools and methods for the mechanistic analysis of airport pavements. This phase includes a comparison between the layered elastic analysis, finite element method and some of the material constitutive models available.

In Phase 3 the proposed methodology to incorporate climatic factors in pavement design were implemented in the form of coding in Python language. To that end, failure models, also known as damage model equations, were coded in order to convert pavement mechanistic responses into a pavement damage factor with the goal of quantifying rutting and fatigue damage. This phase also included the application of the proposed methodology in the case study of Toronto Pearson International Airport.

Lastly, Phase 3 also included a study of the effects of the shortening of the freezing seasons for frost and thaw penetration depths and frost heave in Canadian Airports. A total of three methodologies proposed by the Ministry of Transportation of Ontario (MTO), the Ministère des Transports du Québec’s (MTQ) and Transport Canada Civil Aviation (TCCA) were evaluated, and different climate change scenarios were assessed.

3.2 Cumulative Rutting and Fatigue Damage

Airport pavement transfer functions connect pavement responses to the number of coverages that the pavement can carry. Coverages can be defined as the number of repetitions of the maximum strain before failure. Rutting and fatigue coverages are determined by distinct models. The number of coverages to rutting failure is defined in FAARFIELD 1.41 by a bilinear model, as presented in Equation 3.1 (Kawa, 2017).

$$\begin{aligned} C &= 10^{\left(\frac{1}{a+b+\varepsilon}\right)^{\frac{1}{c}}}\ (coverages > 1000) \quad or \\ C &= \left(\frac{0.00414131}{\varepsilon}\right)^{8.1}\ (coverages \leq 1000) \end{aligned} \tag{3.1}$$

Where,

- $a = -0.163768916705$ (Dimensionless)
- $b = 185.192806802$ (Dimensionless)
- $c = 1.65054449461$ (Dimensionless)
- ε is the extreme vertical strain at the top of the subgrade (Dimensionless)

To determine the number of coverages to fatigue failure, the older FAARFIELD version 1.305 used the “Heukelom and Klomp” failure model, according to Equation 3.2 (Loizos A. , Armeni, Plati, & Cliatt, 2019).

$$Log_{10}(C) = 2.68 - 5 * Log_{10}(\varepsilon_h) - 2.665 * Log_{10}(E_{AC}) \quad 3.2$$

Where,

- C = the number of coverages to fatigue failure (Dimensionless)
- ε_h = the horizontal tensile strain at the AC bottom (Dimensionless)
- E_{AC} = the modulus of elasticity of AC layers (psi)

Therefore, the old fatigue failure model was only related to the critical strains and stiffness of the AC layer. Version 1.42 of FAARFIELD, however, introduced the use of a new model, based on the Ratio of Dissipated Energy Change (RDEC) (Loizos A. , Armeni, Plati, & Cliatt, 2019). The mathematical function is defined according to Equations 3.3 and 3.4 (Shen & Carpenter, 2007).

$$C = 0.4801 * PV^{-0.9007} \quad 3.3$$

$$PV = 44.422 * {\varepsilon_h}^{5.14} * S^{2.993} * VP^{1.85} * GP^{-0.4063} \quad 3.4$$

Where,

- ε_h = horizontal/tensile strain at the bottom of the asphalt concrete layer (Dimensionless)
- S = Flexural stiffness of HMA mix from the laboratory fatigue test (MPa)
- VP = volumetric parameter, $VP = \frac{V_a}{V_a+V_b}$ (Dimensionless)
- V_a = the air voids of mixture (%)
- V_b = the asphalt content by volume (Dimensionless)
- GP = the aggregate gradation parameter, $GP = \frac{P_{NMS}-P_{PCS}}{P_{200}}$ (Dimensionless)
- P_{NMS} = the percent of aggregate passing the nominal maximum size sieve (%)
- P_{PCS} = the percent of aggregate passing the primary control sieve (%)
- P_{200} = the percent of aggregate passing No.200 (0.075mm) sieve (%)

The RDEC model considers that the number of cycles to fatigue failure (C) is fundamentally related to a Plateau Value (PV). In many asphalt-beam fatigue tests it has been found that the “plateau value” (PV) of RDEC is a reliable predictor of the number of cycles to fatigue failure. Note that the Plateau Value is intrinsically related to gradation parameters of the asphalt concrete mix and asphalt content. Default values for the above parameters have been assigned in FAARFIELD to represent typical P-401 mixtures. The default values are:

- S = 4136.8 Mpa (600,000 psi)
- V_a = 3.5%
- V_b = 12.0%
- P_{NMS} = 95%
- P_{PCS} = 58%

- $P_{200} = 4.5\%$

The default values used to calculate the number of coverages to fatigue failure cannot be altered in FAARFIELD, therefore, it is not possible to adjust it according to the actual asphalt mix used in a certain project.

Since the number of coverages can differ from the number of passes due to aircraft wander, a coverage-to-pass (C/P) ratio needs to be computed. Wander is the width over which the centerline of the aircraft traffic is normally distributed for 75% of the time (HoSang, 1978).

In FAARFIELD, the values of wander are considered separately for each aircraft in the total mix (Brill, 2018). If, for example, a wander of 1.788 m is considered, the value of the standard deviation is calculated as the one that corresponds to $P\left(\frac{-1.788}{2} < X \leq \frac{1.788}{2}\right) = 0.75$. The same can be stated as the subtraction of the cumulative functions, $F(0.894) - F(0.894) = 0.75$. The standard normal distribution z at the referred points of the function X are -1.150349 and 1.150349, therefore, the standard deviation of the normal function will be $\sigma = 0.77716$.

The normalized function with average equal to zero and standard deviation of 0.77716 is presented in Figure 3.2. The shaded area in the picture corresponds to 75% of the area under the curve. The x axis represents the distance from the centerline (0) of the aircraft wheels, to which the path can vary to the right or to the left.

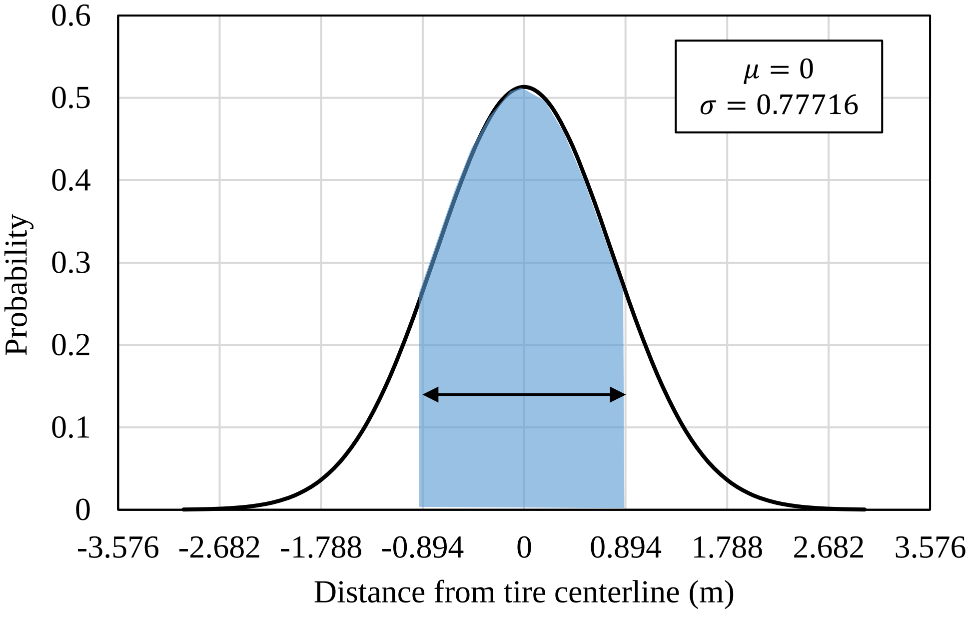

Figure 3.2: Normal distribution density function $N(0,0.77716)$ for a wander of 1.788 m.

The C/P ratio can be defined as the probability that any part of the effective tire width covers the center point of a given strip, as presented by Equation 3.5 (Kawa, 2012).

$$(C/P)_i = \sum_{k=1}^{N_t} P\left(\left(x_i - \frac{w_{eq}}{2}\right) \leq x_k \leq \left(x_i + \frac{w_{eq}}{2}\right)\right) \tag{3.5}$$

Where,

- N_t = number of tires for the gear (Dimensionless)
- x_i = lateral distance from centerline to the midpoint of strip i (cm)
- x_k lateral distance from centerline to the centerline of tire k (cm)
- w_{eq} = effective tire width (cm)

In the FAARFIELD design procedure, the pavement surface is divided into 82 longitudinal strips, each 25.4 cm-wide (10 inches-wide), for a total pavement width of 2,082.8 cm (820 inches), and the C/P ratio is computed for each offset i. The effective tire width w_{eq} is the width being affected by the load, on the critical layer being studied. This can be measured either at the top of the subgrade, for the subgrade vertical strain criterion, or at the bottom of the asphalt concrete layer, for the horizontal strain criterion. The tires can be considered either separate or combined, depending on if the response lines overlap, as presented in Figure 3.3 (Kawa, 2012).

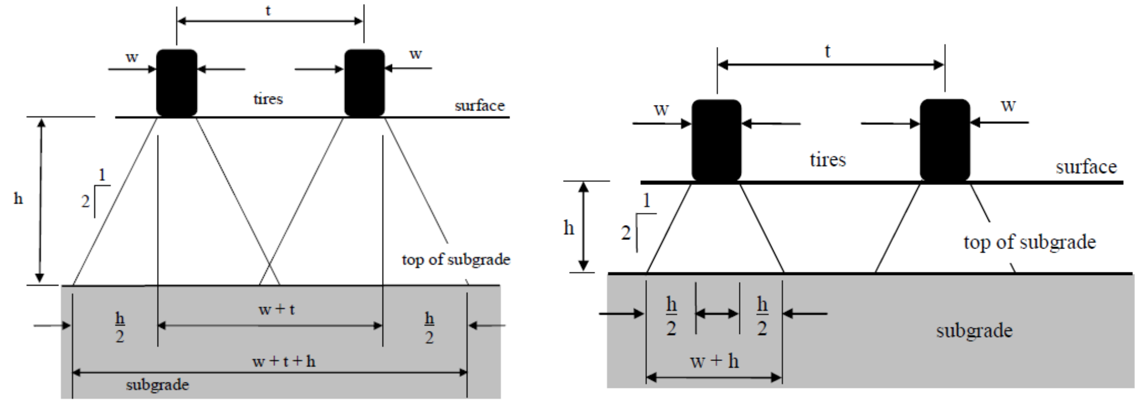

Figure 3.3: Equivalent tire width in which (a) response lines overlap, (b) response lines don't overlap (Kawa, 2012).

Therefore, the effective tire width should be calculated according to Equation 3.6:

If response lines overlap: $w_{eq} = w + t + h$
If response lines don't overlap: $w_{eq} = w + h$ 3.6

Where,

- h = total pavement thickness to the top of subgrade (cm)
- t = distance between tires (cm)
- w = tire contact width (cm)

Up to version 1.4, FAARFIELD design procedure would account for the effect of aircraft gears in tandem as part of the C/P ratio computation. In this procedure, the tandem factor was computed as a straight-line interpolation between the number of wheels in tandem (for shallow structures) and unity (for deep structures). The calculation process has changed in the most recent versions of FAARFIELD, and the cumulative damage caused by an aircraft mix is now defined as presented in Equations 3.7 and 3.8 (Tuleubekov, 2016):

$$CDF_i = \sum_{A=1}^{m} (C/P)_i^{(A)} * P_A * D(yi) \tag{3.7}$$

$$D(yi) = \sum_{k=1}^{n} s_k * \frac{1}{C(\varepsilon_k)} \tag{3.8}$$

Where,

- m = number of aircraft types in the traffic mix (Dimensionless)
- P_A = total number of passes of aircraft A in the design period (Dimensionless)
- $D(yi)$ is the damage computed at offset yi (Dimensionless)
- n is the total number of extremum points of strain (Dimensionless)
- ε_k are the critical strain values (Dimensionless)
- C is the number of coverages according to Equations 3.3 (Dimensionless)
- s_k is a factor characterizing the k^{th} extremum strains, as presented by Equation 3.9 (Dimensionless)

$$s_k = \left\{ \begin{matrix} 1\ if\ \varepsilon_k\ is\ maximum \\ -1\ if\ \varepsilon_k\ is\ minimum \\ 0\ if\ \varepsilon_k\ is\ not\ extremum \end{matrix} \right\} \tag{3.9}$$

3.3 Rutting damage

The impact of two climate parameters on rutting will be evaluated. The parameters are as follows:

- Temperature: through the weakening of the AC mix
- Increased saturation levels and flooding: through the weakening of the subgrade

3.3.1 Temperature influence on rutting damage

Asphalt concrete is a composite material that exhibits time and temperature-dependent properties. That means that the asphalt concrete stiffness can change depending on the ambient temperature and loading rate.

The mechanical behavior of asphalt concrete mix can be obtained through the complex moduli E^* employed as a function of the master curve. The dynamic modulus master curve expresses the modulus of asphalt concrete as a function of temperature and loading rate. The main difference between the resilient modulus and the dynamic modulus test is the sensibility to capturing the visco-elasticity of asphalt materials, since the dynamic test covers a wider range of temperatures and loading frequencies.

In the Mechanistic Empirical Design Guide, MEPDG (2004), there are 3 project levels. Each level requires a certain degree of accuracy of the input values. Level 1 would be equivalent to an executive project, and it require extensive amounts of laboratory data. However, the results at this stage are more accurate. Level 2 requires certain laboratory tests, but some of the values can be assumed from previous projects or from the literature. Level 3 corresponds to an initial stage of the project, where most of the values are typical results from the literature.

For a project at Level 1, the dynamic modulus master function is defined by a sigmoidal function, according to Equation 3.10 (ARA, Inc., ERES Consultants Division, 2004):

$$\log(E^*) = \delta + \frac{\alpha}{1 + e^{\beta+\gamma(\log t_r)}} \tag{3.10}$$

Where,

- E^* = dynamic modulus (psi)
- t_r = time of loading at the reference temperature, according to Equation 3.11.
- δ, α = fitting parameters; for a given set of data, δ represents the minimum value of E^* and $\delta + \alpha$ represents the maximum value of E^* (Dimensionless)
- β, γ = parameters describing the shape of the sigmoidal function (Dimensionless)

The sigmoidal function describes the time dependancy of the modulus at a reference temperature. The temperature dependency of the modulus is incorporated into shift factors, as described in Equations 3.11 and 3.12 (ARA, Inc., ERES Consultants Division, 2004).

$$t_r = \frac{t}{a(T)} \tag{3.11}$$

$$\log(t_r) = \log(t) - \log\,[a(T)] \tag{3.12}$$

Where,

- t_r = time of loading at a reference temperature (s)
- t = time of loading at a given temperature of interest (s)
- $a(T)$ = shift factor as a function of temperature (Dimensionless)
- T = temperature of interest (Rankine)

By using Equations 3.11 and 3.12, the dynamic modulus E^* can be calculated using the time of loading at a reference temperature. In the level 1 analysis, the master curves and the corresponding shift factors should be determined in laboratory through the dynamic modulus test. For levels 2 and 3, the dynamic modulus master curve can be developed using the modified Witczak's sigmoidal function presented in Equation 3.13, from information available from material specifications or volumetric design of the mixture (ARA, Inc., ERES Consultants Division, 2004).

$$\begin{aligned}\log(E^{*}) &= 3.750063 + 0.02932\rho_{200} - 0.001767(\rho_{200})^{2} - 0.002841\rho_{4} - 0.058097V_{a} \\ &- 0.802208\left(\frac{V_{beff}}{V_{beff} + V_{a}}\right) \\ &+ \frac{3.871977 - 0.0021\rho_{4} + 0.003958\rho_{38} - 0.000017(\rho_{38})^{2} + 0.005470\rho_{34}}{1 + e^{(-0.603313 - 0.313351\log(f) - 0.393532\log(\eta))}}\end{aligned} \tag{3.13}$$

Where,

- E^{*} = dynamic modulus (psi)
- f = loading frequency (Hz)
- η = bitumen viscosity, 10^{6} (Poise)
- V_{a} = air void content (%)
- V_{beff} = effective bitumen content, % by volume (%)
- ρ_{34} = cumulative % retained on the ¾ in sieve (%)
- ρ_{38} = cumulative % retained on the 3/8 in sieve (%)
- ρ_{4} = cumulative % retained on the No. 4 sieve (%)
- ρ_{200} = % passing the No. 200 sieve (%)

Of all existing predictive models, the modified Witczak E* predictive equation is considered one of the most rational and comprehensive. It was developed based upon 2750 test points and 205 different asphalt mixtures. Due to its structure as a sigmoidal curve, it can be used to estimate the stiffness of a HMA mix at a wide temperature and frequency range (Bari, 2005).

In this equation, the dynamic modulus is estimated considering a sinusoidal loading, with loading frequency f. The frequency f can be related to the duration of the load on the pavement, which can be determined through Equation 3.14 (Huang Y. H., 2004).

$$f = \frac{1}{2\pi d} \tag{3.14}$$

The loading duration d depends on the aircraft speed s (cm/s) and the tire contact radius a (cm), according to Equation 3.15 (Huang Y. H., 2004).

$$d = \frac{12a}{s} \tag{3.15}$$

It is of common practice to consider the contact radius of an elliptical tire footprint to be circular (Kuo, Mahgoub, & Holliday, 2004). Therefore, by assuming a circular contact between the tires of the aircraft and the pavement, a can be determined according to Equation 3.16:

$$a = \sqrt{\frac{A_c}{\pi}} \quad 3.16$$

In which, A_c is the contact area (cm^2), which can be estimated by dividing the weight by the tire pressure. The bitumen viscosity η also plays an important role in the determination of the dynamic modulus. At unaged conditions, the viscosity of the binder can be determined by Equation 3.17:

$$loglog\eta = A + VTSlogT_R \quad 3.17$$

Where,

- T_R = temperature (Rankine)
- A = regression intercept (Dimensionless)
- VTS = regression slope of viscosity temperature susceptibility (Dimensionless)

For projects Level 3, in which no test data is available, A and VTS can be estimated from the Performance Grade (PG) of the asphalt binder, as presented in Table 3.1 (ARA, Inc., ERES Consultants Division, 2004).

Table 3.1: Recommended A and VTS parameters based on asphalt PG grade (ARA, Inc., ERES Consultants Division, 2004).

High Temp Grade	**Low Temperature Grade**													
	-10		**-16**		**-22**		**-28**		**-34**		**-40**		**-46**	
	VTS	**A**	**VTS**	**A**	**VTS**	**A**	**VTS**	**A**	**VTS**	**A**	**VTS**	**A**	**VTS**	**A**
46									-3.901	11.504	-3.393	10.101	-2.905	8.755
52	-4.570	13.386	-4.541	13.305	-4.342	12.755	-4.012	11.840	-3.602	10.707	-3.164	9.496	-2.736	8.310
58	-4.172	12.316	-4.147	12.248	-3.981	11.787	-3.701	11.010	-3.350	10.035	-2.968	8.976		
64	-3.842	11.432	-3.822	11.375	-3.680	10.980	-3.440	10.312	-3.134	9.461	-2.798	8.524		
70	-3.566	10.690	-3.548	10.641	-3.426	10.299	-3.217	9.715	-2.948	8.965	-2.648	8.129		
76	-3.331	10.059	-3.315	10.015	-3.208	9.715	-3.024	9.200	-2.785	8.532				
82	-3.128	9.514	-3.114	9.475	-3.019	9.209	-2.856	8.750	-2.642	8.151				

To calculate the correct bitumen viscosity η, one needs to consider the aging of the asphalt binder. There are two main concerns around aging, the one that happens during mixing/compaction, and the aging during the long term in-situ. The viscosity also must be adjusted for different air void contents and as a function of depth. According to the Global Aging System (GAS) model proposed by MEPDG (2004), the aged viscosity at time t and depth z depends on the mean annual air temperature, the original binder viscosity at 77°F, the initial air voids in the mix, and the aged viscosity.

GAS was developed from viscosity measurements using capillary viscometers, penetration and softening point measurements, transformed to viscosity over a range of temperatures (Farrar, Harnsberger, Thomas, & Wiser, 2006). In this system, the short-term aging is presented by Equation 3.18 (ARA, Inc., ERES Consultants Division, 2004).

$$\begin{gathered} loglog(\eta_{t=0}) = a_0 + a_1 loglog(\eta_{orig}) \\ a_0 = 0.054405 + 0.004082 * code \\ a_1 = 0.972035 + 0.010886 * code \end{gathered} \qquad 3.18$$

Where,

- $\eta_{t=0}$ = mix/lay-down viscosity (cP)
- η_{orig} = original viscosity (cP)
- $code$ = hardening ratio (Dimensionless)

The hardening ratio has the purpose of adjusting the model for a particular asphalt tendency to age during mixing, hauling and compaction (Farrar, Harnsberger, Thomas, & Wiser, 2006). To consider the hardening ratio, a hardening code is used. The hardening code values vary from -1, representing a good to excellent resistance to hardening, to +2, representing a poor hardening resistance. The surface long-term aging model is presented in Equation 3.19 (ARA, Inc., ERES Consultants Division, 2004).

$$loglog(\eta_{aged}) = \frac{loglog(\eta_{t=0}) + At}{1 + Bt} \qquad 3.19$$

Where,

- η_{aged} = aged viscosity (cP)
- $A = -0.004166 + 1.41213(C) + (C)\log(Maat) + (D)loglog(\eta_{t=0})$
- $B = 0.197725 + 0.068384\log{(C)}$
- $C = 10^{274.494946 - 193.831\log(T_R) + 33.9366\log{(T_R)}^2}$
- $D = -14.5521 + 10.47662\log(T_R) - 1.88161\log(T_R)^2$
- $Maat$ = mean annual air temperature (°F)
- T_R = temperature (Rankine)
- t = time (months)

The binder viscosity must also be adjusted according to the percentage air voids in the AC mix and the air void projected change within time. This is done through an adjustment factor F_v, which is a function of the air voids at the time of interest, as presented in Equations 3.20, 3.21, and 3.22 (ARA, Inc., ERES Consultants Division, 2004).

$$loglog(\eta_{aged})' = F_v * loglog(\eta_{aged}) \qquad 3.20$$

$$F_v = \frac{1 + 1.0367 * 10^{-4}(VA)(t)}{1 + 6.1798 * 10^{-4}(t)} \qquad 3.21$$

$$VA = \frac{VA_{orig} + 0.011(t) - 2}{1 + 4.24 * 10^{-4}(t)(Maat) + 1.169 * 10^{-3}\left(\frac{t}{\eta_{orig,77}}\right)} + 2 \qquad 3.22$$

Where,

- $\left(\eta_{aged}\right)'$ = aged viscosity adjusted according to the percentage air voids (cP)
- F_v = adjustment factor (Dimensionless)
- VA_{orig} = initial air voids (%)
- $\eta_{orig,77}$ = original binder viscosity at 77°C (MPoise)

The aged viscosity must be adjusted to the depth of interest, as proposed in Equation 3.23.

$$\eta_{t,z} = \frac{\eta_t(4+E) - E(\eta_{t=0})(1-4z)}{4(1+Ez)} \qquad 3.23$$

$$E = 23.83e^{-0.0308Maat}$$

Where,

- $\eta_{t,z}$ = Aged viscosity at time t, and depth z (MPoise)
- η_t = Aged surface viscosity at a certain time, also named $loglog\left(\eta_{aged}\right)'$ (MPoise)
- z = Depth (in)

Finally, the aged viscosity at time t, and depth z, can be imputed into Equation 3.13 to obtain the AC dynamic modulus. Once the modulus of the AC is estimated for a temperature and loading rate of interest, this information can be used to estimate stresses and strains at critical locations, and ultimately, to calculate damage.

3.3.2 Moisture influence on rutting damage

Excess moisture can decrease the stiffness of the granular layers and subgrade, making the pavement more susceptible to permanent deformation. The proposed analysis of rutting damage due to excess moisture relates the subgrade material properties with the variation in degree of saturation from the optimum condition.

To determine the variations in the resilient modulus of the subgrade with time, this research proposes a similar approach to the MEPDG (2004), in which an environmental adjustment factor (F_{env}) is used to modify the optimum resilient modulus ($M_{R_{opt}}$) of the soil according to variations in moisture and temperature. The resilient modulus at any given period can be expressed as presented in Equation 3.24 (ARA, Inc., ERES Consultants Division, 2004).

$$M_R = F_{env} * M_{R_{opt}} \qquad 3.24$$

The F_{env} factor adjusts the optimal resilient modulus for three main conditions: (1) frozen materials (F_f), (2) thawed materials recovering to an equilibrium state (F_r), (3) unfrozen, fully recovered materials or materials that were never frozen (F_u). Figure 3.4 presents an example of calculation of an average F_{env} for a period of 2 weeks, for each pavement layer.

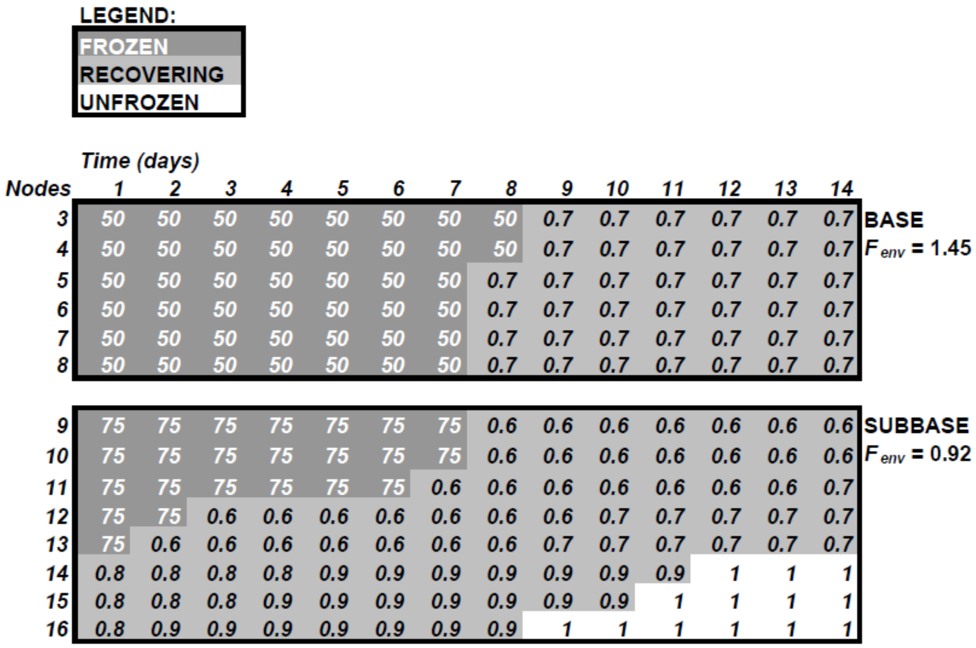

LEGEND:
FROZEN
RECOVERING
UNFROZEN

Time (days)

Nodes	1	2	3	4	5	6	7	8	9	10	11	12	13	14	
3	50	50	50	50	50	50	50	50	0.7	0.7	0.7	0.7	0.7	0.7	**BASE**
4	50	50	50	50	50	50	50	50	0.7	0.7	0.7	0.7	0.7	0.7	F_{env} = 1.45
5	50	50	50	50	50	50	50	0.7	0.7	0.7	0.7	0.7	0.7	0.7	
6	50	50	50	50	50	50	50	0.7	0.7	0.7	0.7	0.7	0.7	0.7	
7	50	50	50	50	50	50	50	0.7	0.7	0.7	0.7	0.7	0.7	0.7	
8	50	50	50	50	50	50	50	0.7	0.7	0.7	0.7	0.7	0.7	0.7	
9	75	75	75	75	75	75	75	0.6	0.6	0.6	0.6	0.6	0.6	0.6	**SUBBASE**
10	75	75	75	75	75	75	75	0.6	0.6	0.6	0.6	0.6	0.6	0.6	F_{env} = 0.92
11	75	75	75	75	75	75	0.6	0.6	0.6	0.6	0.6	0.6	0.6	0.7	
12	75	75	0.6	0.6	0.6	0.6	0.6	0.6	0.6	0.7	0.7	0.7	0.7	0.7	
13	75	0.6	0.6	0.6	0.6	0.6	0.6	0.6	0.7	0.7	0.7	0.7	0.7	0.7	
14	0.8	0.8	0.8	0.8	0.9	0.9	0.9	0.9	0.9	0.9	0.9	1	1	1	
15	0.8	0.8	0.8	0.9	0.9	0.9	0.9	0.9	0.9	0.9	1	1	1	1	
16	0.8	0.9	0.9	0.9	0.9	0.9	0.9	0.9	1	1	1	1	1	1	

Figure 3.4: Example computations of F_{env} (ARA, Inc., ERES Consultants Division, 2004).

The frozen adjustment factor (F_f) is a function of the frozen resilient modulus M_{Rfrz} and the optimum resilient modulus, according to Equation 3.25.

$$F_F = \frac{M_{Rfrz}}{M_{Ropt}} \qquad 3.25$$

The unfrozen adjustment factor (F_u) is used when the soil is fully recovered from thawing. It takes place when the number of hours elapsed since thawing started (Δt) is greater than the number of hours required for the material to recover (T_R). In this case, F_u is equal to the resilient modulus ratio $\frac{M_R}{M_{Ropt}}$, according to Equation 3.26.

$$log\frac{M_R}{M_{R_{opt}}} = a + \frac{b-a}{1 + EXP\left(ln\frac{-b}{a} + k_m * \left(S - S_{opt}\right)\right)} \qquad 3.26$$

The resilient modulus ratio $\left(\frac{M_R}{M_{Ropt}}\right)$ at any given time is defined according to Equation 3.26, where,

- $\frac{M_R}{M_{R_{opt}}}$ = Resilient modulus ratio; M_R is the resilient modulus at a given time and $M_{R_{opt}}$ is the resilient modulus at the optimum condition
- a = Minimum of $log\frac{M_R}{M_{R_{opt}}}$
- b = Maximum of $log\frac{M_R}{M_{R_{opt}}}$

- k_m = Regression parameter
- $S - S_{opt}$ = Variation in degree of saturation from the optimum condition, expressed in decimal

The values of a, b, and k_m varies for coarse-grained and fine-grained materials, as defined in Table 3.2.

Table 3.2: Values of a, b, and k_m for coarse-grained and fine-grained materials (ARA, Inc., ERES Consultants Division, 2004)

Parameter	**Coarse-Grained Materials**	**Fine-Grained Materials**	**Comments**
a	-0.3123	-0.5934	Regression parameter
b	0.3	0.4	Conservatively assumed, corresponding to modulus ratios of 2 and 2.5, respectively
k_m	6.8157	0.1324	Regression parameter

Figure 3.5 shows an example of the resilient modulus ratio versus moisture for course-grained materials. There is a clear pattern showing that when the degree of saturation increases, the resilient modulus decreases. The predictions of this model, in contrast with actual data from the literature for course-grained materials show good correlation.

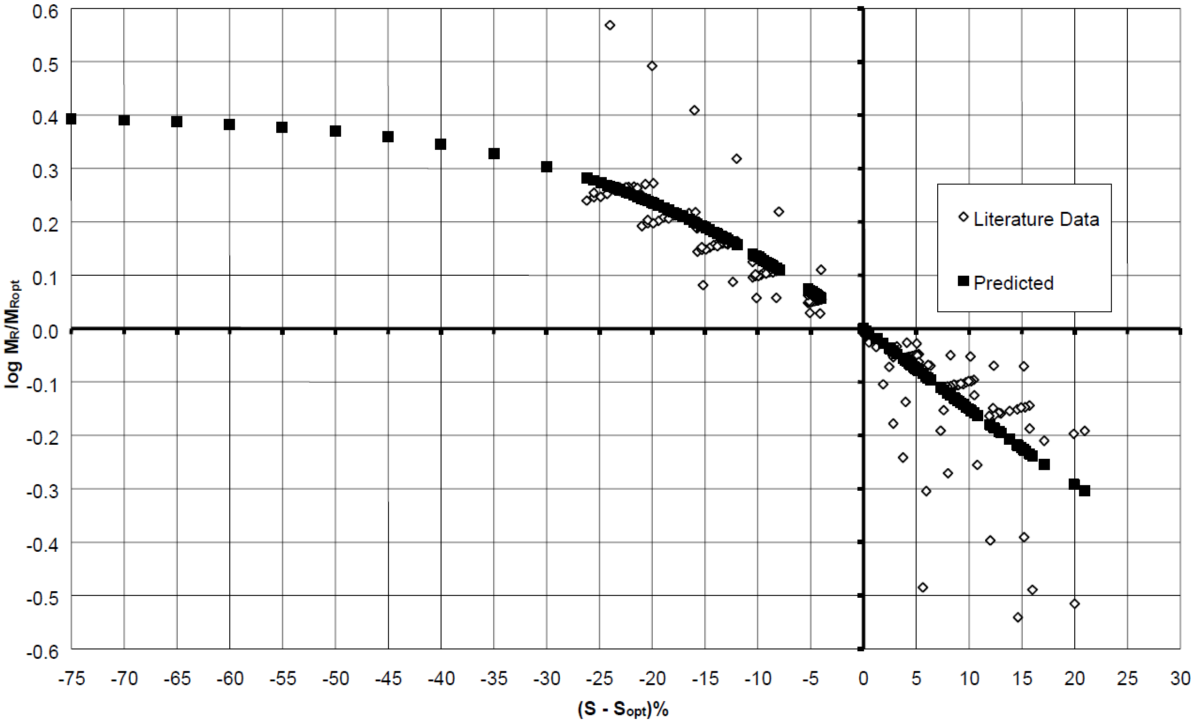

Figure 3.5: Resilient modulus ratio versus moisture for fine-grained materials (ARA, Inc., ERES Consultants Division, 2004).

During the construction period, the subgrade is usually in the optimum moisture content with small variations bellow or above. In the MEPDG (2004), the optimum moisture content S_{opt}, is obtained through Equation 3.27.

$$S_{opt} = 6.752 * (P_{200} * PI)^{0.147} + 78 \tag{3.27}$$

where,

- S_{opt} = optimum moisture content (%)
- ρ_{200} = % passing the No. 200 sieve (decimal)
- PI = Plasticity Index (%)

Sometime after the construction period, the moisture content changes in the direction of a degree of equilibrium S_{equil}, which could be reached in months or years of operation. When the moisture changes to an equilibrium, the resilient modulus will also change (Zhao, Ma, & Zhang, 2018).

If ground water levels are stable and there are no significant cracks in the AC layer, it can be said that the saturation S presented in Equation 3.26 is essentially at the state of equilibrium, unless freezing or thaw recovery is in progress. The equilibrium degree of saturation S_{equil} is expressed by the Fredlung and Xing sigmoidal function (Xing & Fredlund, 1994), also called the soil-water characteristic curve (SWCC), as presented in Equations 3.28 and 3.29.

$$S_{equil} = C(h) * \frac{\theta_{sat}}{\left(\ln\left(exp(1) + \left(\frac{h}{a_f}\right)^{b_f}\right)\right)^{c_f}} \tag{3.28}$$

$$C(h) = 1 - \frac{\ln\left(1 + \frac{h}{h_r}\right)}{\ln\left(1 + \frac{1.45 * 10^5}{h_r}\right)} \tag{3.29}$$

where,

- θ_{sat} is the saturated volumetric water content (decimal)
- h is the equilibrium suction or matric suction (psi)
- a_f, b_f, c_f and h_r are coefficients correlated to PI, P_{200}, and D_{60} as presented below:

If $P_{200}PI > 0$:

$$a_f = \frac{0.00364(P_{200}PI)^{3.35} + 4(P_{200}PI) + 11}{6.895}$$

$$\frac{b_f}{c_f} = -2.313(P_{200}PI)^{0.14} + 5 \tag{3.30}$$

$$c_f = 0.0514(P_{200}PI)^{0.465} + 0.5$$

$$\frac{h_r}{a_f} = 32.44e^{0.0186(P_{200}PI)}$$

If $P_{200}PI = 0$:

$$a_f = \frac{0.8627(D_{60})^{-0.751}}{6.895}$$

$$b_f = 0.75$$

$$c_f = 0.1772\ln(D_{60}) + 0.7734 \qquad 3.31$$

$$\frac{h_r}{a_f} = \frac{1}{D_{60} + 9.7e^{-4}}$$

The saturated volumetric water content (θ_{sat}) is computed by:

$$\theta_{sat} = \frac{\theta_{opt}}{S_{opt}} \qquad 3.32$$

where,

- θ_{opt} is the optimum volumetric water content (%)
- S_{opt} = optimum moisture content (%), as presented in Equation 3.27

The optimum volumetric water content (θ_{opt}) is computed by:

$$\theta_{opt} = \frac{w_{opt} * \gamma_{dmax}}{\gamma_{water}} \qquad 3.33$$

where,

- γ_{dmax} = maximum dry density (lb/in^3)
- w_{opt} = optimum gravimetric moisture content (%)
- γ_{water} = unit weight of water (lb/in^3)

The optimum gravimetric moisture content w_{opt} is computed by:

If $P_{200}PI > 0$:

$$w_{opt} = 1.3 * (P_{200}PI)^{0.73} + 11 \qquad 3.34$$

If $P_{200}PI = 0$:

$$w_{opt(T99)} = 0.6425 * (D_{60})^{-0.1038} \qquad 3.35$$

If layer is not a base course:

$$\mathrm{w}_{opt} = \mathrm{w}_{opt(T99)} \tag{3.36}$$

If $P_{200}PI = 0$, layer is a base course

$$\Delta\mathrm{w}_{opt} = 0.0156 * \left(\mathrm{w}_{opt(T99)}\right)^2 - 0.1465 * \mathrm{w}_{opt(T99)} + 0.9$$
$$\mathrm{w}_{opt} = \mathrm{w}_{opt(T99)} - \Delta\mathrm{w}_{opt} \tag{3.37}$$

where, D_{60} is the effective grain size corresponding to 60 percent passing by weight (mm).

The maximum dry density γ_{dmax} is computed by:

$$\gamma_{dmax} = \frac{G_s * \gamma_{water}}{1 + \frac{\mathrm{w}_{opt} + G_s}{S_{opt}}} \tag{3.38}$$

where G_s is the specific gravity (dimensionless).

The matric suction (h) can be defined as the capillary pressure of the soil (i.e., $\mathrm{u}_a - \mathrm{u}_w$, where u_a is the pore-air pressure and u_w is the pore water pressure). The relationship between the soil suction and the moisture content can be depicted by the soil-water characteristic curve (SWCC) (Xing & Fredlund, 1994), as presented in Figure 3.6.

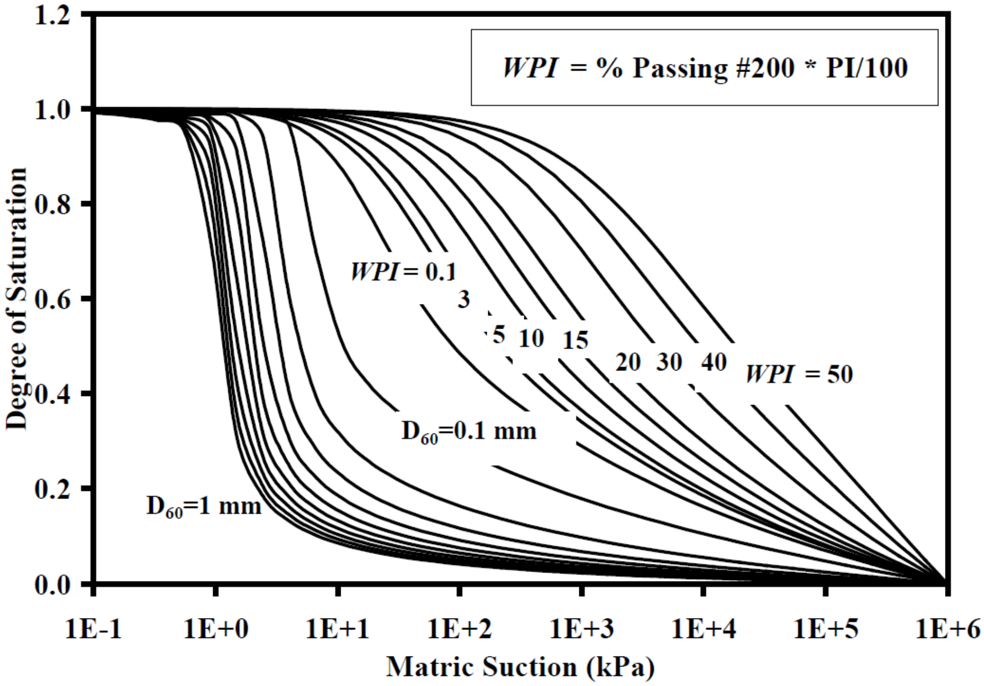

Figure 3.6: SWCC based on D_{60} and $P_{200}PI$ (Zapata, Andrei, Witczak, & Houston, 2007)

The soil suction depends mainly on climatic factors and soil index properties (Zapata, Yugantha, & William, 2009). The environmental factors can be quantified by the Thornthwaite's Moisture Index (TMI), and the soil properties are the P_{200} and PI.

The MEPDG (2004) presents the matric suction as a function of the ground water table (GWT) depth and the unit weight of water, as presented by Equation 3.39.

$$h = y_{GWT} * \gamma_{water} \tag{3.39}$$

where,

- y_{GWT} = ground water table depth (in)
- γ_{water} = unit weight of water (lb./in^3)

This is a simplistic consideration, since the soil suction can depend on many other factors such as (Zapata, Yugantha, & William, 2009):

- Annual precipitation
- Potential evapotranspiration
- Deficit of water
- Runoff of water

The equation used in the MEPDG (2004) to define the equilibrium degree of saturation (S_{equil}) is only valid for soils whose volumetric properties change (i.e., due to swelling or shrinkage) is insignificant when associated with moisture content variation or under external loading. In other words, the equation is only valid when the soil has a constant void ratio. This assumption is reasonable in the case of non-plastic and low-plasticity soils; however, for soils with high plasticity or collapsing potential, the variation of void ratio on the Soil Water Characteristic Curve (SWCC) should be considered (Zapata & Houston, 2008) (Han, Vanapalli, & Zou, 2017).

The recovering adjustment factor (F_r) accounts for the decrease in the resilient modulus when the soil is thawed, and the recover in the soil resistance that happens as the soil drains. To that end, F_r is a function of the Reduction Factor (RF), the Recovery Ratio (RR), and the soil resilient modulus ratio $\left(\frac{M_R}{M_{Ropt}}\right)$ at normalized equilibrium degree of saturation S_{equil}, according to Equation 3.40 and Equation 3.41.

$$S_{equil} = C(h) * \frac{1}{\left(\ln\left(exp(1) + \left(\frac{h}{a_f}\right)^{b_f}\right)\right)^{c_f}} \tag{3.40}$$

If $(S_{equil} - S_{opt}) < 0$,

$$F_r = RF + \left(\frac{M_R}{M_{Ropt}} * RR\right) - (RR * RF) \tag{3.41}$$

If $\left(S_{equil} - S_{opt}\right) \geq 0$

$$F_r = \left(\frac{M_R}{M_{Ropt}}\right) * (RF + RR - (RR * RF))$$

The Reduction Factor (RF) is calculated according to Equation 3.42 (ARA, Inc., ERES Consultants Division, 2004).

$$RF = \frac{M_{Rmin}}{smaller\ of\ (M_{Rfunrz}, M_{Ropt})} \quad 3.42$$

where M_{Rmin} is the resilient modulus of the soils just after thawing, divided by the smaller between the resilient modulus of natural unfrozen material (M_{Rfunrz}) or the optimum resilient modulus (M_{Ropt}). MEPDG (2004) has recommended values for RF given for coarse-grained materials and fine-grained materials as a function of P_{200} and the Plasticity Index (PI), according to Table 3.3 and Table 3.4.

Table 3.3: Recommended values of RF for coarse-grained materials (P_{200}<50%) (ARA, Inc., ERES Consultants Division, 2004).

Distribution of Coarse Fraction	P_{200} (%)	**PI<12%**	**PI=12%-35%**	**PI>35%**
Mostly Gravel $P_4 < 50\%$	<6	0.85	-	-
	6-12	0.65	0.7	0.75
	>12	0.60	0.65	0.70
Mostly Sand $P_4 > 50\%$	<6	0.75	-	-
	6-12	0.60	0.65	0.7
	>12	0.50	0.55	0.6

Table 3.4: Recommended values of RF for fine-grained materials (P_{200}>50%) (ARA, Inc., ERES Consultants Division, 2004).

P_{200} (%)	**PI<12%**	**PI=12%-35%**	**PI>35%**
50-85	0.45	0.55	0.60
>85	0.40	0.50	0.55

The Recovery Ratio RR is a function of the number of hours elapsed since thawing started (Δt) and the recovery period (T_R) according to Equation 3.43.

$$RR = \frac{\Delta t}{T_R} \quad 3.43$$

The recovery period (T_R) represents the number of hours required for the material to recover after thawing and it depends mainly on the percentage of fines and the soil plasticity index (PI). In the MEPDG (2004), the following reference values are used:

- T_R = 90 days for sands/gravels with $P_{200} * PI < 0.1$
- T_R = 120 days for sands/gravels with $0.1 < P_{200} * PI < 10$
- T_R = 150 days for sands/gravels with $P_{200} * PI > 10$

As an example, after a flooding event occurs, the matric suction is lowered due to excess water, and most of the layers can reach saturation levels of 100%. As the water drains out of the pavement structure, the matric suction is raised until it reaches its normal suction levels. The damage incurred during the immediate post flooding period can be conceptually defined according to Equation 3.44 (Wang, Huang, Rattanachot, Lau, & Suwansawas, 2015).

$$D_{IPFP} = \int_{0}^{T} D\{L(t), h(t)\}dt \tag{3.44}$$

L(t) is the traffic load and $h(t)$ is the matric suction level at a specific time t. It is not possible to find a continuous function that would translate the continuous recovery of the matric suction, therefore, Equation 3.44 can be adjusted by considering the soil suction to increase into discrete intervals of time and have one single record of the matric suction and the respective traffic-load at each interval.

The water drainage after a flooding event can occur at different rates, depending on the severity of the event, and the subgrade permeability. The permeability of granular soils is greatly affected by their grain size distribution (Elhakim, 2016). Although it is ideal to measure permeability through laboratory constant and falling head permeability tests, or field permeability tests, an alternative to estimate soil drainage is to use empirical correlations available. There are several correlations that were developed to, empirically, evaluate soil permeability using grain size distribution, however, one of the most well-known correlations was proposed by Hazen as presented in Equation 3.45.

$$k(m/s) = C * {D_{10}}^{2} \tag{3.45}$$

C is a constant with typical values ranging between 0.4 and 1.2 and is typically taken as 1 (Elhakim, 2016), and D_{10} is the equivalent particle diameter corresponding to 10% passing by weight. Also, typical values of permeability, according to the soil classification, can be obtained through Table 3.5.

Evidence shows that a wet-dry cycle does not adversely affects subgrade stiffness, that is, the strength of the subgrade soil can be recovered after a flood if it is given enough time to dry (Wang, Huang, Rattanachot, Lau, & Suwansawas, 2015), therefore, this research considered that the resilient modulus of the subgrade fully recovers after the flooding waters are completely drained, and the pavement returns to its equilibrium degree of saturation.

Table 3.5: Permeability based on soils classification (Look, 2007)

Soil Type	Description	USC symbol	Permeability, m/s
Gravels	Well Graded	GW	10^{-3} to 10^{-1}
	Poorly Graded	GP	10^{-2} to 10
	Silty	GM	10^{-7} to 10^{-5}
	Clayey	GC	10^{-8} to 10^{-6}
Sands	Well Graded	SW	10^{-5} to 10^{-3}
	Poorly Graded	SP	10^{-4} to 10^{-2}
	Silty	SM	10^{-7} to 10^{-5}
	Clayey	SC	10^{-8} to 10^{-6}
Inorganic Silts	Low Plasticity	ML	10^{-9} to 10^{-7}
	High Plasticity	MH	10^{-9} to 10^{-7}
Inorganic Clays	Low Plasticity	CL	10^{-9} to 10^{-7}
	High Plasticity	CH	10^{-10} to 10^{-8}
Organic	With Silts/Clays of Low Plasticity	OL	10^{-8} to 10^{-6}
	With Silts/Clays of High Plasticity	OH	10^{-7} to 10^{-5}
Peat	Highly Organic Soils	Pt	10^{-6} to 10^{-4}

3.4 Fatigue damage

The impact of three climate parameters on fatigue are going to be evaluated:

- Temperature: through the weakening of the AC mix
- Daily thermal oscillations: through the weakening of the AC mix
- Moisture: through the weakening of granular layers and subgrade leading to lack of support on the bottom of AC layer.

3.4.1 Temperature influence in fatigue cracking

The MEPDG (2004) affirms that, in general, fatigue damage for roads is maximum at 7.6 to 12.7 cm (3 to 5 in) of HMA thickness, and the damage tends to decrease when the AC thickness increases. Laboratory testing also shows that the alligator cracking area decreases when the AC mixes are stiffer, as presented in Figure 3.7.

Very small thickness shows to have low alligator cracking percentage in Figure 3.7. This happens because under this circumstance the AC layer will be mostly under compressive stress. So, either the AC must be very thin and soft, or thick and stiff. However, thin AC layers will be associated with other pathologies, such as rutting due do the increased stress on the lower layers for example.

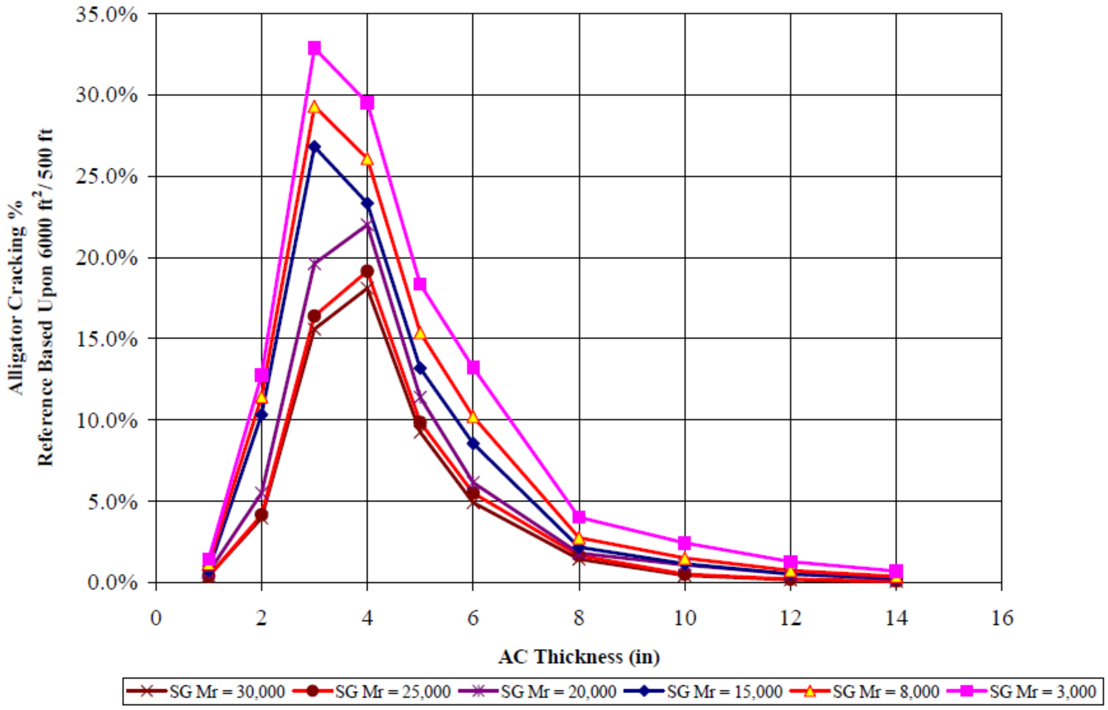

Figure 3.7: Effect of AC thickness and subgrade support on alligator cracking (ARA, Inc., ERES Consultants Division, 2004).

The mechanism of fatigue cracking can happen from bottom to top, or from top to bottom. The bottom-up cracks occur when the HMA layer deflects under wheel loads, resulting in a tensile strain at the bottom of the layer. The repetition of this stress can lead to cracks at the bottom layer to initiate and propagate to the surface. This phenomenon happens sooner when thin or weak HMA layers were designed to a certain magnitude of loads, or if the base/sub-base is weak, because of inadequate compaction or elevated moisture content, for example. Most fatigue cracks occur from the bottom up, however, there is evidence that cracks can also initiate at the surface and propagate downward. This can occur due to the aging of the binder, or shear forces at the HMA surface (ARA, Inc., ERES Consultants Division, 2004).

For a pavement design purpose, the fatigue performance of asphaltic materials is generally evaluated at a fixed temperature (Bodin, Terrier, Perroteau, Hornych, & Marsac, 2010). In FAARFIELD, for example, the software considers the pavement performing as it was under 32°C all year long; hence, it considers that the stiffness of the asphalt concrete remains constant along the year.

Laboratory test results of the tensile strain ε_t and its characteristic curve under different temperature can be seen at Figure 3.8. It can be noted in the figure that the relationship between temperature and the tensile strain ε_t is not linear.

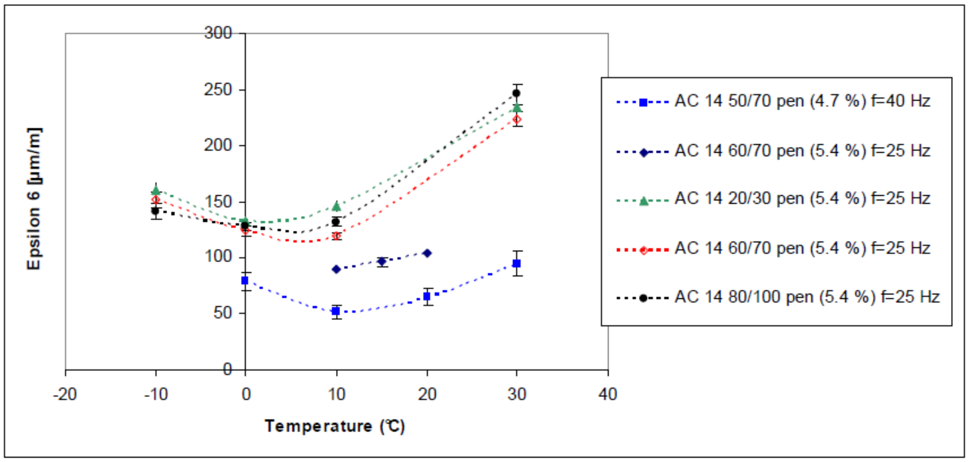

Figure 3.8: Tensile strain controlled tests at different temperatures (Bodin, Terrier, Perroteau, Hornych, & Marsac, 2010)

The MEPDG (2004) affirms that temperature directly affects the complex modulus of the asphalt concrete mix, interfering in overall pavement responses, including tensile strains and ultimately affecting fatigue cracking. The complex modulus is the representation of the modulus of a viscoelastic material as the sum of the real and imaginary parts. The real part is the dynamic modulus |E∗|, defined as the ratio between the amplitudes of stress and strain signals and the imaginary part represents the phase angle φ (Lundström, Isacsson, & Ekblad, 2003).

The variation of the complex modulus at the frequency of 25 Hz is presented at Figure 3.9, for temperatures between -10 and 40 °C. The dynamic modulus presented at part (a) decreases with temperature, while the imaginary part shown at part (b) exhibits a bell-shaped curve. Figure 3.10 presents similar results for the dynamic modulus, even though the frequency of loading was 10 Hz.

There are several models to characterize fatigue damage, most of them include the tensile strain and the stiffness of the asphalt as main factors influencing the fatigue. Other factors that contribute to the fatigue life include the HMA layer thickness and traffic.

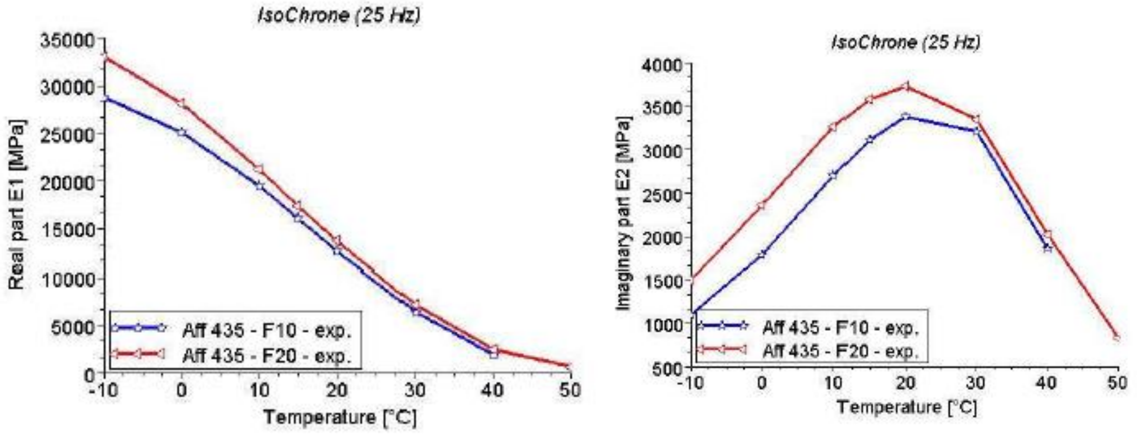

(a) (b)

Figure 3.9: Complex modulus data for two different materials at the frequency of 25 Hz (a) real part (b) imaginary part (Bodin, Terrier, Perroteau, Hornych, & Marsac, 2010).

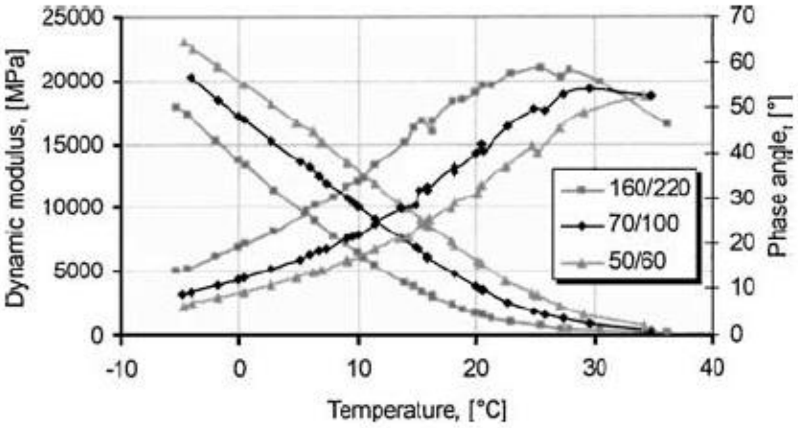

Figure 3.10: Complex modulus data for three different materials at the frequency of 10 Hz (Lundström, Isacsson, & Ekblad, 2003).

3.4.2 Thermal-induced fatigue damage

Daily temperature fluctuations can impact fatigue cracking; however, existing pavement design methods do not consider it as a factor that affects the pavement performance. Predictions of pavement design life for fatigue criteria can be distinctively changed when this factor is considered.

Temperature-induced fatigue damage can be accounted in the prediction of the alligator cracking through the method proposed by Islam (Islam, 2015). According to this method, to calculate damage, first it is necessary to define the allowable number of oscillations during the pavement's life N_{ft}, which is dependent on two main variables, strain induced by thermal fluctuations ε and the material's stiffness E in Psi. The relationship is expressed in Equation 3.46.

$$N_{ft} = 1.4423 * 10^{-8} * \left(\frac{1}{E}\right)^{0.4168} * \left(\frac{1}{\varepsilon}\right)^{3.458} \tag{3.46}$$

The thermal strain can be estimated by $\varepsilon = \alpha * \Delta T$, where ΔT is the monthly average day-night temperature fluctuation, and α is the strain per degree change in temperature (με/^{o}C). The α-value can be directly determined in the laboratory or in the field using Equation 3.47.

$$\alpha = \frac{\Delta L/L_o}{\Delta T} \tag{3.47}$$

L_o is the original length of the samples and ΔL is the change in length due to change in temperature by ΔT. Islam (2015) has developed an empirical equation based on experimental studies to describe the behavior of the AC α-value with temperature, based on field values for the Coefficient of Thermal Contraction (CTC) and Coefficient of Thermal Expansion (CTE) determined using field strain sensors. The average of the CTC and the CTE values were considered the α-value as presented in Figure 3.11.

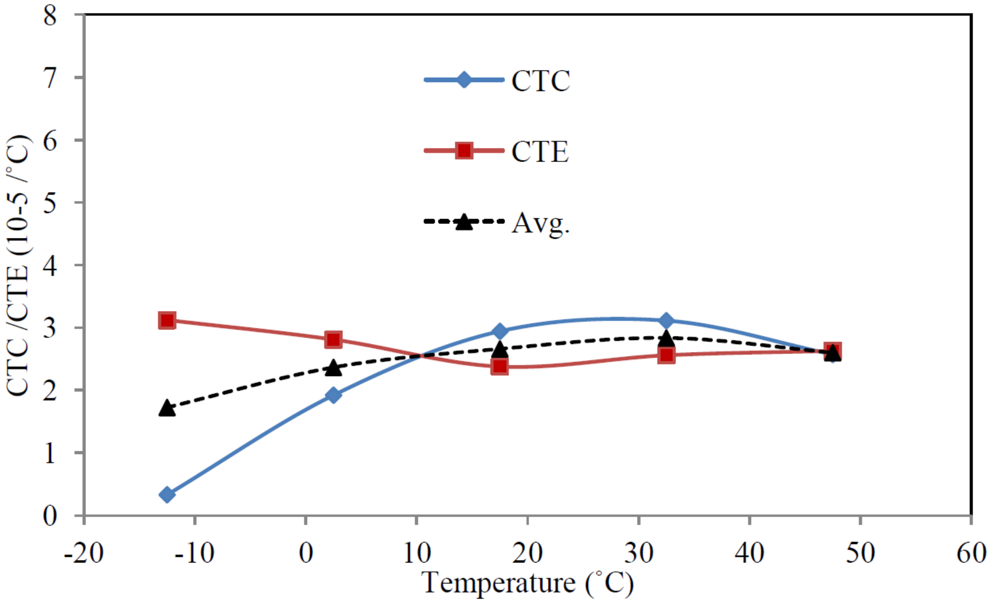

Figure 3.11: Temperature-dependent α-value (Islam, 2015).

Figure 3.11 shows the α-value presents a non-linear behavior. It increases with temperature; reaches a peak and then decreases with the continued increase in temperature. Using the best fit curve represented by the black dotted line in Figure 3.11, the α-value at any temperature can be determined using Equation 3.48.

$$\alpha = -0.006T^2 + 0.356T + 22.633 \tag{3.48}$$

T is the monthly average temperature of the AC. Once the allowable number of oscillations N_{ft} is determined, the thermal damage ratio D_2 can be calculated through Equation 3.49:

$$D_2 = \sum_{i=1}^{q} \frac{n_i}{N_{ft,i}} \qquad 3.49$$

where n_i is the number of temperature load repetitions in period i, and N_{ft} is the allowable number of oscillations during the pavement's life. Islam proposes a series of 8 steps to determine the temperature-induced fatigue damage D_2, and a 9th step to calculate the total fatigue damage D, as described below:

1. Take the average temperatures at the different periods (say, months) of analysis
2. Calculate the α-values at the different periods of analysis using Equation 3.48
3. Predict the maximum temperature y_{max} and the minimum temperature y_{min} at the bottom of AC. Calculate the average temperature fluctuation for that period $\Delta T = y_{max} - y_{min}$
4. Determine the thermal strain, $\varepsilon = \alpha * \Delta T$
5. Determine the stiffness of AC
6. Predict the allowable number of load repetition for temperature fluctuations (Equation 3.46)
7. Determine the damage ratio for thermal fatigue damage (Equation 3.49)
8. Apply the damage shift factor.
9. Determine the total damage index $(D = D_1 + D_2)$, where D_1 is the load-induced fatigue damage and D_2 is the thermal fatigue damage.

In step 8 both D_1 and D_2 are multiplied by a damage shift factor that ranges from 0.000398 to 0.004 based on the thickness of the AC, as presented in Table 3.6.

Table 3.6: Damage shift factor used in damage ratio (Islam, 2015).

AC thickness (cm)	Damage Shift Factor
<5.08	0.000398
5.08-10.16	0.002935
10.16<	0.004

In step 3 of the methodology proposed by Islam (2015), the author suggests that the maximum and minimum AC temperatures should be calculated at the bottom of the AC. Another research published in 2008, however, suggests that ΔT should actually be measured near the pavement surface (Rajbongshi & Das, 2008). Measuring near the surface seems more reasonable given that the fracture mechanics of thermal fatigue cracking considers that the crack begins at the surface and progress downward through the asphalt concrete (Lytton, Shanmugham, & Garret, 1983).

For cases in which the AC thickness is thin (for example, 5 or 6 cm thick), the difference between measuring ΔT just below the surface or at the bottom of the AC may not be so significant, however, in cases in which the AC is thick, the difference will be much higher. The effects of temperature-induced fatigue damage have not been deeply explored in the literature, and more discussions on the location where ΔT should be measured and the α-values needs to be developed in future research.

3.4.3 Moisture influence on fatigue cracking

Fatigue cracking can be worsened by elevated moisture content in the granular layers and subgrade, due to the decrease in support. This happens because the tensile strain can be increased with the reduction of stiffness of the materials below it.

The methodology used to assess the fatigue damage caused by excess moisture in the subgrade will follow the same methodology explained in section 3.3.2, in which an environmental adjustment factor (F_{env}) is used to modify the optimum resilient modulus ($M_{R_{opt}}$) of the soil according to variations in moisture and temperature.

Knowing the resilient modulus of the subgrade along the year, as well as the other pavement layers, it is possible to determine the extreme tensile strains at the bottom of the AC. The tensile strains measured at each sub-season can be used to estimate the number of coverages C as presented in Equation 3.3, and ultimately, to estimate the cumulative fatigue damage, as presented in Equation 3.7.

3.5 Pavement Responses

Section 2.3 has discussed the advantages and disadvantages of using the Layered Elastic Design (LED) or the Finite Element Analysis (FEA) to calculate pavement stresses and strains. One of the findings from the review of the literature is that current research often tends to show preference to very complex analysis that can take several hours to converge, even though, this may pose some difficulties with respect to practicality for routine analysis cases from an industry perspective.

There are currently different methods and software packages that can either directly or indirectly predict airport pavement responses. However, the influence of using these different tools on the accuracy of the results has not yet been discussed in reference to an actual field test in the existing literature. This can be especially crucial when studying the behavior of transportation infrastructure under the effect of climate change. Therefore, to contribute to the understanding of the mechanistic analysis methods, this research modeled two pavement test sections and compared the predicted results with the field measurements.

The first case study focused on a purely linear elastic approach, for which two LED based software (i.e., KENLAYER and NonPAS) and one FEM based software (i.e., ABAQUS) was used. For the second case study, a non-linear elastic approach was pursued. Therefore, KENLAYER and NonPAS were used while utilizing the layered theory in a non-linear approximation manner. Furthermore, simulations for the second case study were also performed using GT-PAVE, a FEM-based software. The analysis of the pavement responses is presented in Chapter 4: of this thesis.

3.6 Frost and Thaw Considerations

Knowing how climate change can impact airport pavement frost and thaw conditions is essential for better planning of future projects in Canada. However, there are currently no specific studies available in the literature to inform decision making in this area. To this end, this thesis analyzes how climate change can affect frost/thaw penetration and frost heave in several locations across Canada.

3.6.1 Frost Penetration and Frost Heave

In the early stages of spring, the soil starts to thaw from the surface downward, as well as from the bottom of pavement upward. During this time, excess moisture can be trapped into the subgrade surface by the bottom soil that is still frozen, weakening the material. Therefore, traffic loads end up being applied in weak saturated foundation, causing great damage to the pavement (Daniel, et al., 2018), appearing in the form of cracks and surface deformation caused by frost heaving and differential heaving (St-Laurent, 2012).

There are several methods to calculate frost penetration depth, where almost all of these methods are related to the freezing index (FI), which is a measure of the severity of freezing condition during the winter season. *FI* is calculated as the summation of daily average air temperatures over the freezing period (TCCA, 1992). Figure 3.12 shows an example of the calculation of the FI over the winter of 1996/1997 in Beatrice, ON.

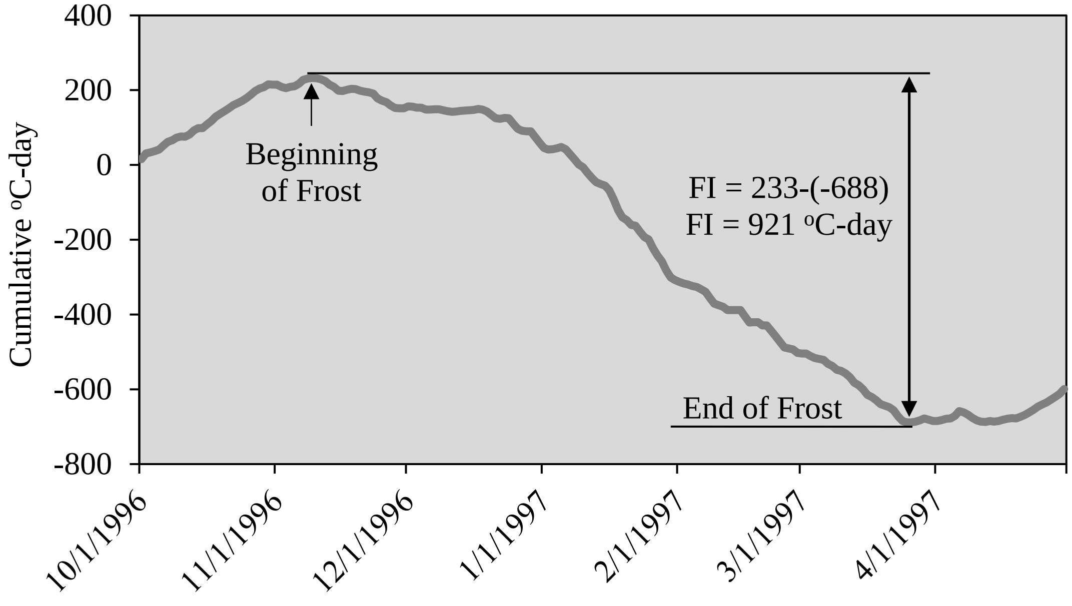

Figure 3.12: Determination of the freezing index for Beatrice, Ontario, over the winter of 1996/1997.

According to the TCCA manual of pavement structural design ASG-19, the frost protection depth should be calculated using a minimum 10-year average freezing index (TCCA, 1992). Site air freezing index measures should be available from airfield data records, based on meteorological observations. If not available, Transport Canada allows an estimation to be made from a map of freezing indices provided in the ASG-19 manual, as can be seen in Figure 3.13.

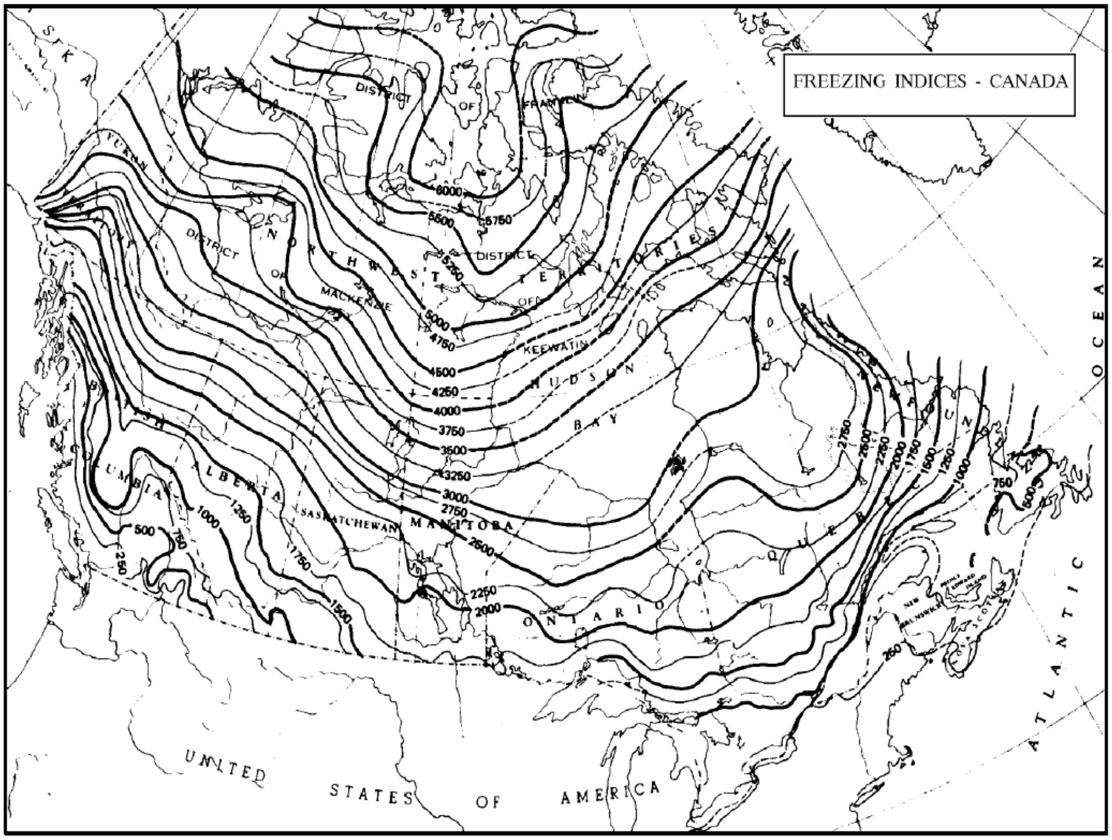

Figure 3.13: Freezing indices in Canada (TCCA, 1992).

Limiting the depth of frost action into the subgrade soils can limit the potential for frost heave and thaw weakening. This is achieved by defining a minimum pavement thickness and by excavating the soil susceptible to frost penetration preferably to the full depth. However, when the latter approach is not possible, ASG-19 advises that at least 1 m should be excavated (TCCA, 1992). To define if a soil is frost susceptible or not, TCCA relies on the soil gradation. In its classification, the subgrade soil is non-frost-susceptible if it has less than 10 percent passing the 0.075 mm sieve.

The equation proposed by TCCA to calculate frost penetration depth is empirical. The method is based on the results published by Argue & Denyes (Argue & Denyes, 1974), which has evaluated 39 sites across Canada, with 93 observations to predict frost depth in asphalt surfaced pavements. The calculation of the frost penetration depth in asphalt surfaced pavements according to the Pavement Structural Design Training Manual ATR-021 proposed by TCCA should be done as presented in Equation 3.50 (TCCA, 1995).

$$T_{min} = -61 + 6.8 * \sqrt{F} \tag{3.50}$$

T_{min} is the minimum thickness of the pavement structure (cm) and F is the average annual air freezing index ($C^o - Days$). Another available method to classify the soil frost susceptibility is the Chamberlain Method, used by the Ministry of Transportation of Ontario (MTO) (Chamberlain, 1981). This method defines the soil according to the material proportions of sand, silt, and clay as, acceptable, borderline, or unacceptable material, as can be seen in Figure 3.14.

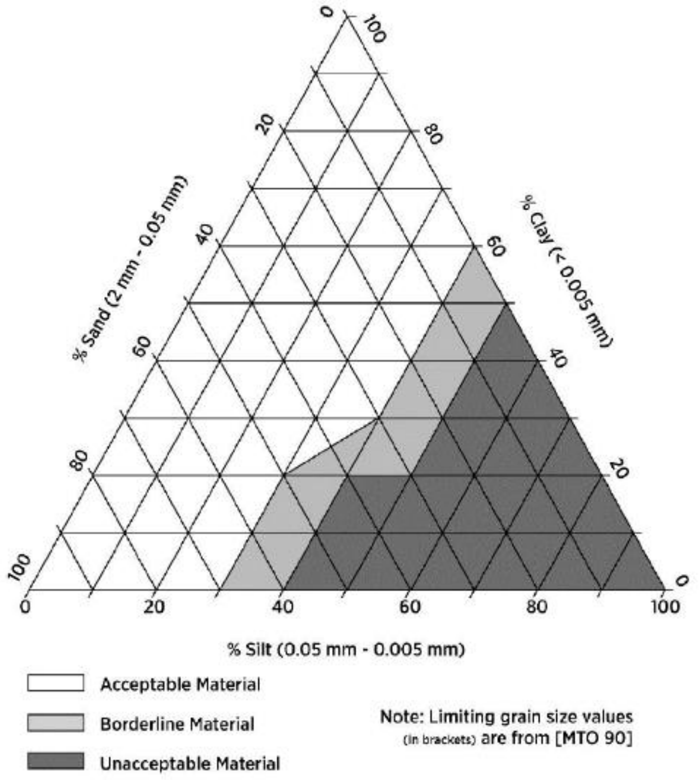

Figure 3.14: Frost susceptibility of soils (Chamberlain, 1981).

To calculate the frost penetration depth, the MTO uses the empirical curve presented in Equation 3.51.

$$P = -32.8 + 5.78\sqrt{F} \qquad 3.51$$

P is the frost penetration depth (cm) and F is the freezing index ($℃ - days$). This equation was developed based on mean frost depth observations in Ontario highways from 1970 to 1975 (MTO, 2013).

The equations to predict frost depth penetration recommended by the TCCA and the MTO are both empirical. The main difference relies on the number of sites evaluated. The TCCA method used field data from various locations across Canada, while the MTO relied on frost depth records from Ontario sites only.

The Ministère des Transports du Québec’s (MTQ) uses a mechanistic approach to predict frost depth and frost heave as a function of climate, subgrade soil properties and pavement thickness. This analysis method tends to require more detailed site investigation than other methods, but it has shown through validation procedures to have good results in predicting frost penetration depth (St-Laurent, 2012).

The MTQ approach is based on the SSR model developed in Finland (Saarelainen, 1992), in which the calculation of the frost depth is based on the balance of the heat balance at the frost front. The method accounts for the segregation potential, which is a measure of the susceptibility of a soil to frost, that could be measured in the laboratory or estimated through empirical equations. Material property variables such as dry density, particle mineralogy, water content and specific surface area are some of the inputs, providing source for calculation of thermal conductivities, latent heat, and other important material parameters.

The MTQ uses i3c-me which is a mechanistic software for pavement design and performance prediction, developed by the NSERC industrial research Chair on the interaction of heavy loads/climate/pavement of Laval University (Chair i3C), under the direction of Prof. Dr. Guy Doré.

The i3c-me software includes a module specific to predict frost penetration and frost heave as a function of climate, subgrade soil properties and pavement design (St-Laurent, 2012), (Grellet, Richard, & Pérez-González., 2019). In this method, frost penetration depth is calculated based on a maximum frost heave as threshold design criteria. The method allows not only the calculations of frost depth of a previously defined pavement structure, but also the associated frost lifting (Grellet, Richard, & Pérez-González., 2019).

The input information in the i3c-me software consists of two parts: the characteristics of the structure's materials and winter-specific climatic data. The thermal conductivity parameters can be defined manually, or the user can utilize default values proposed from database. Geotechnical parameters can also be estimated from default materials. The frost depth calculations are based on the thermal energy balance at the freezing front, as presented in Figure 3.15.

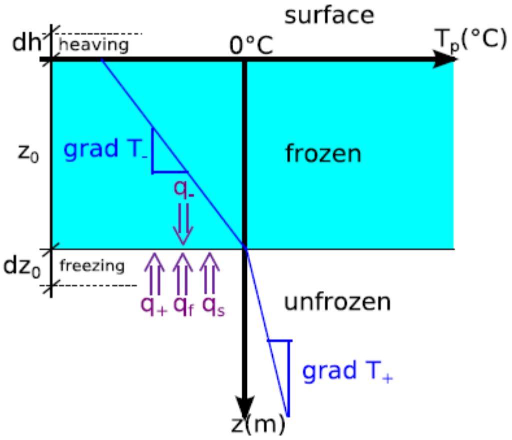

Figure 3.15: Thermal balance at freezing front (St-Laurent, 2012).

The thermal balance (W/m²) relationship at the freezing front is defined according to Equation 3.52 (St-Laurent, 2012):

$$q_- = q_+ + q_f + q_s \tag{3.52}$$

where,

- q_- = thermal flux that escapes from the freezing front towards the surface, by crossing the frozen layers, W/m²
- q_+ = geothermal flux, W/m²
- q_f = thermal flux generated by the change of phase when interstitial water changes to ice, W/m²
- q_s = thermal flux generated by additional segregation water when ice lenses form, W/m²

Equation 3.52 is applied daily with incremental time steps (dt) set to determine the successive advances of the freezing front dz_0. A screen shot of the software i3c-me output is shown in Figure 3.16.

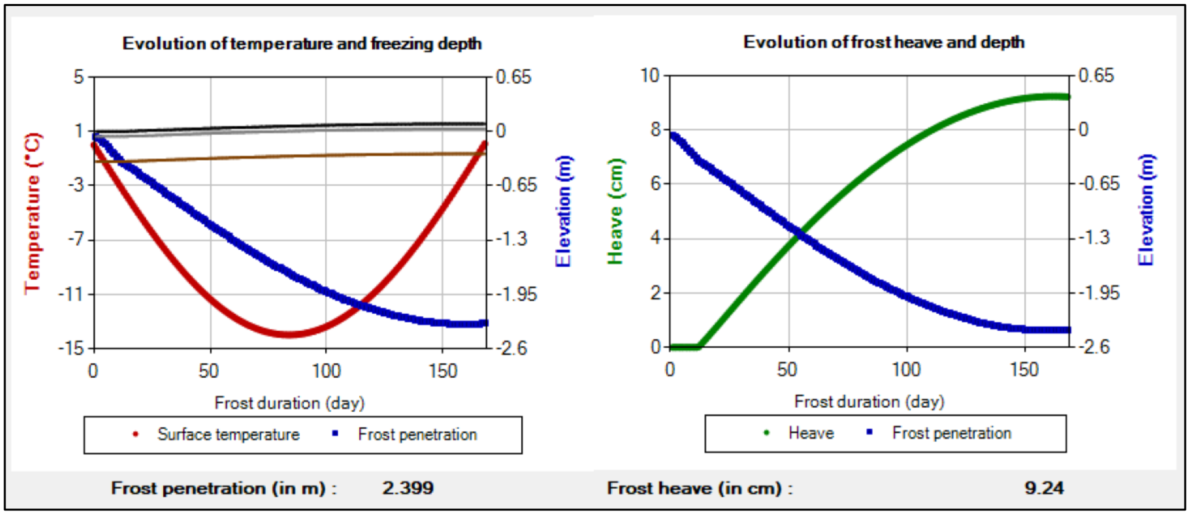

Frost penetration (in m) : **2.399**

Frost heave (in cm) : **9.24**

Figure 3.16: Determination of frost depth and associated heaving (Grellet, Richard, & Pérez-González., 2019).

The result is an estimation of frost penetration depth and frost heave, as presented in the bottom of Figure 3.16. To calculate frost depth and frost heave, the air-surface transfer coefficient (n-factor) also needs to be defined. The n-factor is defined as the ratio between the surface temperature in freezing conditions and the air temperature in freezing conditions. This value depends on the atmospheric conditions (hours of sunshine, cloud cover, wind, humidity, pollution, etc.), the absorption capacity of the surface layer (albedo, color, texture, sun exposure, inclination, orientation, etc.) and the thermal regime below the surface. Andersland and Ladanyi proposed typical values for the n-factor according to the surface conditions. The researchers suggested that for asphalt pavements n-value most probably ranges from 0.9 to 0.95, while for concrete pavements this range would be between 0.7 to 0.9 (Andersland & Ladanyi, 2003).

Lastly, when predicting the frost penetration through the MTQ methodology, the rigorous frost index (FI_r) needs to be defined. FI_r represents an incremented frost index that accounts for colder than average winters. The i3c-me software offers two options for determining it. The first option uses an estimate that represents a winter that would correspond to the average of the three coldest winters over a thirty-year period, according to Equation 3.53.

$$FI_r = 1.143 * FI_n + 220 \tag{3.53}$$

FI_r is the rigorous freezing index $(℃ * days)$ and FI_n is the normal freezing index $(℃ - days)$ or just freezing index, as previously defined. The second option follows a probabilistic approach that considers the history of winters for a defined period. For that purpose, the standard deviation, and the average of the freezing index distribution for a specified period need to be calculated.

3.6.2 Permafrost Thawing

While southern areas of Canada may benefit from the shortening of the winter season, northern provinces will likely suffer with increased differential thaw settlement, frost heave and a decrease in overall pavement strength due to permafrost thawing and higher number of freeze-thaw cycles. Figure 3.17 shows a Canadian map that provides the classification of permafrost based on the proportion of land that is underlain by frozen layers within a given area. The southern areas in Canada are not underlain by permafrost, while northern areas are underlain by discontinuous or continuous permafrost layers.

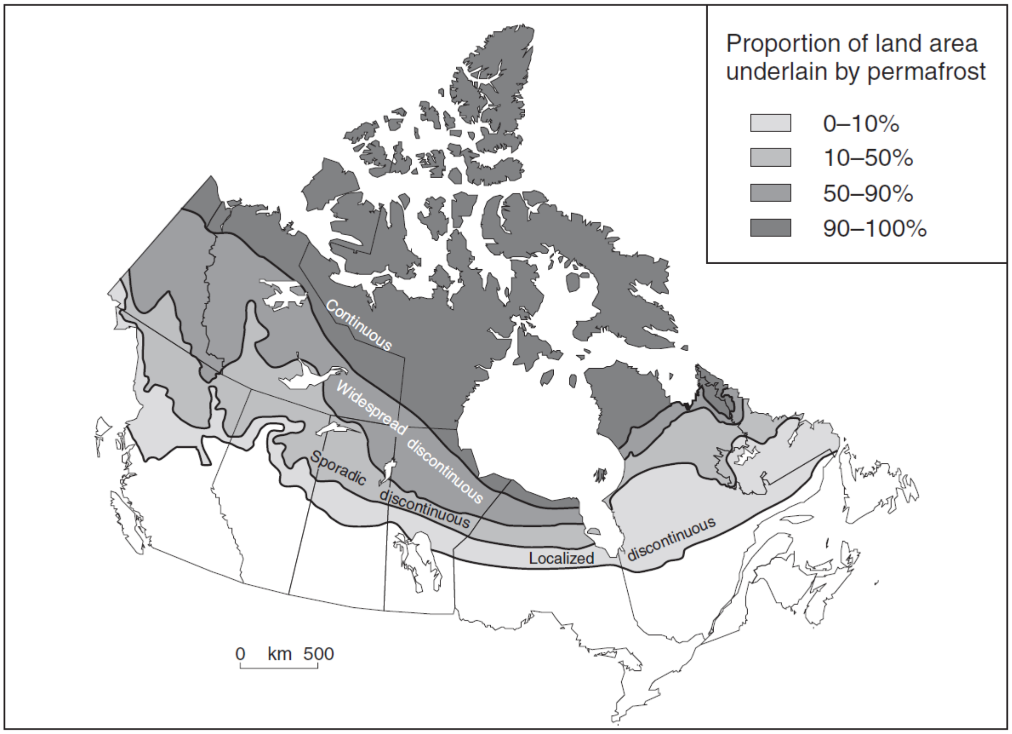

Figure 3.17: Permafrost zones of the Canadian permafrost region (Smith & Burgess, 2004).

The thawing of previously permanent frozen layers can cause serious damage to pavement structures due to settlement. Soil strength from ice bonding will be reduced as the ground water thaws, and this will lead to ground instability and higher incidence of slope failure in pavements (Smith & Burgess, 2004). The effects of a rise in number of freeze-thaw cycles, on the other hand, includes the accelerated degradation of asphalt concrete materials (Abreu, 2019), a decrease in asphalt concrete structural capacity such as Marshall Stability (Özgan & Serin, 2013) and a decrease in tensile strength ratio of the asphalt mixture as a result of moisture-induced damages (Feng, Yi , Wang, & Chen, 2010).

TCCA affirms that an optimum approach for designing pavements over permafrost areas is to provide a pavement and embankment thickness such that thawing does not reach the existing in-situ subgrade material. Whenever this alternative becomes uneconomical, the airport pavement design should be based on the bearing strength of the thawed subgrade soil.

Therefore, the depth of thaw plays an important role in the design and performance of pavements located over permafrost areas. A study published by Argue and Denyes (1974) recorded observations of the thaw penetration depth in gravel runways in Canada (Argue & Denyes, 1974). Based on the observations, a relationship between the depth of thaw and the thawing index in gravel runways was stablished according to Equation 3.54 (TCCA, 1995).

$$X = -81.3 + 9.5\sqrt{I} \tag{3.54}$$

X is the depth of thaw penetration (cm) and I is the thawing index (^{o}C-days), calculated as the summation of daily average air temperatures over the thawing period (TCCA, 1992). This equation was used in this study to predict thaw penetration depth in several airports over northern regions in Canada.

3.7 Implementation

The solution process to design flexible airport pavements in FAARFIELD was presented in section 2.2.1. The software considers the Cumulative Damage Factor (CDF) concept, which assumes that the contribution of each aircraft type in a given traffic mix results in accumulated damage for the pavement. The process to calculate the thickness of the layers is iterative, consisting of 4 main analysis steps: (1) inputs, including aircraft mix, pavement structure and materials, and definition of design life, (2) mechanistic calculations (stresses/strains), (3) calculation of the allowable aircraft number of departures in the design period, and (4) the cumulative damage. If the cumulative damage is different than 1, the thickness of the layers can be adjusted, and the process goes in a loop until CDF reaches the optimum value. This iterative process was illustrated in Figure 2.9.

Accounting for the ambient conditions in a closed-form software, such as FAARFIELD, is not possible, since the current practice does not consider the variation in weather parameters like temperature and moisture, as an input for design practices. The consideration of climate variation along the pavement service life is detrimental to incorporate climate change predictions in the current design practices, nevertheless, it is not possible to assess the damage caused by climate fluctuation in a closed-form solution.

For this reason, this research proposes a methodology that enables the structural design of flexible airport pavements considering climate variations along the year, and climate change. The methodology follows 7 steps that can be incorporated in airport design practices, the steps being: (1) obtain hourly climatic data, (2) calculate and process the pavement temperature profile (3) estimate the seasonal asphalt concrete dynamic modulus and the soil Resilient Modulus (4) calculate pavement stresses and strains (5) determine the number of coverages and allowable departures (6) calculate the Cumulative Damage Factor (CDF) for rutting and fatigue (7) adjust the layer thicknesses if CDF is different than 1 and repeat the process until damage equals 100%. These steps will be further discussed in the following sections, accompanied by the results of a case study that is analyzed under different climate change scenarios. The flowchart in Figure 3.18 summarizes these steps.

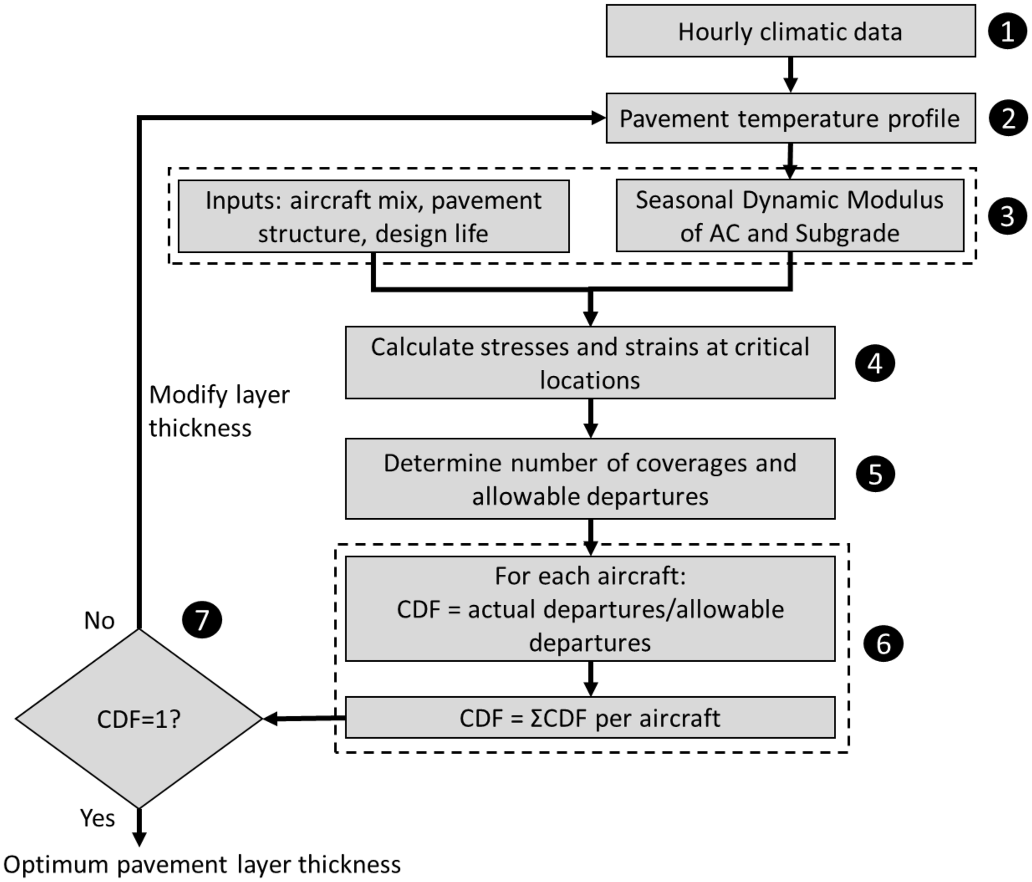

Figure 3.18: Proposed Solution Process.

3.7.1 Hourly Climatic Data and Pavement Temperature Profile

Obtaining hourly climatic data is the first step in the process. The data necessary in this phase includes climatic data (i.e., air temperature and wind speed), meteorological data (solar radiation), and pavement surface radiation properties (i.e., albedo, emissivity, and absorption coefficients). Section 5.1 has more information on sources available for download of the information necessary in this phase.

The second step is to determine the pavement temperature profile. The temperature profile is the pavement temperature gradient at different depths throughout the year, which can be useful to determine in what state the pavement subgrade is at (i.e., frozen, thawed, or unfrozen), and the temperature of the AC along the year. The temperature gradient can be calculated through a finite control volume method using the Temperature Estimate Model for Pavement Structures (TEMPS) software.

3.7.2 Asphalt Concrete and Subgrade Modulus

The third step is to determine the dynamic modulus of the asphalt concrete and the resilient modulus of the subgrade, according to each sub-season temperature record. To determine the dynamic modulus of the asphalt concrete, the modified Witczak sigmoidal function was used as previously explained in Section 3.3.1. The main model inputs are the loading rate, temperature, binder and volumetric design information.

To determine the variations in the resilient modulus of the subgrade per sub-season, this research uses a similar approach to the MEPDG (2004), in which an environmental adjustment factor (F_{env}) is used to modify the optimum resilient modulus ($M_{R_{opt}}$) of the soil according to variations in moisture and temperature. The procedures to estimate F_{env} were described in section 3.3.2.

Before moving to the next step, it is necessary to gather information on the aircraft mix and aircraft characteristics within the mix, such as the gross taxi weight, tire pressure, percent weight on main gear, tire spacing, number of annual departures and annual growth. It is also necessary to define the pavement design life and the initial thickness of the layers.

3.7.3 Calculate Stresses and Strains at Critical Locations

The fourth step is to calculate pavement stresses and strains at critical locations. Flexible pavement design codes typically use the Layered Elastic Design (LED) approach for its structural analysis (Heymsfield & Tingle, 2019). Some of the available LED based tools for pavements structural analysis are: KENLAYER, CHEVRON, DAMA, ELSYM5, BISAR, EVERSTRESS, and NonPAS. The Finite Element Method (FEM) can also be used to obtain flexible pavement responses. Some of the available two-dimensional FEM based tools are the ILLI-PAVE, GT-PAVE and MICH-PAVE and some of the general-purpose three-dimensional software are ABAQUS, ANSYS and ADINA. This research used KENLAYER to obtain pavement responses in the climate change scenarios. More information about each method available and the advantages and disadvantages of each was provided in section 2.3.

3.7.4 Number of Coverages, Allowable Departures and CDF

Step 5 consists in the calculation of number of coverages and allowable departures. Coverages can be defined as the number of repetitions of the maximum strain before failure. More information on the process to calculate the number of coverages to rutting failure were presented in section 3.3.1 and the equations that describes the number of coverages for fatigue failure were presented in section 3.4.1.

Step 6 has the goal of calculating the cumulative damage (CDF) caused by each individual aircraft and to sum up the damage to estimate the total damage of the fleet mix. The equations and procedures to determine the CDF were described in Section 3.3.1.

The last step is to check if the total cumulative damage is equal to one. That means 100% damage or pavement failure, at the end of the design life. If the CDF is higher than one, the thickness of the layers needs to be increased, and if the CDF is smaller than one, the thickness of the layers can be decreased, until an optimal design is reached.

In this research, steps 3, 5 and 6 have been implemented in Python codes for a more automated process. Python is a general-purpose programming language that has been ranked as one of the most popular programming languages according to results on feedback provided by 19,696 developers surveyed in 2020 (Jet Brains, 2021).

3.8 Summary

This chapter discussed the research methodology, including an overall view of each phase of the study and a detailed explanation of the equations and tools used to perform all types of analysis proposed in the thesis. The research methodology was divided into three phases, consisting of (1) data collection, (2) modeling and (3) implementation.

For the data collection, the sources of climate and climate change data used over the research were identified. The chapter listed equations that can translate the effects of temperature and moisture in the materials behavior and structural responses. Airport pavement transfer functions were identified, and the concepts of coverage, aircraft wander, coverage-to-pass ratio, and the effects of tandem gears were explained. The modeling tools and methods used in the mechanistic analysis were identified, and their role in the design of airport pavements was discussed.

Lastly, this chapter explained the steps for the implementation of an airport pavement design methodology that can account for climate and climate change parameters. The proposed process to calculate the thickness of the layers is iterative, consisting of 7 main analysis steps, where each step of the analysis was detailed throughout the chapter.

Chapter 4: Mechanistic Analysis

4.1 Case Study 1 (A380 PEP)

To better compare the modeling results from LED and FEA tools, with actual in-situ responses, a case study of an international airport in France was considered in this research, where the Airbus Industry, in partnership with the Service Technique des Bases Aériennes (STBA) and the Laboratoire Central des Ponts et Chaussées (LCPC), launched the A380 Pavement Experimental Program (PEP). The research aimed to provide full-scale data for a better understanding of flexible pavements structural behavior against wide body aircrafts for comparison to theoretical simulations. The test facility was built in Toulouse, consisting of a variety of subgrade soil categories for flexible pavements. The field database resulted from an extensive instrumentation. The structural response of each pavement layer was generated through strain gauges that were able to measure deflections and elongations (LCPC/AIRBUS/STBA, 2001).

The results of the A380 PEP were used to develop the transfer functions present in the airport pavement design software Alize-Airfield, with the aim to convert the calculated mechanistic response values to pavement distresses (Heymsfield & Tingle, 2019). The results of these full-scale tests and Alize-Airfield simulations were used in this research to compare with those from NonPAS, KENLAYER, and the FEM models developed in ABAQUS.

4.1.1 Material Properties

Considering the materials as being isotropic and linear elastic is very convenient because of the low number of parameters required in the analysis (only the Young modulus and Poisson’s ratio). Although the untreated granular materials usually present a non-linear elastic behavior, breaking down the untreated granular materials into several sublayers can make it possible to reproduce the non-linear elastic behavior by a linear elastic model with a relatively good accuracy. To implement the subdivision of the granular materials in sublayers, an adjustment was carried out by the PEP researchers through successive iterations on the modulus of the materials. Four (4) structures were built at the test facility, namely structures A, B, C and D, however, structure A encountered problems in its initial construction, and the tests in this section were discontinued.

Table 4.1 presents the layer properties of structures B, C and D tested on Toulouse Blagnac Airport (LCPC/AIRBUS/STBA, 2001). The three structures are composed of 8 cm of asphalt concrete (AC) in the surface layer, followed by 24 cm of Bituminous Gravel (GB) in the base course. The third layer is composed of a high-quality crushed gravel (GRH) with varying thickness, while the subgrade was constituted of clay materials mixed with gravel (LCPC/AIRBUS/STBA, 2001). Structure-B has the slimmer gravel layer of only 20 cm, followed by Structure-C, and lastly Structure-D which is the most robust with two gravel layers summing a total of 140 cm.

Table 4.1: Layer thickness and material properties. Source: (LCPC/AIRBUS/STBA, 2001).

Structure B		**Structure C**		**Structure D**	
Materials and thickness	**Moduli (MPa)**	**Material and thickness**	**Moduli (MPa)**	**Material and thickness**	**Moduli (MPa)**
AC 8 cm	3000	AC 8 cm	3000	AC 8 cm	6000
GB 24 cm	5000	GB 24 cm	5000	GB 24 cm	8000
GRH 20 cm	80	GRH 60 cm	110	GRH 70 cm	100
Subgrade 100 cm	80	Subgrade 100 cm	50	GRH 70 cm	70
Substratum	15000	Subgrade 100 cm	150	Subgrade 200 cm	60
-	-	Substratum	15000	Substratum	15000

The modulus of the bituminous materials was estimated according to the temperature during the tests and the simulator speed, which was approximately 2 km/h. The modulus values of the AC and GB materials remained the same for both the B and C structures because the average temperature in the bituminous layers was approximately 16℃. On the other hand, the AC and GB layers in structure D exhibited higher moduli because the average temperature of the bituminous materials during these tests were measured to be 12℃, which was lower than the other two structures (LCPC/AIRBUS/STBA, 2001).

4.1.2 Loading Parameters (A380 PEP)

For the purposes of modeling, each pneumatic load was considered as a uniform static vertical pressure, applied over a circular area on the pavement surface. It was also considered that the contact pressure is the same as the inflation pressure of the tire. Two loading configurations were considered in the analysis: 1) a tandem axle with dual wheels, and 2) a tridem axle with dual wheels, resulting in 4 and 6 wheels, respectively. The weight, pressure, radius and distance between axles and dual wheels are presented in Table 4.2, and a schematic of the gear configuration of the two loading vehicles is presented in Figure 4.1.

Table 4.2: Load description. Adapted from: (LCPC/AIRBUS/STBA, 2001).

Type	**Weight/wheel (KN)**	**Tire pressure (MPa)**	**Contact Radius (cm)**	**Dual wheels spacing (m)**	**Axle Spacing (m)**
4 wheels	232	0.88	28.97	1.12	1.47
6 wheels	239	1.53	22.3	1.40	1.45

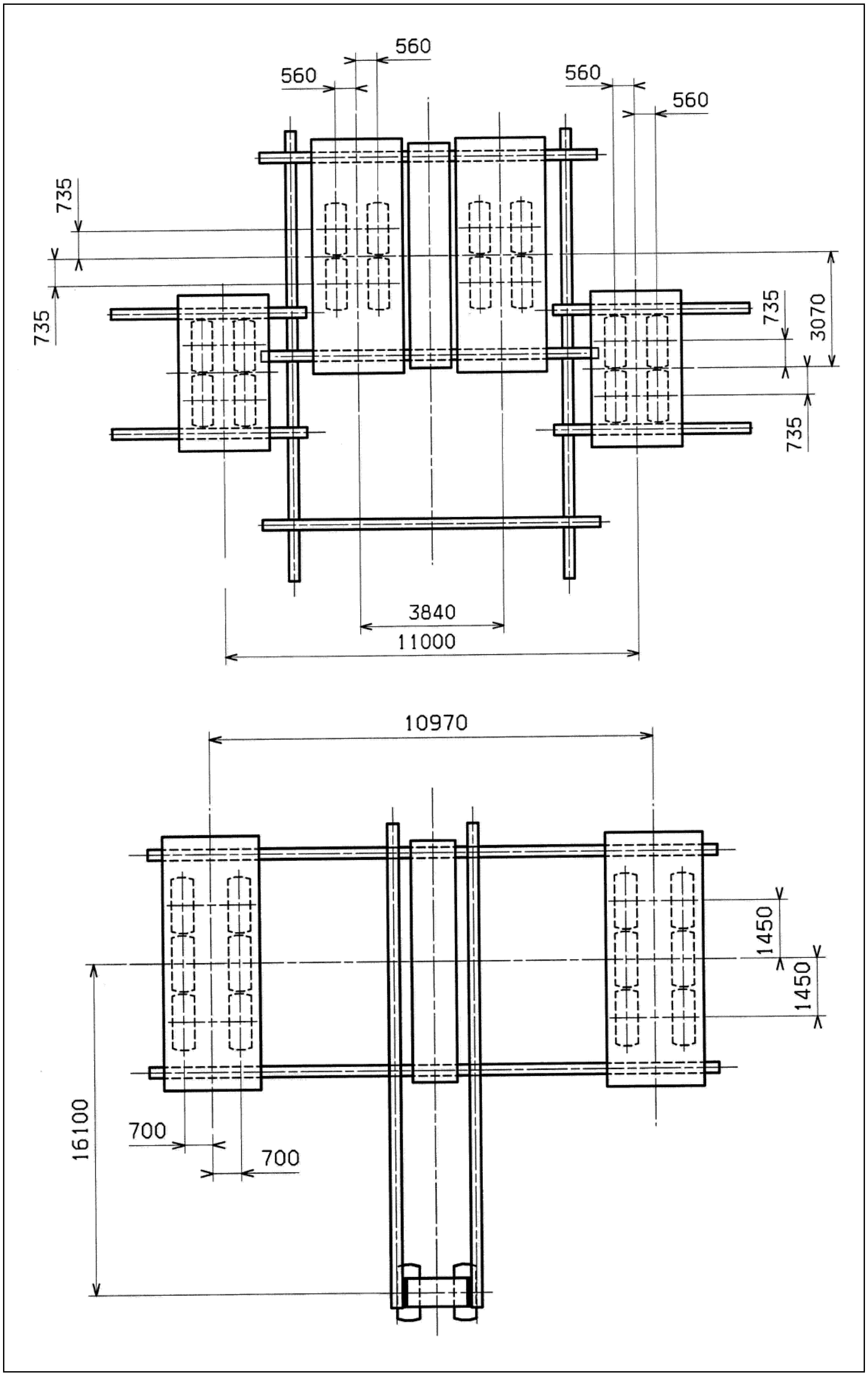

Figure 4.1: Gear configuration. Top: 4-wheel gears; bottom: 6-wheel gears.

4.1.3 Results: Case Study I

4.1.3.1 Vertical Strains

The vertical compressive strain (in micro-strains) measured at the top of the unbonded granular base and at the top of the subgrade layers are presented in Table 4.3 and Table 4.4, respectively. The tables present the results from full-scale measurements and the simulations in Alize, KENLAYER, NonPAS and ABAQUS. The rightmost column of the tables shows that all four software resulted in values close to the in-situ measurements.

Table 4.3: Vertical strain at the top of the base layer (in micro-strains).

Load type		**6-Wheel**			**4-Wheel**			
Structure type		**B**	**C**	**D**	**B**	**C**	**D**	
Results	Measured*	1596	1161	836	1301	1024	868	
	Alize*	1447	1155	983	1304	1025	882	
	KENLAYER	1409	1172	946	1352	1084	900	
	NonPAS	1419	1171	942	1357	1087	900	
	ABAQUS	1492	1210	1025	1375	1080	906	Average
Comparison	Alize to measured	9%	1%	18%	0%	0%	2%	5%
	KENLAYER to measured	12%	1%	13%	4%	6%	4%	7%
	NonPAS to measured	11%	1%	13%	4%	6%	4%	6%
	ABAQUS to Measured	6%	4%	23%	6%	5%	4%	8%

*Results published by (LCPC/AIRBUS/STBA, 2001).

From the presented results, it can be noted that KENLAYER had an average difference of 7% when compared to the vertical strains measured at the top of the base, and 6% when compared to the strains measured at the top of the subgrade. NonPAS, on the other hand, had an average difference of 6% when compared to the strains measured at the top of the base, and 5% when compared to the strains measured at the top of the subgrade, an average difference only slightly smaller than what was presented by KENLAYER.

The analysis performed with ABAQUS considered the pavement to be 6 m wide by 6 m long and a subgrade depth of 6 m. The mesh elements were finer near the load, starting at a range of 5 cm, and coarser in more distant areas. Like the premise adopted in all axisymmetric numerical models, the structures built in ABAQUS considered the layers contact to be fully bonded. Regarding the boundary conditions, the structures could move freely in the vertical direction and were constrained from moving in the horizontal direction. The deformed shape of structure B under 6 wheels in ABAQUS can be seen in Figure 4.2.

Table 4.4: Vertical strain at the top of the subgrade (in micro-strains).

Load type		**6-Wheel**			**4-Wheel**			
Structure type		**B**	**C**	**D**	**B**	**C**	**D**	
Results	Measured*	1162	1612	1061	1202	1327	844	
	Alize*	1278	1632	1016	1188	1536	842	
	KEN LAYER	1124	1518	976.9	1197	1547	858.6	
	NonPAS	1139	1518	976	1205	1547	843	
	ABAQUS	1262	1642	1060	1242	1554	852	Average
Comparison	Alize to measured	10%	1%	4%	1%	16%	0%	5%
	KENLAYER to measured	3%	6%	8%	0%	17%	2%	6%
	NonPAS to measured	2%	6%	8%	0%	17%	0%	5%
	ABAQUS to Measured	9%	2%	0%	3%	17%	1%	5%

*Results published by (LCPC/AIRBUS/STBA, 2001).

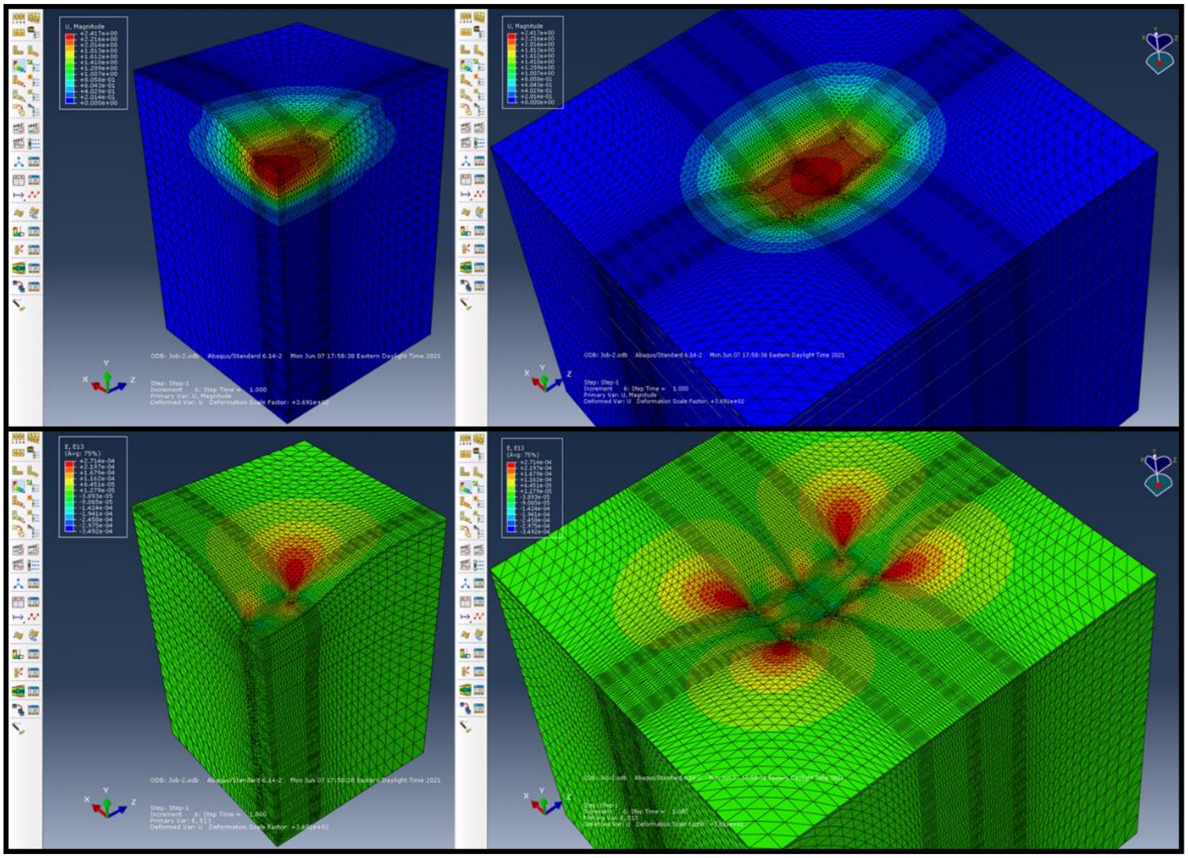

Figure 4.2: Deformed shape of pavement structure B under 6 wheels in ABAQUS. Colors represent displacement (top) and horizontal strains (bottom) at the top of the pavement.

The ABAQUS results presented in Table 4.3 and Table 4.4 show a good fit for most of the vertical strains considering both the top of the base and the top of the subgrade, with an average difference of only 8 and 5%, respectively. Vertical strain at the top of the base layer for structure D, under the 6-wheel bogie, had a difference of 23%, however, this result is close to Alize, which predicted strains about 18% higher than the measured values. For the 4-wheels bogie, the strains estimated at the top of the subgrade were 17% higher than the full-scale values. Nevertheless, the predicted vertical strain on the top of the subgrade in the 4-wheels bogie case is coherent with what was estimated in KENLAYER and NonPAS. The same results from Table 4.3 and Table 4.4 are presented in Figure 4.3 and Figure 4.4, respectively, to provide a graphic perspective.

It is possible to note from Figure 4.3 and Figure 4.4 that the variability of the various models can be significant. In Figure 4.3 for example, structure B under the 6-wheel vehicle, the maximum micro-strain is predicted by ABAQUS (1492), and the minimum micro-strain is predicted by KENLAYER (1409), a variability of 83 micro-strains between the two pieces of software. In most cases, the strains predicted by ABAQUS were higher than the other software. KENLAYER and NonPAS results are in proximity in all scenarios, and in some cases the results were the same. The results from Alize show that the software predictions were sometimes lower, sometimes higher than the other software.

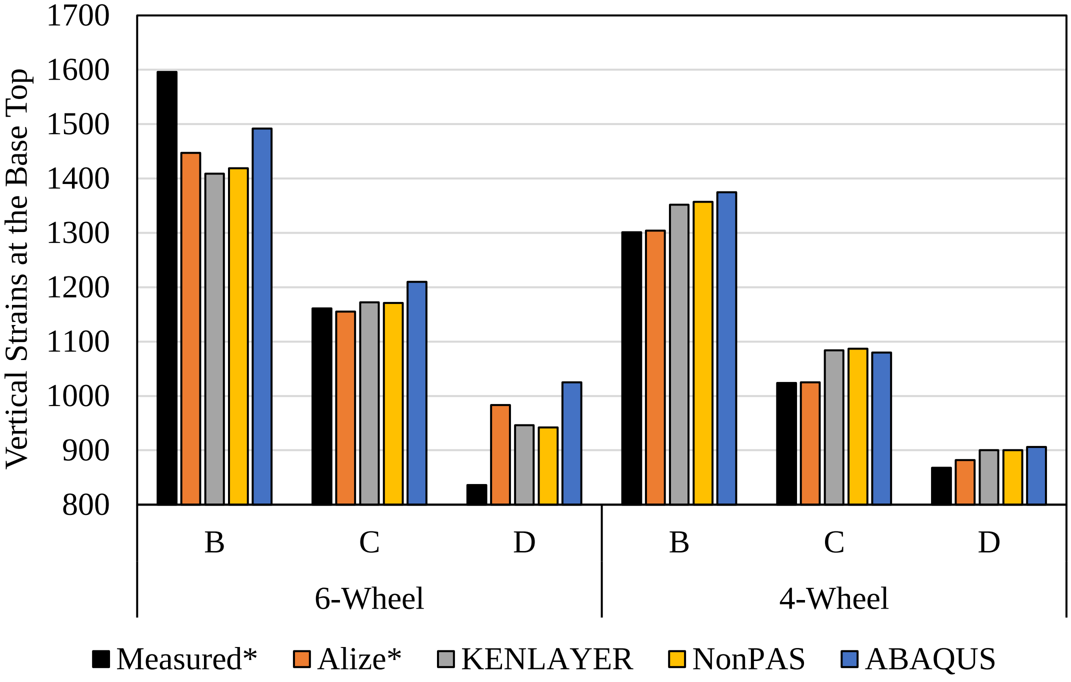

*Results published by (LCPC/AIRBUS/STBA, 2001).

Figure 4.3: Vertical strain at the top of the base layer (in micro-strains).

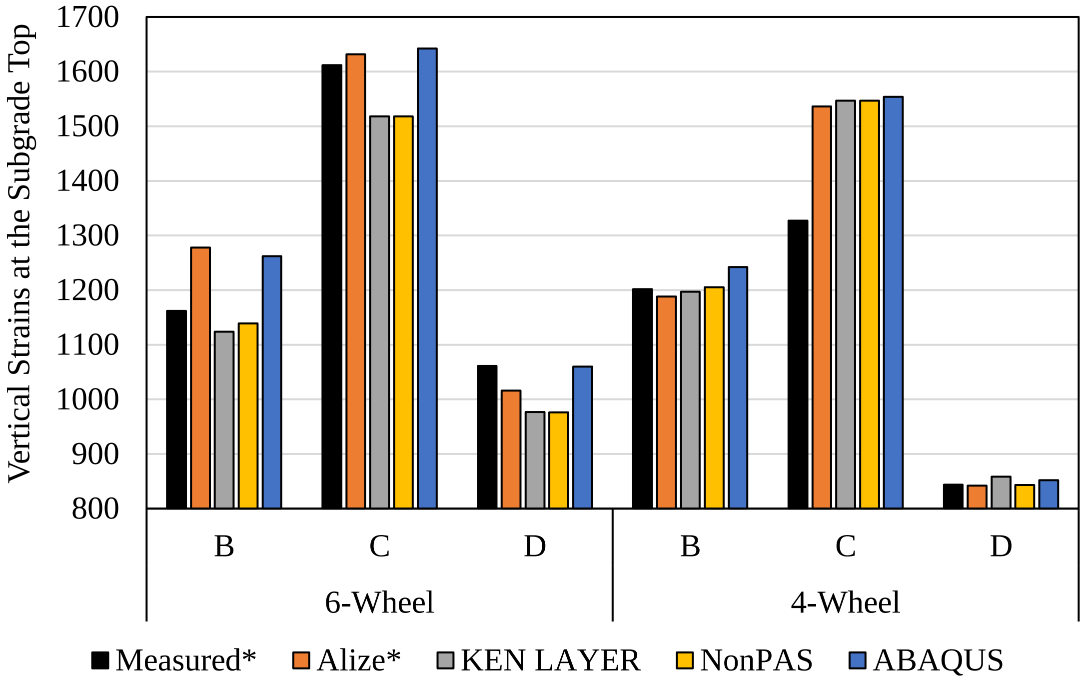

*Results published by (LCPC/AIRBUS/STBA, 2001).

Figure 4.4: Vertical strain at the top of the subgrade (in micro-strains).

It is important to note that each analysis performed in ABAQUS during this study took around a couple of hours to converge. This computational time can vary greatly depending on the machine capacity; however, the time will always greatly exceed the analysis performed by a layered-elastic-based software using the same processing capacity.

A one-way Analysis of Variance (ANOVA) was performed to investigate if there is a statistically significant difference between the simulated values from Alize, KENLAYER, NonPAS, ABAQUS, and the field measured vertical micro-strains. ANOVA is a statistical test used to analyze the difference between the means of more than two groups of data (Devore, 2011). The null hypothesis H_0 in ANOVA indicates that there are no differences in the population between the means of the individual groups.

The ANOVA method assesses the relative size of variance among group means (between group variance, also called Mean Square for Treatments MSTr) compared to the average variance within groups (within group variance, also called Mean Square for Error MSE) as presented in Equation 4.1 (Devore, 2011).

$$F_{observed} = \frac{\text{between group variance}}{\text{within group variance}} = \frac{MSTr}{MSE} \qquad 4.1$$

If the ratio $F_{observed}$ is greater than expected by chance, the null hypothesis can be rejected, which means that at least one mean is substantially different than the others. To reach a statistical conclusion, it is necessary to compare the $F_{observed}$ value with the critical value

$F_{critical}$ at a certain α (error level). Table 4.5 and Table 4.6 show the results of the ANOVA analysis with an α error level pre-set at 0.05, for the vertical micro-strains at the base and top of subgrade, respectively.

Table 4.5: ANOVA results for vertical micro-strains at the base top.

Source of Variation	***SS***	***df***	***MS***	***$F_{observed}$***	***$F_{critical}$***	***P-value***
Between Groups	9926.4	4	2481.6	0.046733	2.75871	0.995609
Within Groups	1327548.6	25	53101.9			
Total	1337475	29				

Table 4.6: ANOVA results for vertical micro-strains at the subgrade top.

Source of Variation	***SS***	***df***	***MS***	***$F_{observed}$***	***$F_{critical}$***	***P-value***
Between Groups	23415.8	4	5854.0	0.072394	2.75871	0.989866
Within Groups	2021567.9	25	80862.7			
Total	2044983.8	29				

In Table 4.5 and Table 4.6, *SS* stands for Sum of Squares, *df* stands for Degrees of Freedom, and *MS* stands for Mean Square. It is possible to note that in both tables $F_{observed}$ is smaller than $F_{critical}$, therefore, the null hypothesis cannot be rejected, which means that there are no significant differences in the population between the means of the individual groups, Alize, KENLAYER, NonPAS, ABAQUS, and the field measured vertical micro-strains.

The *P-value* is the probability of obtaining an $F_{observed}$ ratio as large or larger than the one observed. The *P-value* probability will be smaller than the α error level established at 0.05 in case the null hypothesis is rejected. The *P-values* presented at Table 4.5 and Table 4.6 are much greater than 0.05, confirming that the null hypothesis cannot be rejected.

4.1.3.2 Horizontal Strains

The horizontal micro-strains measured at the bottom of the bituminous base layer during the full-scale tests are presented in Table 4.7 along with the results of the KENLAYER, NonPAS and ABAQUS simulations.

KENLAYER, NonPAS and ABAQUS had results that were very different from what was measured in the field, with an average difference of 23% for KENLAYER and 24% for NonPAS and ABAQUS. When compared to KENLAYER and NonPAS, it can be noted that the predicted horizontal strains from ABAQUS were closer to the field measurements for structure C. While KENLAYER led to a difference of 20% and 35%, and NonPAS resultd in 29% and 36% differences, ABAQUS results were closer with a smaller difference of 17% and 3%, for the 6- and 4-wheel cases, respectively.

Table 4.7: Horizontal micro-strains at the bottom of the bituminous gravel base.

Load Type	**6-Wheel**			**4-Wheel**			
Structure type	**B**	**C**	**D**	**B**	**C**	**D**	
Measured*	303	291	329	224	224	320	
KENLAYER	324	348	259	281	303	231	
NonPAS	349	376	279	302	305	279	
ABAQUS	228	243	177	214	216	165	Average
KENLAYER to measured	7%	20%	21%	26%	35%	28%	23%
NonPAS to measured	15%	29%	15%	35%	36%	13%	24%
ABAQUS to Measured	25%	17%	46%	4%	3%	49%	24%

*Results published by (LCPC/AIRBUS/STBA, 2001).

For structure B under 4-wheel bogie, ABAQUS simulations showed good agreement when compared to the measured horizontal strains, with a difference of only 4%, while KENLAYER and NonPAS had a difference of 26% and 35% respectively. However, the results were not so good in the 6-wheel bogie case, in which ABAQUS had a difference of 25%, while KENLAYER and NonPAS had a 7% and 15% difference, respectively. Lastly, the ABAQUS predictions for Structure-D was found to have the biggest deviation from the in-situ measurements. The difference from the field measurements was 46 and 49% for the 6- and 4-wheel bogie scenarios, much higher than the differences presented by KENLAYER and NonPAS predictions.

Further examining the in-situ responses, it can be realized that this difference can most probably be due to an inconsistency in the field measured horizontal strains for Structure D. In other words, Structure D had a significantly stronger structure as compared to structures B and C, with thicker gravel layers. Also, the moduli of the asphalt layers are considerably higher in structure D (i.e., 6000 and 8000 MPa compared to only 3000 and 5000 MPa from the other structures). A more robust structure should consequently lead to smaller horizontal strains; however, this was not the case based on the reported in-situ responses of the Structure D. Therefore, a significant difference was found between the modeling and measured values for Structure D. There may be several sources for this discrepancy in the field measurements, but this falls beyond the scope of the current study. The same results from Table 4.7 are presented in Figure 4.5, to assist with a visual comparison between software.

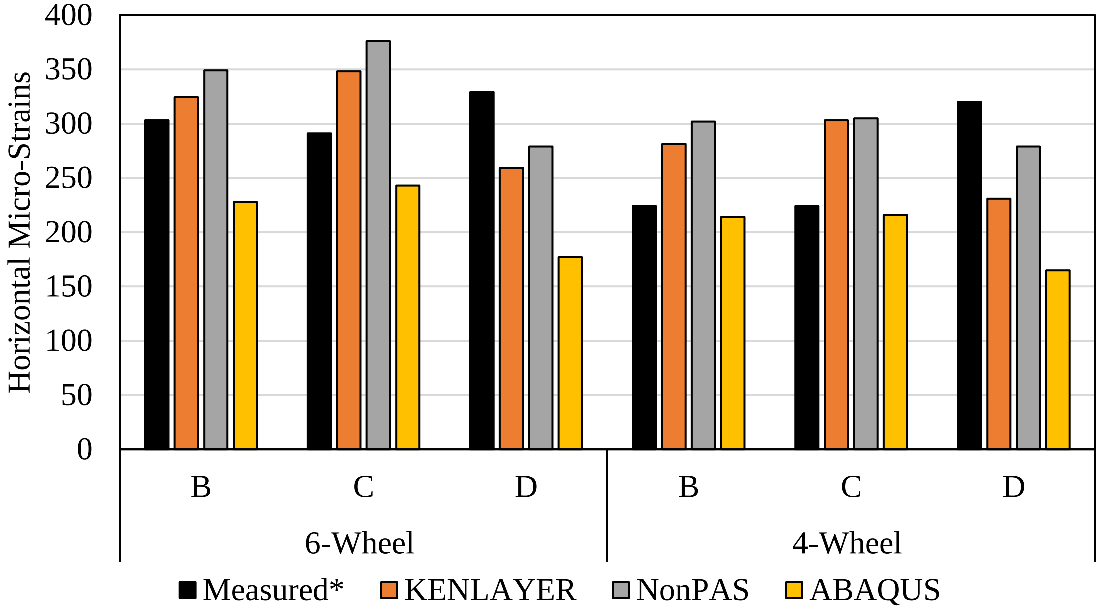

*Results published by (LCPC/AIRBUS/STBA, 2001).

Figure 4.5: Horizontal micro-strains at the bottom of the bituminous gravel base.

It can be seen from Figure 4.5 that the variability among the software continued accentuated among the results of the horizontal micro-strains at the bottom of the bituminous gravel base. In structure B under the 6-wheel vehicle, for example, the maximum micro-strain is predicted by NonPAS (349), and the minimum micro-strain is predicted by ABAQUS (228), a variability of 121 micro-strains between the two software. Differently from the results of vertical strains, the horizontal strains predicted by ABAQUS were lower than the other software in all cases. KENLAYER and NonPAS results continued to be in proximity for most scenarios, with the exception of structure D, 4-wheel results.

In order to achieve better results in terms of the horizontal strains, the time dependence of the bituminous materials would have to be carefully considered in the numerical models. This becomes especially important for the case of the investigated full-scale testing, in which the visco-elastic behavior of the bituminous materials was certainly accentuated due to the low speed of the applied loads at about 2 km/h.

A one-way ANOVA was performed to investigate if there is a statistically significant difference between the simulated values from KENLAYER, NonPAS, ABAQUS, and the field measured horizontal micro-strains at the bottom of the bituminous gravel base. Table 4.11 shows the results of the ANOVA analysis with an α error level pre-set at 0.05.

Table 4.8: ANOVA results for horizontal micro-strains at the bottom of the bituminous gravel base.

Source of Variation	***SS***	***df***	***MS***	$F_{observed}$	$F_{critical}$	***P-value***
Between Groups	39251.2	3	13083.7	8.070644	3.098391	0.001018
Within Groups	32423.1	20	1621.2			
Total	71674.3	23				

It is possible to note in Table 4.8 that the $F_{observed}$ is greater than $F_{critical}$, and that the *P-value* is smaller than the α error of 0.05. Therefore, the null hypothesis is rejected, which means that there is a significant difference in the population between the means of the individual groups, KENLAYER, NonPAS, ABAQUS, and the field measured horizontal micro-strains. In a case where a significant difference is detected among the group means, it is necessary to examine what specific pair of group means shows difference.

To compare specific group means, it is necessary to perform post hoc tests, also known as multiple comparisons. Tukey's Honest Significant Difference (HSD) test is a post hoc test commonly used to assess the significance of differences between pairs of group means. When using Turkey`s HSD test it is possible to set the experiment-wise error rate for the entire set of comparisons, which is not possible when performing multiple t-student tests, for example.

To perform the Turkey's HSD test, first it is necessary to define the critical value of the Tukey HSD $Q_{critical}$, based on the number of groups, the degrees of freedom within the groups, and the significance level in the studentized range distribution. For a number of groups equal to 4, degrees of freedom within the groups equal to 20, and a significance level of 0.05, $Q_{critical}$ is equal to 3.9585. Next, it is necessary to calculate the Tukey test $Q_{statistic}$ for each pair of groups being compared, according to the Equation 4.2 (National Institute of Standards and Technology, 2002).

$$Q_{statistic} = \frac{|\bar{x}_i - \bar{x}_j|}{\sqrt{\text{MSE}}} * \sqrt{H_{i,j}} \qquad 4.2$$

where,

- $\bar{x}_i$, $\bar{x}_j$ = groups i and j means
- MSE = Mean Square Error
- $H_{i,j}$ = harmonic mean of the number of observations in groups i and j. When the sample sizes between the groups are equal, the harmonic mean is simply the common sample size

Similar to the ANOVA test, the null hypothesis H_0 indicates that there are no differences in the population between the means of the individual groups. If the calculated $Q_{statistic}$ is greater than expected by chance ($Q_{critical}$), the null hypothesis can be rejected, which means that the means are substantially different. Table 4.9 shows the results of the Turkey's

HSD test comparison between each software (KENLAYER, NonPAS and ABAQUS) and the field measured results.

Table 4.9: Turkey's HSD test

Comparison	$Q_{statistic}$	**> or <**	$Q_{critical}$	**Accept or Reject**
KENLAYER vs Measured	0.57	<	3.9585	Accept
NonPAS vs Measured	2.03	<	3.9585	Accept
ABAQUS vs Measured	4.55	>	3.9585	Reject

According to the results presented at Table 4.9, there is a significant difference between the means of the measured values, and the ABAQUS simulated micro-strains at the bottom of the bituminous gravel base, however, for the KENLAYER and NonPAS comparison, the results showed that there was no significant difference between the group means.

4.2 Case Study (NAPTF)

The National Airport Pavement Test Facility (NAPTF) traffic tests have been widely used by various researches in the analysis of non-linear pavement models (Gopalakrishnan, 2004), (Kim, Tutumluer, & Kwon, 2009), (Mojarrad, 2011). The test sections were constructed to generate full-scale data to support the investigation of airport pavements performance subject to new generation aircrafts (Gopalakrishnan, 2004).

The field database used in this research was generated through an extensive instrumentation that included static sensors and dynamic gages. The structural response instrumentation included Multi-Depth Deflectometers (MDDs), Pressure Cells (PCs) and Asphalt Strain Gauges (ASGs), installed within the pavement sections to measure load-induced responses (Gopalakrishnan, 2004).

The software used in this analysis were KENLAYER, NonPAS and GT-PAVE. Because in GT-PAVE all parameters must be defined in imperial units, the next section will present the material properties in the imperial unit system for consistency.

4.2.1 Material Properties (NAPFT)

The structure analyzed in this study is named MFC, where *M* stands for a medium subgrade strength, *F* stands for a flexible pavement type, and *C* stands for conventional, indicating that the base and sub-base layers are not stabilized. The MFC structure is composed of 5 inches (12.7 cm) of asphalt concrete layer (P-401), followed by 8 inches (20.32 cm) of granular base (P-209), and 12 inches (30.48 cm) of granular subgrade (P154), on the top of a medium strength subgrade with a CBR of approximately 8% (Gopalakrishnan, 2004). The material properties of each layer are presented in Table 4.10.

Table 4.10: Pavement geometries and material properties modified from (Gopalakrishnan, 2004) and (Kim, Tutumluer, & Kwon, 2009).

Pavement Layer	Thickness (in.)	E or M_r (psi)	Poisson's Ratio	Material Properties				Cohesion (psi)	Internal Friction (deg)	Density (pcf)
AC	5	1,199,172	0.35	Isotropic and linear elastic				-	-	156.0
Base	8	Nonlinear	0.38	Nonlinear: Uzan model				11.0	60	158.1
				K1 (psi)	K2	K3	-			
				1,493.9	0.4	0	-			
Sub-base	12	Nonlinear	0.38	Nonlinear: Uzan model				26.4	44	123.0
				K1 (psi)	K2	K3	-			
				1,000.8	0.64	0	-			
Subgrade	94.8	Nonlinear	0.40	Nonlinear: bilinear model				13.1	0	90.9
				K1 (psi)	K2	K3	K4			
				9,108.4	6.09	420	570			

4.2.2 Loading Parameters (NAPFT)

Similar to Case Study 1, each pneumatic load was considered as a uniform static vertical pressure, applied over a circular area on the pavement surface. It was also considered that the contact pressure is the same as the inflation pressure of the tire. The loading cart used in the tests simulated a six-wheel dual-tridem type aircraft gear configuration, in which each individual wheel had a load of 40,000 lb, and a uniform tire pressure of 188 psi. Table 4.11 presents the details of the loading gear.

Table 4.11: Load description. Adapted from: (LCPC / AIRBUS / STBA, 2001).

Type	Weight/wheel (lb)	Tire pressure (psi)	Contact Radius (in)	Dual wheels spacing (in)	Axle Spacing (in)
6 wheels	40,000	188	8.23	54	57

4.2.3 Results: Case Study 2

Three pavement responses were analyzed in case study 2: the maximum compressive stress at the top of the subgrade (σ_c), the maximum vertical displacement at the pavement surface δ_v, and the horizontal strain at the bottom of the AC (ε_h). The simulations were performed in GT-PAVE, NonPAS, and KENLAYER, and the results were compared to full-scale measurements. The full-scale stresses and displacements, as well as the simulated responses from ABAQUS were obtained from the study of (Kim, Tutumluer, & Kwon, 2009), while the full-scale strains were obtained from the study of (Gopalakrishnan, 2004). The results are presented in Table 4.12.

Table 4.12: Simulated pavement responses compared to field measurements.

Analysis	**Software**	**σ_c (MPa)**	**δ_v (mm)**	**ε_h (micro-strain)**
Results	Measured	0.10*	1.82*	310.00**
	ABAQUS	0.09*	1.65*	-
	GT-PAVE	0.11	1.76	432.78
	NonPAS	0.08	5.00	476.55
	KENLAYER	0.09	3.99	653.00
Comparison	ABAQUS to measured	14%	9%	-
	GT-PAVE to measured	7%	3%	40%
	NonPAS to measured	7%	175%	54%
	KENLAYER to measured	9%	119%	111%

*Results published by (Kim, Tutumluer, & Kwon, 2009)

**Results published by (Gopalakrishnan, 2004)

The results show that all software were quite successful in predicting the maximum compressive stress at the top of the subgrade. The absolute difference from the full-scale measurements was about 7% for both GT-PAVE and NonPAS, while KENLAYER presented a difference of 9%. It is surprising that the stresses predicted from ABAQUS (Kim, Tutumluer, & Kwon, 2009) presents a bigger difference of 14%. The bar chart presented in Figure 4.6 (a) shows the maximum compressive stress at the top of the subgrade for all the software in blue, compared to the full-scale measurements in green, which overall indicates a good agreement with most of the programs underpredicting the compressive stress values except for GT-PAVE that tended to overpredict the stress.

The bar chart presented in Figure 4.6 (b) shows the vertical displacement predicted by all software in blue, compared to the full-scale measurements in green. Only ABAQUS and GT-PAVE were able to successfully predict the vertical displacements at the pavement surface, with an absolute difference of 9% and 3% from the field measurements, respectively. NonPAS and KENLAYER predicted displacements that are much higher than the full-scale results, with a difference of 175% and 119% respectively.

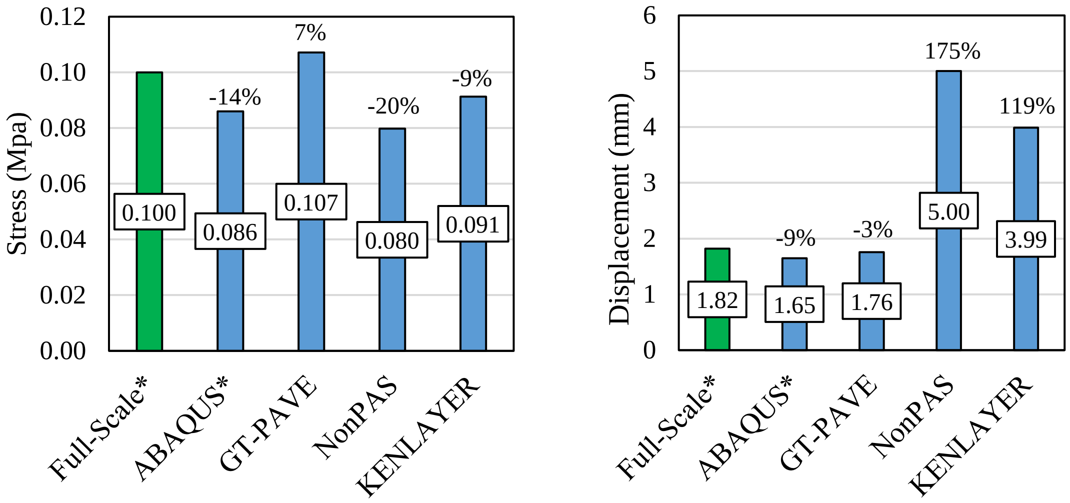

(a) (b)

*Results published by (Kim, Tutumluer, & Kwon, 2009)

Figure 4.6: (a) Maximum compressive stress at the top of the subgrade and (b) maximum vertical displacement at the pavement surface (mm)

In a similar way, Figure 4.7 presents the maximum horizontal strain at the bottom of the AC (micro-strain) predicted by all software in blue, compared to the full-scale measurements in green. The results reveals that all the software predictions were far from what was measured in the field, with a difference of 40%, 54%, and 111% from GT-PAVE, NonPAS, and KENLAYER, respectively. This is consistent with the finding from the Case Study 1, with the reason being probably the same as pointed out earlier, that is, to achieve better results regarding the horizontal strains, the visco-elastic behavior of the bituminous materials would have to be carefully considered in the numerical models, to account for the time and temperature dependency of the asphalt layers.

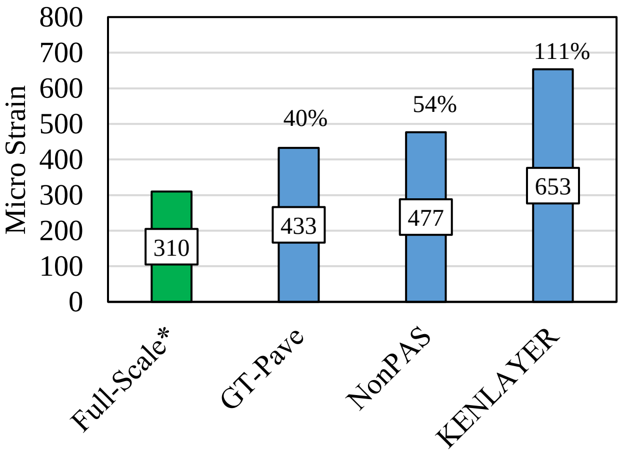

*Results published by (Gopalakrishnan, 2004)

Figure 4.7: Maximum horizontal strain at the bottom of the AC (micro-strain)

4.3 Summary

This chapter discussed the ability of different computational tools used for mechanistic analysis of airfield pavements. Every software would have certain advantages and limitations, therefore, when performing mechanistic analysis and design of airport pavements, one should have in mind the level of accuracy that needs to be reached as well as the affordable computational time. To this end, two case studies based on full-scale pavement test sections were simulated and the predicted results were compared with the field measurements. The first case study compared simulations from two layered elastic software (i.e., KENLAYER and NonPAS), as well as one finite element software (i.e., ABAQUS), using a purely linear elastic approach. The second case study compared simulations from two layered elastic software (i.e., KENLAYER and NonPAS) as well as one finite element software (i.e., GT-PAVE), using a non-linear elastic approach.

The results from both case studies indicate that KENLAYER and NonPAS can have good agreement with field measurements when predicting pavement vertical strains and stresses at the top of the subgrade. However, the calculated vertical displacements could be far from the field measurements (as demonstrated in Case 2). This indicates that the layered elastic analysis would be a good alternative to be used in cases where rutting, and consequently the compressive stress at the top of the subgrade, is the dominant mechanism contributing to the overall pavement performance.

The results of both case studies demonstrate that ABAQUS and GT-PAVE can successfully predict the compressive stresses as well as the vertical surface displacements. In case study 2, GT-PAVE even outperformed the ABAQUS predictions. This points out that although the superposition of pavement responses can lead to some levels of error when nonlinearity of materials is being considered, this approach can still provide relatively accurate results.

A 2D axisymmetric modelling software can provide relatively accurate results in a much shorter time as compared to a 3D simulation using a general-purpose software. This highlights why the former approach is currently more popular in many design applications, while the latter is utilized mainly in research and when there is a need to further investigate the effect of loading (i.e., contact area, stress distribution, transient characteristics) or materials properties.

Lastly, the predicted horizontal strains at the bottom of the asphalt mix layer were far from the field measurements for all software analysis in both case studies; this points out to the need for proper consideration of the visco-elastic behavior of the bituminous materials in both the analytical and numerical models.

Chapter 5: Cumulative Damage Analysis

The 7-step methodology proposed in Section 3.7 was implemented in the case study of the Toronto Pearson International Airport. The proposed method, however, can be applicable to any airport, since it guides the designers in a broad way that can be easily implemented in the design of airport pavements in different locations in the world.

5.1 Data Collection

For the study of the current climate, the data collection includes past hourly temperature data, solar radiance, wind speed and surface albedo. For this scenario, the data was downloaded from the National Solar Radiation Database (NSRD) (National Renewable Energy Laboratory, 2022). Temperature and wind records are also available at the Environment Canada website (Govenment of Canada, 2022), however, the main advantage of using the NSRD is the availability of solar radiance data.

For the climate change scenarios, two main sources were used: Climate Atlas of Canada and the Weather Morph. Climate Atlas of Canada (Prairie Climate Centre, 2022) was used to evaluate frost/thaw conditions while the Weather Morph was used to obtain predictions of future temperature data. To that end, a web-based application called “Weather Morph: Climate Change Weather File Generator” was used to generate the hourly temperature records. The web-based application has data available for many locations across the world with combinations of four gas emission scenarios in three time-horizons: 2020s, 2050s and 2080s (Jiang, Liu, Czarnecki, & Zhang, 2019). The data is available at http://139.62.210.131/weatherGen/.

Field data used to implement to proposed methodology consist of:

- Bore holes, including subgrade material type, gradation, and Plasticity Index (PI)
- Aircraft fleet mix, annual departures and predicted % growth

All field data was kindly shared by Toronto Pearson International Airport for the purpose of this research and is detailed in the next section.

5.2 Background on Toronto Pearson International Airport

It was showed in sections 2.1.1 and 2.1.4 that there are strong warming and precipitation trends in the territories located in the south areas of Canada, therefore, when choosing the case study, an airport located in the south of Canada was preferred.

Toronto Pearson International Airport is Canada’s busiest airport. In 2019, the airport had 50.5 million passengers and handled 452,800 flights. The airport process over 45 percent of Canada’s air cargo and can carry the heaviest aircrafts in world, such as the Antonov-225 (Greater Toronto Airports Authority, 2020).

To accommodate such a large traffic of people and cargo, Pearson has five runways, 3 main and 2 crosswind, and 30 taxiways, constructed of concrete, asphalt or a combination of the two. The shortest runway at the airport has 2,744 meters long and 61 meters wide, while the longest has 3,390 meters long and 61 meters wide (Greater Toronto Airports Authority, 2020). An aerial view of the airport can be seen in Figure 5.1.

Figure 5.1: Aerial view of the Toronto Pearson International Airport (National Business Aviation Association, 2020)

5.2.1 Temperature and Precipitation Trends

Toronto Pearson Airport (YYZ) has experienced a significantly increment of its lowest and maximum temperature, reaching a difference of 4.4°C in the past 70 years (Abreu, 2019). A clear trendline can be seen in Figure 5.2, which presents the annual maximum pavement surface temperature for Toronto Airport through the years, from 1950 to 2020, with a continuing trend up to 2040. The figure shows that the annual maximum surface temperature increased in 1.6°C in the referred period.

Figure 5.3 presents the decennial precipitation since 1950, at Vancouver (YVR), Montreal (YUL), and Toronto (YYZ) airports. Two main conclusions can be taken from this figure, the first is that those airports receive a significant amount of precipitation annually, what makes them more susceptible to suffer moisture damage, and the second is that the annually precipitation amount is gradually, but consistently, increasing.

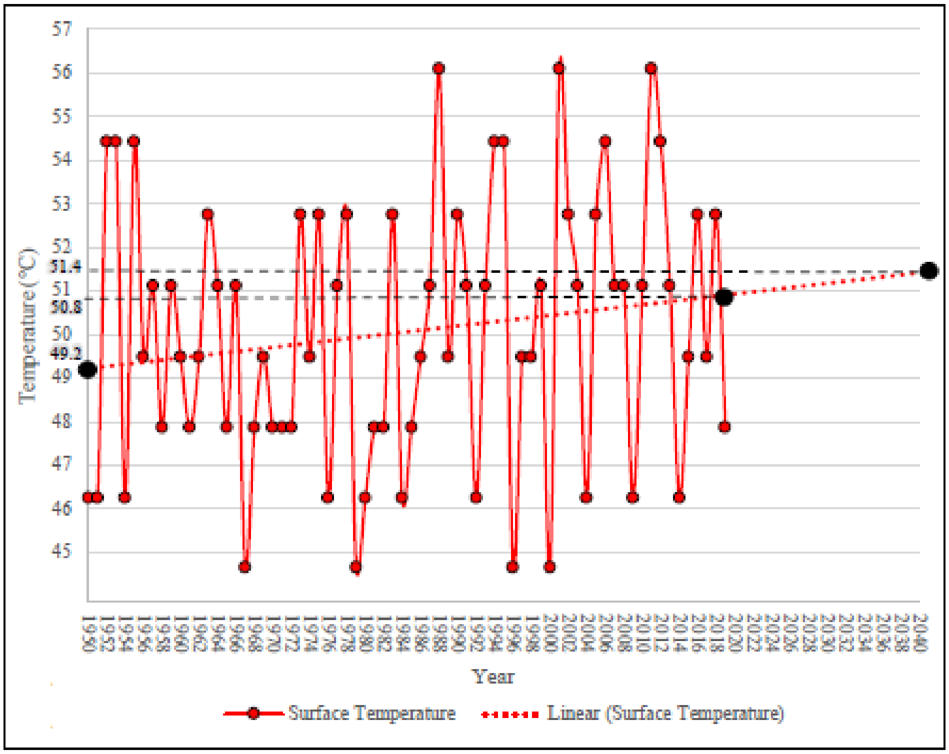

Figure 5.2: Annual Maximum Pavement Surface Temperatures at YYZ, modified from (Abreu, 2019).

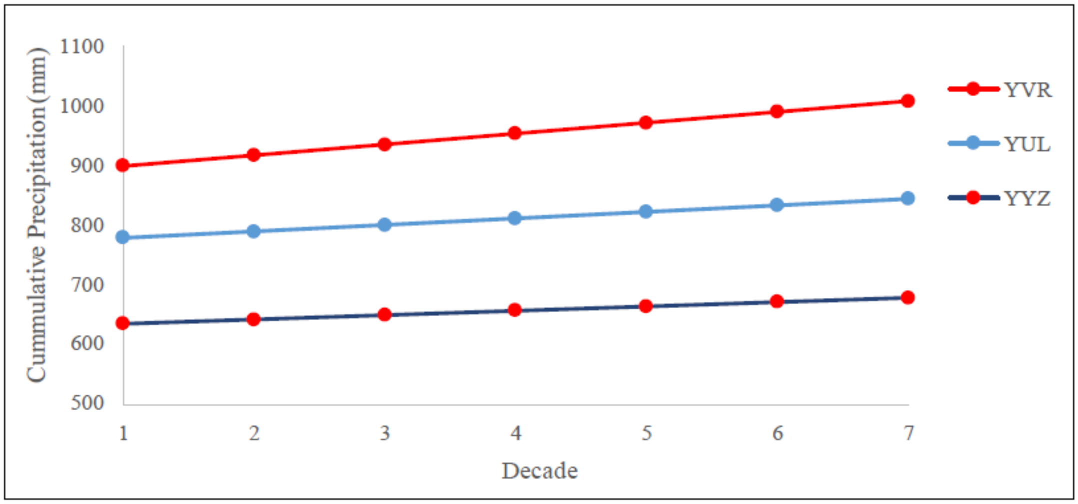

Figure 5.3: Decennial Precipitation since 1950, at YVR, YUL and YYZ. Modified from (Abreu, 2019).

5.2.2 Soil Data

Considering borehole data provided by the Greater Toronto Airports Authority (GTAA), the predominant subgrade material in the airport is Sandy Lean Clay with Gravel. The frost susceptibility is low to moderate. The tested soil materials presented 8.8% of gravel, 29% of sand, 32.5% of silt and 29.7% of clay.

Table 5.1 shows more information about the subgrade soil, such as the plastic and liquid limit, the percent passing sieve #200 (p_{200}), the grain size corresponding to 60% passing by weight (D_{60}) and the CBR. The optimum resilient modulus of the subgrade was considered as 51.71 MPa.

Table 5.1: Subgrade properties at Pearson (source: granted by GTAA).

Soil Type	Sandy Lean Clay with Gravel
Plastic Limit (PL)	17.2%
Liquid Limit (LL)	29.6%
Plasticity Index (PI)	12.4
p_{200}	62.1%
D_{60}	0.066 mm
CBR	5%

According to the soil classification system defined in the ASTM D2487-17, the existing soil at the Toronto Pearson airport can be classified as a low-plasticity clay (also called lean clay). In this case, the assumption of a constant void ratio is acceptable, and the equilibrium degree of saturation (S_{equil}) can be calculated through Equation 3.28.

5.2.3 Traffic

In 2019, 50.5 million passengers travelled through Toronto Pearson airport and about 452,800 flights were handled (GTAA, 2020). In 2020 and 2021 the number of flights decreased drastically due to the COVID19 pandemic, totaling 32,899 and 6,383 movements in 2020 and 2021 respectively. It is believed that the number of flights will resume its normal levels in the next few years, and Toronto Pearson Airport will continue to grow in the long term. For this reason, the traffic information used in this analysis will be based in the total movements of 2019, and the growth predictions will be based in the airport master plan published in 2018 (GTAA, 2018).

The airport master plan predicts that aircraft movements (takeoffs and landings) will grow at a rate of 1.5% as a high estimate, while its low estimate predicts growth at a rate of 1.13%. Considering the impact of COVID19 pandemic, the author will assume the lowest growth rate prediction of 1.13%.

An airport runway design is greatly influenced by the type of aircrafts serving an airport. To perform the structural design of a runway, first it is necessary to define the aircraft fleet mix, that is, the percentage of aircraft, by type or category, that operates at the airport.

A presentation given by Kevin Chee in the Ontario Asphalt Pavement Council OAPCs' seminar showed that the busiest runway of Toronto Pearson Airport in 2017 was runway 05-23, managing 45% of the aircraft movements, and more recent information shared by the Greater Toronto Airports Authority (GTAA) with the author shows that runway 05-23 continued to have 45% of the total movements in 2019. The movements distribution in the runways of Toronto Pearson Airport can be seen in Figure 5.4.

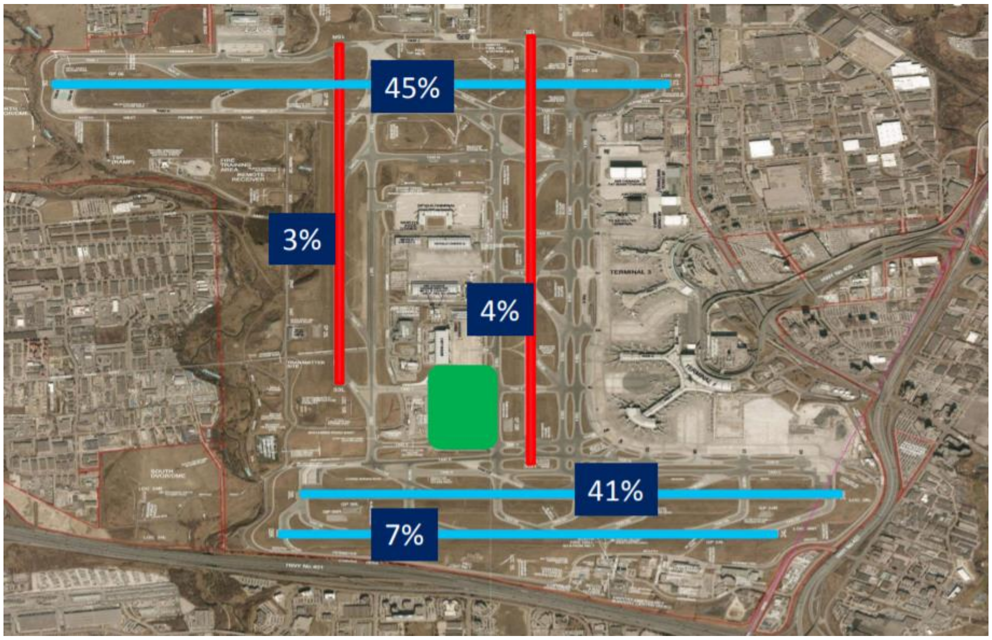

Figure 5.4: Flight distribution over airport runways (Chee & Ahmed, 2018).

The aircraft fleet mix presented at Table 5.2 was developed based on the traffic occurred in 2019, according to data shared by the GTAA with the author. It is a common practice to consider the aircraft wheel load to have a circular contact area with a flexible pavement. FAARFIELD, however, defines the wheel contact as elliptical, following the guidelines given by Huang, 1993 (Huang, 1993), in which the contact length is about 1.6 times longer than the contact width. Table 5.3 presents the loading characteristics of the most critical aircraft of the fleet mix, that is, the B777-300 ER, as considered by FAARFIELD.

Table 5.2: Traffic Inputs.

Aircraft	**Gross Taxi Weight (kg)**	**Annual Departures at 05-12**	**Annual Growth**	**Total Departures**
A320-200 std	73900	7063	1.13	157222
A321-100 std	83400	5679	1.13	126415
B767-300	159665	5301	1.13	118000
Bombardier CL-604/605	21863	3495	1.13	77799
B777-300 ER	352441	3056	1.13	68027
B787-9	254692	2803	1.13	62395
B777-200	248120	3799	1.13	84566
A330-300 std	230900	842	1.13	18743
B787-8	228383	579	1.13	12889
A310-300	142900	772	1.13	17185

Aircraft	**Gross Taxi Weight (kg)**	**Annual Departures at 05-12**	**Annual Growth**	**Total Departures**
B747-400	397801	245	1.13	5454
B747-400 Belly	397801	245	1.13	5454
A380-800 WV000	562000	105	1.13	2337
A380-800 WV000 Belly	562000	105	1.13	2337
DHC-7	19867	30830	1.13	686276
B737-800	79242	19706	1.13	438656
CRJ100/200	21636	8552	1.13	190368

Table 5.3: B777-300 loading characteristics.

Gross Taxi Weight (kg)	**Tire Pressure (kPa)**	**Percent GW on Gear**	**Dual Tire Spacing (m)**	**Tandem Tire Spacing (m)**	**Tire Contact Width (cm)**	**Tire Contact Length (cm)**	**Tire Contact Area (cm^2)**
352441	1503	0.475	1.397	1.463	38	60.9	1820.45

5.2.4 Existing Runway Structure

According to the GTAA, the pavement structure from a typical flexible runway in Toronto Pearson Airport consists of three layers, namely an AC layer of 12.5 cm thickness, followed by a granular base of 30 cm and a granular sub-base of 90 cm. The materials have similar characteristics to the standard materials from FAARFIELD as described in Table 5.4.

Table 5.4: Typical flexible pavement structure.

Layer Material	**Thickness (cm)**
P401-P403 HMA	12.5
P-209 Crushed Aggregate	30
P-154 uncrushed aggregate	90
Sandy Clay Subgrade, M_R = 51.71 MPa	-

A presentation given by Chris Stewart in 2010 says that the overall pavement thickness in Toronto Airport runways has not been updated since 1993, and that the runways were designed for the critical aircraft at the time, which was the B747-400. Steward says that newer aircraft such as the B777- 200LR/300ER, A340-500/600, and A380 are all more critical for the determination of a suitable pavement structure, and that failure to improve the pavement structure will result in reduced service life (Stewart, 2010).

The same presentation proposes a new design based on the Transport Canada Manual of pavement structural design ASG-19 and FAA in which the AC thickness should be increased from 12.5 to 20 cm, while keeping the same thickness of the granular layers.

Even though this was proposed in 2010, information given by GTAA to the author in 2021 says that the flexible runways have not yet been adjusted to meet new large aircraft requirements.

5.2.5 Asphalt Performance Grade and Asphalt Mix

In the year of 1998, the Ontario Hot Mix Producers Association, on behalf of MTO/ORBA, established equivalencies between the asphalt penetration standards and the Performance Grading (PG). The asphalt grade for the surface course in Toronto Pearson International Airport was determined to be PG 64-28, however, in 2002, the asphalt grade had to be elevated to a PG 70-28, to accommodate for the heavy aircrafts operating and the high temperatures at the airport area. Later, a polymer modified asphalt started to be used, to increase the stiffness of the asphalt at higher temperatures, mainly to reduce rutting and shoving problems (Stewart, 2010).

Pearson Airport is constantly under small and capital maintenance operations. The airport operators announced the rebuilding of sections of Taxiway H and the rehabilitation of Runway 15L/33R entirely, during the year of 2020 (Greater Toronto Airports Authority, 2020).

An asphalt mix to be used at one of the taxiways of Toronto Pearson International Airport was collected and analyzed by Abreu. The binder had a PG 70-28J, and the mix used 5.2% of asphalt cement. The percentage air voids of the mix were found to be 3.9 and the Voids in Mineral Aggregate, VMA (%) were 16.5. The gradation of the aggregates in the asphalt mix can be seen in Table 5.5 (Abreu, 2019).

Table 5.5: Asphalt Mix Gradation used in runway of Toronto Pearson International Airport. Modified from (Abreu, 2019).

Sieve Size (mm)	% Passing
26.5	-
19	-
16	100
13.2	98
9.5	80.3
4.75	54.3
2.36	38.7
1.18	25.3
0.6	17.5
0.3	10.3
0.15	5.5
0.075	3

A summary of the input required to calculate the dynamic modulus of the mix is presented at Table 5.6. In this table, f is the loading rate, V_a is the air void content, V_{beff} is the effective binder content, and $\rho_{34}, \rho_{38}, \rho_4$ represent cumulative percent retained on the standard sieves #¾, #3/8, #4, and # 200, respectively. The granular materials were assumed to have similar characteristics to the standard materials from FAARFIELD, therefore, the base was considered as a P-209 Crushed Aggregate and the sub-base as a P-154 uncrushed aggregate.

Table 5.6. Input parameters to estimate the AC dynamic modulus master curve.

Parameter	f **(Hz)**	V_a **(%)**	V_{beff} **(%)**	ρ_{34} **(%)**	ρ_{38}**(%)**	ρ_4 **(%)**	ρ_{200} **(%)**
Value	4.3	3.9	12.6	0.00	19.70	45.70	3.00

5.2.6 Freezing indices

As explained in section 3.6.1, the freezing index (FI) is a measure of the severity of freezing conditions during the winter season. It is calculated as the summation of daily average air temperatures over the freezing period (TCCA, 1992). A publication from 1973 shows that the freezing index for the region of Toronto, based on the period of 1931 to 1960, was approximately 500 degree-days (F) (Figure 5.5).

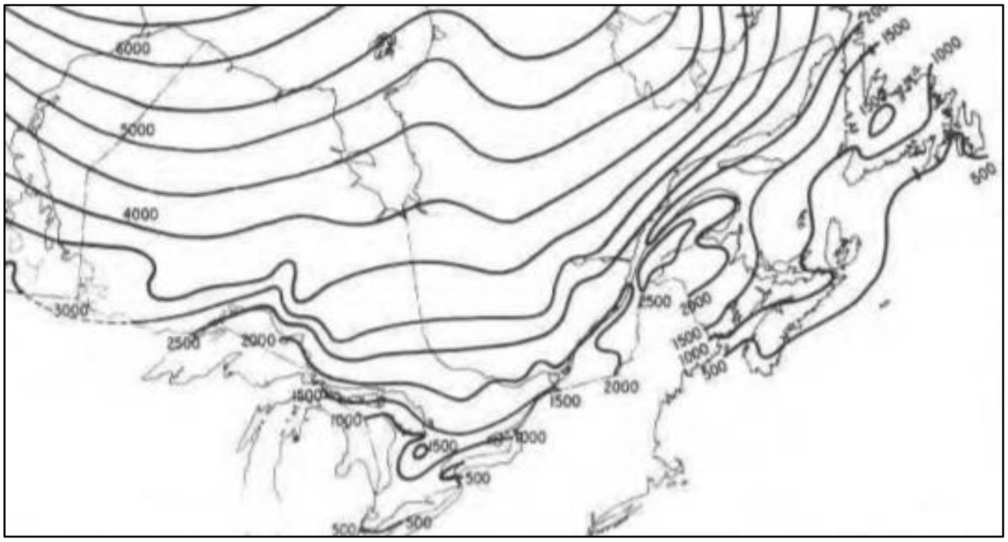

Figure 5.5: Normal freezing index in degree-days, based on the period 1931 to 1960. Modified from (Boyd, 1973).

Data collected from the Climate Atlas of Canada shows that the average freezing index in Toronto region from the year of 1950 to 2003 corresponded to 467.1 degree-days (F), however, more recent data presents a freezing index of 406.35 for the period of 2003 to 2013 (Prairie Climate Centre, 2020). The historical records per year, as well as the FI prediction trend according to the gas emission scenario 8.5 is presented in Figure 5.6.

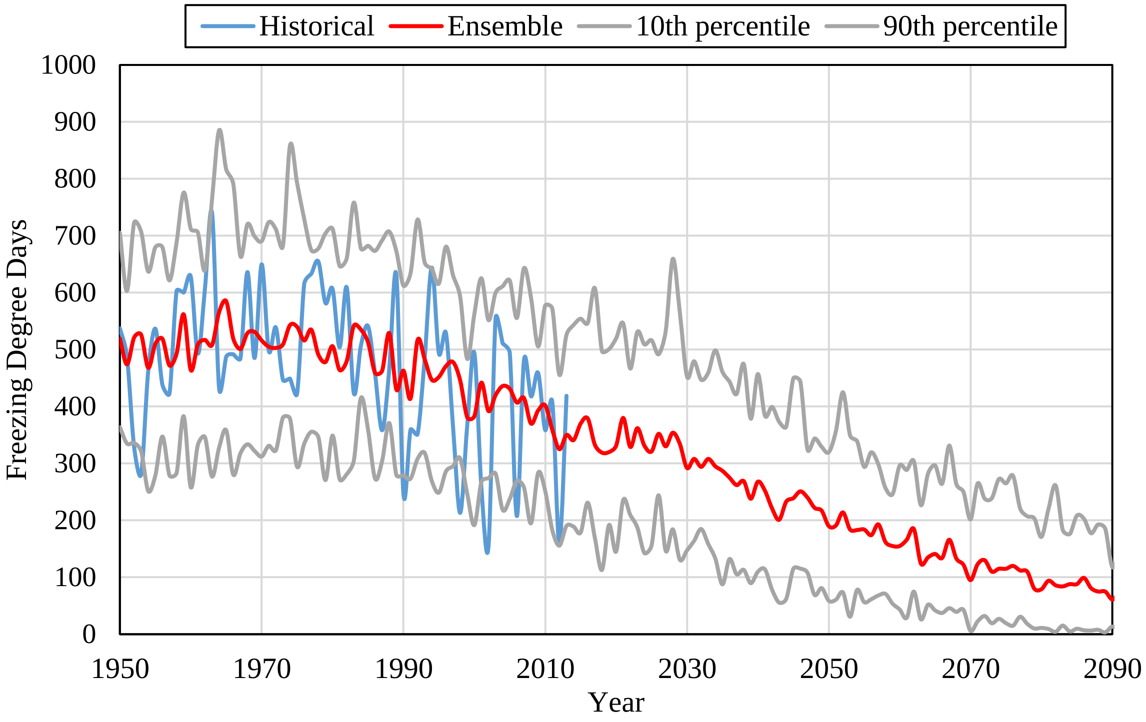

Figure 5.6: Freezing degree-days in the municipality of Toronto: historical values and future prediction.

According to Figure 5.6, if climate warming continues its trend, the freezing index will continue to decrease in Toronto region. If predictions become reality, in the next 20 years the municipality of Toronto will experience a FI close to 200 degree-days.

5.3 FAARFIELD Design

The hot mix asphalt standard material in FAARFIELD is the P-401/403. This material has a fixed modulus value pre-set in the program at 1379 MPa (200,000 Psi). The manual affirms that this modulus was conservatively chosen and corresponds to a pavement temperature of approximately 32°C (FAA, 2016), therefore, the software considers that the AC would perform as it was under 32°C all year long.

To estimate a modulus that would be more coherent with the AC described in the Section 5.2.5, the modified Witczak sigmoidal function presented at Equation 3.13 was used. The main input necessary to calculate the modulus consisted of the asphalt mix gradation, Performance Grade (PG), initial air voids, effective asphalt content, aircraft characteristics such as tire pressure, weight and speed, and lastly, temperature. The resulting modulus of the hot mix asphalt at 32°C is 1721 MPa, which is 25% higher than the stand AC stiffness used in FAARFIELD.

The required data for the design in FARFIELD consists of the soil resilient modulus or CBR, the layer materials and traffic, all of which were defined in sections 5.2.2, 5.2.3, and

5.2.4. Table 5.7 presents the resulting thickness of the pavement layers for a design life of 20 years, as well as the modulus and Poisson ratio attributed in FAARFIELD.

Table 5.7: Pavement Design performed in FAARFIELD.

No.	Type	Thickness (cm)	Modulus (MPa)	Poisson's Ratio
1	P-401 HMA Surface	30.4	1721	0.35
2	P-209 Crushed Aggregate	30	485.21	0.35
3	P-154 Uncrushed Aggregate	90	138.61	0.35
4	Subgrade	-	51.71	0.35

The pavement design in FAARFIELD shows the need for a more robust structure than what is currently in place, since when maintaining the base and sub-base layer thickness constant, the AC was 17.9 cm thicker than the present layer. The CDF results points out that the B777-300 ER airplane brings 99% of the rutting damage contribution, while the B787-900 had a contribution of 1%, and the rest of the mix had neglectable contribution to the rutting damage. Table 5.8 presents the cumulative rutting and fatigue CDF of the aircraft fleet mix from FAARFIELD, and its respective P/C ratio.

Table 5.8: Cumulative CDF from FAARFIELD.

Aircraft	Rutting CDF Contribution	Rutting P/C Ratio	Fatigue CDF Contribution	Fatigue P/C Ratio
A320-200 std	0	1.08	0.08	1.91
A321-100 std	0	1.08	0.09	1.84
B767-300	0	1.06	0.08	1.02
Bombardier CL-604/605	0	1.21	0.00	2.31
B777-300 ER	0.99	1.04	0.18	0.72
B787-9	0.01	1.03	0.16	1.14
B777-200	0	1.04	0.06	0.75
A330-300 std	0	1.03	0.03	1.06
B787-8	0	1.04	0.03	1.04
A310-300	0	1.08	0.01	0.95
B747-400	0	1.06	0.01	0.96
B747-400 Belly	0	1.06	0.01	0.96
A380-800 WV000	0	1.04	0.00	1.06
A380-800 WV000 Belly	0	1.03	0.01	0.78
DHC-7	0	1.22	0.01	2.33
B737-800	0	1.09	0.30	1.84
CRJ100/200	0	1.2	0.00	2.22

5.3.1 Validation of Python Codes

The equations described in the methodology section to calculate rutting and fatigue damage were implemented in Python codes, developed by the author. To verify the damage codes, the author performed the calculation of the CDF caused by the B777-300 ER under the same circumstances considered in FAARFIELD. The first part of the verification process was to certify that the P/C values for the B777-300 ER were the same as presented in Table 5.8 (that is, 1.04 for rutting and 0.72 for fatigue). To that end, the aircraft wander was defined as 178.8 cm, the lateral distance from the centerline of the runway to the centerline between the tires was considered as 548.5 cm, and other aircraft characteristics were defined according to Table 5.3, which resulted in P/C values of 1.036 and 0.716 for rutting and fatigue, respectively. The P/C values resulting from the Python codes, when rounded, are essentially equal to FAARFIELD.

The same structural conditions defined in Table 5.7 were used to obtain stresses and strains through KENLAYER (circular tire contact) and ABAQUS (circular and elliptical tire contact). The model in ABAQUS was built using a mesh of 8 cm near the loads and 30 cm in the rest of the model; the contact between layers was defined as rough, and the model dimensions were 12x12 meters wide, by 13.504 m deep (the subgrade being 12 m deep). A boundary condition was defined at the lateral walls of the simulated pavement elements which prevents it from moving in the horizontal direction but letting it free to move in the vertical direction. The bottom of the subgrade element was constrained from any movement. This type of boundary condition is usually imposed to represent the confinement of the soil. Figure 5.7 shows the subgrade divided in half for a better perspective (ZY view), with contours in deformed shape, colors representing the compressive strains.

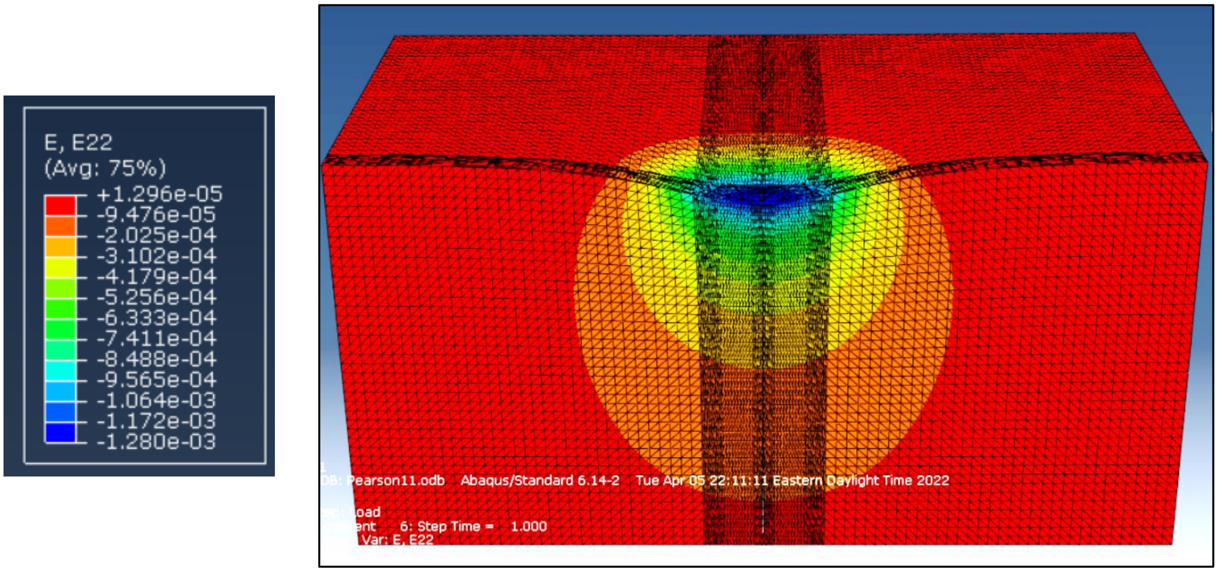

Figure 5.7: Compressive Strains at Subgrade Top in ABAQUS.

The results of compressive strains at the subgrade top and tensile strains at AC bottom for both ABAQUS and KENLAYER are presented in Table 5.9.

Table 5.9: Pavement responses.

Software	Tire contact	Compressive Strain at subgrade top	Tensile Strain at AC bottom
KENLAYER	Circular	0.001280	-0.0003799
ABAQUS	Circular	0.001282	-0.0002959
ABAQUS	Elliptical	0.001280	-0.0002886

The results for compressive strains at the subgrade top were very similar for both KENLAYER and ABAQUS, with almost no difference between the strain of circular and elliptical contact areas (0.15% difference). However, the tensile strains at AC bottom from the two models with circular contact area from KENLAYER and ABAQUS presented results with a 28% difference. The difference between circular and elliptical contact shape in ABAQUS was only 2.5%.

FAARFIELD uses the Layered Elastic Design (LED) to obtain the pavement critical strains. Generally, when LED is used for flexible pavement design, it is assumed that each tire has a circular contact area, because of its axisymmetric nature. Most LED tools available only enable the users to consider the contact area between tire and pavement as circular. FAARFIELD, however, considers the contact area to be elliptical. Because the author could not have access to a LED based software that would allow for modeling an elliptical contact area, KENLAYER was used instead.

The critical pavement responses were then used to estimate the number of coverages to failure. The CDF was calculated considering the B777-300 ER number of departures of 68,027 in a 20-year design period. The results of the cumulative rutting damage over the design period can be seen in Figure 5.8.

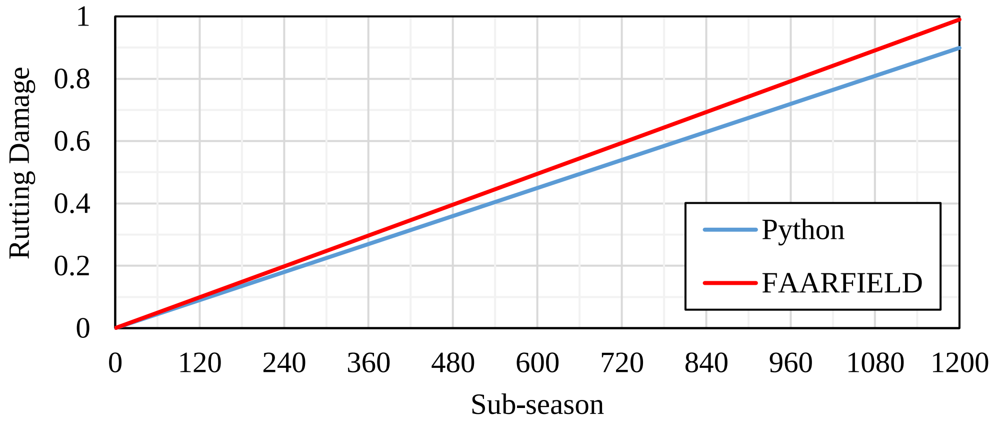

Figure 5.8: Rutting Damage at Validation Phase.

As previously mentioned, FAARFIELD attributed a cumulative damage of 0.99 for the B777-300 ER over the design period. The calculations implemented in Python resulted in a damage of 0.9 for the same aircraft, that is, a difference of -9%. The author attribute the difference in the results to the tire contact shape, which were assumed as circular instead of elliptical. Despite the limitations in duplicating FAARFIELD procedures, the transfer function codes implemented in Python were considered satisfactory.

5.4 Current Climate

The first steps to perform an analysis that considers the climate variations is to obtain hourly climate data and to estimate the pavement temperature gradient along the pavement depth. To that end, 10 years hourly past climate data was downloaded from the National Solar Radiation Database (NSRD), originated from the nearest station to Toronto Pearson International Airport, ranging from the years of 2010 to 2019 (National Renewable Energy Laboratory, 2022). The 10-year data was averaged to correspond to 1-year hourly records. The data obtained on the website was the air temperature, wind speed, solar radiance and albedo at the Toronto Pearson Airport site. To determine the pavement temperature gradient, the finite control volume method was used though TEMPS.

5.4.1 Pavement temperature profile

Temperature affects both unbound and bound materials strength. In bonded materials such as asphalt concrete, temperature has a high correlation with the stiffness, because of the viscoelastic properties that asphalt presents, however, it also plays an important role in the behavior of unbonded layers. For example, granular layers can be susceptible to freezing, and this is followed by a great increase in the material modulus. However, when the layers thaws, it can lead to a drastic decrease in the modulus. For this reason, a model that predicts the temperature of the pavement layers in different depths is necessary for accurate computations of the material’s modulus throughout the year.

In general, temperature prediction models for pavements can be divided in three categories: analytical, numerical, and empirical. The analytical and numerical models usually are developed considering the heat conduction under certain boundary conditions, while the empirical models are based on statistical analysis (Chen, Wangb, & Xie, 2019).

There are a number of methods available to accomplish the prediction of the pavement temperature, including the Asphalt Institute (AI) model, the Long-Term Pavement Performance (LTPP) model, the American Association of State Highway and Transportation Officials (AASHTO) model, the Mechanistic Empirical design model, among many others. The model assumptions, analysis parameters, solution methodology and application areas in those methods can vary significantly.

The Long-Term Pavement Performance (LTPP) program was one of the pioneer research projects on pavement temperature prediction. The strategic highway research program (SHRP) established the LTPP program on approximately 2,500 sites throughout North America, in order to capture a broad range of pavement types and climatic conditions (Diefenderfer, Al-Qadi, & Diefenderfer, 2006). The SUPERPAVE binder selection procedure is based on the LTPP models for the lowest and highest temperatures expected at a job (Mohseni, 1998). The LTPP model, however, is limited to predicting the AC temperature only, excluding the other pavement layers.

The MEPDG (2004) uses the Climatic-Materials-Structural (CMS) model, developed at the University of Illinois. This is a one-dimensional heat transfer model used to determine frost penetration and temperature distribution in the pavement system. The inputs considered are the heat capacity of the pavement materials, thermal conductivity of the pavement materials, pavement surface absorptivity and emissivity, air temperature, wind speed and incoming solar radiation (ARA, Inc., ERES Consultants Division, 2004).

Even though this method provides good predictions of pavement temperature, it does not illustrate the physics of heat transfer adequately due to the assumption of a steady-state surface and constant bottom boundary conditions. Another limiting factor is that the solar radiation is estimated from a regression equation, even though it can easily be obtained from reliable sources, such as the National Solar Radiation Database (NSRDB) (Alavi, Pouranian, & Hajj, 2014).

An alternative method to predict the pavement temperature profile is the finite control volume method. The method can be easily implemented through the software TEMPS - Temperature Estimate Model for Pavement Structures. TEMPS is a software that forecasts hourly temperatures at any depth in a pavement structure through the Finite Control Volume Method (FCVM) (Liu, 2020). This model provides a good understanding of the heat energy balance in the system.

The inputs used in TEMPS are very similar to the ones used in the MEPDG (2004) climate model, including climatic data (air temperature and wind speed), meteorological data (solar radiation), and pavement surface radiation properties (albedo, emissivity, and absorption coefficients) (Alavi, Pouranian, & Hajj, 2014).

Albedo can be defined as the reflectivity of the pavement at solar wavelengths, and it can play an important part in the pavement temperature. The higher the albedo, the higher is the reflected energy back to its surroundings, therefore, less energy is absorbed into the pavement (Gui, Phelan, Kaloush, & Golden, 2007). The National Solar Radiation Database provides both hourly solar radiation and surface albedo, and the values can be used to predict pavement temperature profile.

The emissivity of a surface represents the ratio of the radiation emitted by the surface at a given temperature to the radiation emitted by a blackbody at the same temperature (Cengel, 2003). This parameter depends on the pavement color, texture and temperature, and for asphaltic materials a typical value can be considered as 0.93 (Solaimanian & Kennedy, 1993).

Similar to emissivity, the absorption depends on the pavement color, texture and composition, and it correlates with the amount of available solar energy that is absorbed by the pavement surface. Absorption and emissivity usually present very similar values and sometimes can be identical (Solaimanian & Kennedy, 1993). For a level three type project, the MEPDG (2004) classifies the absorption of flexible pavements as follows (ARA, Inc., ERES Consultants Division, 2004):

- Weathered asphalt (gray): 0.80 – 0.90
- Fresh asphalt (black): 0.90 – 0.98

Specific heat capacity can be defined as the amount of heat that must be added or removed from a unit mass of asphalt concrete to change its temperature by one degree (Mrawira & Luca, 2006). The study of Mrawira & Luca (2006) found values of specific heat capacity that range from 940 to 2000 J/kg*K, while the MEPDG (2004) recommends using a range that varies from 921.1 to 1674.72 J/kg*K.

Thermal conductivity can be defined as the rate at which heat energy is transferred across the unit area of a material. The research of Gui et al. (2006) obtained values varying from 0.6 to 2.6 W m^{-1} $^{o}C^{-1}$ (Gui, Phelan, Kaloush, & Golden, 2007), Mrawira and Luca obtained results ranging from 1.7 to 2.1 W m^{-1} $^{o}C^{-1}$ (Mrawira & Luca, 2006), while the MEPDG (2004) recommends a narrower range, from 0.76 to 1.40 W m^{-1} $^{o}C^{-1}$ for asphalt concrete materials.

The work of Khan et al. (2009) presents typical values of thermo-physical parameters for a pavement base, sub-base, and frost-susceptible soil. The researchers separated the conductivity in thawed and frozen periods, as presented in Table 5.10 (Khan, Mrawira, & Hildebra, 2009).

Table 5.10: Thermo-physical parameters of pavement layers, modified from (Khan, Mrawira, & Hildebra, 2009).

Layer	Dry Density (kg/m^3)	Thawed conductivity (W/m K)	Frozen conductivity (W/m K)	Heat capacity (J/kg K)	Water content frozen/thawed (decimal fraction)
Crushed gravel base	2330	3.63	3.83	1038	0.05
Crushed gravel sub-base	2446	3.98	4.15	1131	0.04
Subgrade	1550	1.20	2.00	710	0.04

The parameters used to determine the pavement temperature gradient in this thesis are presented in Table 5.11 and Table 5.12. The material properties agree with the literature reviewed above, and the surface albedo was obtained through the NSRD and averaged per month, as presented in Table 5.12. Lastly, emissivity and absorption were both considered to be 0.93.

A print screen from TEMPS showing the materials definition can be seen in Figure 5.9, and the climatic data input is showed in Figure 5.10. The surface characteristics, including albedo, emissivity and absorption are presented in Figure 5.11. The pavement structure definition was done according to Table 5.7, and a print screen of this step on TEMPS is presented in Figure 5.12. The last step is the mesh generator, which was defined as having a spacing of 1 cm.

Table 5.11: Material Properties.

Material Type	**Identifier Color**	**Specific Heat Capacity (J/kg°K)**	**Conductivity (W/m°K)**	**Density (kg/m^3)**
AC	Black	1298	1.08	2374
Base	Gray	1038	3.63	2330
Sub-base	Gray	1131	3.98	2446
Subgrade	Gray	710	1.2	1550

Table 5.12: Surface Albedo.

Month	**Albedo**	**Month**	**Albedo**	**Month**	**Albedo**
January	0.72	May	0.16	Sept	0.16
Feb	0.75	June	0.16	Oct	0.16
March	0.41	July	0.17	Nov	0.27
April	0.20	August	0.16	Dez	0.51

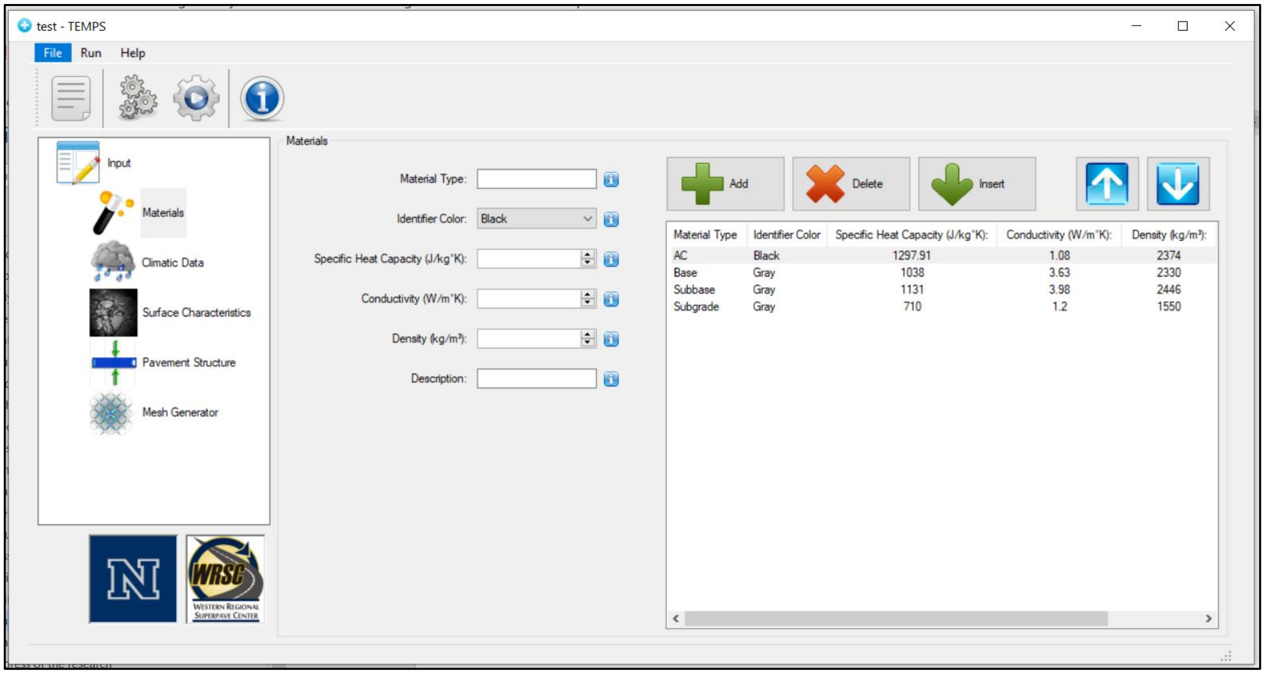

Materials

Material Type:

Identifier Color: Black

Specific Heat Capacity (J/kg°K):

Conductivity (W/m°K):

Density (kg/m³):

Description:

Material Type	Identifier Color	Specific Heat Capacity (J/kg°K):	Conductivity (W/m°K):	Density (kg/m³):
AC	Black	1297.91	1.08	2374
Base	Gray	1038	3.63	2330
Subbase	Gray	1131	3.98	2446
Subgrade	Gray	710	1.2	1550

Figure 5.9: Pavement material properties inputs in TEMPS.

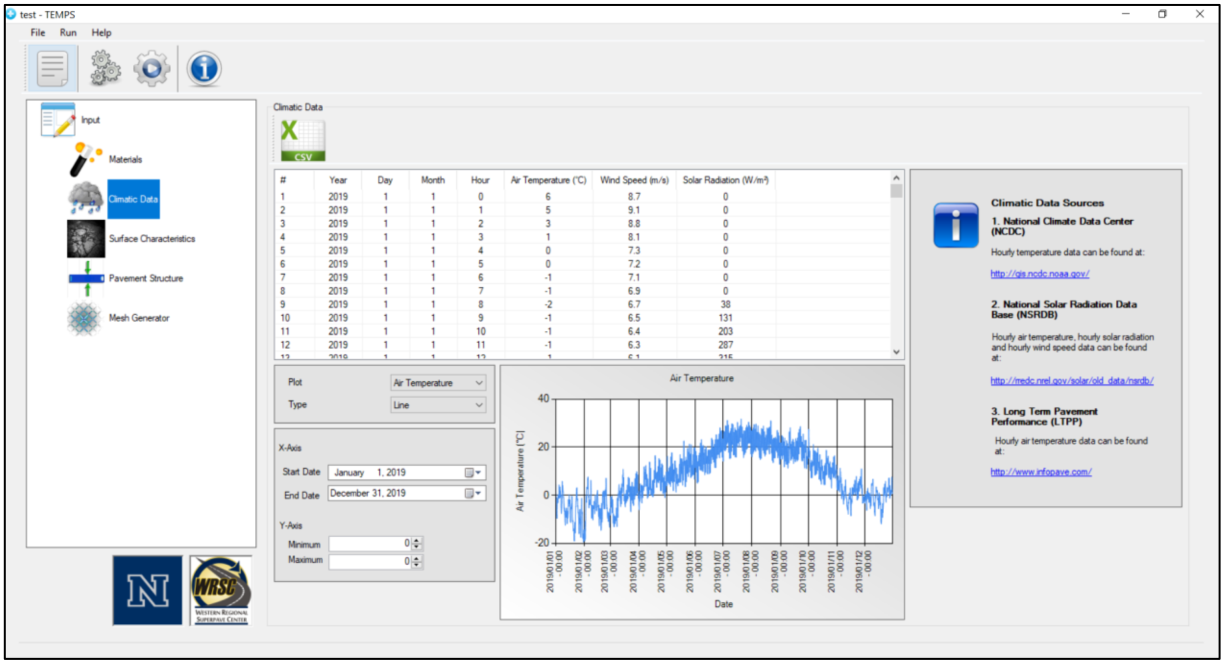

#	Year	Day	Month	Hour	Air Temperature (°C)	Wind Speed (m/s)	Solar Radiation (W/m²)
1	2019	1	1	0	6	8.7	0
2	2019	1	1	1	5	9.1	0
3	2019	1	1	2	3	8.8	0
4	2019	1	1	3	1	8.1	0
5	2019	1	1	4	0	7.3	0
6	2019	1	1	5	0	7.2	0
7	2019	1	1	6	-1	7.1	0
8	2019	1	1	7	-1	6.9	0
9	2019	1	1	8	-2	6.7	38
10	2019	1	1	9	-1	6.5	131
11	2019	1	1	10	-1	6.4	203
12	2019	1	1	11	-1	6.3	287

Plot: Air Temperature
Type: Line

X-Axis
Start Date: January 1, 2019
End Date: December 31, 2019

Y-Axis
Minimum: 0
Maximum: 0

Climatic Data Sources

1. National Climate Data Center (NCDC)

Hourly temperature data can be found at:

http://gis.ncdc.noaa.gov/

2. National Solar Radiation Data Base (NSRDB)

Hourly air temperature, hourly solar radiation and hourly wind speed data can be found at:

http://rredc.nrel.gov/solar/old_data/nsrdb/

3. Long Term Pavement Performance (LTPP)

Hourly air temperature data can be found at:

http://www.infopave.com/

Figure 5.10: Climatic input data in TEMPS.

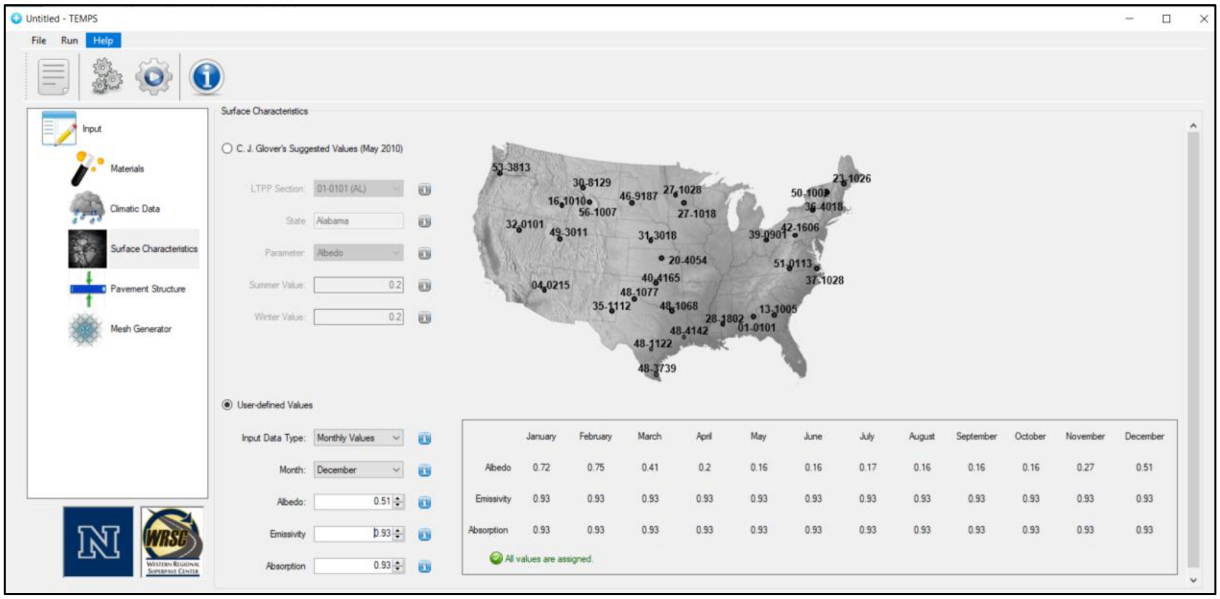

Surface Characteristics

○ C. J. Glover's Suggested Values (May 2010)

LTPP Section: 01-0101 (AL)
State: Alabama
Parameter: Albedo
Summer Value: 0.2
Winter Value: 0.2

● User-defined Values

Input Data Type: Monthly Values
Month: December
Albedo: 0.51
Emissivity: 0.93
Absorption: 0.93

	January	February	March	April	May	June	July	August	September	October	November	December
Albedo	0.72	0.75	0.41	0.2	0.16	0.16	0.17	0.16	0.16	0.16	0.27	0.51
Emissivity	0.93	0.93	0.93	0.93	0.93	0.93	0.93	0.93	0.93	0.93	0.93	0.93
Absorption	0.93	0.93	0.93	0.93	0.93	0.93	0.93	0.93	0.93	0.93	0.93	0.93

✓ All values are assigned.

Figure 5.11: Surface Characteristic input data in TEMPS.

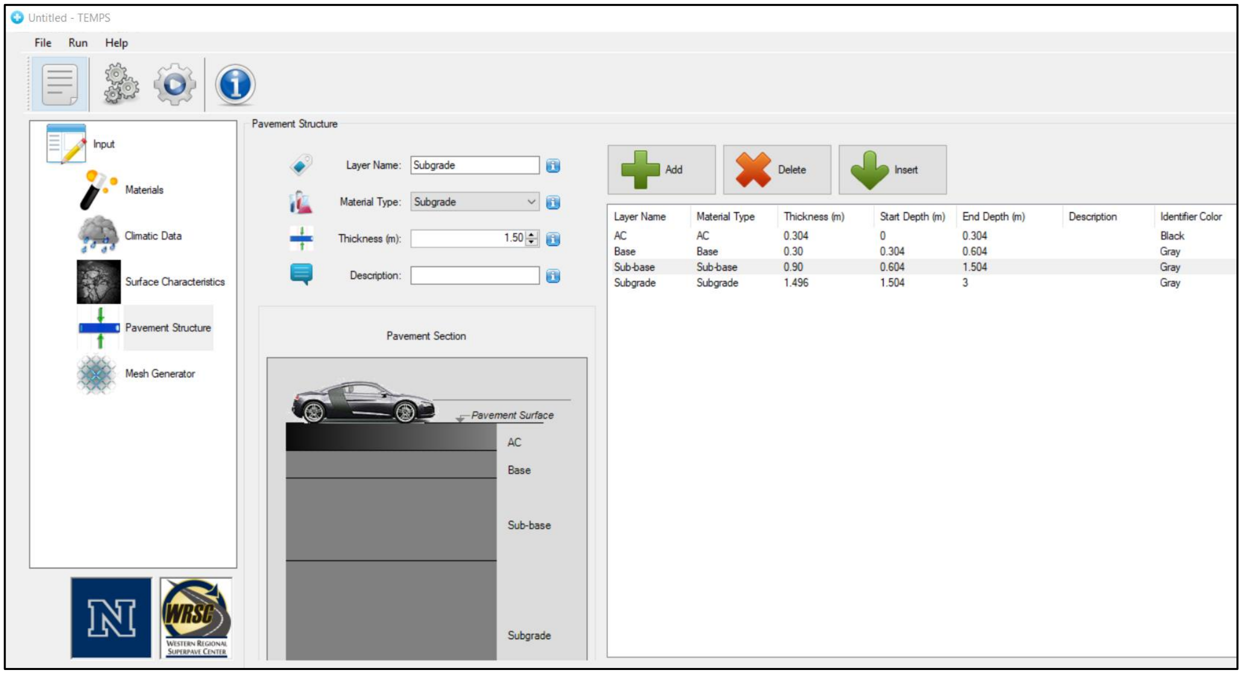

Pavement Structure

Layer Name: Subgrade

Material Type: Subgrade

Thickness (m): 1.50

Description:

Layer Name	Material Type	Thickness (m)	Start Depth (m)	End Depth (m)	Description	Identifier Color
AC	AC	0.304	0	0.304		Black
Base	Base	0.30	0.304	0.604		Gray
Sub-base	Sub-base	0.90	0.604	1.504		Gray
Subgrade	Subgrade	1.496	1.504	3		Gray

Figure 5.12: Pavement structure input data in TEMPS.

The results of the temperature profile simulation in TEMPS can be seen in Figure 5.13.

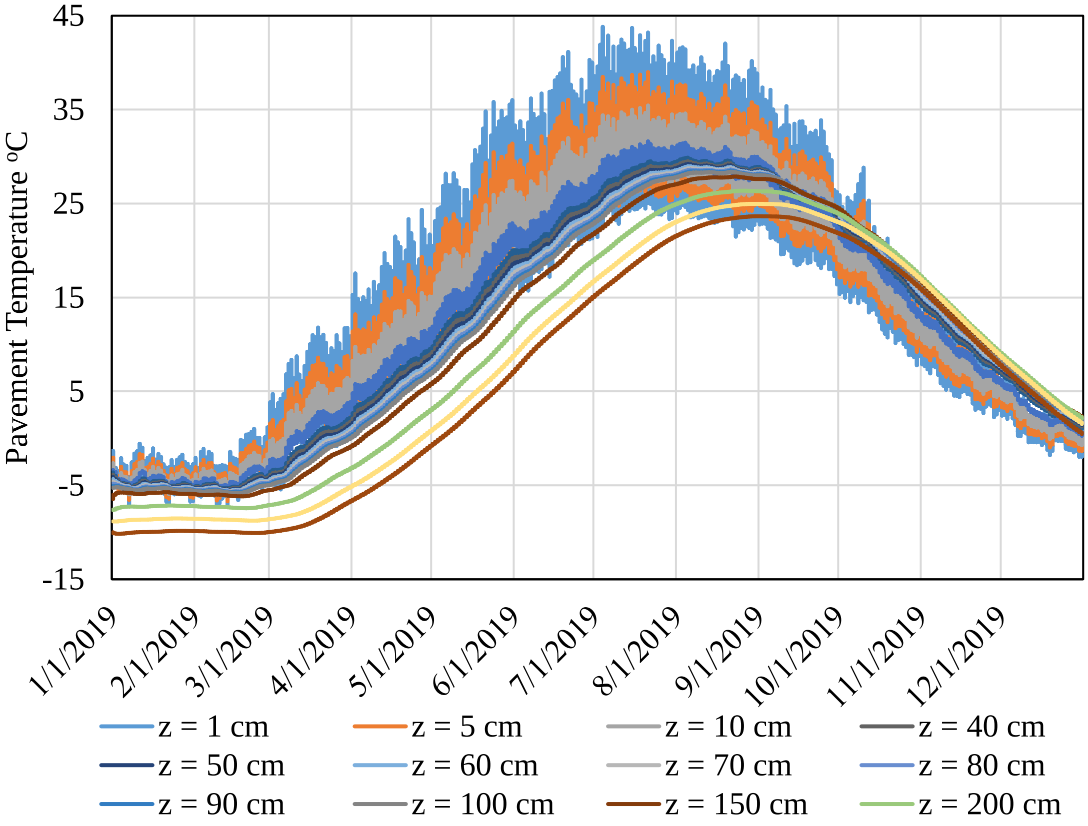

Figure 5.13: Pavement temperature profile simulation in TEMPS.

Figure 5.13 indicates that the maximum temperature at a depth of 1 cm is of 44°C and that the temperature gradient varies within the pavement depth. From the months of March through July, the pavement surface layers often presented higher temperatures than the lower layers, and in those months, temperature decreases with depth, while in the months of August through February, this is not necessarily true. It is also important to point out that the surface temperature layers vary a lot within a short period of time during most part of the year, however, it seems to be more stable during the winter.

5.4.2 Bitumen Viscosity and Loading Rate

Bitumen viscosity is a function of temperature and loading rate. The effect of loading rate can be estimated considering a sinusoidal loading, with frequency f, to represent the cyclic application of dynamic loads on pavements. The duration of the load on a pavement depends on the aircraft speed, s, and the tire contact radius, a (Huang Y. H., 2004), as previously discussed in Section 3.3.1.

In the FAARFIELD design performed in Section 5.3, it was showed that the most critical aircraft amongst the aircraft fleet mix is the B777-300 ER. Table 5.8 shows that the aircraft was responsible for 99% of the rutting damage contribution. For this reason, all analysis performed forward in this thesis considers the B777-300 ER only. To calculate the loading frequency f, a typical aircraft taxiing speed of 30 km/h was used. The tire circular contact area was considered to have a radius of 24.07 cm, based on the weight and tire pressure described in Table 5.3. The loading frequency of the B777 at this speed was calculated as 0.46 Hz. The binder and volumetric design parameters used to estimate the AC modulus were defined in Section 5.2.5.

To determine the correct viscosity of the pavement binder, the effect of aging must be considered. The two main considerations are the aging that happens during mixing/compaction, and the aging during the long term in-situ. The viscosity also must be adjusted for different air void contents and as a function of the depth. According to the Global Aging System (GAS) model proposed by the MEPDG (2004), the aged viscosity at time t and depth z can be calculated as a function of the mean annual air temperature, the original binder viscosity at 77°F, initial air voids, and aged binder viscosity. All equations to calculate binder viscosity and loading frequency were presented in section 3.3.1.

The short-term aging is dependent on the original viscosity, cP, the mix/lay-down viscosity, and the hardening ratio. The hardening ratio has the purpose of adjusting the model for a particular asphalt tendency to age during mixing, hauling and compaction (Farrar, Harnsberger, Thomas, & Wiser, 2006). To consider the hardening ratio, a hardening code is used. The hardening code values vary from -1, representing a good to excellent resistance to hardening, to +2, representing a poor hardening resistance. For the case study, the hardening code used is 0, which represents an average expected hardening ratio.

The long-term aging is calculated considering the mean annual air temperature $Maat$, the current temperature, and the time in months. The $Maat$ for Pearson International Airport was obtained from the 10 years hourly past climate data downloaded from the National Solar Radiation Database (NSRD), ranging from the years of 2010 to 2019.

The viscosity also must be adjusted according to the percentage air voids in the AC mix and the air void change with time. This is done through an adjustment factor F_v, which is a function of the air voids at the time of interest. The initial air voids in the case study is 3.9%. Lastly, the aged viscosity is also a function of the layer depth, z.

The mix/lay-down viscosity $\eta_{t=0}$ and the final viscosity $\eta_{t,z}$ adjusted according to the percentage air voids and depth are presented in Table 5.13, for a variety of temperatures, at the depths of 6.3 cm and 15.2 cm.

Table 5.13: Binder mix/lay-down viscosity and final viscosity at different temperatures.

Temperature	**z = 6.3 cm**		**z = 15.2 cm**	
	$\boldsymbol{\eta_{t=0}}$ **MPoise**	$\boldsymbol{\eta_{t,z}}$ **MPoise**	$\boldsymbol{\eta_{t=0}}$ **MPoise**	$\boldsymbol{\eta_{t,z}}$ **MPoise**
-10	2.13E+09	1.39E+06	3.42E+05	5.20E+06
-5	1.82E+08	8.05E+04	5.76E+06	1.64E+05
0	1.11E+04	1.22E+04	1.11E+04	1.61E+04
5	2.40E+03	2.48E+03	2.40E+03	2.76E+03
10	5.79E+02	5.86E+02	5.79E+02	6.09E+02
15	1.55E+02	1.55E+02	1.55E+02	1.56E+02
20	4.53E+01	4.52E+01	4.53E+01	4.49E+01
25	1.44E+01	1.44E+01	1.44E+01	1.42E+01
30	4.95E+00	4.93E+00	4.95E+00	4.86E+00
35	1.82E+00	1.82E+00	1.82E+00	1.79E+00
40	7.17E-01	7.15E-01	7.17E-01	7.07E-01
45	2.99E-01	2.98E-01	2.99E-01	2.96E-01
50	1.32E-01	1.32E-01	1.32E-01	1.31E-01
55	6.11E-02	6.11E-02	6.11E-02	6.09E-02
60	2.97E-02	2.97E-02	2.97E-02	2.97E-02

It is possible to note from Table 5.13 that the binder viscosity is highly affected by temperature variations. For example, at -10^{o}C at the depth of 6.3 cm, $\eta_{t,z}$ was equal to 1.39E+06, while at 60^{o}C it was equal to 2.97E-02. It is also evident that the depth considered has some impact in the binder viscosity in the cases of very low temperature, however, the viscosity was little influenced by the depth in higher temperature cases.

5.4.3 AC Modulus

To determine the dynamic modulus of the asphalt concrete in the case study, the modified Witczak's sigmoidal function was used, as presented in Equation 3.13 . The main model inputs are the loading rate, binder viscosity and volumetric design information. A summary of the inputs required to calculate the asphalt concrete modulus are presented in Table 5.14.

Table 5.14: Input parameters to estimate the dynamic modulus master curve.

Parameter	Description	Value	Units
$\eta_{t,z}$	Binder viscosity	Varies	MPoise
f	Loading rate	0.46	Hz
V_a	Initial air void content	3.9	Percent by total mixture volume
V_{beff}	Effective asphalt content	12.6	Percent by total mixture volume
ρ_{34}	Cumulative percent retained on ¾ sieve	0.00	Cumulative percent by weight of aggregate
ρ_{38}	Cumulative percent retained on 3/8 sieve	19.70	Cumulative percent by weight of aggregate
ρ_4	Cumulative percent retained on #4 sieve	45.70	Cumulative percent by weight of aggregate
ρ_{200}	Percent passing #200 sieve	3.00	Cumulative percent by weight of aggregate

In FAARFIELD, the stiffness of the default AC material is pre-defined as 1380 MPa. This modulus has been chosen corresponding to a pavement temperature of approximately 32℃, according to Equation 5.1, defined by Witczak, 1989 (Loizos, Armeni, & Pl, 2017):

$$log_{10}(E_{AC}) = 1.53658 - 0.006447 * T - 0.00007404 * T^2 \qquad 5.1$$

Where E_{AC} is the asphalt modulus (10^5 psi) and T is the asphalt temperature in Fahrenheit. A comparison of the AC modulus resulting from the methodology utilized by FAARFIELD and the modified Witczak's sigmoidal function used by the MEPDG (2004) is presented in Figure 5.14.

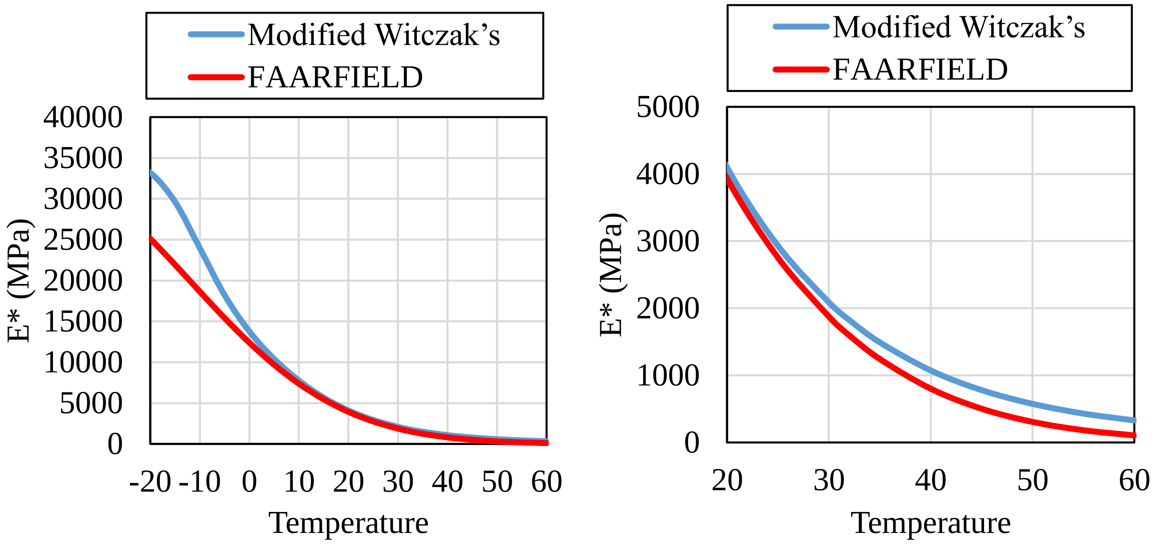

(a) (b)

Figure 5.14: Effect of temperature in the AC mix stiffness (a) temperature range from -20 to 60 (b) temperature range from 20 to 60.

In the comparison presented in Figure 5.14, the results from the modified Witczak's function were calculated according to the parameters defined in Table 5.14, with an AC mix that is one month old, at a depth of 6.3 cm. It can be noted from Figure 5.14, parts (a) and (b), that the highest the temperature, the lowest is the material stiffness. It is evident from Figure 5.14 (a) that the modified Witczak's function results in significantly higher modulus for the temperatures ranging from -20 to 0°C, and that the difference between the models narrows after 0°C.

The equations described in the methodology Section 3.3.1 to calculate the AC modulus were implemented in Python codes, developed by the author. With the codes, it was possible to estimate hourly records of the AC dynamic modulus according to the hourly temperature values. For the incremental damage calculations of rutting and fatigue, the AC modulus needs to be processed within every month. To that end, a normalized function is estimated, based on the mean value and standard deviation from the dataset.

The modulus distribution curve was divided into five sub-seasons, each sub-season representing 20% of the frequency distribution. This is accomplished by determining the temperatures corresponding to standard normal deviates of -1.2816, -0.5244, 0, 0.5244, and 1.2816, which correlates to 10, 30, 50, 70 and 90% accumulated frequencies within a given period, as presented by Figure 5.15.

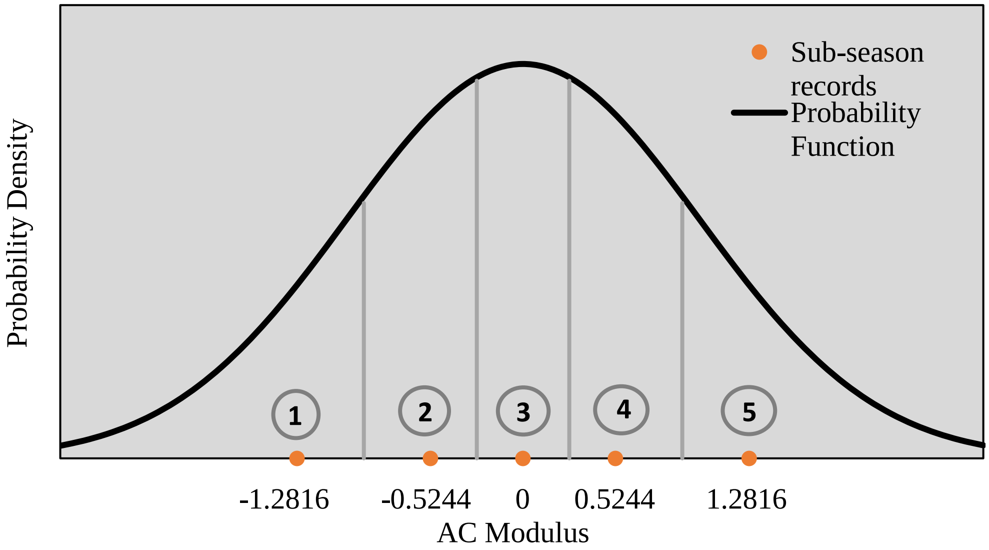

Figure 5.15: Modulus distribution per month.

It is important to note that each sub-season also represents 20% of the monthly traffic. The results of the AC modulus distribution per sub-season using the 10-year average temperature dataset from 2010 to 2019 are presented in Table 5.15.

The maximum resilient modulus calculated was 28,271, in the month of December, sub-season 60, while the minimum resilient modulus was 1,026, in the month of July, sub-season 31. Analyzing the data in this format allows for considering extreme temperature events and its effect on the material modulus, however, pondering for a lower frequency.

This results in a more accurate prediction of the performance compared to using a constant modulus over the year.

Table 5.15: AC modulus per sub-season.

Sub-season #	Month	z-value	AC Modulus (MPa)
1	Jan	-1.2816	15736
2	Jan	-0.5244	16694
3	Jan	0	17358
4	Jan	0.5244	18022
5	Jan	1.2816	18981
6	Feb	-1.2816	16687
7	Feb	-0.5244	18560
8	Feb	0	19857
9	Feb	0.5244	21154
10	Feb	1.2816	23028
11	Mar	-1.2816	8701
12	Mar	-0.5244	11902
13	Mar	0	14118
14	Mar	0.5244	16335
15	Mar	1.2816	19535
16	Apr	-1.2816	4636
17	Apr	-0.5244	6816
18	Apr	0	8326
19	Apr	0.5244	9836
20	Apr	1.2816	12016
21	May	-1.2816	2063
22	May	-0.5244	3451
23	May	0	4413
24	May	0.5244	5375
25	May	1.2816	6763
26	Jun	-1.2816	1349
27	Jun	-0.5244	2204
28	Jun	0	2796
29	Jun	0.5244	3387
30	Jun	1.2816	4242
31	Jul	-1.2816	1026
32	Jul	-0.5244	1605
33	Jul	0	2005
34	Jul	0.5244	2406
35	Jul	1.2816	2985
36	Aug	-1.2816	1203
37	Aug	-0.5244	1781
38	Aug	0	2181
39	Aug	0.5244	2581
40	Aug	1.2816	3159
41	Sep	-1.2816	1813
42	Sep	-0.5244	2538
43	Sep	0	3040
44	Sep	0.5244	3542
45	Sep	1.2816	4267
46	Oct	-1.2816	3518
47	Oct	-0.5244	4846
48	Oct	0	5765
49	Oct	0.5244	6684
50	Oct	1.2816	8012
51	Nov	-1.2816	7973
52	Nov	-0.5244	10749
53	Nov	0	12671
54	Nov	0.5244	14593
55	Nov	1.2816	17368
56	Dec	-1.2816	19126
57	Dec	-0.5244	21828
58	Dec	0	23698
59	Dec	0.5244	25569
60	Dec	1.2816	28271

5.4.4 Subgrade Modulus

Changes in temperature and moisture can influence the subgrade soil resilient modulus. Such variations can be estimated using an adjustment factor that, multiplied by the optimum resilient modulus, can result in a stiffness that is specific for each sub-season. The detailed steps to obtain the soil resilient modulus were described in Section 3.3.2, and the equations were implemented in Python codes, developed by the author.

5.4.4.1 *Number of hours elapsed since thawing started (Δt)*

At the end of the winter season, when the soil temperature starts to reach positive values, the frozen water present in the pavement layers, as well as the snow accumulated over the season, begins to melt. When this happens, the subgrade soil stiffness drastically decreases. With time, the thawed materials start recovering to an equilibrium state that is mainly dependent on the Recovery Ratio (RR), a variable that is directly correlated to the number of hours elapsed since thawing started (Δt), and the number of hours required for the material to recover (T_R).

As explained in Session 3.3.2, the recovery period T_R is determined by the percentage of fines and the soil plasticity index (PI). In the case study of Toronto Pearson International Airport, the plasticity index (PI) is equal to 12.4, and the percentage passing #200 sieve is 62.1%, as defined in Table 5.1. Therefore, $P_{200} * PI = 7.7$ and $T_R = 120$ days.

The number of hours elapsed since thawing started (Δt) is an important variable that reflects the subgrade state, that is, if the subgrade is frozen, recovering, or unfrozen. The hourly temperature records defined for each day, time, and depth are used to calculate Δt. If the temperature at a certain moment and depth is below zero, then, Δt is equal to 0. If the temperature is above zero, then, Δt will be equal to the number of hours elapsed since unfrozen conditions started.

For the incremental damage calculations of rutting and fatigue, Δt needs to be processed within every month. Knowing the hourly records of Δt for each month, a normalized function is estimated, based on the mean value and standard deviation from the dataset. Similarly to the sectioning process of the AC modulus, the Δt monthly distribution curve is divided into five sub-seasons, representing 20% of the frequency distribution. This is accomplished by determining the Δt records corresponding to standard normal deviates of -1.2816, -0.5244, 0, 0.5244, and 1.2816, which correlates to 10, 30, 50, 70 and 90% accumulated frequencies within a given period. An example of the results of the quintile Δt distribution at 1 cm depth and at 150 cm depth from the subgrade surface are presented in Table 5.16.

Table 5.16: Quintile Δt distribution at 1 cm and 150 cm depth from subgrade surface.

Sub-season #	Month	z-value	Δt at 1 cm Depth	Δt at 150 cm Depth
1	Jan	-1.2816	0	0
2	Jan	-0.5244	0	0
3	Jan	0.0000	0	0
4	Jan	0.5244	0	0
5	Jan	1.2816	0	0
6	Feb	-1.2816	0	0
7	Feb	-0.5244	0	0

Sub-season #	Month	z-value	Δt at 1 cm Depth	Δt at 150 cm Depth
8	Feb	0.0000	0	0
9	Feb	0.5244	0	0
10	Feb	1.2816	0	0
11	Mar	-1.2816	0	0
12	Mar	-0.5244	0	0
13	Mar	0.0000	0	0
14	Mar	0.5244	0	0
15	Mar	1.2816	0	0
16	Apr	-1.2816	14	0
17	Apr	-0.5244	164	0
18	Apr	0.0000	267	0
19	Apr	0.5244	371	0
20	Apr	1.2816	521	0
21	May	-1.2816	717	27
22	May	-0.5244	880	184
23	May	0.0000	993	293
24	May	0.5244	1105	402
25	May	1.2816	1268	559
26	Jun	-1.2816	1458	754
27	Jun	-0.5244	1616	912
28	Jun	0.0000	1725	1021
29	Jun	0.5244	1833	1129
30	Jun	1.2816	1991	1287
31	Jul	-1.2816	2181	1477
32	Jul	-0.5244	2344	1640
33	Jul	0.0000	2457	1753
34	Jul	0.5244	2569	1865
35	Jul	1.2816	2732	2028
36	Aug	-1.2816	2925	2221
37	Aug	-0.5244	3088	2384
38	Aug	0.0000	3201	2497
39	Aug	0.5244	3313	2609
40	Aug	1.2816	3476	2772
41	Sep	-1.2816	3666	2962
42	Sep	-0.5244	3824	3120
43	Sep	0.0000	3933	3229
44	Sep	0.5244	4041	3337
45	Sep	1.2816	4199	3495
46	Oct	-1.2816	4389	3685
47	Oct	-0.5244	4552	3848
48	Oct	0.0000	4665	3961
49	Oct	0.5244	4777	4073
50	Oct	1.2816	4940	4236

Sub-season #	Month	z-value	Δt at 1 cm Depth	Δt at 150 cm Depth
51	Nov	-1.2816	5130	4426
52	Nov	-0.5244	5288	4584
53	Nov	0.0000	5397	4693
54	Nov	0.5244	5505	4801
55	Nov	1.2816	5663	4959
56	Dec	-1.2816	5853	5149
57	Dec	-0.5244	6016	5312
58	Dec	0.0000	6129	5425
59	Dec	0.5244	6241	5537
60	Dec	1.2816	6404	5700

It is possible to note from Table 5.16 that at a depth of 1 cm from the subgrade surface, the thawing process started early April, while at a depth of 150 cm, the thawing process started early May.

5.4.4.2 Equilibrium degree of saturation

The subgrade is usually in the optimum moisture content with small variations bellow or above, during the construction period. However, after some time, the moisture content tends to change in the direction of a degree of equilibrium, which could be reached in months or years of operation (Zhao, Ma, & Zhang, 2018). The equilibrium degree of saturation S_{equil} is computed in MEPDG (2004) using the matric suction (h), and the soil-water characteristic curve (SWCC), as previously explained in Section 3.3.2.

The matric suction (h) can be defined as the capillary pressure of the soil (i.e., $\mathrm{u}_a - \mathrm{u}_w$, where u_a is the pore-air pressure and u_w is the pore water pressure). The soil suction depends mainly on soil index properties, such as P_{200} and PI, and climatic factors such as the Thornthwaite's Moisture Index (TMI). The TMI encompasses the following environmental factors (Zapata, Yugantha, & William, 2009):

- Annual precipitation
- Potential evapotranspiration
- Deficit of water
- Runoff of water

The MEPDG (2004) presents the matric suction as a function of the ground water table (GWT) depth and the unit weight of water, as presented in Equation 3.39, however, this is a simplistic consideration, since the soil suction can depend on many other factors (Zapata, Yugantha, & William, 2009).

The GWT can be defined as the level in the ground above which pores are unsaturated, and below which pores are saturated. The GWT level moves up and down over the year due to variations in rainfall, evapotranspiration and pumping of wells (Simpson, H., 2015). The GWT level to be used in the matric suction computation can be either the best estimate of the annual average depth or a seasonal average depth, in case a clear pattern of variation can be seen among the monitoring wells stations.

For the case study of Toronto Pearson Airport, the optimum degree of saturation S_{opt} is equal to 87.1%. S_{opt} does not change with variations in the matric suction, since it is a function of the Plasticity Index and the percent passing number 200 sieve. The equilibrium degree of saturation S_{equil}, on the other hand, is highly affected by changes in the matric suction. Changes in the airport soil saturation S_{equil} according to the matric suction are presented in Figure 5.16.

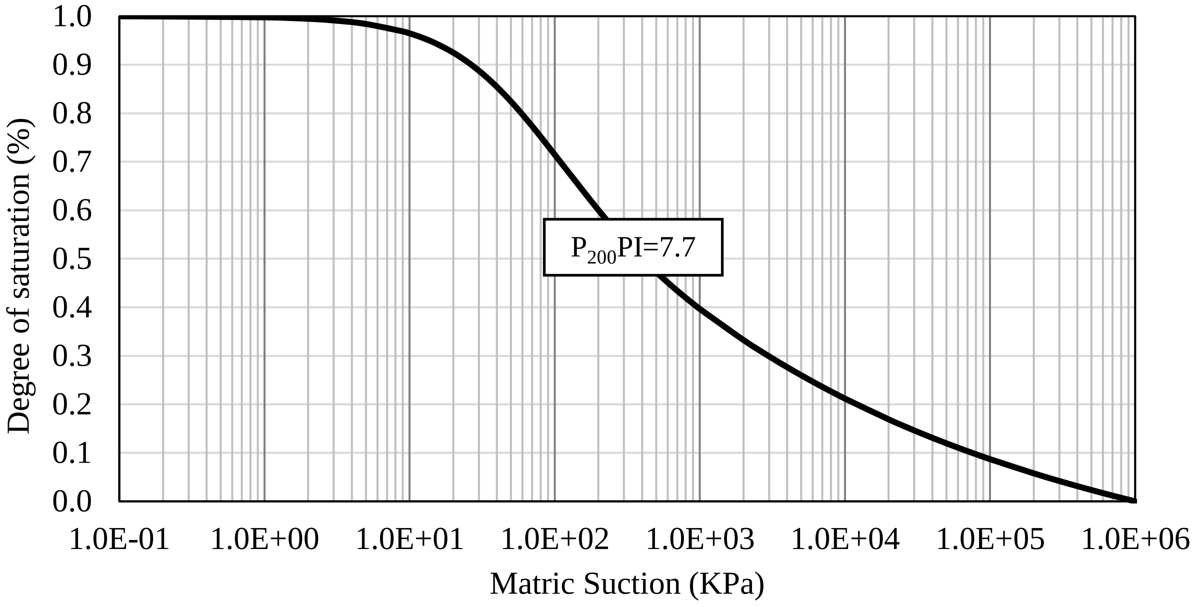

Figure 5.16: Variation in the degree of saturation with matric suction.

Matric suction is the soil capillary pressure. The smaller the capillary pressure, the higher is the soil ability to retain water. Therefore, smaller matric suctions will lead to higher degree of saturation in the subgrade soil.

5.4.4.3 Environment Adjustment Factor and Subgrade Modulus

The pavement subgrade modulus is highly influenced by changes in temperature and moisture levels. To determine such variations, this research uses a similar approach to the MEPDG (2004), in which an environmental adjustment factor (F_{env}) is used to modify the optimum resilient modulus ($M_{R_{opt}}$) of the soil according to variations in moisture and temperature over time, as presented in Section 3.3.2 of this thesis. The resilient modulus at any given period can be expressed by Equation 3.24, which is presented below one more time (ARA, Inc., ERES Consultants Division, 2004).

$$M_R = F_{env} * M_{R_{opt}}$$

The F_{env} factor adjusts the soil optimal resilient modulus for three main conditions: (1) frozen materials (F_f), (2) thawed materials recovering to an equilibrium state (F_r), (3) unfrozen, fully recovered materials or materials that were never frozen (F_u).

The number of hours elapsed since thawing started Δt is directly correlated to the environment adjustment factor F_{env}. If the temperature at a certain moment and depth is below zero, then, Δt is equal to 0 and the frozen factor F_F is used to estimate the soil resilience. If the temperature is above zero, then, Δt will be equal to the number of hours elapsed since unfrozen conditions started. In this case, if Δt is bellow 120, the recovering factor F_R will be applied, while if Δt is above 120, the unfrozen factor F_U will be used to estimate the resilient modulus of the subgrade. The adjustment factor F_{env} along the year for the Toronto Pearson Airport is presented at Figure 5.17, considering matric suctions of 49 kPa and 293 kPa.

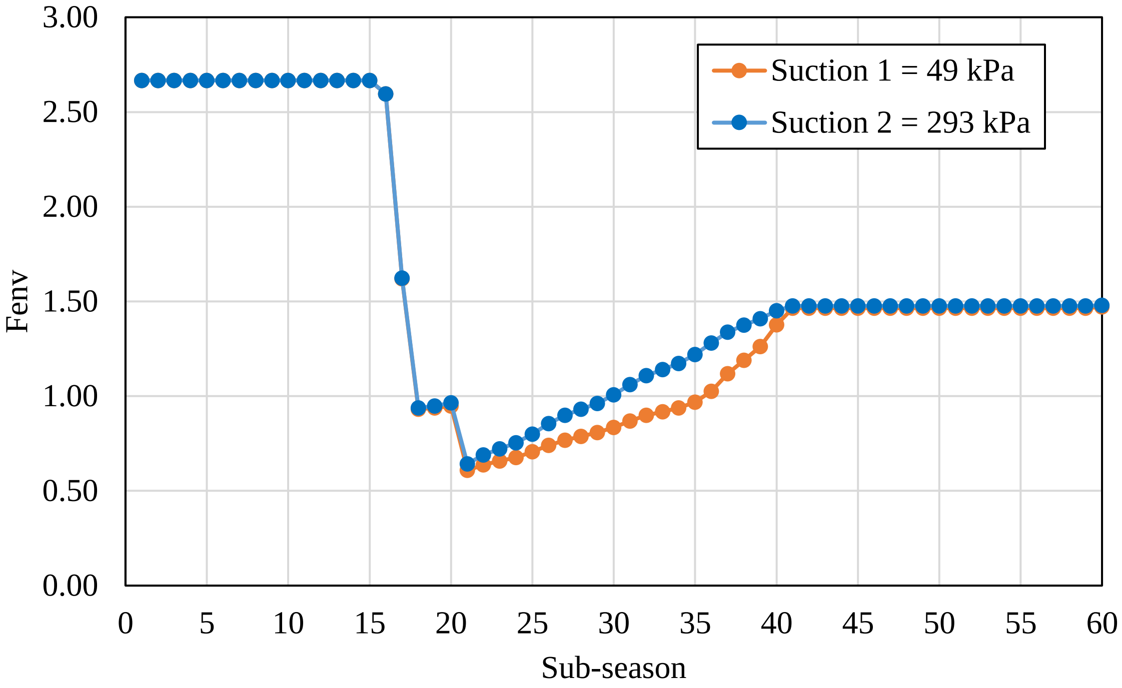

Figure 5.17: Environmental Adjustment Factor.

Figure 5.17 shows that F_{env} is constant at 2.7 during the sub-seasons 1 to 16, that is, from January until the end of March. That happens because the subgrade soil is frozen during this time, therefore, the resilient modulus is higher than the optimum resilient modulus. As soon as the subgrade temperature reaches positive values, F_{env} decreases drastically. This represents the period when the ice is melting, and the subgrade is completely soaked. After that, there is a recovery period that starts at sub-season 22 until approximately sub-season 40, which is equivalent to the months of May through August. Finally, when the soil has completely recovered, F_{env} reaches a constant value, starting at sub-season 41 until 60, which represents the months of September to December.

The recovering adjustment factor is correlated to the matric suction. In the case in which the suction is at 49 kPa, the recovery period F_{env} reaches lower values when compared to the suction of 293 kPa. Soils with higher matric suction have a smother recovery when compared to low suction soils.

The subgrade optimum resilient modulus was defined as 51.71 MPa according to the soil type and CBR tests, as presented in Section 5.2.2. The environmental adjustment factor was multiplied to the optimum resilient modulus to find the average stiffness of the subgrade soil per sub-season, considering the matric suctions of 49 kPa and 293 kPa. The results of the seasonal modulus can be seen in Table 5.17.

Table 5.17: Subgrade Modulus.

Sub-season	**Month**	M_r **(MPa) -** $h = 293$ **kPa**	M_r **(MPa) -** $h = 49$ **kPa**
1	Jan	138	138
2	Jan	138	138
3	Jan	138	138
4	Jan	138	138
5	Jan	138	138
6	Feb	138	138
7	Feb	138	138
8	Feb	138	138
9	Feb	138	138
10	Feb	138	138
11	Mar	138	138
12	Mar	138	138
13	Mar	138	138
14	Mar	138	138
15	Mar	138	138
16	Apr	134	134
17	Apr	84	84
18	Apr	49	48
19	Apr	49	48
20	Apr	50	49
21	May	33	31
22	May	36	33
23	May	37	34
24	May	39	35
25	May	41	37
26	Jun	44	38

Sub-season	**Month**	**M_r (MPa) - $h = 293$ kPa**	**M_r (MPa) - $h = 49$ kPa**
27	Jun	47	40
28	Jun	48	41
29	Jun	50	42
30	Jun	52	43
31	Jul	55	45
32	Jul	57	46
33	Jul	59	47
34	Jul	61	49
35	Jul	63	50
36	Aug	66	53
37	Aug	69	58
38	Aug	71	61
39	Aug	73	65
40	Aug	75	71
41	Sep	76	76
42	Sep	76	76
43	Sep	76	76
44	Sep	76	76
45	Sep	76	76
46	Oct	76	76
47	Oct	76	76
48	Oct	76	76
49	Oct	76	76
50	Oct	76	76
51	Nov	76	76
52	Nov	76	76
53	Nov	76	76
54	Nov	76	76
55	Nov	76	76
56	Dec	76	76
57	Dec	76	76
58	Dec	76	76
59	Dec	76	76
60	Dec	76	76

In the analysis, the minimum modulus of the subgrade was approximately 31 MPa and 33 MPa, for matric suctions at 293 kPa and 49 kPa, respectively. The calculated modulus of the subgrade and AC, as well as the standard modulus for the base and sub-base layers were used to obtain the stresses and strains at critical locations in the pavement, and ultimately to estimate damage.

5.4.5 Pavement Responses

According to Burmister’s theory, flexible pavements can be considered as layered systems, each layer being homogeneous, isotropic, and linearly elastic with an elastic modulus E and a Poisson ratio ν (Huang Y. H., 2004). To calculate the stresses and strains in a structure utilizing the layered elastic analysis (LEA), the main inputs are:

- The pavement design characteristics, that is, the number and thickness of the layers, and the material properties, such as the elastic modulus E and Poisson ratio ν.
- The loading characteristics, including weight, tire pressure and tires configuration.

As a continuation of the case study of Toronto Pearson International Airport, the design characteristics used in this analysis were defined according to Table 5.7, and it consists of an AC layer of 30.4 cm, a granular base of 30 cm, a granular sub-base of 90 cm on the top of the subgrade. The AC and subgrade modulus varies according to the temperature and moisture conditions, as presented in Table 5.15 and Table 5.17. The loading characteristics were defined according to the critical aircraft, the B777-300 ER, with the aircraft attributes presented in Table 5.3. The computer program used to obtain the pavement critical responses was the KENLAYER. The software is LEA based, and it considers the loading condition to be applied in a uniform circular area.

In order to compute rutting damage, one needs to measure the critical responses at the top of the subgrade soil, and to compute fatigue damage, the responses are measured at the AC bottom. To account for the effect of aircraft gears in tandem, the extremum strain records must be computed, to estimate damage at the critical offset yi. The effect that tandem aircraft gears can have in the damage calculations was further explained in Section 3.2.

To determine the extreme strains at critical locations, the pavement strains along offset x were plotted considering the offset y at 0, 34.925 and 69.85. A schematic of the B777-300 ER wheel spacing is presented in Figure 5.18.

Because the total pavement structure of the case study is thick (1.504 m), there is only one extreme compressive strain record at the subgrade top. The maximum compressive strain in this case was measured at the location (146.3, 69.85), represented by the red dot in Figure 5.18. The results of the compressive strains along the x axis are presented in Figure 5.19.

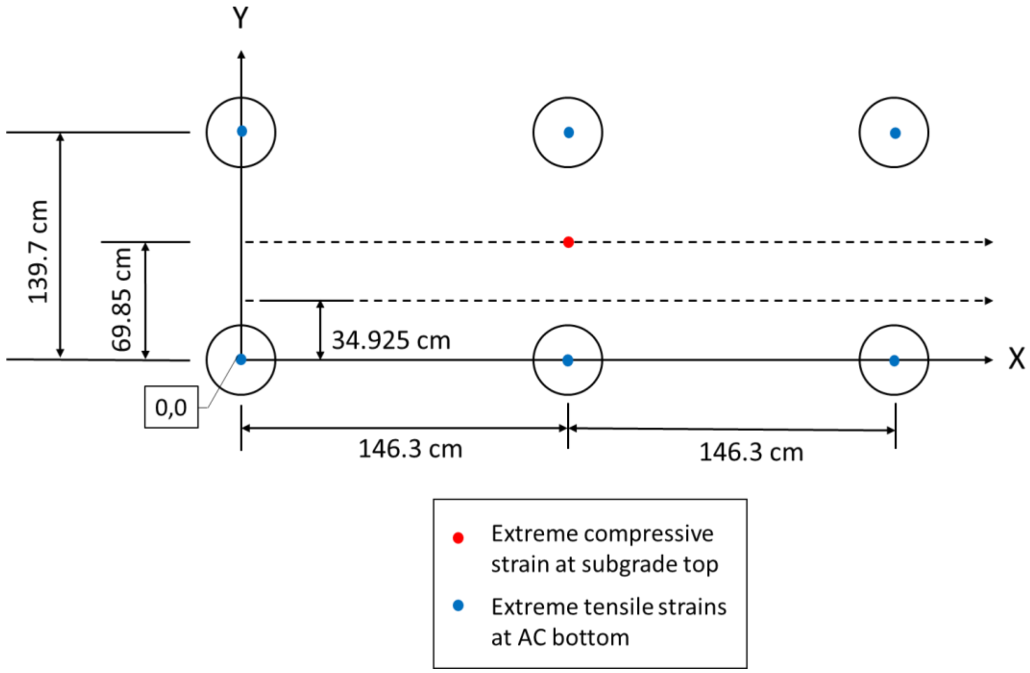

Figure 5.18: B777-300 ER wheel spacing schematics.

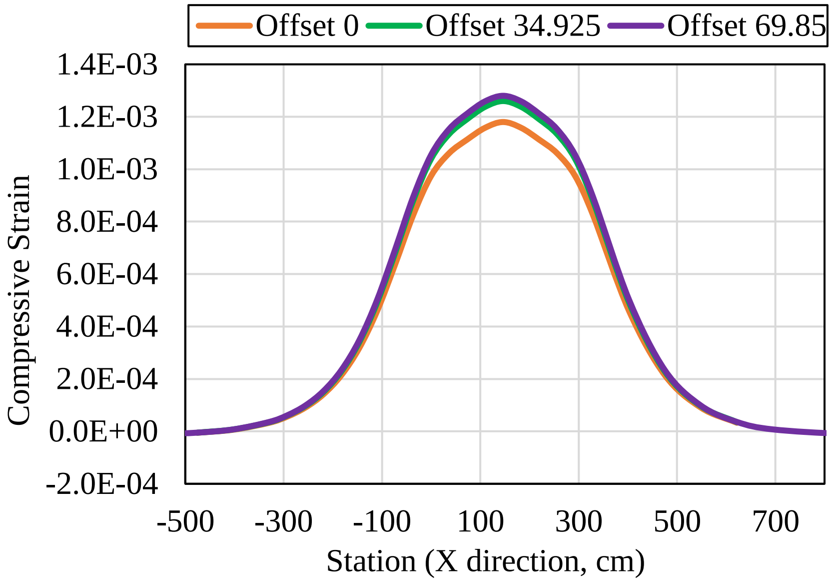

Figure 5.19: Compressive strains at subgrade top.

The tensile strains at the AC bottom, on the other hand, have 3 extreme points along the X axis, each one located at the wheel center. The results of the tensile strains along the x axis are presented in Figure 5.20.

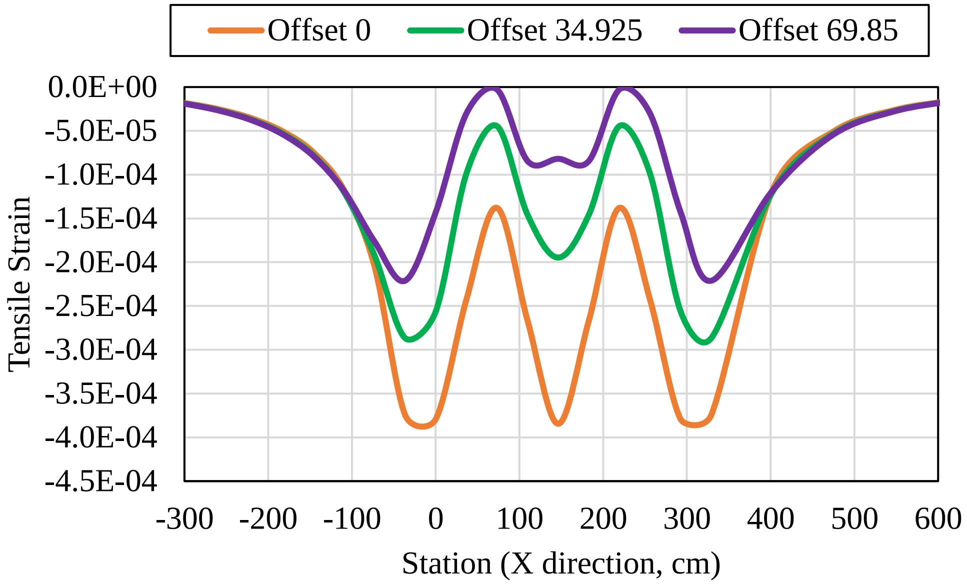

Figure 5.20: Tensile strains at AC bottom.

For the tensile strains, the maximum responses happened at the y offset 0. In this offset, the middle peak was the maximum strain record, while the first and last peaks were the minimum extreme records. Table 5.18 presents the maximum compressive strain at the subgrade top, as well as the maximum and minimum tensile strains at the AC bottom, for each sub-season.

Table 5.18: Pavement critical strains per sub-season.

Sub-season	**Month**	**Comp Strain** ε_c	**Max Tensile Strain** ε_t	**Min Tensile Strain** ε_t
1	Jan	5.03E-04	-1.42E-04	-1.38E-04
2	Jan	4.99E-04	-1.38E-04	-1.33E-04
3	Jan	4.96E-04	-1.35E-04	-1.30E-04
4	Jan	4.93E-04	-1.32E-04	-1.28E-04
5	Jan	4.88E-04	-1.28E-04	-1.24E-04
6	Feb	4.99E-04	-1.38E-04	-1.33E-04
7	Feb	4.90E-04	-1.30E-04	-1.26E-04
8	Feb	4.84E-04	-1.25E-04	-1.21E-04
9	Feb	4.79E-04	-1.21E-04	-1.17E-04
10	Feb	4.71E-04	-1.15E-04	-1.11E-04
11	Mar	5.43E-04	-1.94E-04	-1.91E-04
12	Mar	5.24E-04	-1.65E-04	-1.61E-04
13	Mar	5.12E-04	-1.51E-04	-1.46E-04
14	Mar	5.01E-04	-1.39E-04	-1.35E-04

Sub-season	**Month**	**Comp Strain** $\boldsymbol{\varepsilon_c}$	**Max Tensile Strain** $\boldsymbol{\varepsilon_t}$	**Min Tensile Strain** $\boldsymbol{\varepsilon_t}$
15	Mar	4.86E-04	-1.26E-04	-1.22E-04
16	Apr	5.86E-04	-2.65E-04	-2.62E-04
17	Apr	8.18E-04	-2.29E-04	-2.25E-04
18	Apr	1.17E-03	-2.23E-04	-2.17E-04
19	Apr	1.14E-03	-2.06E-04	-2.00E-04
20	Apr	1.09E-03	-1.88E-04	-1.82E-04
21	May	1.68E-03	-3.67E-04	-3.65E-04
22	May	1.55E-03	-3.21E-04	-3.17E-04
23	May	1.47E-03	-2.95E-04	-2.90E-04
24	May	1.41E-03	-2.73E-04	-2.67E-04
25	May	1.33E-03	-2.48E-04	-2.42E-04
26	Jun	1.45E-03	-3.93E-04	-3.94E-04
27	Jun	1.35E-03	-3.60E-04	-3.58E-04
28	Jun	1.30E-03	-3.37E-04	-3.34E-04
29	Jun	1.25E-03	-3.17E-04	-3.13E-04
30	Jun	1.19E-03	-2.92E-04	-2.87E-04
31	Jul	1.27E-03	-4.05E-04	-4.11E-04
32	Jul	1.20E-03	-3.85E-04	-3.85E-04
33	Jul	1.16E-03	-3.68E-04	-3.66E-04
34	Jul	1.12E-03	-3.50E-04	-3.48E-04
35	Jul	1.08E-03	-3.27E-04	-3.24E-04
36	Aug	1.10E-03	-4.04E-04	-4.06E-04
37	Aug	1.04E-03	-3.78E-04	-3.77E-04
38	Aug	1.01E-03	-3.59E-04	-3.58E-04
39	Aug	9.78E-04	-3.41E-04	-3.39E-04
40	Aug	9.44E-04	-3.18E-04	-3.16E-04
41	Sep	9.64E-04	-3.77E-04	-3.76E-04
42	Sep	9.45E-04	-3.43E-04	-3.41E-04
43	Sep	9.35E-04	-3.23E-04	-3.20E-04
44	Sep	9.25E-04	-3.05E-04	-3.02E-04
45	Sep	9.13E-04	-2.84E-04	-2.80E-04
46	Oct	9.26E-04	-3.06E-04	-3.03E-04
47	Oct	9.04E-04	-2.69E-04	-2.65E-04
48	Oct	8.91E-04	-2.50E-04	-2.45E-04
49	Oct	8.78E-04	-2.34E-04	-2.29E-04
50	Oct	8.62E-04	-2.15E-04	-2.10E-04
51	Nov	8.62E-04	-2.15E-04	-2.10E-04

Sub-season	Month	Comp Strain ε_c	Max Tensile Strain ε_t	Min Tensile Strain ε_t
52	Nov	8.32E-04	-1.87E-04	-1.81E-04
53	Nov	8.13E-04	-1.72E-04	-1.67E-04
54	Nov	7.95E-04	-1.60E-04	-1.55E-04
55	Nov	7.72E-04	-1.47E-04	-1.41E-04
56	Dec	7.59E-04	-1.40E-04	-1.34E-04
57	Dec	7.40E-04	-1.30E-04	-1.25E-04
58	Dec	7.27E-04	-1.25E-04	-1.20E-04
59	Dec	7.15E-04	-1.20E-04	-1.15E-04
60	Dec	6.99E-04	-1.14E-04	-1.09E-04

5.4.6 Cumulative Damage

5.4.6.1 Coverages and Coverage-to-Pass Ratio

The failure models in FAARFIELD connect a calculated structural response to the number of coverages the pavement can carry. For flexible pavements, the structural responses are the extreme vertical strains at the top of the subgrade and the extreme horizontal strains at the bottom of the asphalt concrete layer. Coverage can be defined as the number of repetitions of an extreme strain. Because of aircraft wander, the number of coverages can differ from the number of passes, therefore, it is necessary to calculate the Pass-to-Coverage (P/C) ratio.

The number of coverages to rutting failure depends only on the extreme vertical strains at the top of the subgrade, according to Equation 3.1. The number of coverages to fatigue failure, on the other hand, depends not only on the extreme tensile strains, but on the flexural stiffness of the HMA, and the volumetric parameters of the mix, as given in Equations 3.3 and 3.4.

To calculate the number of rutting and fatigue coverages, the strains were defined according to Table 5.18. The flexural stiffness of the mix used is the default value from FAARFIELD, and it is equal to 4,136.85 MPa (600,000 psi). The volumetric parameters were defined in Section 5.2.5. The number of coverages to failure for rutting and fatigue are presented in Table 5.19.

Table 5.19: Number of coverages to failure.

Sub-season	Month	Rutting Coverage	Fatigue Coverage (Max Strain)	Fatigue Coverage (Min Strain)
1	Jan	1.00E+25	5.28E+07	6.03E+07
2	Jan	1.00E+25	6.03E+07	7.15E+07

Sub-season	Month	Rutting Coverage	Fatigue Coverage (Max Strain)	Fatigue Coverage (Min Strain)
3	Jan	1.00E+25	6.67E+07	7.95E+07
4	Jan	1.00E+25	7.40E+07	8.54E+07
5	Jan	1.00E+25	8.54E+07	9.89E+07
6	Feb	1.00E+25	6.03E+07	7.15E+07
7	Feb	1.00E+25	7.95E+07	9.18E+07
8	Feb	1.00E+25	9.53E+07	1.11E+08
9	Feb	1.00E+25	1.11E+08	1.29E+08
10	Feb	1.00E+25	1.40E+08	1.65E+08
11	Mar	1.00E+25	1.25E+07	1.34E+07
12	Mar	1.00E+25	2.63E+07	2.95E+07
13	Mar	1.00E+25	3.97E+07	4.64E+07
14	Mar	1.00E+25	5.83E+07	6.67E+07
15	Mar	1.00E+25	9.18E+07	1.07E+08
16	Apr	1.00E+25	2.94E+06	3.10E+06
17	Apr	1.00E+25	5.78E+06	6.27E+06
18	Apr	9.39E+05	6.53E+06	7.41E+06
19	Apr	2.85E+06	9.43E+06	1.08E+07
20	Apr	1.92E+07	1.44E+07	1.67E+07
21	May	1.71E+03	6.51E+05	6.67E+05
22	May	4.45E+03	1.21E+06	1.28E+06
23	May	8.88E+03	1.79E+06	1.94E+06
24	May	1.87E+04	2.56E+06	2.84E+06
25	May	6.39E+04	3.99E+06	4.47E+06
26	Jun	1.39E+04	4.74E+05	4.69E+05
27	Jun	5.02E+04	7.12E+05	7.30E+05
28	Jun	1.26E+05	9.66E+05	1.01E+06
29	Jun	3.50E+05	1.28E+06	1.36E+06
30	Jun	1.87E+06	1.88E+06	2.03E+06
31	Jul	2.96E+05	4.12E+05	3.85E+05
32	Jul	2.30E+06	5.21E+05	5.21E+05
33	Jul	1.14E+07	6.43E+05	6.59E+05
34	Jul	7.23E+07	8.11E+05	8.32E+05
35	Jul	2.29E+09	1.11E+06	1.16E+06
36	Aug	3.74E+08	4.17E+05	4.08E+05
37	Aug	5.01E+10	5.68E+05	5.75E+05
38	Aug	7.24E+02	7.21E+05	7.30E+05

Sub-season	Month	Rutting Coverage	Fatigue Coverage (Max Strain)	Fatigue Coverage (Min Strain)
39	Aug	8.09E+02	9.15E+05	9.40E+05
40	Aug	9.30E+02	1.26E+06	1.30E+06
41	Sep	6.40E+02	5.75E+05	5.82E+05
42	Sep	8.01E+02	8.90E+05	9.15E+05
43	Sep	9.05E+02	1.18E+06	1.23E+06
44	Sep	5.76E+03	1.53E+06	1.60E+06
45	Sep	1.39E+28	2.13E+06	2.28E+06
46	Oct	2.32E+21	1.51E+06	1.58E+06
47	Oct	6.22E+38	2.74E+06	2.94E+06
48	Oct	1.00E+25	3.85E+06	4.23E+06
49	Oct	1.00E+25	5.23E+06	5.78E+06
50	Oct	1.00E+25	7.74E+06	8.63E+06
51	Nov	1.00E+25	7.74E+06	8.63E+06
52	Nov	1.00E+25	1.48E+07	1.72E+07
53	Nov	1.00E+25	2.17E+07	2.49E+07
54	Nov	1.00E+25	3.04E+07	3.52E+07
55	Nov	1.00E+25	4.50E+07	5.46E+07
56	Dec	1.00E+25	5.64E+07	6.91E+07
57	Dec	1.00E+25	7.95E+07	9.53E+07
58	Dec	1.00E+25	9.53E+07	1.15E+08
59	Dec	1.00E+25	1.15E+08	1.40E+08
60	Dec	1.00E+25	1.46E+08	1.80E+08

The number of coverages and the number of passes is different due to aircraft wander, therefore, passes and coverages must be related through the C/P ratio. The steps to calculate the C/P ratio were discussed in Section 3.1. The characteristics of the B777-300 ER used to obtain the C/P ratio are presented at Table 5.20:

Table 5.20: Aircraft parameters to calculate the C/P ratio

Aircraft Characteristics	
Aircraft Wander	1.788 m
Tandem Tire Spacing	1.463 m
Dual Tire Spacing	1.397 m
x_k	5.485 m

Where x_k is the lateral distance from centerline of the runway to the centerline between the tires. When computing the C/P ratio, the pavement is divided into 82 longitudinal strips (i), 10-inch-wide. The C/P ratio must be computed for each strip offset (x_i), which consists of the distance from the runway centerline to the center of strip i.

The final value of $(C/P)_i$ will be the summation of the coverage-to-pass ratio for all extreme strains. For example, it was showed in Figure 5.18 that there were six extreme strains at the bottom of the AC, located under each aircraft wheel. In this situation, $(C/P)_i$ should be calculated for the wheels in the left and multiplied by 3 to account for the 3 wheels in tandem, and again calculated for the wheels in the right, and multiplied by 3. Finally, $(C/P)_i$ will be the summation of the probabilities calculated for the left and right wheels. The results of the fatigue $(C/P)_i$ ratio is presented in Figure 5.22.

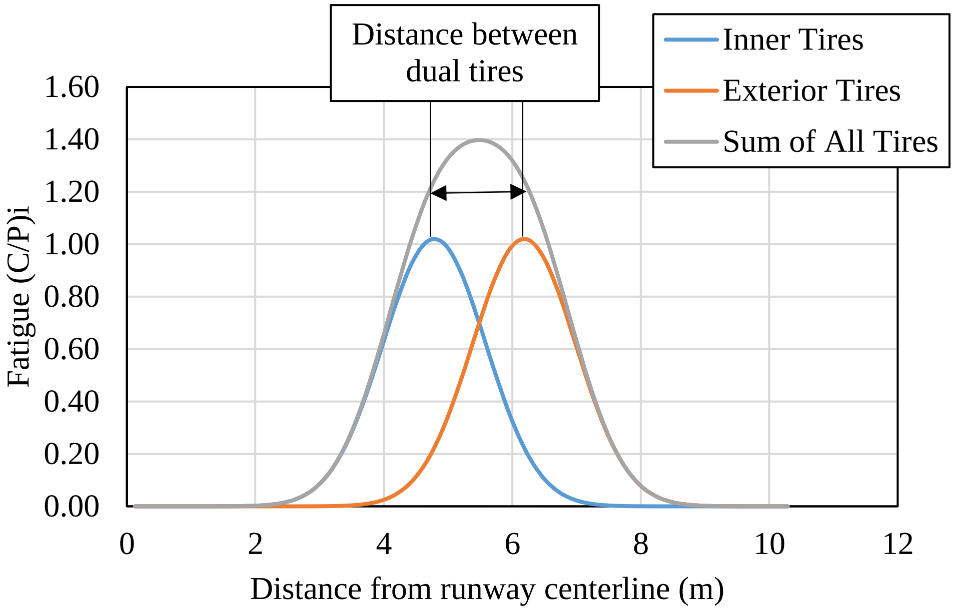

Figure 5.21: Fatigue $(C/P)_i$ ratio for a B777-300 ER.

It can be noted in Figure 5.22 that the maximum $(C/P)_i$ for all tires is equal to 1.4. The calculation procedure for the rutting $(C/P)_i$ is more simplified, since there was only one extreme strain measured at the top of the subgrade. The results of the rutting $(C/P)_i$ are presented in Figure 5.22. In this case, the maximum $(C/P)_i$ was equal to 0.96.

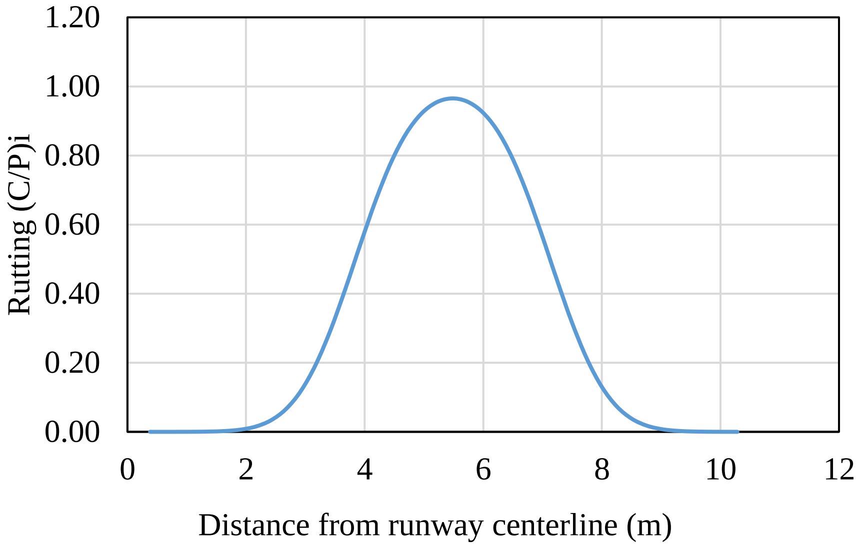

Figure 5.22: Rutting $(C/P)_i$ ratio for a B777-300 ER.

5.4.6.2 Cumulative Damage Factor

The Cumulative Damage Factor (CDF) is the amount of the structural fatigue life of a pavement that has been consumed, and it is expressed through the ratio of the applied load repetitions by the allowable load repetitions to failure (Ali Shafabakhsh & Kashi, 2015). The cumulative damage caused by an aircraft mix is defined as presented in Equations 3.7 and 3.8 (Tuleubekov, 2016), repeated below:

$$CDF_i = \sum_{A=1}^{m} (C/P)_i^{(A)} * P_A * D(yi)$$

$$D(yi) = \sum_{k=1}^{n} s_k * \frac{1}{C(\varepsilon_k)}$$

Where, m = number of aircraft types in the traffic mix; P_A = total number of passes of aircraft A per sub-season; $D(yi)$ is the damage computed at the offset yi, n is the total number of extremum points of strain, ε_k are the extreme strain values, C is the number of coverages according to Equation 3.1, and s_k is a factor characterizing the k^{th} extremum strains.

In the case study, the B777-300 ER $(C/P)_i$ for the rutting and fatigue criteria were calculated in Section 5.4.6.1, and they are equal to 0.96 and 1.4 respectively. The total number of passes of the B777-300 ER per sub-season P_A is equal to 58. The matric suction was considered to be 293 kPa. The extreme strain values s_k were presented in Table 5.18, and the number of coverages per extreme strain $C(\varepsilon_k)$ was presented in Table 5.19. The results of the rutting and fatigue CDF are presented in Figure 5.23 and Figure 5.24, respectively, considering the proposed methodology versus FAARFIELD. Figure 5.23 (a) and Figure 5.24 (a) illustrate the damage over one year (60 sub-seasons) while Figure 5.23 (b) and Figure 5.24 (b) show the estimated damage over 20 years.

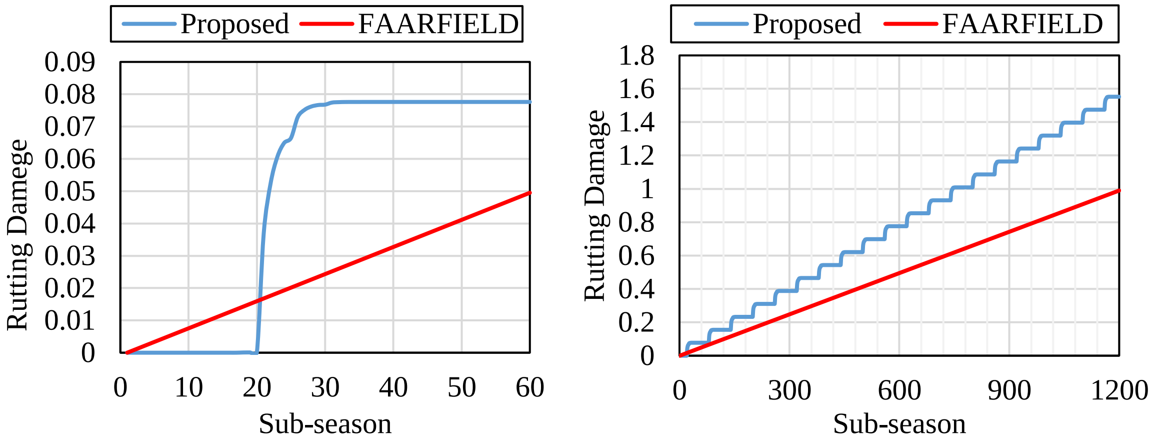

Figure 5.23: Cumulative rutting damage (a) over one year (b) over twenty years.

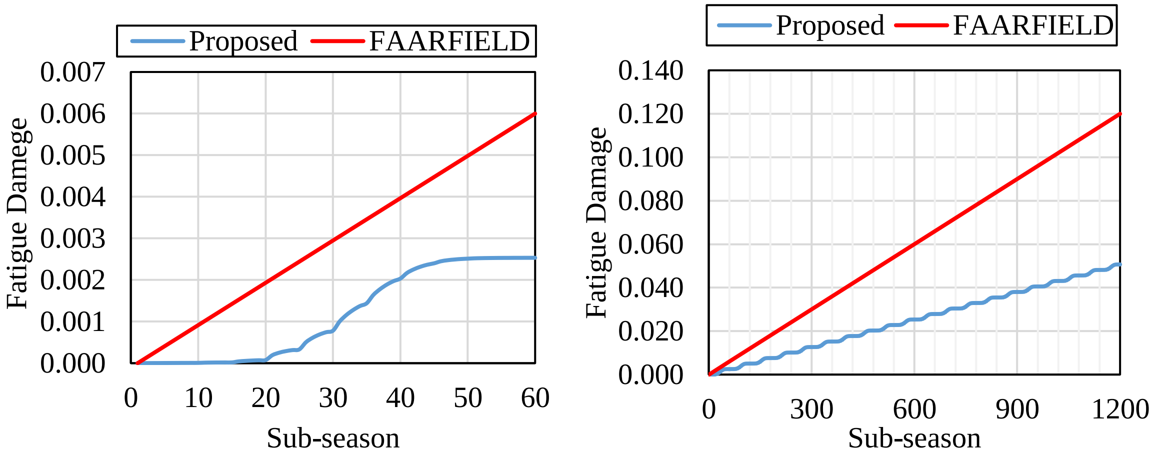

Figure 5.24: Cumulative fatigue damage (a) over one year (b) over twenty years.

It is possible to notice from Figure 5.23 (a) that the most significant rutting damage occurs during the sub-seasons 20 to 30, which are equivalent to the months of May and June. The total damage caused by the B777-300 ER over the 20-year period is of 1.55, compared to 0.99 from FAARFIELD, therefore, the rutting damage predicted from the proposed methodology is 57% higher than the predicted damage from FAARFIELD. The considerations of the current climate result in a shorter service life than FAARFIELD of about 7 years due to the increased rutting damage.

In terms of the fatigue damage, it can be noted from Figure 5.24 (a) that the most significant damage occurs during sub-seasons 20 to 45, which are equivalent to the months of May until middle September. Figure 5.24 (b) shows that the total fatigue damage estimated through the proposed methodology is lower than what is proposed by FAARFIELD; the software indicates that the total fatigue damage caused by the B777-300 ER over the 20-year period is 0.12, while in the proposed methodology is of 0.051. This can be mainly attributed to two reasons: first, because the damage during the cooler seasons is very low, considering that the pavement layers are frozen and therefore, very stiff during this period; second, because the proposed methodology considered the specific characteristics of the asphalt mix, such as the percentage air voids and the effective asphalt content, which are superior to the default values considered in FAARFIELD, lowering the total fatigue damage.

5.4.7 Thermal-induced Fatigue Damage

Daily temperature fluctuation can have an impact on fatigue cracking. To assess the possible effects of temperature-induced fatigue damage, this research used the methodology proposed by Islam, which was previously explained in Section 3.4.2 (Islam, 2015). The application of the method followed eight steps, as presented below:

1. The first step in this process was to take the average temperature per month at the top of the AC layer. To that end, the temperature predictions from TEMPS were used, as described in Section 5.4.1, at a depth of 1 cm below the pavement surface.
2. The α-value for each month was estimated through Equation 3.48, and it mainly depends on the average temperature determined in step 1.
3. Predicted the maximum temperature y_{max} and the minimum temperature y_{min} at the top of the AC. Calculated the average temperature fluctuation for that period $\Delta T = y_{max} - y_{min}$.
4. Determined the thermal strain, $\varepsilon = \alpha * \Delta T$.
5. Determined the stiffness of AC using the MEPDG (2004) sigmoidal function, considering the average temperature calculated in step 1.
6. Predicted the allowable number of load repetition for temperature fluctuations (Equation 3.46), which mainly depends on the thermal strain and AC stiffness as per steps 4 and 5, respectively.
7. Determined the damage ratio for thermal fatigue damage (Equation 3.49).
8. To obtain the temperature-induced fatigue damage D_2, the damage ratio n/N was multiplied by a shift factor of 0.004, which according to Table 3.6 is suitable for AC layer thickness greater than 10.16 cm.

The results from each step are presented in Table 5.21. The annual damage is equal to the sum of the monthly damage (sum of column 8), and it is equal to 0.029. The temperature-induced fatigue damage calculated for 20 years is equal to 0.59. To calculate the total fatigue damage, the temperature-induced damage must be summed to the load-induced damage. In the case of the Current Climate scenario, the total fatigue damage is equal to 0.051+0.59=0.64.

The damage of 0.64 is greater than the 0.12 fatigue damage calculated by FAARFIELD. Even though the fatigue damage has significantly changed when considering temperature fluctuation stress, the pavement design would still be governed by rutting damage, since the calculated fatigue damage is smaller than 1.0.

Table 5.21: Steps to obtain the temperature-induced fatigue damage.

Month	(1)	(2)	(3)	(4)	(5)	(6)	(7)		(8)
	Av. temp (^{o}C)	α	**Av. ΔT**	**Thermal strain, ε**	**Av. Mr (Psi)**	N	n	n/N	D_2
1	-4.1	21.07	3.0	64.1	2,516,947	9774	31	3.17E-03	1.27E-05
2	-3.6	21.27	4.0	84.7	2,879,283	3531	28	7.93E-03	3.17E-05
3	2.8	23.59	9.2	217.3	2,047,138	157	31	1.98E-01	7.91E-04
4	10.6	25.74	13.6	349.1	1,207,313	38	30	7.92E-01	3.17E-03
5	20.2	27.38	16.4	449.4	639,887	21	31	1.50E+00	6.01E-03
6	26.8	27.87	17.1	477.5	405,350	20	30	1.48E+00	5.93E-03
7	31.6	27.89	17.2	479.9	290,785	23	31	1.36E+00	5.43E-03
8	30.2	27.91	15.9	445.2	316,202	29	31	1.08E+00	4.34E-03
9	25.0	27.78	13.3	369.8	440,861	47	30	6.35E-01	2.54E-03
10	15.8	26.76	9.1	242.6	835,925	156	31	1.99E-01	7.97E-04
11	7.0	24.82	5.9	146.9	1,837,236	634	30	4.73E-02	1.89E-04
12	1.1	23.00	3.3	75.2	3,436,280	4964	31	6.24E-03	2.50E-05

5.4.8 Assumptions in Current Climate Scenario

Most data used to run the current climate damage analysis originates from field data granted by the GTAA. The main data used to implement the proposed methodology is:

- Bore hole data, including subgrade material type, gradation, and PI
- The current pavement structure, including material types and layer thickness
- Traffic data that includes annual departures and predicted % growth

Specific aircraft information, such as the Gross Taxi Weight and wheel spacing were found in the aircraft manuals, widely available online. Even though the majority of the inputs used in the analysis were based on field data, some assumptions had to be made. The main assumptions are:

#Temperature gradient:

- All material property parameters used to determine the pavement temperature gradient were assumed based on the literature, as presented in Table 5.11

#AC Dynamic Modulus

- The aircraft speed was set at 30km/h, representing a typical taxiing speed
- The hardening code was set at zero, which represents an average expected hardening ratio of the binder
- The depth (z) to obtain the binder viscosity was set at 6.35 cm (2.5 inches)

#Subgrade Stiffness

- The matric suction at the current climate scenario was assumed to be at 293 kPa. Direct measurements of the matric suction are recommended

#FAARFIELD Design

- In the FAARFIELD design, the base material was considered as a P-209 Crushed Aggregate and the sub-base as a P-154 uncrushed aggregate

#Fatigue Damage

- The flexural stiffness of the AC mix was set at 4136.85 MPa (600,000 psi)
- The aircraft wander was set at 178.8 cm
- The tire contact width was set at 38 cm, which is the same contact width proposed by FAARFIELD for the B777-300 ER aircraft

#Rutting Damage

- The aircraft wander was set at 178.8 cm
- The tire contact width was set at 38 cm, which is the same contact width proposed by FAARFIELD for the B777-300 ER aircraft

5.5 Climate Change Scenarios

Four climate change scenarios were analyzed under the proposed methodology, they are: Temperature Increase, Lower Matric Suction and two Flooding Events. Each scenario was compared to the cumulative damage resulting from the Current Climate analysis and the results from the standard FAARFIELD analysis.

5.5.1 Temperature Increase

There are a few mathematical methods to project future weather, among which the morphing method could be named as one of the most well-known approaches. A web-based application called “Weather Morph: Climate Change Weather File Generator” can be used to generate hourly future weather data for many locations across the world considering four gas emission scenarios in three time-horizons: 2020s, 2050s and 2080s (Jiang, Liu, Czarnecki, & Zhang, 2019). In this research, the temperature increase scenario used data available at http://139.62.210.131/weatherGen/, under gas emission scenario RCP 8.5 in the year of 2050. The matric suction was set at 293 kPa. Combining the proposed methodology with this hourly dataset, a comparison of the rutting and fatigue damage caused by the B777-300 ER was made, as presented in Figure 5.25 and Figure 5.26, considering the proposed methodology versus FAARFIELD.

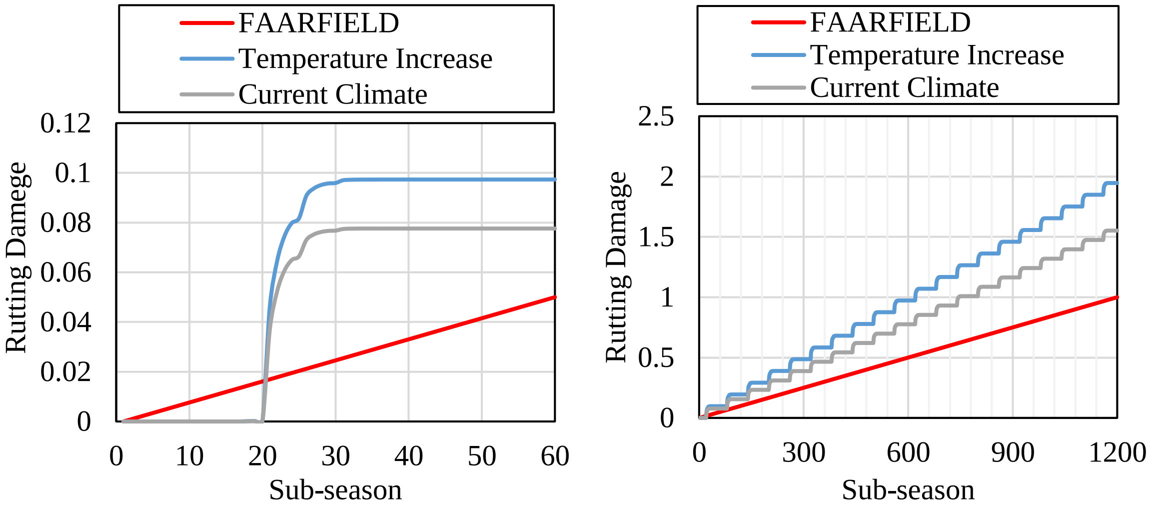

Figure 5.25: Cumulative rutting damage (a) over one year (b) over twenty years.

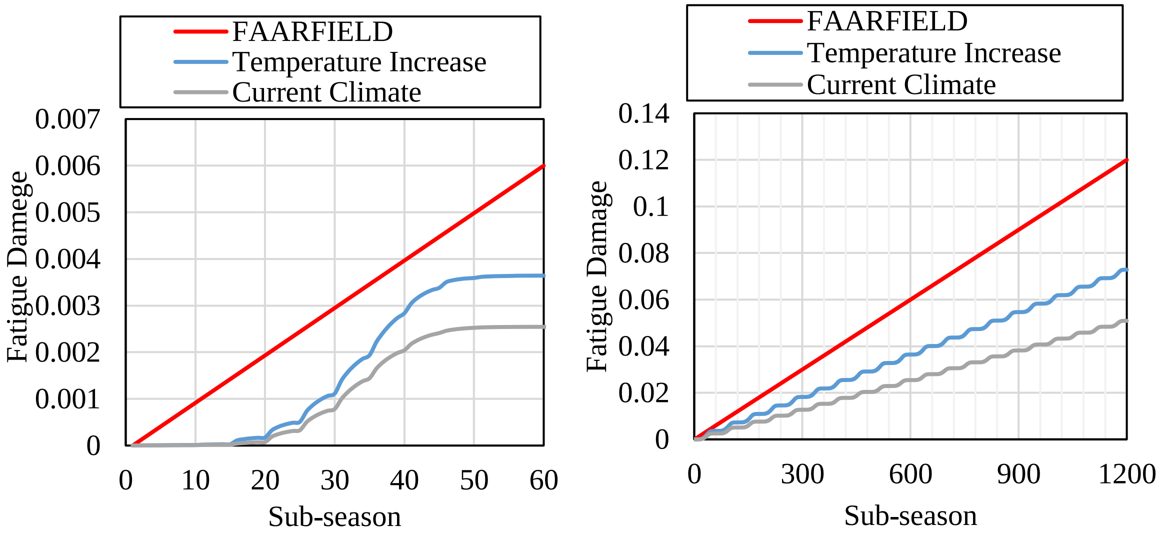

Figure 5.26: Cumulative fatigue damage (a) over one year (b) over twenty years.

As indicated by Figure 5.25, the total cumulative rutting damage at the end of the 20 years would be 1.95 under the Temperature Increase scenario, as compared to a damage value of 1.55 from the Current Climate scenario using the proposed methodology, or 0.99 according to the traditional FAARFIELD method. Therefore, when considering the potential increase in temperature due to the climate change, rutting damage can be 25% higher than the Current Climate scenario, and 97% higher than the conventional design through FAARFIELD, which implicates in a shortening of the service life of the flexible airfield pavement by about 10 years.

Figure 5.26 (b) shows that the total fatigue damage under the temperature increase scenario is 0.0723, compared to 0.05068 from the current climate scenario, or 0.12 according to the FAARFIELD method. Even though the total fatigue damage predicted by the proposed methodology is still smaller than FAARFIELD, its value increased in 43% compared to the

Current Climate analysis. Therefore, the results from a potential rise in temperature, if not associated with changes in moisture levels or flooding events, will be more critical in terms of fatigue damage.

5.5.2 Lower Matric Suction

Under the Lower Matric Suction scenario, the temperature records were considered the same as the Current Climate scenario, while the matric suction was assumed to be 49 kPa. As explained in section 5.4.4.2, matric suction is the soil capillary pressure. The smaller the capillary pressure, the higher is the soil ability to retain water. Therefore, smaller matric suctions will lead to higher degree of saturation in the soil.

The effect of changes in the matric suction on the expected pavement damages can be investigated through the use of the proposed methodology and based on the adjustment of the modulus values. Results of the rutting and fatigue damages, considering the B777-300 ER movements, are presented in Figure 5.27 and Figure 5.28.

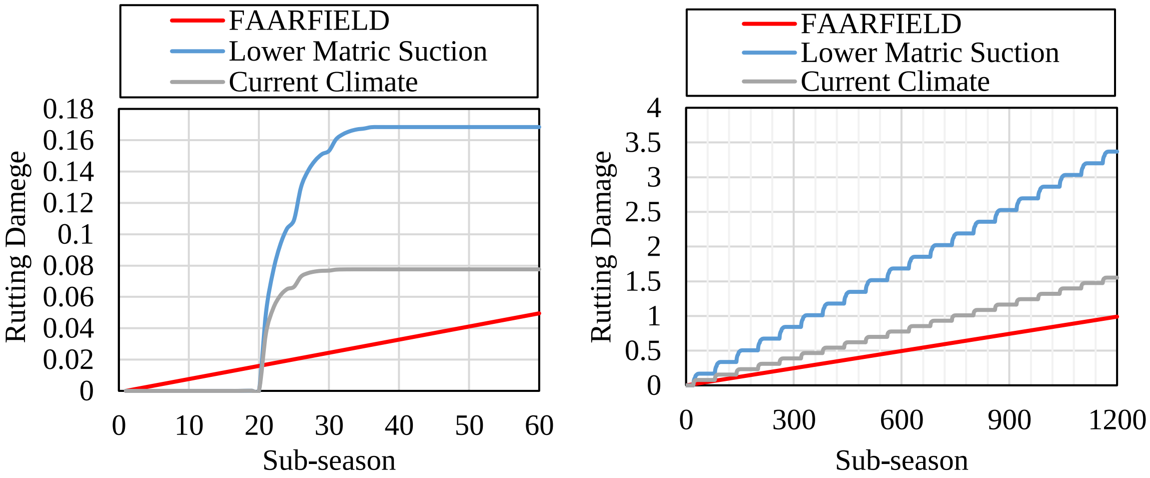

Figure 5.27: Cumulative rutting damage (a) over one year (b) over 20 years

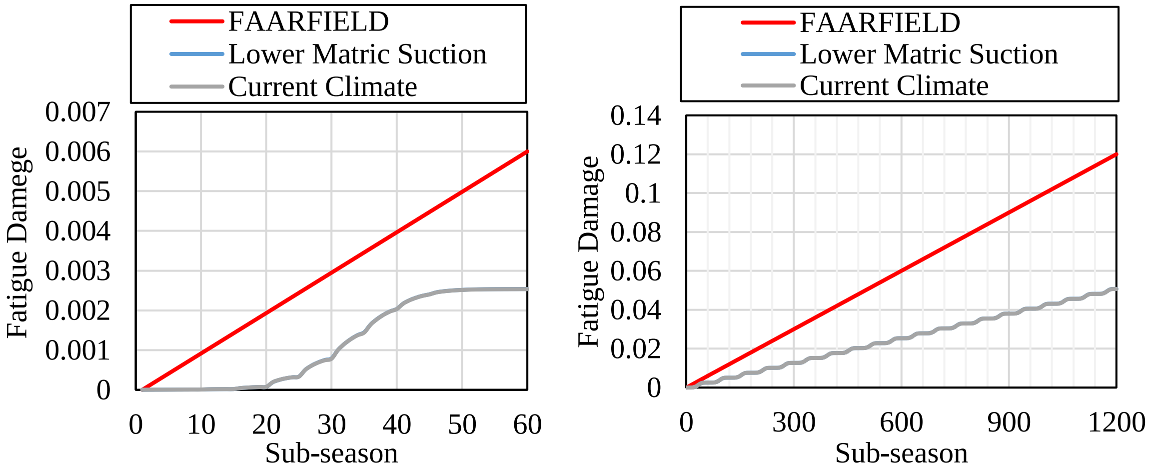

Figure 5.28: Cumulative fatigue damage (a) over one year (b) over 20 years

By comparing the results from the previously discussed scenarios and the Lower Matric Suction scenario, as demonstrated by Figure 5.23 (a), Figure 5.25 (a) and Figure 5.27 (a), it can be recognized that the high damage season was extended when saturation levels were higher. The annual result from Figure 5.27 (a) shows that high rutting damage levels happens in this case through sub-seasons 20 to 35, which is equivalent to the months of May, June and July, that is, one month more than what was predicted in the Current Climate analysis. Figure 5.27 (b) shows that the total rutting damage at the end of 20 years in this case was accounted at 3.37, compared to 1.55 from the Current Climate scenario and 0.99 from FAARFIELD. It can, therefore, be concluded that increasing the subgrade soil saturation level due to the decrease in the matric suction results in worsening the rutting damage by 117% when compared to the Current Climate scenario, and 240% when compared to the traditional FAARFIELD analysis, resulting in a pavement service life of only 6 years.

The fatigue results from Figure 5.28, on the other hand, indicate a total fatigue damage of 0.05074, which is less than 1% higher than the results from the Current Climate scenario (i.e., 0.05068). However, it is still much lower than the damage of 0.12 predicted by FAARFIELD. Therefore, the fatigue damage was not significantly influenced by the lowered subgrade soil stiffness due to the lowered matric suction.

5.5.3 Flooding Events

It was demonstrated in the Lower Matric Suction scenario that changes in the saturation level can affect the total predicted damage over the service life of flexible airfield pavements. Therefore, under this scenario the effect of an extreme event such as flooding is further evaluated. This analysis considered the additional damages from a flooding event, by simulating a condition in which the subgrade would be completely saturated due to intense precipitation. This hypothetical scenario occurs in the summer, starting on August 13th.

In the occasion of a flooding event, the soil would be completely saturated, and the matric suction would equal zero (0). As time goes by, the soil would drain, and the matric suction would slowly recover to the equilibrium level of 293 kPa. To evaluate the effects of the rate at which the soil matric suction recover, over pavement damage after a flooding event, two scenarios were evaluated, one assuming the matric suction increase at 50 kPa/sub-season until it reaches 293 kPa, and another with the matric suction increase at 25 kPa/sub-season.

In Scenario 1, the soil returns to its equilibrium matric suction in 36 days, and in Scenario 2, the equilibrium matric suction is reestablished in 72 days. The results from Scenario 1 are presented in Figure 5.29 and Figure 5.30.

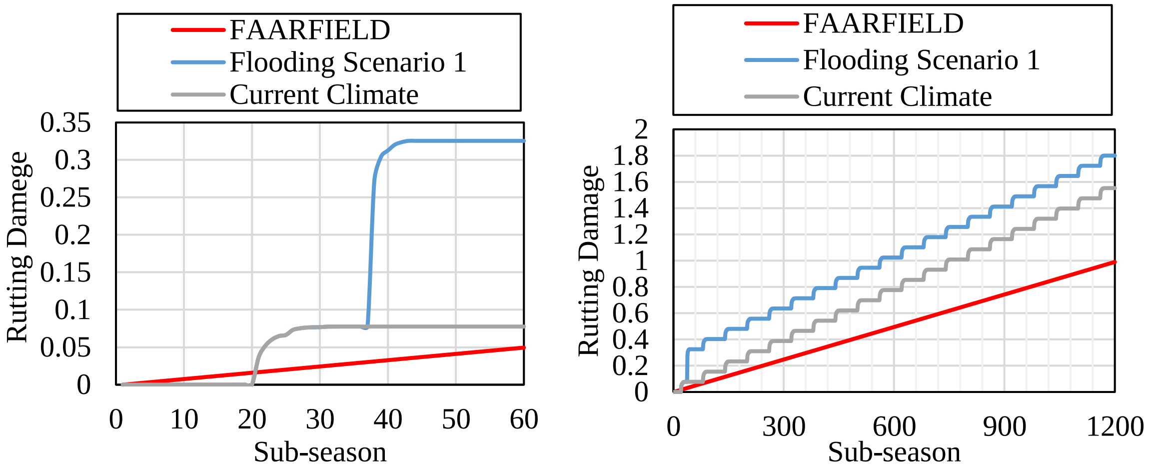

Figure 5.29: Cumulative rutting damage (a) over one year (b) over 20 years.

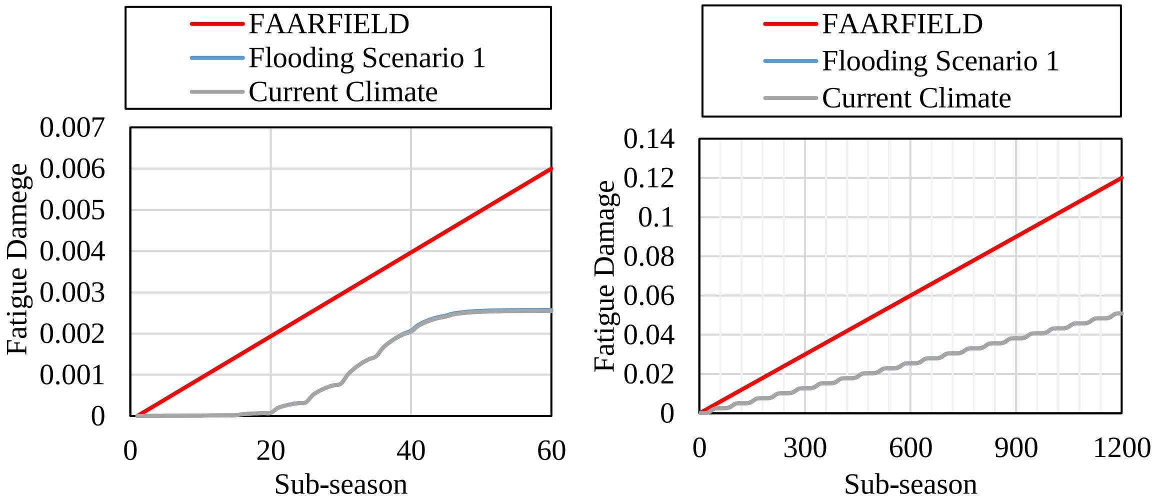

Figure 5.30: Cumulative fatigue damage (a) over one year (b) over 20 years.

The total rutting damage during the year in which flooding Scenario 1 happened was found to be equal to 0.3, as presented in Figure 5.29 (a), which is equivalent to about 6 years of damage under normal circumstances (CDF=0.99 over 20 years). The total rutting damage over 20 years, presented in Figure 5.29 (b), was accounted at 1.80. Therefore, the total rutting damage under the flooding Scenario 1 is 16% higher than the damage predicted by the Current Climate scenario and 82% higher than the rutting damage predicted by the traditional FAARFIELD method.

The yearly fatigue damage, on the other hand, increased less than 1% when compared to the Current Climate scenario. It should be noted that this outcome may be associated with the fact that this scenario only considered the weakening of the subgrade due to the flooding and did not account for any stiffness reduction in the base, sub-base, and asphalt concrete layers. In an actual flood event, however, those layers may also get affected, which will most likely increase fatigue damage as well as rutting. The results from Scenario 2 are presented in Figure 5.31 and Figure 5.32.

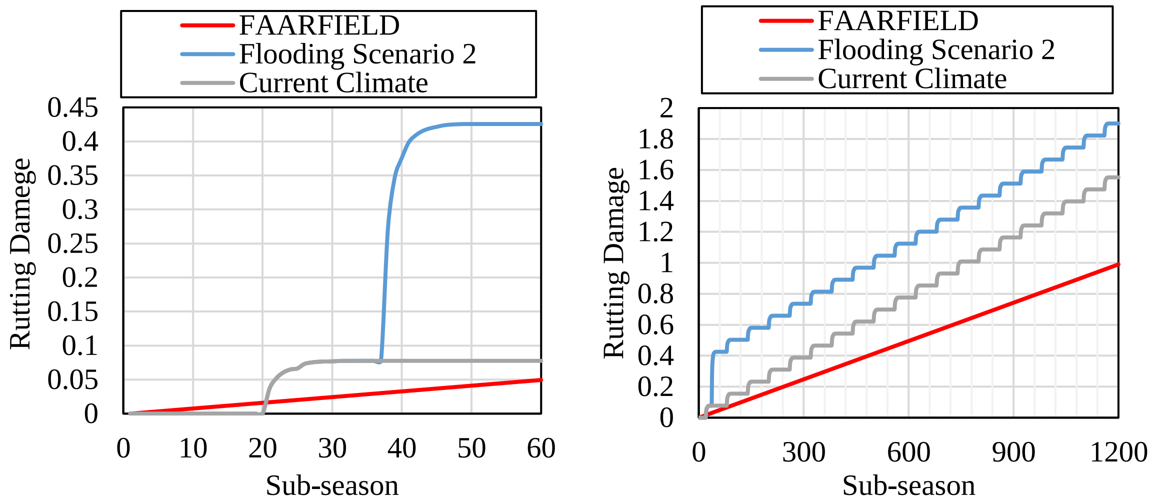

Figure 5.31: Cumulative rutting damage (a) over one year (b) over 20 years.

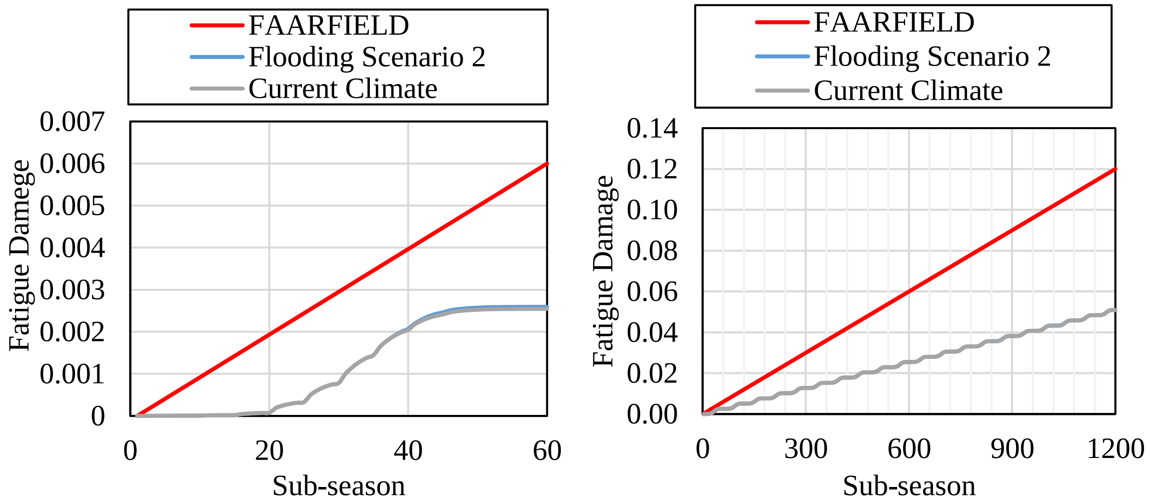

Figure 5.32: Cumulative fatigue damage (a) over one year (b) over twenty years.

In this scenario, the total rutting damage at the end of year 1 was 0.43, as can be seen in Figure 5.31 (a), which is equivalent to 8.7 years of damage under normal circumstances (CDF=0.99 over 20 years). It can be noted in Figure 5.29 (b) that the rutting damage over 20 years was accounted at 1.90. The rutting damage under the flooding event Scenario 2 is 22% higher than the damage computed at the Current Climate scenario and 92% higher than the damage predicted by the traditional FAARFIELD method. The yearly fatigue damage under the flooding Scenario 2 was less than 1% higher than the damage predicted by the Current Climate scenario. Such results are consistent with flooding Scenario 1, in which the flooding event presented a neglectable increment to the fatigue CDF.

5.6 Discussion

The cumulative rutting and fatigue damages, as well as the predicted service life from all scenarios evaluated in this study are summarized in Table 5.22. For a better understanding, a summary of the rutting damage and predicted service life are also presented in a graphical format in Figure 5.33 and Figure 5.34.

Table 5.22: Damage and Predicted Service Life Summary.

Climate Scenarios	**Fatigue**		**Rutting**			**Predicted Service Life**
	Fatigue Damage	**% Difference to "Current Climate"**	**Rutting Damage**	**% Difference to FAARFIELD**	**% Difference to "Current Climate"**	
FAARFIELD	1.200E-01	-	0.99	-	-	20.0
Current Climate	5.068E-02	-	1.55	57%	-	12.8
Temperature Increase	7.235E-02	42.8%	1.95	97%	25%	10.2
Lower Matric Suction	5.074E-02	0.1%	3.37	240%	117%	5.9
Flooding Event 1	5.070E-02	0.04%	1.80	82%	16%	11.0
Flooding Event 2	5.074E-02	0.1%	1.90	92%	22%	10.4

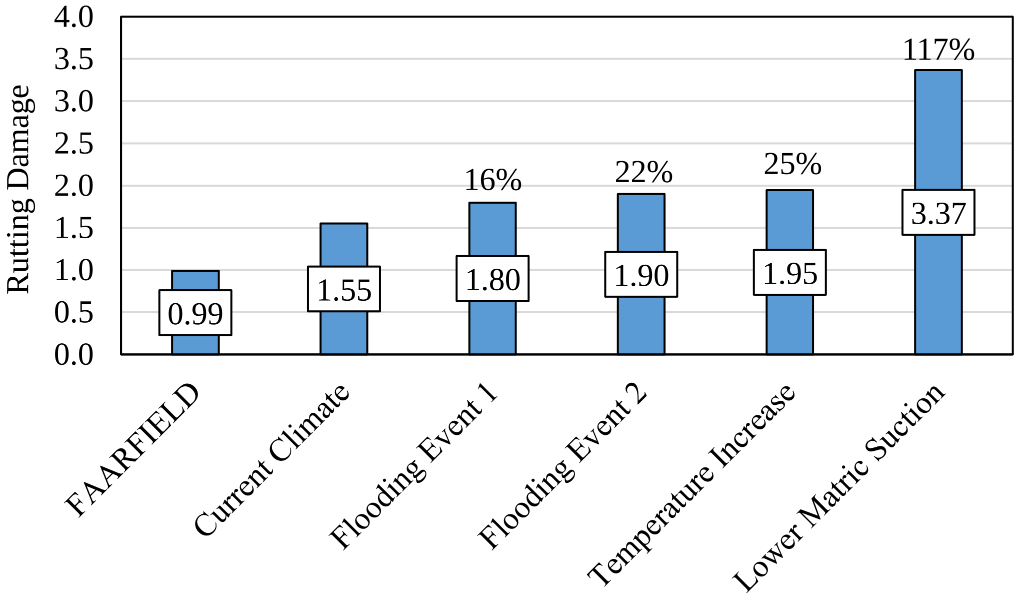

Figure 5.33: Rutting damage predicted for all scenarios

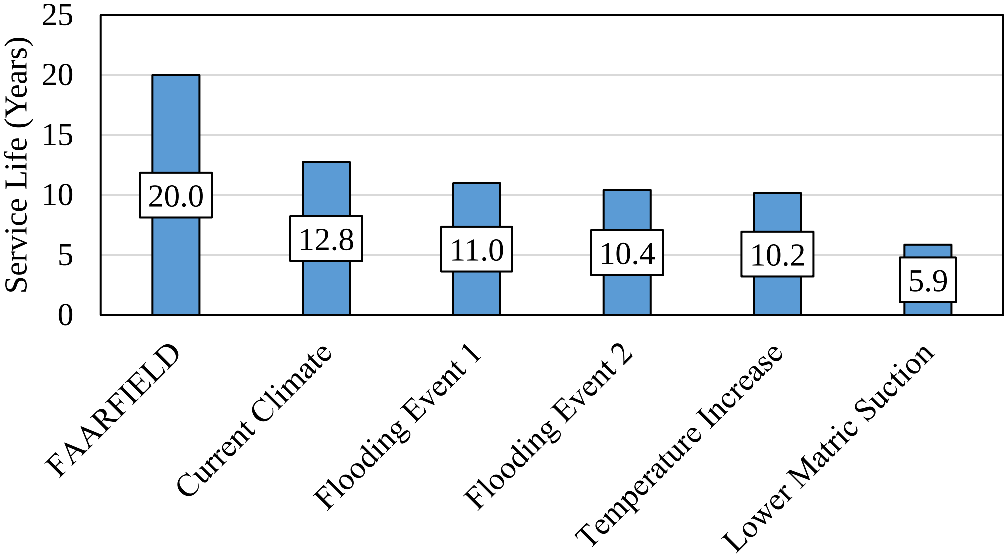

Figure 5.34: Service Life predicted for all scenarios

Aside from the thermal-induced fatigue damage, the fatigue CDF estimated through the proposed methodology in all the scenarios was found to be smaller than the total damage estimated from the traditional FAARFIELD analysis. This can be explained in light of the fact that FAARFIELD considers that the AC stiffness is constant throughout the year and equivalent to the value at the temperature of 32°C, however, the damage during the colder seasons was calculated to be much lower since the pavement layers are frozen during this time. Among all climate change scenarios evaluated, fatigue damage seemed to be little affected by changes in soil saturation, which is present at the "Lower Matric Suction" scenario, and "Flooding Events". However, the effects of the "Temperature Increase" scenario presented fatigue damages that are 43% higher than the "Current Climate" scenario.

All the scenarios demonstrated a higher rutting damage than what was predicted through FAARFIELD. The "Current Climate" scenario was based on the past temperature data from the years of 2010 to 2019 and a matric suction of 293 kPa, and it resulted in a rutting damage that was 57% higher than what was estimated through FAARFIELD, with a service life that was 7 years shorter. The effects of higher temperature under the "Temperature Increase" scenario showed rutting damages that were 25% higher and a service life that was 2.6 years shorter than the "Current Climate" scenario. By comparing the impacts of temperature increase in rutting and fatigue damage, when the scenario is not associated with changes in moisture, it is possible to conclude that a potential rise in temperature due to climate change can be more critical in terms of fatigue damage. It is important to note that this scenario simulated temperature predictions corresponding to the year of 2050, with average temperatures being about 5°C above the current climate scenario.

The flooding scenarios 1 and 2 showed an increase in rutting damage of 16% and 22% when compared to the "Current Climate" analysis. Scenario 2 exhibited greater impacts since it considered a slower matric suction recovery rate after flooding. The pavement service life could be reduced to 11 years in Scenario 1 and 10.4 years in Scenario 2 if no rehabilitation measures are taken after the event.

From the results of different climate change scenarios, it could be recognized that the highest rutting damage happened due to the lower matric suction scenario. A lower matric suction directly affects the saturation levels and lowers the subgrade stiffness, especially during the recovery season. The results showed that the decrease in the matric suction could increase damage in the order of about 117% when compared to the "Current Climate" scenario and decrease the pavement service life down to only six (6) years.

In light of the results of the "Lowe Matric Suction" scenario, it is important to consider that the matric suction can vary along the year due to variations in rainfall, evapotranspiration, ground water table levels and pumping of wells, and it is difficult to predict if the suction will rise or decrease in a certain region, due to the effects of climate change. Although there is strong evidence of the rising temperature and increasing incidence of extreme weather events such as flooding in Canada, it would be hard to make predictions about future matric suction levels. If an airport goes through a significant rise in the subgrade saturation levels in the future, the airport authorities would typically have to take measurements and attempt facilitating the drainage of the excess water in a more efficient way, or to enhance the pavement structure, or impose operation limitations for certain periods of time.

5.7 Summary

This research chapter implemented the methodology proposed toward the structural design of a flexible airport pavement to account for the climate-induced impacts on the predicted pavement performance. The methodology was applied to the case study of the Pearson International Airport, using actual field data. To assess the possible effects of climatic parameters and climate change on the airport pavement performance, first, the methodology was cross-verified by the design of a flexible pavement structure using FAARFIELD to ensure that a total CDF=1 was achieved. Then, the same layer thickness resulting from the FAARFIELD design was used to evaluate current climate and climate change effects on the CDF of the most critical aircraft (i.e., B777-300 ER) from the traffic fleet mix operated at the airport. A total of five scenarios were evaluated throughout the research, including the Current Climate, Temperature Increase, Lower Matric Suction, and two Flooding Events.

The results of the proposed design method showed that the traditional FAARFIELD analysis can possibly overestimate fatigue damage, and underestimate rutting damage. The outcomes also show that climate change can increase pavement damage and shorten the pavement service life in ranging from 7 to 14 years in the scenarios evaluated. Considering the variations in climatic conditions due to the climate change, the proposed methodology can yield major benefits in terms of quantifying these impacts, which can ultimately help with design of more resilient transportation infrastructure such as airfield pavements. This platform enables accounting for climate variations, temperature increase and extreme events such as flooding in the design of flexible airport pavements.

Chapter 6: Frost and Thaw Considerations

Two main analyses were performed in this section. First, the results from MTO, MTQ and TCCA methods were compared with frost depth measured from the field data. Second, the analysis evaluated the impacts of climate change projections on frost penetration, frost heave and thaw depth in several Canadian Airports.

In the first analysis, the field data was obtained mainly from the Long Term Pavement Performance (LTPP) database and includes nine cities located in Canada and the United States. Among the evaluated cases under the first analysis, only one case (i.e., St. Célestin, QC) was not obtained from the LTPP database, rather through the published data from Boutonnet & St-Laurent (Boutonnet, Savard, Lerat, St-Laurent, & Pouliot, 2003). The field data was then compared to the frost penetration depths calculated according to each site's freezing index, in the case of the MTO and TCCA, and soil characteristics, in the case of the MTQ.

In the second analysis, a total of ten Canadian airports were evaluated. The selected locations represent different climate scenarios within the country and compare how differently climate change can impact frost/thaw penetration depth in those cities. Table 6.1 shows the locations evaluated in each analysis.

Table 6.1: Locations evaluated in analysis I and II.

Analysis I	**Analysis II**
Canada: • Winnipeg, MB • Viscount, SK • Beatrice, ON • St. Célestin, QC USA • New Haven, VT • Bemidji, MN • Great Falls, MT • Hamlin, NY • Virden, MB	Not underlain by permafrost • Toronto Airport (YYZ) • Montréal International Airport (YUL) • Québec City International Airport (YQB) • Calgary International Airport (YYC) • Regina International Airport (YQR) • Winnipeg International Airport (YWG) Underlain by Permafrost • Yellowknife Airport (YZF) • Iqaluit International Airport (YFB) • Baker Lake Airport (YBK) • Cambridge Bay Airport (YCB)

It is important to note that Toronto, Montreal, Quebec, Calgary, Regina and Winnipeg International Airports are located in the regions not underlain by permafrost. On the other hand, Yellowknife Airport is located in the discontinuous permafrost zone, and Iqaluit, Cambridge Bay and Baker Lake Airport are located in the continuous permafrost zone. For the airports over the discontinuous and continuous permafrost zones, the depth of thaw penetration was evaluated, while the airports over the unfrozen zone were evaluated over the frost penetration depth and frost heave perspectives.

In the first analysis of this study, the rigorous freezing index (used in the MTQ methodology) was considered to be the same as the normal freezing index. In the second analysis, the rigorous freezing index was determined through Equation 3.53.

6.1 Analysis I: Methods Comparison

The field data includes four cities located in Canada and five cities located in the USA. Table 6.2 shows the field data, including the section ID according to the LTPP website, the year in which the frost depth data was collected, the closest city to the data collection point and the maximum frost penetration depth recorded in the referred year. The last two columns of the table include the Annual Mean Temperature (AMT, ℃) and the Air Freezing Index (FI, ℃*days), for which the raw data was obtained through Environment Canada (Government of Canada, 2021) for the cases in Canada and the National Solar Radiation Database (NSRDB) (National Solar Radiation Database (NSRDB), s.d.) for the cases in the USA. The AMT was calculated considering the annual mean temperature from the two years referenced in column 2 of Table 6.2.

Table 6.2: Field Data.

ID	Year	Soil Description	Closest City	Frost Depth (cm)	AMT (℃)	FI ℃*days
83_3802	93/94	Fat Inorganic Clay	Winnipeg, MB	178	2.60	1775
87_1622	96/97	Sandy Silt	Beatrice, ON	152	4.78	921
-	98/99	Silty Clay	St. Célestin, QC	130	5.10	666
50_1002	02/03	Poorly Graded Gravel with Silt and Sand	New Haven, VT	177	11.00	963
27_6251	02/03	Poorly Graded Sand with Silt	Bemidji, MN	178	4.58	1339
30_0114	03/04	Poorly Graded Sand with Silt	Great Falls, MT	76	8.25	486
36_0801	03/04	Silty Sand	Hamlin, NY	71	4.25	1170
83_1801	02/03	Silty Sand	Virden, MB	178	9.08	461
90_6405	95/96	Fat Inorganic Clay	Viscount, SK	177	2.75	1607

All locations shown in Table 6.2 are asphalt concrete surfaced pavements, and the n-factor was assumed to be 0.9 for all pavements. The frost penetration varies from 71 to 178 cm, Hamlin having the smallest and Winnipeg the highest frost penetration depth. Hamlin also showed the smallest Freezing Index among all cities, while the highest FI was attributed to Viscount. Table 6.3 presents the pavement structure for each site, subgrade soil description, and soil classification according to the Unified Soil Classification System (USCS).

Table 6.3: Pavement Structure and Subgrade Type.

Closest City	**Pavement Structure: Material (thickness in cm)**	**Soil Type**	**Soil Class**
Winnipeg, MB	AC (15.24) Concrete (24.89) Granular (12.446) Granular (14.986)	Fat Inorganic Clay (CH)	CH
Beatrice, ON	AC (14.48) AC (11.68) Granular (17.02) Granular (66.80)	Sandy Silt (ML)	ML
St. Célestin, QC	AC (18) Granular (30) Granular (42)	Silty Clay (CL)	CL
New Haven, VT	AC (7.62) AC (13.97) Granular (65.53)	Poorly Graded Gravel with Silt and Sand (GM)	GM
Bemidji, MN	AC (8.64) AC (14.73) Granular (25.91)	Poorly Graded Sand with Silt (SP)	SP
Great Falls, MT	AC (19.05) Granular (31.50)	Poorly Graded Sand with Silt (SP)	
Hamlin, NY	AC (3.05) AC (9.65) Granular (21.34)	Silty Sand (SM)	SM
Virden, MB	AC (11.18) Granular (14.22) granular (33.53)	Silty Sand (SM)	
Viscount, SK	AC (15.49) Granular (22.86) Sand Asphalt (6.35)	Silty Sand (SM)	

The complete dataset used for frost depth calculations for St. Célestin site can be found at Boutonnet & St-Laurent, 2003 (Boutonnet, Savard, Lerat, St-Laurent, & Pouliot, 2003). Figure 6.1 shows the comparison between frost depths obtained from field data with those predicted using the MTO, MTQ and TCCA methods. The subgrade soil classification is indicated under each city's name in this bar chart.

When reviewing the fine-grained soils, the results show that MTO's method overestimates the frost depth penetration by 18% for the fat clay (CH) soil type, while it results in about 6% and 10% underestimation in the Sandy Silt (ML) case and Silty Clay (CL) case, respectively. The method also underestimated frost depth by 17% in the case of the poorly graded gravel (GM) and overestimated by 28%, 12% and 37% in the cases of the Silty Sands (SP and SM). For the poorly graded sand soil type, MTO's method overestimated frost depth prediction by 24% in the Great Falls site but could almost perfectly predict the value for the case of Bemidji in Minnesota.

Comparing the results obtained by the TCCA and MTO method, it can be concluded that regardless of the soil type, the two methods consistently provide either an overestimation or underestimation of the frost penetration depth, which can be considered relatively similar to each other. More specifically, TCAA method overestimated the frost depth penetration by 27% for the CL soil, underestimated it by 4% and 12% in the ML and CL. In the case of the poorly graded sands available in Bemidji and Great Falls sites, TCCA overestimated frost depth by 5% and 17%, respectively, while for the poorly graded gravel in New Haven site it underestimated this value by 15%. Furthermore, the TCCA results exhibited overestimation in predicting the frost depth in the range 19% to 48% in the cases of the Silty Sands in Hamlin and Virden.

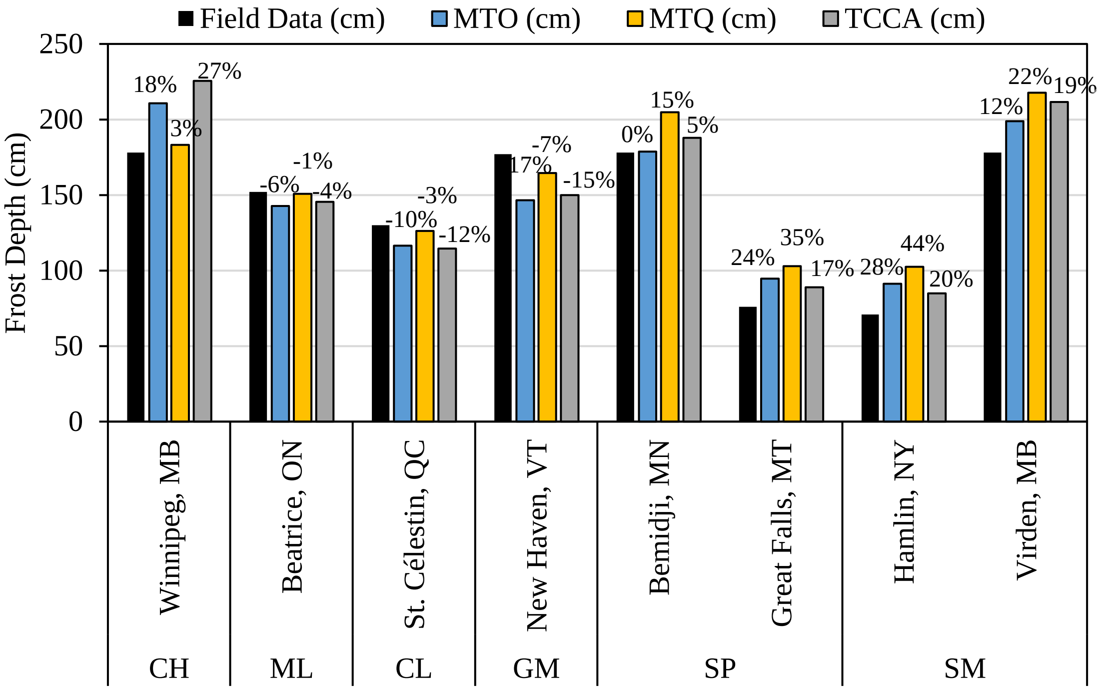

Figure 6.1: Comparison between frost depth field data and prediction methods.

Finally, the MTQ method showed either close to field data or more conservative protection depths in most cases. The only case among those evaluated where the method underestimated frost depth is the GM soil from New Haven, Vermont (-7%). The MTQ method showed the best results within clays, silt, and gravel, with a difference of 3%, -1%, and -3% in cases of the fat clay, sandy silt, and silty clay soil types, which can all be considered relatively very close to the actual measured depths in the field. In terms of the difference in magnitude between the predicted and measured field frost depths, the worst-case scenarios were regarding the sites with silty sands and poorly graded sands, with values being overestimated in the range of 15% to 44% higher than the field measured data. While this is still on the safe side for the purpose of frost protection, such overestimation can lead to overdesigned sections and consequently resulting in unnecessary increase in the pavement construction costs. Nevertheless, the results indicate that MTQ method provides better estimation of the required frost protection for the case studies investigated in this research.

Table 6.4 shows a general comparison between the three methods investigated in this research, along with their maximum and minimum differences when compared with the data measured from the field, as well as the average difference and the standard deviation, considering all values as positive.

Table 6.4: Comparison between methods with reference to the measured field data.

Soil Type	**Course**			**Fine**		
Method	**MTO**	**MTQ**	**TCCA**	**MTO**	**MTQ**	**TCCA**
Min	0%	7%	5%	6%	1%	4%
Max	28%	44%	20%	18%	3%	27%
Standard Deviation	10%	13%	5%	6%	1%	11%
Average Difference	20%	28%	21%	12%	2%	14%

From Table 6.4 it is evident that all the methods provided more accurate results when predicting frost depth of the fine soils. Under the fine soil scenario, the MTQ had the smallest average difference (2%), and a small standard deviation (1%). On the other hand, under the course soil scenario, the MTO had the smallest average difference among the methods (20%), however, the TCCA was not far behind (21%). Regardless of the magnitude differences, the MTQ method provided the most prudent results in terms of rarely underpredicting the frost depth for all the evaluated scenarios.

6.2 Analysis II: Climate Change Scenarios

The parameters needed for the Analysis II were the average annual air temperature (aka Annual Mean Temperature or AMT), the air Freezing Index (*FI*) and Thawing Index (*TI*), soil geotechnical inputs, soil thermal conductivity inputs and the air-surface transfer coefficient. These parameters are further described in Table 6.5 and Table 6.6.

The historical values for the annual mean temperature and the air freezing/thawing indexes were calculated from data available at the Government of Canada website, considering the years from 2012 to 2021 (10-year average) (Government of Canada, 2021). The climate predictions for the year of 2041 and 2061 were obtained though the Climate Atlas of Canada website (Prairie Climate Centre, 2022).

The primary source of Climate Atlas of Canada models is the Pacific Climate Impacts Consortium (PCIC), which has projections of daily temperature data from an ensemble of 24 climate models using two carbon emission scenarios, a “Low Carbon” (RCP 4.5) and a “High Carbon” (RCP 8.5) future scenario. This research considered the ensemble mean of emission scenario RCP 8.5, to perform the climate change simulations.

There is a large amount of uncertainty in climate model projections because the future concentration of greenhouse gases in the atmosphere are not known or predictable in a deterministic manner. For this reason, Canada’s Changing Climate Report says that no likelihoods should be ascribed to the RCP scenarios, as they are all deemed plausible (Environmnet and Climate Change Canada, 2019). The historical and predicted temperature records and freezing indices are presented in Table 6.5.

Table 6.5: Average annual air temperature and air freezing index.

Airport	**AMT**	**AMT 2041**	**AMT 2061**	**FI or *TI**	**FI or *TI 2041**	**FI or *TI 2061**	**Temp. Change 2041**	**Temp. Change 2061**
Toronto (YYZ)	9	11	12	426	252	166	2	3
Montreal (YUL)	8	9	10	758	551	420	1	2
Quebec (YQB)	5	6	8	1144	818	642	1	3
Calgary (YYC)	5	6	7	857	754	675	1	2
Regina (YQR)	3	5	6	1560	1231	1105	2	3
Winnipeg (YWG)	3	5	7	1674	1317	1133	2	4
Yellowknife (YZF)	-4	-1	0	1860*	2099*	3273*	3	4
Iqaluit (YFB)	-8	-6	-4	666*	1015*	1355*	2	4
Baker Lake (YBK)	-10	-7	-6	986*	1474*	1639*	3	4
Cambridge Bay (YCB)	-13	-10	-8	683*	1035*	1310*	3	5

AMT - Annual Mean Temperature (℃), FI - Freezing Index (℃*days)
*TI - Thawing Index (℃-days), Temp. Change - Temperature Change (℃)

It is noticeable that the northern cities such as Yellowknife, Iqaluit (YFB), Baker Lake (YBK) and Cambridge Bay have higher predicted temperature changes, Cambridge Bay presenting the worst-case scenario with a temperature increase of 5℃ in 2061.

To evaluate frost penetration using the MTQ methodology the soil classification and properties need to be known. To that end, two soils were chosen: a Clay (CL) and a Clayey Silt (ML, ML-CL) soil. The parameters defined for the Clay and Clayey Silt soils are presented in Table 6.6.

Table 6.6: Geotechnical and thermal conductivity parameters (Doré, et al., 2019).

Soil	**Geotechnical parameters**				**Thermal conductivity parameters**						
	ρ_S (kg/m^3)	ρ_d (kg/m^3)	w (%)	S_S (m^2/g)	k_S (W/m.℃)	χ (W/m.℃)	η	k_u	k_f	a (MPa^{-1})	SP_0 (mm^2/°K.H)
CL	2750	1300	34	60	2.9	1.7	1.8	1.9	0.9	7.0	5.0
ML	2700	1450	30	40	2.9	1.7	1.8	1.9	0.9	7.0	8.0

Where,

- ρ_S = density of soil solids (kg/m^3)
- ρ_d = dry density (kg/m^3)
- w = water content (%)
- S_S = specific surface area of fine particles (m^2/g)
- k_S = thermal conductivity of soil solid particles (W/m.℃)
- χ = material parameter that considers the effect of the particle shape (W/m.℃)
- η = material parameter that considers the effect of the particle shape (no unit)
- k_u = granularity factor for unfrozen thermal conductivity
- k_f = granularity factor for frozen thermal conductivity

- a = overload coefficient (MPa^{-1})
- SP_0 = segregation potential without vertical load (mm^2/°K.H)

The geotechnical and thermal conductivity parameters are used to calculate the degree of saturation (S_r), latent heat of fusion (L_f), unfrozen and frozen thermal conductivity (k_u and k_f).

6.2.1 TCCA Method

The TCCA manual requires the calculation of the frost penetration of asphalt surfaced pavements to be done through Equation 3.50, while the penetration of thaw in permafrost areas should be calculated using Equation 3.54. The results of the frost depth and thaw penetration using this model for the different Canadian regions in this study can be seen in Figure 6.2 for the areas not underlain by permafrost and Figure 6.3 for the areas underlain by permafrost, respectively.

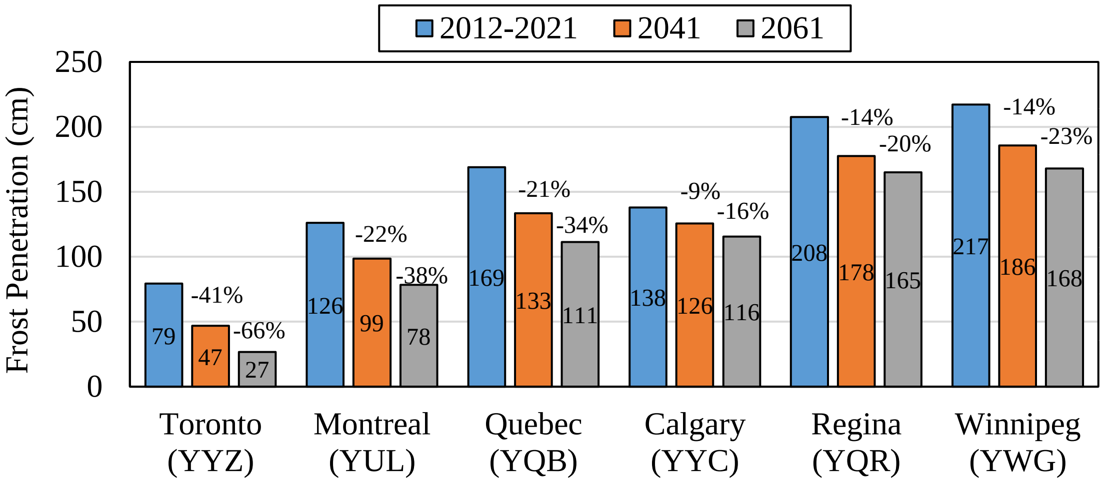

Figure 6.2: Frost Penetration - TCCA

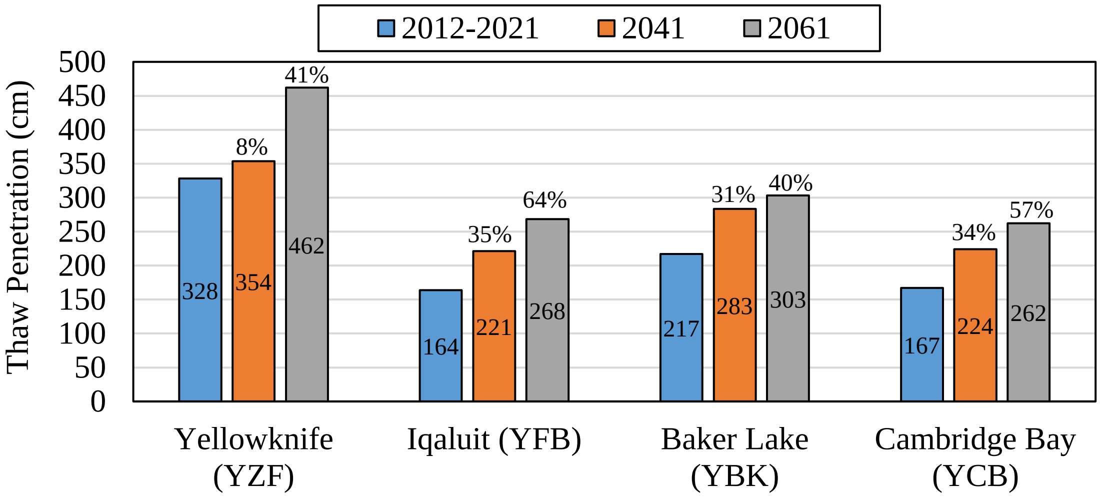

Figure 6.3: Thaw Penetration Depth – TCCA

The results of historical frost penetration range from 79 cm to 217 cm, with Toronto having the smallest and Winnipeg exhibiting the highest frost depth. The maximum percentage of variation in the climate change scenarios are, therefore, expected to happen in Toronto (i.e., -41% and -66%) while it is predicted that Calgary would experience the least level of changes (i.e., -9% and -16%).

It is important to note that among the airports underlain by permafrost, Cambridge Bay and Baker Lake Airports are constituted of gravel runways, while Iqaluit and Yellowknife airports have asphalt surfaced runways. Since the TCCA equation for thawing depth was derived from experiments in gravel runways, the analysis of Iqaluit and Yellowknife can be affected by generalization of the method applicability.

6.2.2 MTO Method

Figure 6.4 presents the frost penetration depth calculated through the MTO methodology. Using this method, the results of historical frost penetration for the analyzed cities range from 87 cm to 204 cm, with Toronto having the smallest and Winnipeg the highest frost penetration depth. Figure 6.4 indicates that Calgary exhibited the smallest decrease in frost penetration depth under both climate change scenarios with a projected reduction of 8 and 14%, while Toronto had the largest projected frost penetration reduction (i.e., a reduction of 32 and 52% at 2041 and 2061, respectively).

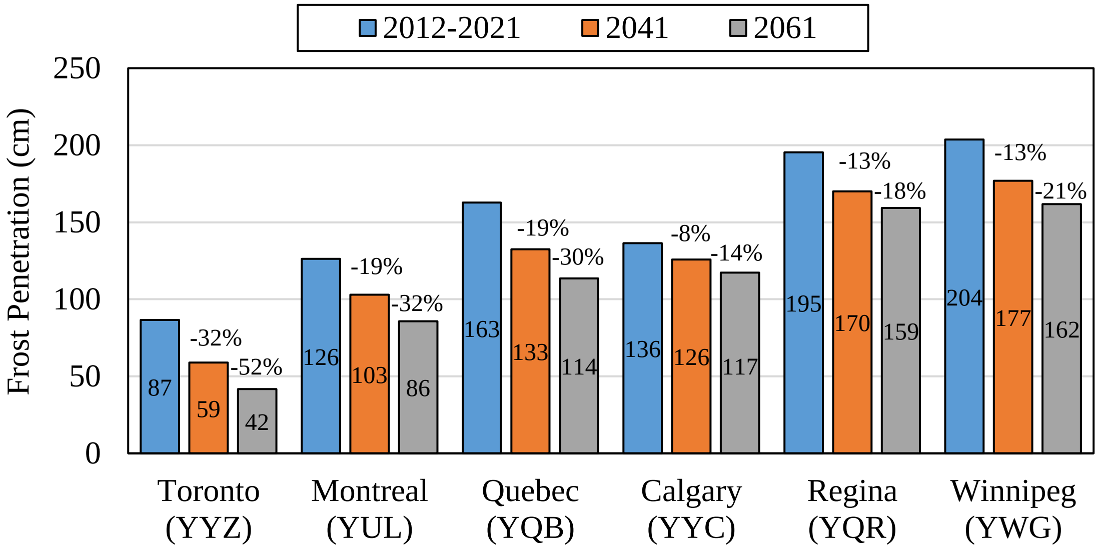

Figure 6.4: Frost Penetration Depth - MTO.

6.2.3 MTQ Method

In this section, MTQ method was used to evaluate the climate change scenarios at horizon times of 2041 and 2061 for different soil types and locations. The results of the frost penetration depth and frost heave for the Clay soil were calculated using the i3c-me tool and are presented in Figure 6.5 and Figure 6.6, respectively.

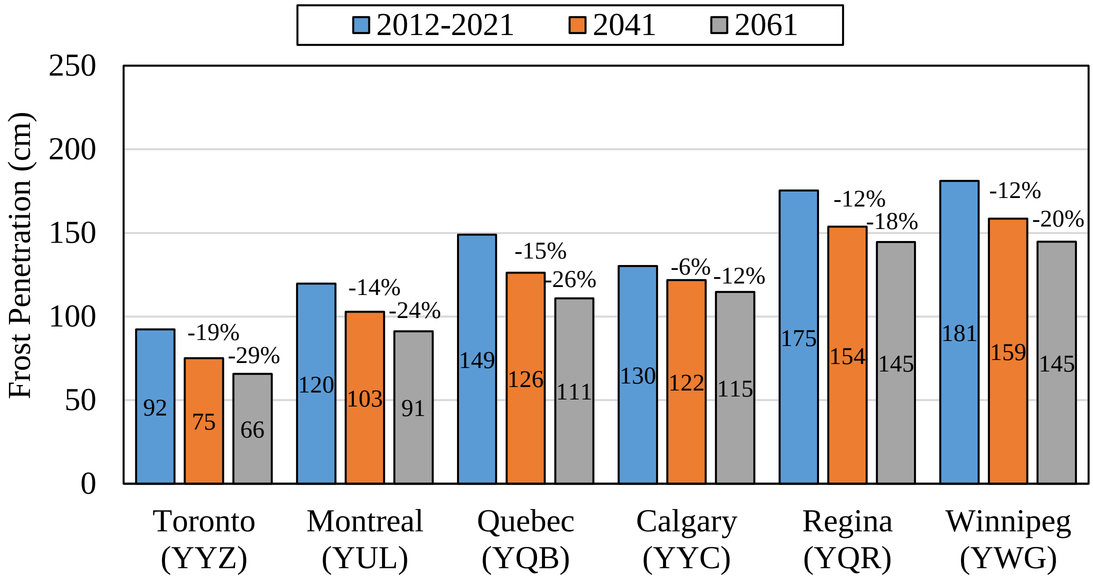

Figure 6.5: Frost Penetration Depth – MTQ, Clay.

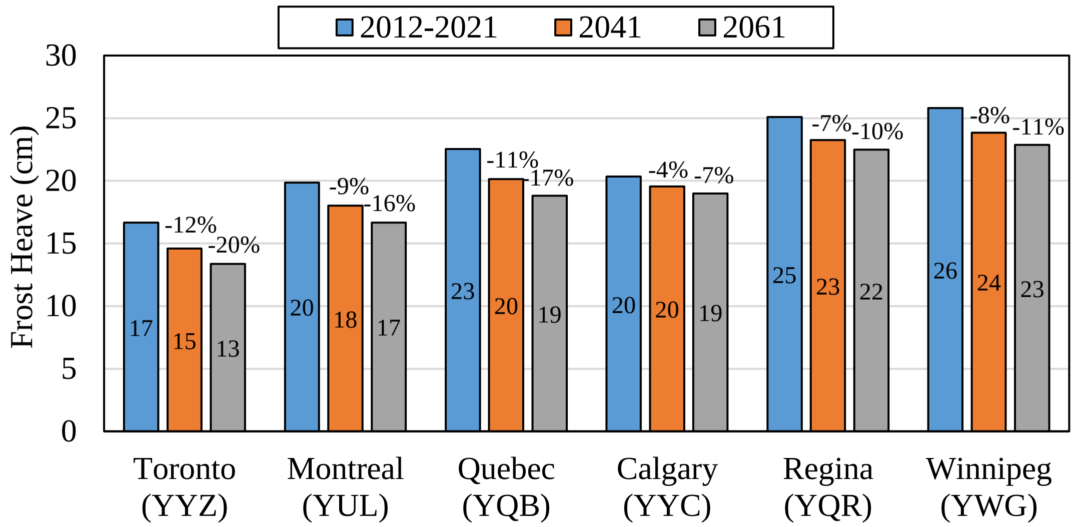

Figure 6.6: Frost Heave – MTQ, Clay.

Figure 6.5 shows that the historical frost penetration depth calculated through the MTQ method ranges from 92 cm to 181 cm, where Toronto shows the smallest while Winnipeg exhibits the highest frost depth. Calgary had the smallest percent decrease in frost penetration depth in both climate change scenarios (-6% and -12%), while Toronto had the greatest (-19% and -29%). On the other hand, as shown in Figure 6.6, the historical frost heave calculated for the selected locations in this study ranges from 17 to 26 cm. Similar to frost penetration depth calculations, Toronto showed the smallest and Winnipeg showed the highest frost heave values. Furthermore, the climate change scenarios show that Calgary may experience the smallest percent decrease in frost heave (-4% and -7%), while Toronto may undergo the highest (-12% and -20%).

The results of frost penetration depth and frost heave for the Clayey Silt (ML, ML-CL) soils are presented in Figure 6.7 and Figure 6.8, respectively.

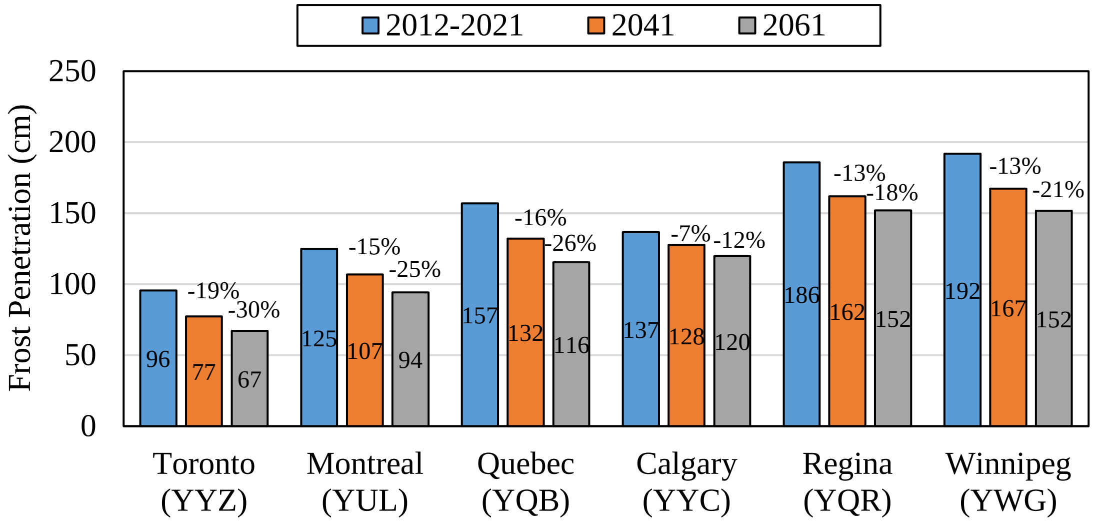

Figure 6.7: Frost Penetration Depth – MTQ, Clayey Silt.

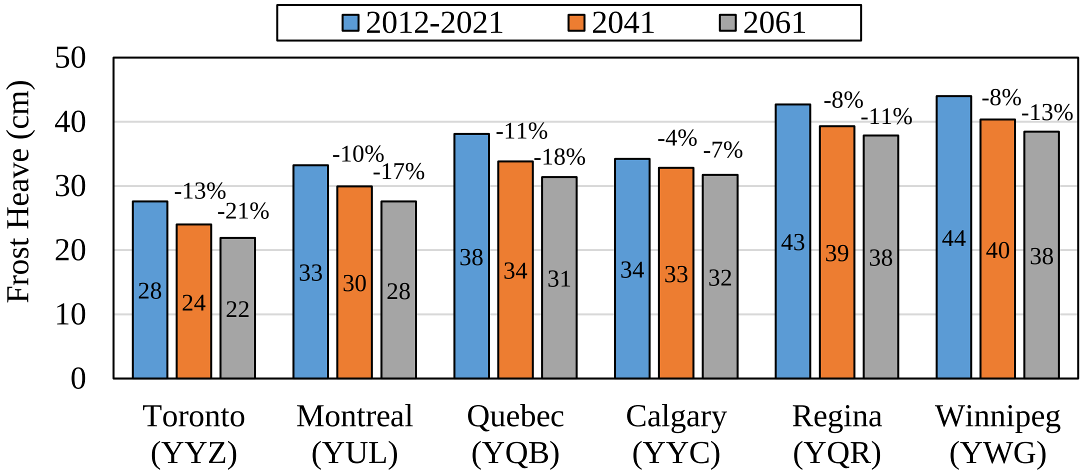

Figure 6.8: Frost Heave – MTQ, Clayey Silt.

In the results presented at Figure 6.7, the historical frost penetration depth ranges from 96 cm to 192 cm, Toronto having the smallest and Winnipeg the highest frost depth. Again, Calgary had the smallest percent decrease in frost penetration depth in both climate change scenarios (-4% and -7%), while Toronto had the greatest (-13% and -21%).

Figure 6.8 shows that the frost heave that was calculated based on historical data ranges from 28 to 44 cm, Toronto having the smallest and Winnipeg the highest frost heave. The climate change scenarios shows that Calgary had the smallest percent decrease in frost heave (-4% and -7%) while Toronto had the highest (-13% and -21%). Figure 6.9 compares the frost heave calculations for the Clay and a Clayey Silt soil in the historical scenario.

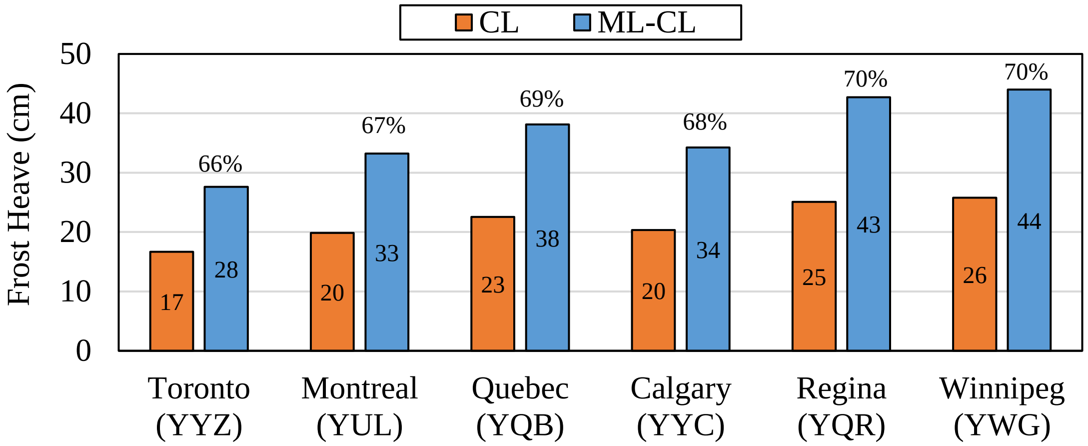

Figure 6.9: Frost heave predictions for a Clay and a Clayey Silt soil.

When comparing frost heave from the clay to the clayey silt soil it is possible to note a great difference. The frost heave calculated for the clayey silt was in average 69% higher than what was calculated for the CL soil. This is because silts are considerably more susceptible to frost heave than clays, in general.

6.3 Discussion

It can be observed from comparing the different frost depth calculation methods in this study that all of them yield better accuracy when predicting frost depth of fine soil types such as clays and silts. Under the fine soil scenario, the MTQ method matched the field data the best; however, it resulted in a considerable overestimation of the frost penetration for the case of the coarse soil scenarios. This can be attributed to the fact that the method's accuracy strongly depends on the material properties as the model inputs. The segregation potential of the subgrade is crucial for determining the frost penetration depth, and the results can be highly biased if incorrect values are used. The author of this research believe that availability of laboratory data regarding the materials could have improved the accuracy of the results for the coarse materials.

Both the MTO and TCCA methods are primarily empirical approaches. Comparing the two methods, MTO performed better than the TCCA model. The results from the MTO analysis also had better accuracy when predicting frost depth of fine soils. As previously explained, the equation used by MTO to estimate frost penetration depth is based on an empirical method and was established through observations made for several highways across Ontario. Consequently, this model is more representative of the frost penetration through the soils that are present in the region (Ministry of Transportation of Ontario, 2013). Nevertheless, due to the empirical nature of both MTO and TCCA models, the method's applicability to various soil types may be limited since they do not account for the specific soil properties. However, both are still very practical approaches to estimate the frost penetration when no information is available about the soil properties.

The climate change predictions for the next 40 years, considering emission scenario RCP8.5, show an increase of up to 5^{o}C in the annual mean temperature and a noticeable decrease in the freezing index for the cities evaluated in this research. The results from all methods indicate that there will be a decrease in frost penetration depth due to climate change that ranges from 12% up to 66%. Frost heave will most likely decrease in all areas not underlain by permafrost, with decline rates that range from 7% to 30%. On the other hand, the thaw penetration projection results show that the cities underlain by permafrost will suffer from an increase in the seasonal active layers depth, since thawing depth will likely increase within a range of 40% to 64% in 2061. It should be emphasized that although such increments might seem modest, soil temperatures in permafrost layers are already close to zero and hence can be highly vulnerable to thawing. In other words, it is important to note that temperature fluctuations around 0^{o}C — as typical freezing temperature for water — could increase the frequency of freeze/thaw cycles and potentially pose further issues with respect to bound pavement materials durability as well.

6.4 Summary

The implications of the shortening of winter seasons for frost and thaw penetration depths and frost heave in Canadian Airports were presented in this chapter. A total of three methodologies proposed by the Ministry of Transportation of Ontario (MTO), the Ministère des Transports du Québec’s (MTQ) and Transport Canada Civil Aviation (TCCA) were evaluated. The following conclusions can be drawn based on the results of this case study:

- From comparing the frost penetration predictions with the actual field measurements, it can be concluded that both the empirical (i.e., MTO and TCCA) and mechanistic (i.e., MTQ) models performed considerably better in case of finer grained soil types, rather coarse subgrade soils. The MTQ model resulted in the highest accuracy.
- The climate change simulation using RCP8.5 for horizon times 2041 and 2061 shows that the warming climate impacts on areas underlain by permafrost should be considered differently than those not underlain by permafrost since changes to the active layer thickness becomes the main concern due to the projected thaw penetration in the former case.
- Both MTO and TCCA methods provide consistent trends of frost penetration prediction for the airport sites investigated in this study when compared with the measured field data. However, due to the climate change impacts and the empirical nature of these methods, moving towards more mechanistic approaches that can account for actual soil properties would be a necessity to avoid overdesigning pavements in non-permafrost areas or under-designing in case of the airports underlain by permafrost.

It is suggested that future research on this matter broaden the number of sites evaluated to include more divers soil types and climate regimes outside North America and simulate more climate change scenarios. The results of this study also indicate the need for including more specific soil properties and ideally utilizing measured values to enhance the reliability of climate change impacts projection through the use of mechanistic models.

Chapter 7: Conclusions, Contributions, and Recommendation for Future Work

7.1 Conclusions

Airport pavement structures have been experiencing shorter service lives and an increase in need for maintenance due to climate change impacts. Accounting for the changes in the environmental factors in airport pavement design can be considered a challenge since most of the available airport pavement design methods do not consider even crucial factors such as moisture and temperature variation in their design practices.

The mechanistic empirical methods, FAARFIELD and APSDS, attribute fixed modulus values for the pavement layers over the design life, disregarding the effects of climate variations in the stiffness of the materials. Therefore, it is not possible to assess the damage caused by climate fluctuation in FAARFIELD and APSDS.

The method proposed by Transport Canada ASG-19 is purely empirical. The Transport Canada design method did not directly consider the impacts of new larger aircraft (NLA) such as the Boeing 777 and the Airbus 380, and it does not incorporate recent advances on the mechanics of the materials, which prevents adaptations to account for the implications of climate and climate change on pavement performance. Because of its empirical nature, the method is unable to provide recommendations towards failure modes.

The airport pavement design methods/tools reviewed, i.e., FAARFIELD, APSDS and ASG-19, do not allow its users to consider the effects of climate change. The method proposed by Transport Canada in the ASG-19 manual has recommendations towards frost protection and subgrade bearing strength spring reductions, however, as an empirical method, ASG-19 does not allow for the consideration of changes in moisture and temperature.

The need for adaptation strategies in design methods has motivated this research to develop an enhanced pavement design and analysis framework that can provide benefits in terms of quantifying climate change impacts on pavement performance, which can ultimately help with the design of more resilient airfield pavements in the future.

The proposed methodology was implemented in the case study of the Toronto Pearson International Airport. The proposed method, however, can be applicable to other locations, soil types and traffic conditions, since it guides the designers in a broad way that can be easily implemented in the design of airport pavements in different locations in the world.

The following conclusions are drawn based on the research conducted in this thesis and are presented under four (4) main headlines which correspond to the main focus areas of this research:

Climate Parameters and Pavement Materials

- The increase in temperature can affect the asphalt mix stiffness, causing an increase in rutting and fatigue when the pavement is loaded under high temperatures.
- The shortening of the freezing season can impact the subgrade frost/thaw conditions, implicating in permafrost thawing and the increase in seasonal active layers over the regions underlain by permafrost.
- The shortening of the freezing season can reduce frost penetration depth and frost heave over the regions not underlain by permafrost.
- The increase in daily thermal oscillations can affect pavement fatigue due to thermal loading.
- The increase in precipitation patterns and flooding events can increase soil moisture conditions, and consequently decrease the subgrade stiffness. This could result in more rutting and fatigue damage to the pavement.

Mechanistic Analysis

A variety of computational tools can be used for mechanistic analysis of airfield pavements. Most computational tools are based on one of the two solutions, the layered elastic analysis (LEA) or the finite element method (FEM). Each type of solution or constitutive model has its advantages and limitations, and the selection of the right modeling method in each case should be based on the level of accuracy that needs to be reached as well as the affordable computational time.

The mechanistic assessment in this thesis integrates the findings of two case studies in which full-scale pavement test sections were compared to numerical and analytical simulations. The first case study compared simulations from two LEA software (i.e., KENLAYER and NonPAS), as well as one finite element software (i.e., ABAQUS), using a purely linear elastic approach. The second case study compared simulations from two layered elastic software (i.e., KENLAYER and NonPAS) as well as one finite element software (i.e., GT-PAVE), using a non-linear elastic approach.

- The results of the two case studies indicated that KENLAYER and NonPAS can have good agreement with field measurements when predicting pavement vertical strains and stresses at the top of the subgrade. However, the calculated vertical displacements can be far from the field measurements (as demonstrated in Case 2).
- The layered elastic analysis would be a good alternative to be used in cases where rutting, and consequently the compressive stress at the top of the subgrade, is the dominant mechanism contributing to the overall pavement performance.
- The results of both case studies show that ABAQUS and GT-PAVE can successfully predict the compressive stresses as well as the vertical surface displacements. In case study 2, GT-PAVE even outperformed the ABAQUS predictions. This points out that although the superposition of pavement responses can lead to some levels of error when nonlinearity of materials is being considered, this approach can still provide relatively accurate results.

- A 2D axisymmetric modelling software can provide relatively accurate results in a much shorter time as compared to a 3D simulation using a general-purpose software. This highlights why the former approach is currently more popular in many design applications, while the latter is utilized mainly in research and when there is a need to further investigate the effect of loading (i.e., contact area, stress distribution, transient characteristics) or materials properties.

Cumulative Damage Analysis

The cumulative damage analysis integrates the findings of five scenarios including the “Current climate”, “Temperature Increase”, “Lower Matric Suction” and two scenarios under “Flooding events”.

- The results of the proposed design method showed that the traditional FAARFIELD analysis can possibly overestimate fatigue damage, and underestimate rutting damage.
- The fatigue damage estimated through the proposed methodology in all the scenarios was found to be smaller than the total damage estimated from the traditional FAARFIELD analysis. This happened because FAARFIELD considers that the AC stiffness is constant over the year, however, the damage during the colder seasons was calculated to be much lower since the pavement layers are frozen during this time.
- Among all climate change scenarios evaluated, fatigue damage was the least affected by changes in soil saturation. However, the effects of the “Temperature Increase” scenario presented fatigue damages that were 43% higher than the “Current Climate” scenario.
- The proposed methodology resulted in higher rutting damage than what was predicted through FAARFIELD for the “Current Climate” scenario. This happened because the damages estimated over the recovering season when the soil is still saturated, accumulated with the damages over the frozen and unfrozen seasons, are higher than the traditional methodology results.
- Comparing the impacts of temperature increase in rutting and fatigue damage, when the scenario is not associated with changes in moisture, it can be concluded that a potential rise in temperature due to climate change can be more critical in terms of fatigue damage.
- The flooding scenarios 1 and 2 showed an increase in rutting damage of 16% and 22% respectively, when compared to the “Current Climate” analysis. It was found through scenario 2 that a slower recover of the matric suction after flooding can significantly increase rutting damage.
- In all climate change scenarios, the highest rutting damage happened due to the lower matric suction. This happened because the matric suction directly affected the saturation levels and lowered the subgrade stiffness especially during the recovery season.
- Changes in the matric suction are difficult to predict. If an airport goes through a significant decrease in the matric suction in the future due to variations in rainfall and ground water table levels, such as the change presented in the “Lower Matric

Suction" scenario, the airport authorities would typically have to take measurements and attempt facilitating the drainage of the excess water in a more efficient way, or to enhance the pavement structure or impose operation limitations for certain periods of time, in order to avoid significant decrease in the pavement design life.

- Climate change can increase pavement damage and shorten the pavement service life in ranging from 7 to 14 years in the scenarios evaluated.

Frost and Thaw Considerations

The considerations on Frost and Thaw conditions integrated two main analyses. The first analysis was a comparison of different methods used to assess frost penetration in pavements with actual field measurements. The second analysis assessed the impacts of climate change projections on frost penetration, frost heave and thaw depth in ten (10) Canadian Airports.

- From comparing the frost penetration predictions with the actual field measurements, it can be concluded that both the empirical (i.e., MTO and TCCA) and mechanistic (i.e., MTQ) models performed considerably better in case of finer grained soil types, rather than coarse subgrade soils.
- Under the fine soil scenario, the MTQ method matched the field data the best; however, it resulted in a considerable overestimation of the frost penetration for the case of the coarse-grained soil scenarios. This can be attributed to the fact that the method's accuracy strongly depends on the material properties as the model inputs.
- Both MTO and TCCA methods provided consistent trends of frost penetration prediction for the airport sites investigated in this study when compared with the measured field data. However, both methods were empirically established through past observations in Canadian sites and may not be representative of other soil types or the changes in climatic conditions.
- The climate change predictions over the next 40 years showed an increase of up to 5^{o}C in the annual mean temperature and a noticeable decrease in the freezing index for the cities evaluated.
- There will be a significant decrease in frost penetration depth due to climate change, and frost heave will most likely decrease in all areas not underlain by permafrost.
- The projections of thaw penetration show that the cities underlain by permafrost will suffer from an increase in the seasonal active layer's depth, since thawing depth will likely increase.

7.2 Contributions

The following list presents the main contributions of this research.

- This thesis performed an overview of the impacts of climate and climate change in flexible pavement materials and identified the most relevant parameters that need to be considered for flexible airfield pavements.

- A critical review of the available airfield pavement design tools/methods was conducted to assess the strengths and limitations in the existing design procedures and their ability to accommodate for climate (change) considerations.
- Four (4) tools (i.e., KENLAYER, NonPAS, ABAQUS and GT-PAVE) available to predict airport pavement responses were compared to field data to assess the accuracy of the results. The holistic view can benefit pavement engineers and researchers by informing them about proper selection of methods/tools to use for their specific cases.
- This research developed an enhanced pavement design and analysis framework to improve the resiliency of flexible airfield pavements in face of the changing climate. The proposed methodology allows for accounting for the combined effect of materials properties, loading, and climatic conditions through a detailed analysis of the pavement responses.
- The impacts of temperature increase, lower matric suction, and flooding events in pavement performance were assessed and quantified using the developed analysis procedure and through a case study. This will facilitate the replication of the proposed method by pavement engineers and designers.
- An evaluation of the existing tools and methods to determine pavement frost/thaw conditions was performed, and recommendations were made towards the suitability of the approaches available and their associated boundary conditions.
- The effects of the shortening of the freezing season in pavement frost/thaw conditions were estimated in ten (10) major airports in Canada.

7.3 Main Research Assumptions and Limitations

The main research assumptions and limitations are the following:

Mechanistic analysis

- In the mechanistic analysis, it was assumed that all AC materials were linear-elastic. The viscoelastic nature of the Asphalt mix was not evaluated, since it would divert from the research focus, and it would have consumed more computational time.
- Non-linear constitutive models were only considered in Case Study 2 of the Mechanistic Analysis chapter.

Cumulative Damage Analysis

- The Witczak sigmoidal function used in this research to model the AC dynamic modulus corresponds to the function used in the original model of the MEPDG, 2004 version. A more recent predictive model was used in newest version of the MEPDG, including the consideration of the shear modulus in the determination of the AC mix stiffness (Bari & Witczak, 2007). The new predictive model was not included in this research.
- To obtain pavement stresses and strains at critical locations, all pavements were modeled assuming that the layer’s interfaces were fully bonded.

- The fleet mix used in the analysis, although realistic for Toronto Pearson Airport, would not represent other airports that don't have similar traffic. In the case of airports that do not have operations of the B777-300 ER, the damage would have most likely been more evenly distributed among the aircrafts in the fleet mix.
- Only the conventional flexible airport pavement (i.e., AC on the top of unbonded granular layers) was considered in the analysis. The results would most likely change if stabilized materials or unconventional structures were used.
- In the temperature increase scenario, only temperature projections under RCP 8.5 were considered. RCP 8.5 refers to a scenario of high emissions of green-house gases. To generate predictions of hourly temperature records the Weather Morph File Generator method was used.
- It was assumed in the flooding scenarios that only the subgrade soil varied in stiffness. Changes in the base and sub-base stiffness were not assessed at this time.

Frost/Thaw considerations

- The analysis of thermal insulation in pavements underlain by permafrost was out of the scope of this thesis.
- In analysis II of the frost and thaw considerations, only temperature projections under RCP 8.5 were considered.

7.4 Recommendations for Future Work

Based on the findings from this research, the following recommendations for future work are proposed:

Mechanistic analysis

- This research has evaluated pavement responses under a few types of materials constitutive models, including the linear elastic and two stress dependent models (Uzan and bilinear). Future research should include other constitutive models such as K-θ, Uzan-Witczak and MEPDG (2004).
- The visco-elastic behavior of bituminous materials should be considered in the numerical models to account for the time and temperature dependency of the asphalt layers, and to achieve better results when predicting horizontal strains.
- The first case study has compared selected software packages with field measurements from three full scale pavement sections, under two (2) loading configurations (therefore, a sample size comparison of six, within each group). The second case study, however, only analyzed one full scale pavement section. Future research should broaden this study to include other pavement sections from the NAPTF experiment.

Cumulative Damage

- To the best of the author's knowledge, there is no closed-form equation that relates the number of Freeze-Thaw cycles, and the AC materials properties and stiffness.

For this reason, it is yet not possible to assertively assess the effects of FT cycles in pavement rutting or fatigue. Therefore, future research should consider testing a large number of AC mixes under the effects of FT cycling to develop equations that can correlate the number of cycles with the stiffness of the material.

- Although a very comprehensive case study was considered in the application of the proposed methodology, it is recommended that future research expands it to other regions in which different soil characteristics and climate zones are present.
- This study considered the effects of climate in the asphalt concrete and subgrade soil material properties only. Future research should assess the effects of temperature and moisture in the base and sub-base layers as well.
- Future research should implement the recent version of the Witczak sigmoidal function to model the AC dynamic modulus, as proposed by Bari & Witczak (2007).
- The models that predict the AC and subgrade modulus were implemented in Python language. The codes were enabled to generate modulus results for pavement sub-layers (i.e., a number of layers within the AC and subgrade). The stratification of the layers, however, would require excessive labor to obtain the pavement stresses and strains (since the LED analysis was done through KENLAYER), and an average resilient modulus for each layer was used instead. Therefore, future research should further investigate the layered elastic design, and the effects that the stratification of the resilient modulus within the layers can have in the analysis.
- Future research should consider pavement material constitutive models that can reflect the stress dependent nature of the granular layers and subgrade. It is recommended that a 2D axisymmetric FEM software is used in this process.

Frost Thaw Considerations

- Even though several Canadian and American sites were evaluated in the frost/thaw analysis, future research should broaden the number of sites to include more diverse soil types and climate regimes outside North America.
- This thesis has considered warming rates corresponding to the gas emission scenario RCP8.5, however, future search should assess the effects of other temperature warming scenarios in pavement frost/thaw conditions.

References

Abreu, E. A. (2019). *Impacts of Climate Change on Canadian Airport Pavements.* University of Waterloo.

Alavi, M. Z., Pouranian, M. R., & Hajj, E. Y. (2014). Prediction of asphalt pavement temperature profile with finite control volume method. *Transportation Research Record*, 96-106.

Ali Shafabakhsh, G., & Kashi, E. (2015). Evaluation of aircraft wheel load on pavement damages by layered elastic method. *International Journal of Damage Mechanics*, 1141-1154.

Andersland, O., & Ladanyi, B. (2003). *Frozen ground engineering.* John Wiley & Sons.

ARA, Inc., ERES Consultants Division. (2004). *Guide for Mechanistic-Empirical Design of New and Rehabilitated Pavement Structures. NCHRP Project 1-37A.* Washington, D.C.: Transportation Research Board, Nacional Research Council.

Argue, G., & Denyes, B. (1974). Estimating the depth of pavement frost and thaw penetrations. *Transportation Research Record*.

Arnold, G. K. (2004). *Rutting of Granular Pavements.* University of Nottingham.

Arrhenius, S. (1896). XXXI. On the influence of carbonic acid in the air upon the temperature of the ground. *The London, Edinburgh, and Dublin Philosophical Magazine and Journal of Science, 41*(251), 237-276.

Bari, J. (2005). *Development of a new revised version of the Witczak E* predictive models for hot mix asphalt mixtures.* Arizona State University.

Bari, J., & Witczak, M. (2007). New Predictive Models for Viscosity and Complex Shear Modulus of Asphalt Binders. *Transportation Research Record*.

Baron Fourier, J. (1878). *The analytical theory of heat.* The University Press.

Bodin, D., Terrier, J., Perroteau, C., Hornych, P., & Marsac, P. (2010). Effect of temperature on fatigue performances of asphalt mixes. *11th International conference on asphalt pavements*.

Boreal Science. (2012). *Temperature Variation: Measuring Thermal Oscillation and Luminosity During a Full Day (Teacher's Guide).* WARD'S Science. Acesso em 27 de 04 de 2020, disponível em https://boreal.com/www.boreal.com/images/TempVarywLght.pdf

Boutonnet, M., Savard, Y., Lerat, P., St-Laurent, D., & Pouliot, N. (2003). Thermal aspect of frost-thaw pavement dimensioning: in situ measurement and numerical modeling. *Transportation Research Record, 1821*(1), 3-12.

Boyd, D. W. (1973). *Normal freezing and thawing degree-days for Canada.* Environment Canada.

Brian, N. M., Susan, L. T., Jean, A., James, T. S., Suzanne, P., & Ken, H. (2007). *The Road Well-Travelled: Implications of Climate Change for Pavement Infrastructure in Southern Canada.* Study for Environment Canada.

Brill, D. R. (2018). Introducing FAARFIELD 1.41: Latest Updates to FAA Airport Pavement Design Procedures. *IX ALACPA Seminar on Airport Pavements.* Quito, Ecuador.

Burmister, D. M., Palmer, L. A., Barber, E. S., & Middlebrooks, T. A. (1944). The theory of stress and displacements in layered systems and applications to the design of airport runways. *Highway Research Board Proceedings*.

Canestrari, F., Cardone, F., Graziani, A., Santagata, F. A., & Bahia, H. U. (2010). Adhesive and Cohesive Properties of Asphalt-Aggregate Systems Subjected to Moisture Damage. *Road Materials and Pavement Design*, 11-32.

Cengel, Y. A. (2003). *Heat Transfer. A practical approach.* New York, NY, USA: McGraw-Hill.

Chai, G., Bell, P., McNabb, K., Wardle, L., & Oh, E. (2022). Comparison of Flexible Airfield Pavement Designs Using FAARFIELD v1. 42 and APSDS 5.0. *Road and Airfield Pavement Technology,* 359-373.

Chamberlain, E. J. (1981). *Frost susceptibility of soil, review of index tests.* COLD REGIONS RESEARCH AND ENGINEERING LAB HANOVER NH.

Chee, K., & Ahmed, M. (2018). FIBER-ENHANCED ASPHALT AT TORONTO PEARSON INTERNATIONAL AIRPORT.

Chen, J., Wangb, H., & Xie, P. (2019). Pavement temperature prediction: Theoretical models and critical affecting factors. *Applied Thermal Engineering*, 113755.

CNN. (18 de 07 de 2022). *High temperatures caused section of UK airport's runway 'to lift'.* Fonte: CNN travel: https://www.cnn.com/travel/article/uk-airport-suspends-flights-amid-melting-runway-reports/index.html

Daniel, J., Jacobs, J. M., Miller, H., Stoner, A., Crowley, J., Khalkhali, M., & Thomas, A. (2018). Climate change: potential impacts on frost–thaw conditions and seasonal load restriction timing for low-volume roadways. *Road Materials and Pavement Design*, 1126-1146.

Devore, J. (2011). *Probability and Statistics for Engineering and the Sciences.* Cengage learning.

Diefenderfer, B. K., Al-Qadi, I. L., & Diefenderfer, S. D. (2006). Model to predict pavement temperature profile: development and validation. *Journal of Transportation Engineering*, 162-167.

Donghui, L. (2020). *Pavement Flooding Risk Assessment and Management in the Changing Climate.*

Doré, G., Grellet, D., Richard, C., Bilodeau, J., Pérez-González, E. L., & Barón H, M. F. (2019). *Mechanistic-Empirical Flexible Pavement Design software: i3c-me User`s Manual.* Québec city.

Elhakim, A. (2016). Estimation of soil permeability. *Alexandria Engineering Journal, 55*(3), 2631-2638.

Environmnet and Climate Change Canada. (2019). *Canada's Changing Climate Report.*

FAA. (2016). *150/5320-6F - Airport Pavement Design and Evaluation.* Federal Aviation Administration.

FAA, Advisory Circular. (1995). *Airport Pavement Design and Evaluation 150/5320-6D.*

Farrar, M. J., Harnsberger, P. M., Thomas, K. P., & Wiser, W. (2006). Evaluation of oxidation in asphalt pavements test sections after four year of service. *International Conference on Perpetual Pavement.* Western Research Institute.

Feng, D., Yi , J., Wang, D., & Chen, L. (2010). Impact of salt and freeze–thaw cycles on performance of asphalt mixtures in coastal frozen region of China. *Cold Regions Science and Technology*, 34-41.

Fleming, J. R. (2005). *Historical perspectives on climate change.* Oxford University Press.

Gary, C., Leigh, W., & Michael, H. (2016). Airfield pavement design for a major airport using FAARFIELD and APSDS. *Proceedings of the Eighth International Conference on Maintenance and Rehabilitation of Pavements*.

Ghanizadeh, A. R., & Ziaie, A. (2015). NonPAS: a program for nonlinear analysis of flexible pavements. *International Journal of Integrated Engineering*.

Godlewski, M. (13 de 05 de 2022). *Hay River Airport Flooded*. Acesso em 30 de 05 de 2022, disponível em FLYING: https://www.flyingmag.com/hay-river-airport-flooded/

Gong, X., Romero, P., Dong, Z., & Sudbury, D. S. (2016). The effect of freeze–thaw cycle on the low-temperature properties of asphalt fine aggregate matrix utilizing bending beam rheometer. *Cold Regions Science and Technology*, 101-107.

Gopalakrishnan, K. (2004). *Performance analysis of airport flexible pavements subjected to new generation aircraft.* University of Illinois at Urbana-Champaign.

Govenment of Canada. (21 de 04 de 2022). *Weather*. Acesso em 07 de 06 de 2022, disponível em Environment and natural resources: https://weather.gc.ca/

Government of Canada. (30 de 10 de 2019). *Floods*. Acesso em 28 de 04 de 2020, disponível em Get Prepared: https://www.getprepared.gc.ca/cnt/hzd/flds-en.aspx

Government of Canada. (25 de 11 de 2021). *Historical Climate Data*. Acesso em 04 de 02 de 2022, disponível em https://climate.weather.gc.ca/

Greater Toronto Airports Authority. (2020). *2020 capital maintenance*. Acesso em 08 de 06 de 2020, disponível em Toronto Pearson: https://www.torontopearson.com/en/corporate/our-future/this-years-projects

Greater Toronto Airports Authority. (2020). *Fast facts*. Acesso em 08 de 06 de 2020, disponível em Toronto Pearson: https://www.torontopearson.com/en/corporate/media/fast-facts

Grellet, D., Richard, C., & Pérez-González., E. L. (2019). *Mechanistic-Empirical Flexible Pavement Design software: i3c-me.*

GTAA. (2018). *Toronto Pearson International Airport Master Plan.* GTAA. Fonte: https://www.torontopearson.com/en/corporate/our-future/master-plan

GTAA. (2020). *GTAA Annual Report 2019.*

Gui, J., Phelan, P. E., Kaloush, K. E., & Golden, J. S. (2007). Impact of pavement thermophysical properties on surface temperatures. *Journal of materials in civil engineering*, 683-690.

Han, Z., Vanapalli, S., & Zou, W.-l. (2017). Integrated approaches for predicting soil-water characteristic curve and resilient modulus of compacted fine-grained subgrade soils. *Canadian Geotechnical Journal*.

Hansen, J., Johnson, D., Lacis, A., Lebedeff, S., Lee, P., Rind, D., & Russell, G. (1981). Climate impact of increasing atmospheric carbon dioxide. *Science*, 957-966.

Heymsfield, E., & Tingle, J. S. (2019). State of the practice in pavement structural design/analysis codes relevant to airfield pavement design. *Engineering Failure Analysis*, 12-24.

HoSang, V. A. (1978). Field survey and analysis of aircraft distribution on airport pavements. *Transportation Research Board Special Report*.

Huang. (1993). *Pavement analysis and design.*

Huang, H., Luo, J., Moaveni, M., Qamhia, I. I., Tutumluer, E., & Tingle, J. S. (2019). Advanced analytical tool for flexible pavement design and evaluation. *Airfield and Highway Pavements 2019: Design, Construction, Condition Evaluation, and Management of Pavements.*, 61-71.

Huang, Y. H. (2004). *Pavement analysis and design* (Vol. 2). Upper Saddle River, NJ: Pearson Prentice Hall.

Intergovernmental Panel on Climate Change. (2014). *Climate change 2014: synthesis report. Contribution of Working Groups I, II and III to the fifth assessment report of the Intergovernmental Panel on Climate Change.* Ipcc.

Islam, M. R. (2015). *Thermal Fatigue damage of asphalt pavement.* University of New Mexico.

Islam, M. R., & Tarefder, R. A. (2015). Temperature-Induced Fatigue Damage of Asphalt Pavement: Model Development and Evaluation. *Transportation Research Board*.

Jameson, G. (2008). *Guide to pavement technology: part 2: pavement structural design.*

Jet Brains. (02 de 03 de 2021). *The State of Developer Ecosystem 2020*. Acesso em 20 de 06 de 2022, disponível em Jet Brains.

Jiang, A., Liu, X., Czarnecki, E., & Zhang, C. (2019). Hourly weather data projection due to climate change for impact assessment on building and infrastructure. *Sustainable Cities and Society, 50*, 101688.

Kawa, I. (2012). *Pass-to-Coverage Computation for Arbitrary Gear Configurations in the FAARFIELD Program.* DOT/FAA/TC-TN12/47.

Kawa, I. (2017). *Development of New Subgrade Failure Model for Flexible Pavements in FAARFIELD.*

Khan, A., Mrawira, D., & Hildebra, E. E. (2009). Use of lightweight aggregate to mitigate frost damage in flexible pavements. *International Journal of Pavement Engineering*, 329-339.

Kim, M., & Tutumluer, E. (2008). Multiple wheel–load interaction in flexible pavements. *Transportation Research Record*, 49-60.

Kim, M., Tutumluer, E., & Kwon, J. (2009). Nonlinear pavement foundation modeling for three-dimensional finite-element analysis of flexible pavements. *International Journal of Geomechanics*, 195-208.

Kuo, S.-S., Mahgoub, H. S., & Holliday, R. D. (2004). Pavement Responses Due to Hard Landings of Heavy Aircraft. *Transportation Research Record, v. 1896*(n. 1), 88-95.

LCPC/AIRBUS/STBA. (2001). *A380 Pavement Experimental Program (PEP), AIRBUS INDUSTRIE, A380 Programme.* Toulouse, France.

Liu, M. (2020). *Evaluating Thermal Regime of Cold Region Roads for Climate Change Adaptation.* Waterloo: University of Waterloo, MS thesis.

Loizos, A., Armeni, A., & Pl, C. (2017). Evaluation of Airfield Pavements Using FAARFIELD. *Airfield and Highway Pavements*, 82-91.

Loizos, A., Armeni, A., Plati, C., & Cliatt, B. (2019). New challenges in evaluating bearing capacity of airfield pavements. *Airfield and Highway Pavements 2019: Innovation and Sustainability in Highway and Airfield Pavement Technology* (pp. 279-289). Reston: American Society of Civil Engineers.

Loizos, A., Armeni, A., Plati, C., & Cliatt, B. (2019). New Challenges in Evaluating Bearing Capacity of Airfield Pavements. *Innovation and Sustainability in Highway and Airfield Pavement Technology*, 279-289.

Look, B. G. (2007). *Handbook of geotechnical investigation and design tables.*

Lundström, R., Isacsson, U., & Ekblad, J. (2003). Investigations of stiffness and fatigue properties of asphalt mixtures. *Journal of materials science*, 4941-4949.

Lytton, R. L., Shanmugham, U., & Garret, B. (1983). *Design of asphalt pavements for thermal fatigue cracking.*

Meyer, M., Flood, M., Keller, J., Lennon, J., McVoy, G., Dorney, C., . . . Smith, J. (2014). *Strategic Issues Facing Transportation, Volume 2: Climate Change, Extreme Weather Events, and the Highway System: Practitioner's Guide and Research Report.* Washington DC: THE NATIONAL ACADEMIES PRESS.

Mills, B. N., Tighe, S. L., Andrey, J., Smith, J. T., Parm, S., & Huen, K. (2017). *Road well-traveled: Implications of climate change for pavement infrastructure in southern Canada.*

Ministry of Transportation of Ontario. (2013). *Pavement Design and Rehabilitation Manual.* Materials Engineering and Research Office.

Mohseni, A. (1998). *LTPP seasonal asphalt concrete (AC) pavement temperature models.* United States: Federal Highway Administration, Office of Engineering Research and Development.

Mojarrad, H. (2011). *Three dimensional nonlinear finite element analysis of airport pavements.* North Carolina State University.

Mrawira, D. M., & Luca, J. (2006). Effect of aggregate type, gradation, and compaction level on thermal properties of hot-mix asphalts. *Canadian Journal of Civil Engineering*, 1410-1417.

MTO. (2013). *Pavement Design and Rehabilitation Manual.* Materials Engineering and Research Office.

Muench, S., & Dam, T. V. (2015). Climate change adaptation for pavements. *FHWA-HIF-15-015*.

NASA. (2020). *Climate Change: How Do We Know?* Acesso em 02 de 04 de 2020, disponível em Global Climate Change, Vital Signs of the Planet: https://climate.nasa.gov/evidence/

NASA. (2020). *Climate Kids*. Acesso em 08 de 04 de 2020, disponível em NASA: https://climatekids.nasa.gov/greenhouse-effect/

National Business Aviation Association. (2020). *Toronto's Pearson Airport Requires General Aviation Flights to File Arrival, Departure Reservations*. Acesso em 08 de 06 de 2020, disponível em NBAA National Business Aviation Association: https://nbaa.org/aircraft-operations/international/region-i-north-america/torontos-pearson-airport-requires-general-aviation-flights-file-arrival-departure-reservations/

National Institute of Standards and Technology. (2002). *NIST/SEMATECH e-Handbook of Statistical Methods, Chapter 7*. National Institute of Standards and Technology. Acesso em 13 de 09 de 2022, disponível em http://www.itl.nist.gov/div898/handbook/

National Renewable Energy Laboratory. (2022). *NSRDB: National Solar Radiation Database*. Acesso em 08 de 06 de 2022, disponível em NREL: https://nsrdb.nrel.gov/

National Solar Radiation Database (NSRDB). (s.d.). *NSRDB Data Viewer*. Acesso em 16 de 02 de 2022, disponível em https://nsrdb.nrel.gov/

NOAA. (2020). *Global Climate Change Indicators*. Acesso em 02 de 04 de 2020, disponível em NOAA National Centers for Environmental Information: https://www.ncdc.noaa.gov/monitoring-references/faq/indicators.php#warming-climate

Özgan, E., & Serin, S. (2013). Investigation of certain engineering characteristics of asphalt concrete exposed to freeze–thaw cycles. *Cold regions science and technology*, 131-136.

Prairie Climate Centre. (2020). *Find & Display Local Data*. Acesso em 10 de 06 de 2020, disponível em Climate Atlas of Canada: https://climateatlas.ca/data/city/458/fdd_null_85/line

Prairie Climate Centre. (2022). *Climate Atlas of Canada*. Acesso em 07 de 06 de 2022, disponível em Climate Atlas of Canada: https://climateatlas.ca/

Prairie Climate Centre. (2022). *Climate Atlas of Canada*. Acesso em 04 de 11 de 2021, disponível em https://climateatlas.ca/

Rajbongshi, P., & Das, A. (2008). Thermal fatigue considerations in asphalt pavement design. *International Journal of Pavement Research and Technology* , 129-134.

Saarelainen, S. (1992). *Modelling frost heaving and frost penetration in soils at some observation sites in Finland: the SSR model.*

Schwartz, C. W. (2002). Effect of stress-dependent base layer on the superposition of flexible pavement solutions. *International Journal of Geomechanics*, 331-352.

Shaw, R., Pulhin, J., & Pereira, J. (2010). *Climate change adaptation and disaster risk reduction: Issues and challenges.* Emerald Group Publishing.

Shen, S., & Carpenter, S. (2007). Development of an asphalt fatigue model based on energy principles. *Asphalt Paving Technology-Proceedings*, 525.

Simpson, H. (2015). *Ground Water - An Important Rural Resource, Understanding Groundwater.* Toronto, Canada: Ministry of Agriculture, Food and Rural Affairs. Fonte: Ground Water - An Important Rural Resource, Understanding Groundwater.

Smith, S. L., & Burgess, M. M. (2004). *Sensitivity of permafrost to climate warming in Canada*. Acesso em 15 de 11 de 2021, disponível em https://doi.org/10.4095/216137

Solaimanian, M., & Kennedy, T. W. (1993). Predicting maximum pavement surface temperature using maximum air temperature and hourly solar radiation. *Transportation Research Record*, 1-1.

Stewart, C. (2010). Best Practices in the Design and Construction of Airfield Asphalt Pavements. *Canadian Airfield Pavement Technical Group (CAPTG).* Calgary, Alberta.

St-Laurent, D. (2012). *Routine mechanistic pavement design against frost heave.* Cold Regions Engineering 2012: Sustainable Infrastructure Development in a Changing Cold Environment.

Swarna, S., Hossain, K., Mehta, Y., & Bernier, A. (2022). Climate Change Adaptation Strategies for Canadian Asphalt Pavements; Part 1: Adaptation strategies. *Journal of Cleaner Production*, 132313.

TCCA. (1992). *Manual of Pavement Structural Design ASG-19.* Transport Canada Civil Aviation.

TCCA. (1995). *Pavement Structural Design Training Manual ATR-021 (AK-77-68-300).* Public Works & Govenment Services Canada.

TCCA. (2008). *AIRCRAFT LOAD RATINGS (ALR's).* Transport Canada, Sdandards Branch, Ottawa, Canada. Fonte: https://tc.canada.ca/sites/default/files/migrated/alr_table_e.pdf

Teltayev, B. B., Rossi, C. O., Izmailova, G. G., & Amirbayev, E. D. (2019). Effect of Freeze-Thaw Cycles on Mechanical Characteristics of Bitumens and Stone Mastic Asphalts. *Applied Sciences*, 458.

Tuleubekov, K. (2016). *Replacement of FAARFIELD Tandem Factors With Cumulative Damage Factor Methodology.*

Tutumluer, E. (1995). *Predicting behavior of flexible pavements with granular bases.* Georgia Institute of Technology.

Vanheule, H., Lu, D., Dutton, D., & Tighe, S. (19 de September de 2017). *Summary of Climate Change and Airfield Pavements Survey*. Acesso em 20 de 04 de 2020, disponível em CAPTG: http://www.captg.ca/docs/pdf/17Presentations/Tuesday%20PM/Summary%20of%20Climate%20Change%20and%20Airfield%20Pavements%20Survey.pdf

Wang, Y., Huang, Y., Rattanachot, W., Lau, K., & Suwansawas, S. (2015). Improvement of pavement design and management for more frequent flooding caused by climate change. *Advances in Structural Engineering, 18*(4), 487-496.

Wardle, L., & Rodway, B. (2010). Advanced design of flexible aircraft pavements. *ARRB Conference, 24th, 2010ARRB.*

Warren, F. J., & Lemmen, D. S. (2014). *Canada in a changing climate: Sector perspectives on impacts and adaptation.* Government of Canada. Fonte: https://www.nrcan.gc.ca/environment/resources/publications/impacts-adaptation/reports/assessments/2014/16309

Wei, S., Ning, L., Biao, M., Junping, R., Hainian, W., & Jian, H. (2015). Impact of freeze-thaw cycles on compressive characteristics of asphalt mixture in cold regions. *Journal of Wuhan University of Technology-Mater*, 703-709.

Whiteley, L. C. (2006). *Pavement Thickness Design for Canadian Airports.* University of Waterloo. University of Waterloo.

Xing, A., & Fredlund, D. (1994). Equations for the soil-water characteristic curve. *Canadian geotechnical journal*, 521-532.

Zapata, C., & Houston, W. (2008). *Calibration and validation of the enhanced integrated climatic model for pavement design.* Transportation Research Board.

Zapata, C., Andrei, D., Witczak, M., & Houston, W. (2007). Incorporation of environmental effects in pavement design. *Road Materials and Pavement Design*, 667-693.

Zapata, C., Yugantha, Y., & William, N. (2009). Matric Suction Prediction Model in New AASHTO Mechanistic–Empirical Pavement Design Guide. *Transportation Research record*, 53-62.

Zhao, H., Ma, L., & Zhang, J. (2018). Estimating the remaining life of airfield flexible pavements considering environmental factors. *HKIE Transactions*.

Zhao, X., Shen, A., & Ma, B. (2018). Temperature Adaptability of Asphalt Pavement to High Temperatures and Significant Temperature Differences. *Advances in Materials Science and Engineering*.

Zhao, X., Shen, A., & Ma, B. (2020). Temperature response of asphalt pavement to low temperatures and large temperature differences. *International Journal of Pavement Engineering*.